

Kinetic and Thermodynamic Aspects of Mg and Mg-Ti hydride Nanomaterials

PROEFSCHIFT

Ter verkrijging van de graad van doctor
aan de Technische Universiteit Delft,
op gezag van de Rector Magnificus prof. ir. K.C.A.M. Luyben,
voorzitter van het College voor Promoties,
in het openbaar te verdedigen op 7 Oktober 2014
door

Anca ANASTASOPOL

Master of Science, Technische Universiteit Delft
geboren te Medgidia, Romania

Dit proefschrift is goedgekeurd door de promotor:

Prof. Dr. F.M. Mulder

Samenstelling promotiecommissie:

Rector Magnificus	Voorzitter
Prof. F.M. Mulder	Technische Universiteit Delft, promotor
Dr. S.W.H. Eijt	Technische Universiteit Delft, co-promotor
Prof. Dr. A. Schmidt-Ott	Technische Universiteit Delft
Prof. Dr. B. Dam	Technische Universiteit Delft
Prof. Dr. P.E. de Jongh	Universiteit Utrecht
Prof. Dr. A. Pundt	Institut für materialphysik, Gottingen
Prof. Dr. A. Züetzel	EMPA, Zurich
Prof. Dr. E.H. Brueck	Technische Universiteit Delft, reservelid

Published by: Ridderprint BV, The Netherlands

Cover: "Hands on " by Nina Middelkoop, Ridderprint BV

ISBN: 978-90-5335-928-0

Copyright©2014Anca Anastasopol

All rights reserved. No part of the material protected by this copyright notice may be produced or utilized in any form or by any means, electronic or mechanical, including photocopying, recording or by any information storage and retrieval system, without written permission from the author and adequate citation.

The research presented in this thesis was funded by AgentschapNL

*Dedicated to my husband Joost, my daughter Nina
and the most remarkable woman I know,
my mother Niculina*

Table of contents

Foreword	1
Chapter 1. Introduction.....	5
Chapter 2. Fractal disperse desorption kinetics and structure of spark discharged Mg and Mg/Pd, Mg/Nb nanocomposites.....	25
Chapter 3. Reduced enthalpy of metal hydride formation for Mg–Ti nanocomposites produced by spark discharge generation	53
Chapter 4. Thermal stability of Mg_yTi_{1-y} and $Mg_yTi_{1-y}H_x$ thin films.....	75
Chapter 5. Structure and hydrogen storage properties of <i>in situ</i> spark discharge generated MgH_x nanoparticles.....	105
Chapter 6. Low temperature hydrogen cycling and structural investigation of <i>in situ</i> spark discharge generated fluorite $Mg_yTi_{1-y}H_x$ nanoparticles.....	127
Chapter 7. Towards air resistant sulfur coated MgH_2 powders	149
Summary /Samenvatting	175
Appendix. Background in X-ray diffraction.....	181
List of Publications	183
Acknowledgements	185
Curriculum vitae	187

Foreword

*“There is a tide in the affairs of men.
Which, taken at the flood, leads on to fortune;
Omitted, all the voyage of their life
Is bound in shallows and in miseries.
On such a full sea are we now afloat,
And we must take the current when it serves,
Or lose our ventures”*

William Shakespeare,
Julius Caesar Act 4, scene 3, 218–224

The need for energy storage takes new shapes with every new generation and is a prerequisite for sustaining technological advancements. But on the overall, there is a great increase in the demand of efficient storage of energy in close connection to the exploitation of renewable energy resources. Whether for stationary or mobile applications, for small or large scale devices, stored energy is needed from a compact, efficient and reliable medium.

The most widely used energy sources nowadays are based on fossil fuels which still represent a staggering 87.1% of the total market according to the latest Intergovernmental Panel on Climate Change (IPCC) report on Renewable Energy.¹

In this context, the interest in renewable energy sources is inextricably linked to the realization of the risks and limitations related to fossil fuels.^{2,3} Thus, during the economic crisis in the 1970's the limited availability of fossil fuels was realized which led to a series of measures for improving energy efficiency of buildings and vehicles. At the same time, research into alternative energy sources was stimulated. In the 1980's, pollution as a result of burning fossil fuels was considered a major problem and measures were taken to counter act it. At the same time, research into alternative energy sources got another nudge. For the great part of the 1990's and early 2000's culminating with the Kyoto Protocol adopted in 1998, CO₂ and other green house gases obtained from burning fossil fuels are seen as the main culprits in the global warming scenario. This has constituted the motor for policy changes, investments and developments of alternative energy sources.^{4,5}

At the same time that the risks of using fossil fuels are the motor for developments in renewable energy, the fluctuating character of some renewable energy sources stimulate the search for more efficient and versatile energy storage methods. Thus, research in energy storage systems is closely linked to the implementation of renewable energy sources with an intermittent character. It is expected that a steady increase in investments and

implementation of renewable and sustainable energy sources will occur over the next decades.¹ Solar and wind power have benefitted of an increase of over 50% and 30% respectively in the total energy production over the last years.^{6,7,8}

The type of energy storage system needed can be divided into stationary and mobile. Aside from fossil fuels, the most widely used energy storage form is pumped hydropower which is exclusively stationary and also currently by far the largest capacity renewable form of energy storage. There is also growing interest in thermal energy storage systems where mostly either phase change materials or underground thermal energy storage is used.

Energy storage for mobile applications includes electrical energy storage in batteries for the most part. Chemical energy storage in fuels such as hydrogen and methane or methanol has the great advantage of having higher energy density and of being potentially easier to integrate into the already existing infrastructure.

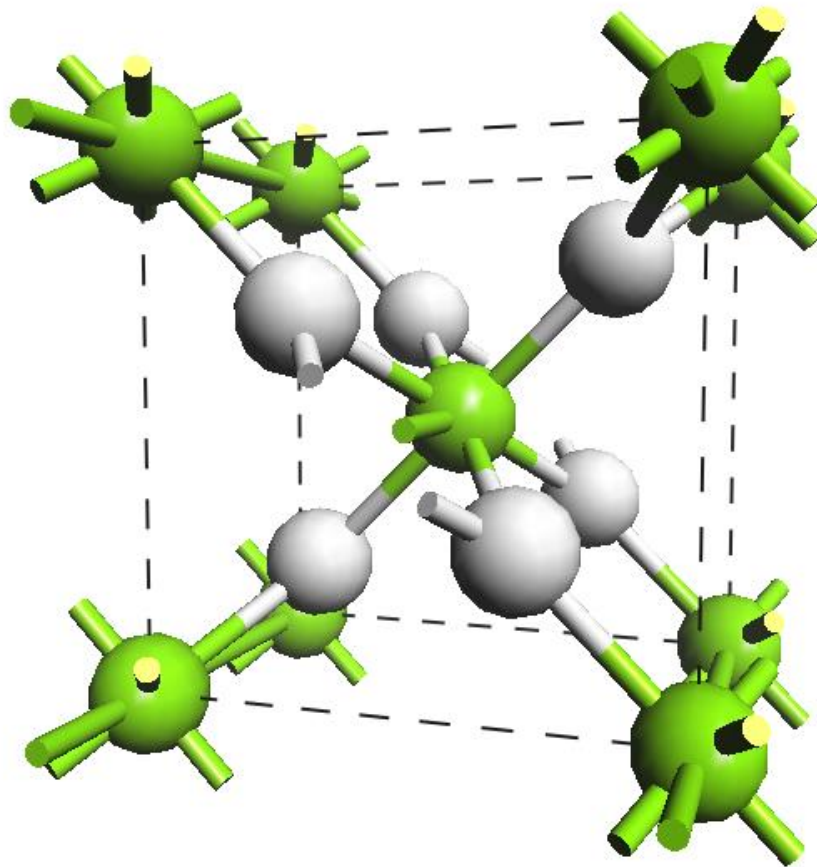
The thesis presented here concerns the storage of hydrogen in light, nanostructured Mg based materials. The research focusses on fundamental and practical aspects such as the stability and the reaction rate of hydrogen uptake and release but also the air sensitivity of the MgH_2 compounds. These aspects are important for the application of MgH_2 as a hydrogen storage medium for mobile or static devices.

References

- (1) IPCC *Special Report on Renewable Energy Sources and Climate Change Mitigation*; Cambridge University Press: United Kingdom and New York, NY, USA, 2011.
- (2) Chu, S.; Majumdar, A. Opportunities and Challenges for a Sustainable Energy Future. *Nature* 2012, *488*, 294-303.
- (3) Turner, J. A. A Realizable Renewable Energy Future. *Science* 1999, *285*, 687-689.
- (4) Schlapbach, L.; Züttel, A. *Nature* 2001, *414*, 353.
- (5) Züttel, A.; Borgschulte, A.; Schlapbach, L. Hydrogen as a Future Energy Carrier. 2008. Weinheim, Wiley-VCH.
- (6) Stampfer, J. F.; Holley, C. E.; Suttle, J. F. The Magnesium-Hydrogen System¹⁻³. *Journal of the American Chemical Society* 1960, *82*, 3504-3508.
- (7) Winsche, W. E.; Hoffman, K. C.; Salzano, F. J. Hydrogen: Its Future Role in the Nation's Energy Economy. *Science* 1973, *180*, 1325-1332.
- (8) Jones, L. W. Liquid Hydrogen As a Fuel for the Future. *Science* 1971, *174*, 367-370.

Chapter 1

Introduction



“Oui, mes amis, je crois que l'eau sera un jour employée comme combustible, que l'hydrogène et l'oxygène, qui la constituent, utilisés isolément ou simultanément, fourniront une source de chaleur et de lumière inépuisables et d'une intensité que la houille ne saurait avoir.”

(Yes, my friends, I believe that water will one day be used as fuel, that hydrogen and oxygen which constitute it, used isolated or together, will provide an inexhaustible source of heat and light, of an intensity that coal is not capable.)

Jules Verne, “L'Île Mystérieuse” (The Mysterious Island)

Soon after the discovery of hydrogen by Cavendish in 1766, its great potential as a fuel is exploited first in a hydrogen balloon and hydrogen dirigible and later as fuel for rocket propulsion. However, its explosive nature led to devastating accidents which made it unpopular for wider scale use.

At the beginning of the 1970's, the energy crisis experienced by the industrialized world turned the attention to finding alternative fuels. Hydrogen is again taken into consideration as a viable alternative to fossil fuels. It is at this time that the discussion of hydrogen as the fuel of the future and the hydrogen economy starts in the scientific community.^{2,3}

There are a few factors that make hydrogen a very attractive energy carrier. The most obvious one is its high gravimetric energy density of 140 MJ/kg compared to 48 MJ/kg for gasoline and 43 MJ/kg for methane. Another useful feature of hydrogen is its versatility as it can react with oxygen explosively when used in a combustion engine but also electrochemically in a fuel cell. In addition, hydrogen has the potential of being a clean fuel because the burning product is water. But above all it is renewable and abundant as it can again be obtained from splitting water molecules into the elements either by electrolysis or by direct solar conversion. This makes a hydrogen cycle possible.^{4,5,6}

The special properties of hydrogen that constitute great advantages, also pose great challenges. The high reactivity of hydrogen means that it does not exist free on earth but it is bound in various chemical compounds such as water, hydrocarbons, carbohydrates and other organic and inorganic compounds. To be used as a fuel its molecular form, H₂ first has to be synthesized and stored. Both these issues are of great importance in a hydrogen economy.

1.1.1. Hydrogen as energy carrier

In normal conditions, hydrogen is a colorless and odorless gas. It is the lightest element and it has three isotopes. The most abundant is protium, ^1H that constitutes over 99.98%. Then deuterium ^2H or D with mass 2 makes up 0.015% and ^3H tritium with mass 3 occurs very rarely in nature since its radioactive decay half life is only 12.32 years and it is mostly obtained from nuclear reactions. Atomic hydrogen is extremely reactive and a strong reducing agent and this is the reason why hydrogen is not found free on earth.

Molecular hydrogen is a stable compound; however, it does not exist free in atmosphere because it reacts with oxygen in a wide composition range. Natural molecular hydrogen is a mixture of 75% *ortho* and 25% *para* hydrogen depending on the orientation of the nuclear spins. *Ortho* hydrogen has the nuclear spins oriented parallel and *para* hydrogen has the nuclear spins oriented anti parallel. They have different physical properties and the conversion of the higher energy level *ortho* to *para* hydrogen at low temperatures has implications in the liquefaction of hydrogen.⁷

Table 1 summarizes some physical properties of molecular hydrogen. The low density of hydrogen even in liquid form leads to a low volumetric energy density of about 8.49 MJ/m³, about three times less than gasoline (31.15 MJ/m³). Apart from its low density, hydrogen also has very high diffusivity in air which in case of leaks is an advantage because it will disperse in air quickly. Its energetic reaction with water makes it also highly explosive in a wide concentration range.

Table 1. *Physical properties of molecular hydrogen*⁷

Property	Value
Molecular weight	2.01594 a.u.
Density of gas (273K, 1 bar)	0.08987 kg/m ³
Density of liquid (20K)	70.6 kg/m ³
Density of solid (14K)	70.8 kg/m ³
Boiling temperature (1 bar)	20 K
Critical temperature	33 K
Critical pressure	12.8 bar

Hydrogen as fuel can be used in mobile devices in an internal combustion engine. Due to its high flammability range (4-75%), low ignition energy (17 kJ) and complete combustion, hydrogen can be used in small concentrations in an air/fuel mixture and still one may obtain high efficiency. But it can also be used as pure hydrogen gas in a spark ignited engine similar to the gasoline engine. The hydrogen internal combustion engine has a higher research octane number, >120 compared to gasoline which is typically in the range 91-99. For this reason, hydrogen-hydrocarbon mixed fuels already exist commercially and they proved superior performance to gasoline fuels.⁸ The burning in air imposes the requirement of a modified engine to reduce burning temperature and residence time, in order to reduce NO_x formation.

The chemical energy from the reaction of hydrogen with oxygen can also be converted directly to electrical energy in hydrogen fuel cells. There are several types of fuel cells varying widely in operating temperatures and efficiencies. In increasing order of operating temperatures, the types of fuel cells are: proton exchange membrane fuel cell (353 K), alkaline fuel cell (333 K-363 K), direct methanol fuel cell (333 K- 403 K), phosphoric acid fuel cell (423 K - 473 K), molten carbonate fuel cell (~ 923 K) and solid oxide fuel cell (723 K - 1273 K).^{8,9}

The low operation temperature make the proton exchange membrane fuel cell the most suitable for mobile applications. The higher temperature operating fuel cells such as the molten carbonate fuel cell and the solid oxide fuel cell have superior efficiency and are more suitable for stationary use in power stations.⁹

1.1.2. Methods for storing hydrogen

In normal conditions of temperature and pressure, hydrogen is a gas with very special physical and chemical properties that make it difficult to handle (see Table 1). The type of storage and transportation needed for hydrogen depends in a great measure on the scale needed. On a large scale, hydrogen can be transported in pipelines very much like natural gas. However, on a small scale and for mobile applications, safe and efficient storage media must be found for the storage and transportation of hydrogen.

According to the aggregation state, hydrogen storage systems can be divided into three main categories:

1. Compressed hydrogen gas cylinders
2. Liquid hydrogen cylinders
3. Solid state storage

Hydrogen can be compressed in high pressure vessels to a density up to 36 kg/m³. The cylinders are built of materials that do not suffer from hydrogen embrittlement such as copper, aluminum and austenitic steels (AISI 316 and AISI 316L). However, the higher volumetric energy density comes at the cost of the gravimetric density because cylinder walls must be thicker to contain the pressure and to limit the hydrogen permeation at high pressures. Depending on the material they are made of and implicitly the maximum pressure of the gas, high pressure vessels can be classified into four categories^{10,11}: Type I (metal cylinders, 200-300 bar), Type II (metallic liner wrapped in a composite resin), Type III (metallic liner fully wrapped in a composite resin, 350-700bar), Type IV (polymeric liner wrapped in a composite resin). Hydrogen can be stored in all these type of cylinders, however, for mobile applications type IV is the most suitable because it is the most resistant to a possible impact or explosion. The high explosive potential of hydrogen coupled with the transportation in high pressure vessels makes it necessary to embed extra safety measures such as a Thermal Pressure Release device (TPRD).^{11,12}

An even higher density of 70.8 kg/m³ can be obtained by liquefying hydrogen and storing it in cryogenic vessels. However, the low critical temperature of hydrogen (33 K) poses some important technological challenges related to the thermal insulation of the vessel and the energy

efficiency of the liquefaction. Thus, the enthalpy change from gaseous H_2 at 300K to liquid H_2 at 20 K is about 12 MJ/kg which represents a fraction of the energy of hydrogen available from combustion making it a less efficient hydrogen storage method. But in practice the total energy loss by storing H_2 as a liquid amounts to 40% of the total combustion energy of 141.8 MJ/kg.

^{13,14 15}

Hydrogen storage in solids presents important advantages in terms of safety and it is more compactly packed than both the liquid and compressed gas alternatives.⁵ The use of light metal hydrides makes solid state tanks for mobile applications possible because of their increased energy density per kg weight. However, they can also be a viable candidate for stationary use in combination with (renewable electricity) power plants. Hydrogen can be produced with the excess energy and then stored for later use when energy production is decreased. This scenario is very likely if fluctuating energy sources such as sun and wind are used. Storage of energy in the form of hydrogen is easily scalable and it can be designed for both short and long term storage.

Though there is a broad range of stable chemical compounds which contain hydrogen, only those chemicals which can release hydrogen gas are considered as hydrogen storage media. Thus, most hydrocarbons will not be considered as hydrogen storage compounds. An exception is represented by cyclohexane which can be reduced to benzene and molecular hydrogen is released.

A great deal of research has been done in the storage of hydrogen in solid compounds, either through weak interactions (physisorption at surfaces) or stronger interactions (interstitial and chemical hydrides).

Compounds that can be used for physisorption of hydrogen are porous chemicals onto which molecular hydrogen is bound by weak Van der Waals interactions. The Van der Waals interaction has two components, one attractive which is a power of -6 to the distance of the hydrogen molecule and the surface and a repulsive term which is a power -12 of the distance. The energy minimum of the potential energy for the hydrogen molecule as an adsorbate ranges between 1 and 10 kJ/mol. This requires cryogenic temperatures for the storage of hydrogen. The typical compounds investigated as potential hydrogen storage media through physisorption are porous carbons^{13,16,17} (activated carbon, carbon nanotubes, graphitic nanofibers), zeolites^{13,18} and metal organic frameworks¹⁹. The hydrogen storage in these type of compounds is entirely reversible and it can reach high gravimetric storage capacity of about 10 wt.% (NOTT-112 at 77 K and 77 bar)^{20,21}. However, the low temperatures that are still needed for the storage of hydrogen can limit their applicability.

Hydrogen can also be bound in solids by chemical bonds in which case the interaction energy is higher than van der Waals interaction in porous materials. With some exceptions in the middle of the periodic table (e.g. Fe, Co), most elements in the periodic system react with hydrogen to produce hydrides. Hydrides can be ionic, covalent, metallic or polymeric and in most cases, a clear distinction between the bonding types cannot be made. Among them, metal hydrides represent very attractive properties as hydrogen storage media. They have very high volumetric storage capacity, 110 kg H_2 /m³ for Mg H_2 compared to 70.8 kg/m³ for liquid H_2 . The magnitude of the metal-hydrogen interaction in binary hydrides varies within very wide limits, from

unstable compounds such as $\text{FeH}_{0.5}$ with enthalpies of formation of $\Delta H = +20 \text{ kJ/molH}_2$ two very stable hydrides such as HoH_2 with $\Delta H = -226 \text{ kJ/molH}_2$ and TiH_2 with $\Delta H = -192 \text{ kJ/molH}_2$.¹³ The stability of MgH_2 is situated in between these values, $\Delta H = -75 \text{ kJ/molH}_2$

In intermetallic compounds such as LaNi_5H_6 or Mg_2NiH_2 , hydrogen can be packed even more tightly at densities higher than $120 \text{ kgH}_2/\text{m}^3$ but at the cost of a decrease in the gravimetric capacity which is important in mobile applications. According to Zuttel et al.¹³ intermetallic hydrides can be classified into seven general classes according to their composition: AB(ex. TiFe), AB_2 (ex. ZrV_2), AB_3 (ex. CeNi_3), AB_5 (ex. LaNi_5H_6), A_2B_7 (ex. Y_2Ni_7), A_6B_{23} (Y_6Fe_{23}), A_2B (ex. Mg_2Ni) and their stability can be estimated according to the Miedema model that the more stable an intermetallic compound is, the less stable its hydride will be.^{22,23}

Because of their incomplete d shell, transition metals can also form complex hydrides. A very attractive compound is Mg_2FeH_6 because of its gravimetric capacity of 5.6 wt% and volumetric capacity of $\sim 150 \text{ kgH}_2/\text{m}^3$. However, most complex hydrides are rather stable with enthalpies of formation $\Delta H < -80 \text{ kJ/molH}_2$. A disadvantage is that the hydrogen desorption reaction is incomplete and occurs in multiple steps at high temperatures. This limits their applicability as hydrogen storage media.

Another class of hydrides that attracted attention because of their light weight and interesting properties are complex hydrides. They are formed of alkaline and earth metals. Among them, the most well studied are NaAlH_4 , LiBH_4 , NaBH_4 and $\text{Mg}[\text{BH}_4]_2$. The biggest challenge with most of these compounds is the fact that they are not directly reversible and that the B containing ones can release toxic BH_3 gases upon decomposition. Moreover, for the complex hydrides the dehydrogenation is not complete and hydrogen is released in multiple steps.

For hydrogen to be an economically viable energy carrier, its storage and transportation needs to fulfill some basic requirements for the storage material: abundant, nontoxic, have a reversible reaction with hydrogen, low cost and safe. For storage of hydrogen in mobile applications, the conditions are even more stringent. According to the Department of Energy of the United States (DOE) among others, light weight and high charging and discharging rates are required in addition.²⁴ Mg is one of the attractive materials that have great potential as hydrogen storage medium in view of its low weight, its high hydrogen density up to 7.4 wt.%, and its natural abundance.

1.1.3. Hydrogen storage in magnesium

Among the various hydrides discussed above, MgH_2 is a very attractive material because its reaction with hydrogen is reversible, Mg is one of the most abundant elements in the earth's crust, making up about 2.1%, it is nontoxic and safe and as far as mobile applications are concerned it is one of the lightest metals.

Interest in magnesium as a hydrogen storage material can be tracked as early as the 1970's.^{3,25} The pioneering work of Bogdanovic et al.^{26,27,28} constitutes the base of what is mostly known today about the interaction of Mg with H.^{27,28,29,30} Very early on into the research, the advantages and

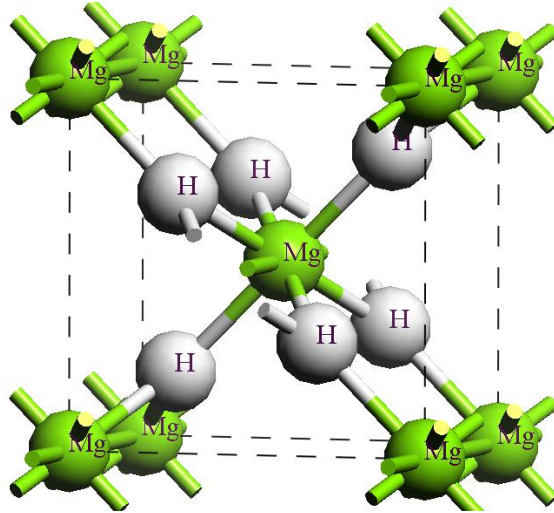


Figure 1.1. Crystalline structure of β -MgH₂ (space group $P4_2/mnm$) isostructural with rutile

disadvantages of using Mg as a hydrogen storage material were established. The main disadvantages are the rather high stability of the MgH₂ ($\Delta H = -75 \text{ kJ/molH}_2$) and the slow kinetics of the hydrogen sorption reaction which can be translated in energetic terms as an activation energy barrier ranging from 140 to 210 kJ/molH₂.^{31,32} Moreover, the high reactivity of Mg with oxygen and water poses again practical difficulties in handling the material.⁷

These very important limitations of MgH₂ have been addressed in the research of Mg-H in the past forty years and constitute the main drivers for the current work. (see section 1.3)

Magnesium is an alkaline-earth metal that crystallizes in a hexagonal closed packed structure, in $P6_3/mmc$ space group. As it can be seen in its phase diagram in Figure 1.2, at equilibrium, metallic magnesium can store low amounts of hydrogen as an interstitial atom in the α phase, typically about 0.131 at.%¹ (the exceptions from this value are discussed in the present thesis in Chapter 5). At higher hydrogen concentrations, a transition to the β -MgH₂ metal hydride phase occurs which crystallizes in a tetragonal rutile type of structure in $P4_2/mnm$ space group (see Figure 1.1.)

Though the rutile MgH₂ is the most stable and well known structure of the compound, a few metastable crystalline structures are also known which are distortions from the tetragonal structure and are obtained at high pressures. Thus, the γ -MgH₂ is isostructural with α -PbO₂ which is an orthorhombic structure in the $Pbcn$ space group. Another high pressure structure is δ -MgH₂ which has a distorted fluorite CaF₂ structure. A fluorite type of hydride is also reported in thin film synthesis of Mg-Ti films. Theoretical studies on the fluorite Mg_yTi_{1-y}H_x structure have predicted a destabilization of the hydride as a function of the ratio of the metals present in the structure. Experimentally, the fluorite hydride was observed in Mg-Ti thin films.³³

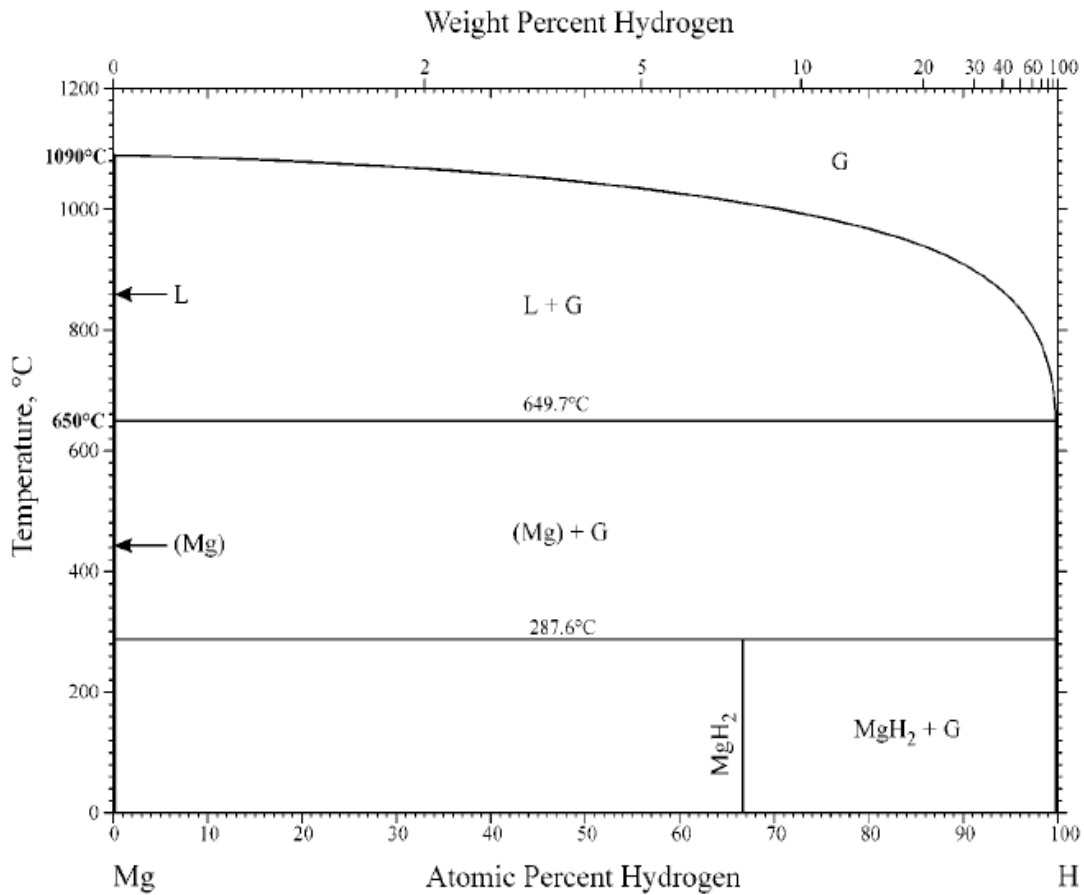


Figure 1.2. *Mg-H phase diagram¹ at 1 bar p_{H_2} equilibrium pressure*

The most commonly used route of increasing the hydrogen sorption kinetics in magnesium hydride is the synthesis of nanocrystalline materials. The most straightforward rationale for nanostructuring is that this reduces diffusion distances for H through the solid phase, and it increases available surface area for reacting with H_2 . Here, two main approaches can be distinguished, the top down approach and the bottom up approach.

The top down method is mostly represented by ball milling and is the most used and accessible method of producing nanocrystalline materials. Important breakthroughs have been obtained in the study of Mg based metal hydrides during ball milling and introducing concepts such as grain refinement at the addition of transition metal based catalysts.^{35,36,37,38,39,40,41}

The bottom up method can either be a physical approach such as magnetron sputter deposition or spark discharge generation and or it can be a wet chemical method of reducing Mg containing organometallic compound. Very interesting results are produced on both the physical and the chemical route with respect to the sorption kinetics and temperatures and reversibility.

Through magnetron sputter deposition and spark discharge generation, the mixture of the elements in the gas phase can lead to unique properties of the end materials.^{42,43,44} Thus, metastable alloys can be prepared in this way. The spark discharge method has the extra advantage of producing nanoparticle agglomerates with primary particle sizes below ~ 20 nm.

The wet chemical method of preparing magnesium nanoparticles can lead to a narrow size distribution of the Mg nanoparticles confined in an organic matrix. However, even though the organometallic compounds are reduced and Mg is produced, the Mg nanoparticles cannot be separated from the reaction matrix^{45,46} and the gravimetric energy density of Mg is also reduced.

Another way in which the slow hydrogenation and dehydrogenation kinetics is addressed is by decreasing the activation energy through the use of transition metal catalysts. The need for transition metal catalysts comes from their ability to spontaneously split the hydrogen molecule into hydrogen atoms. For magnesium, the omnipresent MgO layer makes that this process is energetically costly and makes the hydrogen sorption reaction slow. The most used catalysts are Pd, V, Nb, Ti, Ni, , metals that are more easily reduced during H₂ sorption. ^{40,41,47,48,49,50,51} In the present study, Pd, Nb and Ti were used to decrease the activation energy for hydrogen sorption.

A very important problem of MgH₂ to be tackled is its relatively high stability related to its standard enthalpy of formation of about -75 kJ/molH₂. This value limits the amount of net energy that can be obtained from hydrogen as a fuel since a high operation temperature of about 550 K is required at 1 bar and also makes MgH₂ unsuitable to be used in combination with low temperature fuel cells. An enthalpy of formation of about -40 kJ/molH₂ is the targeted value for a hydrogen storage material.

The use of nanoparticulate magnesium can both directly and indirectly affect thermodynamic properties in the interaction with hydrogen. Theoretical calculations on the stability of magnesium nanoclusters have resulted into an estimated destabilization of 10 kJ/molH₂ for clusters below 1.8nm.⁵² Further, the introduction of nanosized transition metal catalysts to magnesium nanoparticles creates new interfaces which can have a strong influence in the free energy of the hydride system. Also, kinetics of hydrogen sorption can be enhanced due to the small diffusion distances present and the large surface to volume ratios.

Therefore, tailoring Mg-based nanomaterials holds large promises for achieving suitable hydrogen storage properties.

*“So I want to build a billion tiny factories, models of each other,
which are manufacturing simultaneously, drilling holes,
stamping parts, and so on.”*

Richard Feynman, “There’s plenty of room at the bottom”

With his challenge to investigate the “room at the bottom”, Richard Feynman opened an exciting chapter in both science and technology. Life today is hard to imagine without the great improvements that nanotechnology brought. The developments in portable electronic devices, drug delivery systems and electrochemical energy storage are direct results of intense research and investments in nanoscience and nanotechnology. The work that this thesis is based on has at its core the investigation of Mg based nanomaterials for hydrogen storage.

The interest in Mg as a hydrogen storage medium is not a very recent idea.^{25,53,54,55} And yet, new findings on the behavior of Mg as a storage medium for hydrogen are presented in this thesis. The source of the novelty of our results is for a great part based on the use of nanoparticulate Mg. We use nanomaterials as a key tool to accelerate the hydrogen sorption reactions and obtain suitable thermodynamic properties.

1.2. Magnesium nanoparticles synthesized by spark discharge generation

Typically, particles below 100 nm are considered to be nanoparticles. The small size leads to a high surface to volume ratio which has implications on the structure, chemical reactivity and physical properties of the particles.⁵⁶ With these considerations, some of the physical and chemical properties of the Mg –H system can be tuned to make it a viable hydrogen storage system.

For the most part, the nanomaterials presented here are synthesized using a bottom up approach, by spark discharge generation. The technique leads to formation of nanoparticles and agglomerates of nanoparticles in contrast to nano crystallites or nanosized grains as part of larger size particles typically produced in top down approaches such as ball milling.

The production of nanoparticles by using an electric spark discharge generator was first reported in 1988 by Schwyn et al⁵⁷. At that time, 1.3nm Au particles

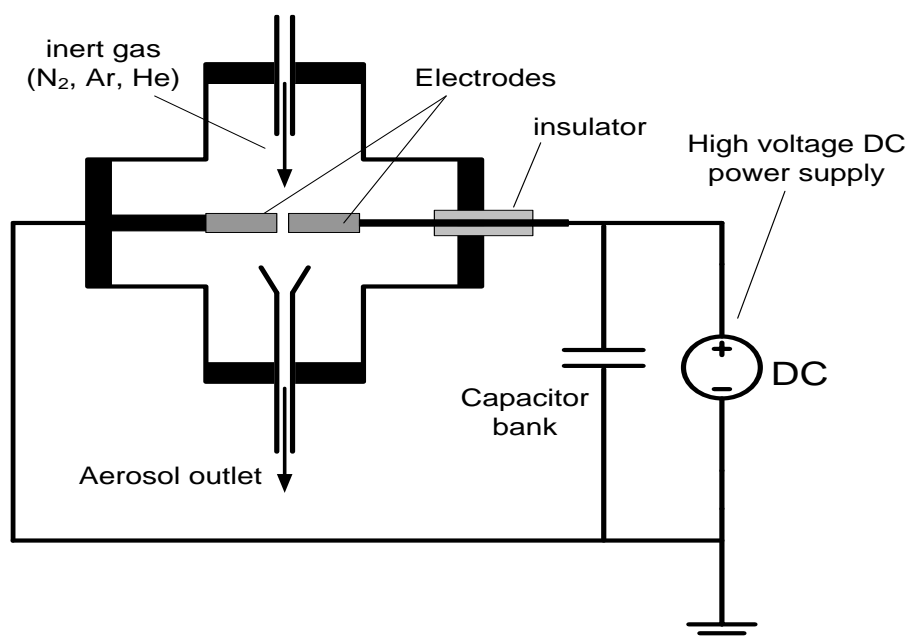


Figure 1.3. *Schematic of the spark discharge generator*

were produced in the aerosol and its pioneers advocated that any conducting materials could be used to produce nanoparticles of high purity and a small size distribution using the spark discharge generator. Indeed, many metal nanoparticle systems have been synthesized during the past decades including the alloys of immiscible metals.

In the spark discharge generator, two conducting electrodes are mounted in the reaction chamber opposing each other at a distance of a few millimeters. They are connected to a capacitor bank and a high voltage power supply which is used to charge a capacitor at constant current. In the reaction chamber, a gas (e.g. Ar, H₂, N₂) is flowing continuously through the gap between the electrodes. When the breakdown voltage of the gas is reached, a discharge between the electrodes occurs and a spark is created. The process is repeated with a frequency ranging typically between 0 – 50 Hz. The high temperature of the spark causes the surface of the electrodes to form vapors which will quickly condense into particles. The aerosol created in this way is carried away with a gas and collected on a polymer filter. In this process particles can grow and show a tendency to agglomerate.

The process can be tuned to the selection of small sized particles by a selection of the flowing gas and flow rate. The use of Mg electrodes poses more constraints in the use of the carrier gas in terms of its purity. The already high reactivity of Mg with oxygen and water is enhanced for nanoparticles. Thus, precautions have to be taken that both the reaction chamber and the carrier gas are baked and respectively purified to remove most of the water and oxygen. A purification system of a double set of water and oxygen traps is used for the purification of the gas.

A very high degree of mixing at atomic scale between different metals is possible in the spark discharge generator can be exploited to create mixed metal aerosols. The setup is very versatile and it can be built in different configurations to create either alloys or mixtures of the elements used. The nanomaterials synthesized and analyzed in the current thesis are a clear

illustration of this versatility. Nanosized Pd and Nb catalysts were mixed with Mg nanoparticles using a double spark discharge generator where in the first chamber Mg nanoparticles are produced and the aerosol is carried through the electrodes of a second spark discharge chamber where Nb or Pd aerosols are produced (see Chapter 2). Tabrizi et al.⁴² already showed that spark discharge generation makes the synthesis of metastable alloys possible using either two different electrodes or mixed electrodes. Here we used the method of two different electrodes of Mg and Ti, to produce Mg/Ti metastable cubic phase (see Chapter 3).

Furthermore, replacing the inert carrier gas (Ar, He) with a reactive one such as H₂, lead to the *in situ* synthesis of a supersaturated Mg-H solid solution which is typically not observed in the conventional synthesis of MgH₂, but also the conventional rutile type MgH₂ (see Chapter 5). Finally, combining the synthesis of metastable Mg-Ti alloy *in situ* with a H₂/Ar carrier gas leads to the direct synthesis of a cubic fluorite type Mg_{1-y}Ti_yH_x which is not only less stable than conventional MgH₂ but has also a low hydrogen desorption activation energy (see Chapter 6) and largely enhanced hydrogen sorption kinetics.

1.3. Overview present thesis

Kinetic and thermodynamic aspects of the hydrogen interaction with magnesium nanoparticles and Mg-Ti nanocomposites generated by spark discharge represent the focus of the current thesis. However, also sputter deposited thin films and ball milled nanoparticles are used as study cases for the introduction of new routes of improving the performance of these types of nanomaterials for hydrogen storage.

In *Chapter 2*, a multiple reaction rates model for the solid state kinetics of desorption is proposed which deviates from the widely applied model known as the Johnson-Mehl-Avrami-Kolmogorov (JMAK). The study is conducted on spark discharge generated magnesium nanoparticles, Mg/Pd and Mg/Nb nanocomposites. They present a fractal like morphology with a primary particle size of 10 nm surrounded by MgO shells of 1-2 nm thick. Using thermal desorption spectroscopy, it is observed that hydrogen desorption starts at remarkably low temperatures of 350 K and extends over a broad temperature range to beyond 700 K. The desorption at low temperatures is due to the presence of nanoparticles while the desorption at higher temperatures is caused by the presence of oxide shells acting as activation barriers. This broad desorption profile together with the structural morphological inhomogeneities observed in the sample constitute the drive for elaborating a kinetic model which will account for the complexity of the sample.

In *Chapter 3*, the study of Mg-Ti nanocomposites reveals important advances related to the compounds obtained and the thermodynamic properties of the system. The observed destabilization of the hydride may be considered a breakthrough when comparing the magnitude of the effect. In spite of the positive enthalpy of mixing between Mg and Ti, Mg-Ti nanocomposites consisted primarily of a metastable body-centered-cubic (bcc) metastable alloy of Mg and Ti. The bcc Mg-Ti alloy transformed upon hydrogenation into the face centered-cubic fluorite Mg_{1-y}Ti_yH_x phase with favorable hydrogen storage properties. Pressure-composition isotherms for

the Mg-Ti-H nanocomposites revealed large differences in the thermodynamics relative to bulk MgH₂, with a much less negative enthalpy of formation of the hydride as high as -45 ± 3 kJ/molH₂, as deduced from van't Hoff plots. The plateau pressures of hydrogenation were substantially higher than those for the constituting elements, i.e. for bulk MgH₂ and bulk TiH₂ in the low temperature range from 423 K to 523 K. The reaction entropy was simultaneously reduced to values down to 84 ± 5 J/K mol H₂, closely following a linear relationship between the enthalpy and entropy that was previously indicated in TiF₃ catalyzed MgH₂ ³⁶.

In *Chapter 4*, the continuous metallic thin film Mg-Ti system is studied from the perspective of its thermal stability. For this purpose, Mg_yTi_{1-y} thin films were synthesized by sputter deposition. They are known to have a high reactivity with hydrogen at low temperatures and pressures which makes them interesting materials for hydrogen storage. A clear segregation of Mg and Ti occurs in the films heated at 573 K on a time scale of ~10h. The prolonged heating treatment (30 h) induces irreversible changes in the microstructure and capping layer that further block the rehydrogenation of the films. Using positron annihilation spectroscopy, an increased concentration of open volume defects is observed as a result of the heating treatment. The defects occurring at phase boundaries between Mg and Ti, or between coherent domains of Mg respectively Ti (so Mg-Mg boundaries or Ti-Ti boundaries) might act as hydrogen traps.

In *Chapter 5*, a structural and thermodynamic study of MgH_x nanoparticles synthesized in situ in the spark discharge generator reveals evidence to the presence of the α -phase in a wider H concentration range which is stably present over time. A decreased enthalpy of formation of about 60 kJ/molH₂ is determined for these non-catalyzed MgH_x spark generated nanoparticles.

In *Chapter 6*, Mg_yTi_{1-y}H_x nanocomposites are synthesized in situ in the spark discharge generator. Structural characterization of the samples revealed that the fluorite Mg_yTi_{1-y}H_x phase is present in the as produced samples. A reduced activation energy of 57 kJ/molH₂ is determined and the samples appear to be stable during hydrogen cycling. The high stability and reversibility of these samples together with the excellent hydrogen sorption properties make it an extremely interesting development, showing that the Mg-Ti nanosystem can in principle yield hydrogen storage with more favorable conditions and with less activation barriers.

In *Chapter 7*, the important aspect of the air sensitivity of the MgH₂ particles is addressed by sulfur coating because the formation of MgO is the main cause for the highest activation energies calculated in Chapter 2 and in addition it normally consumes progressive amounts of the Mg during prolonged exposure to air. The sulfur coating confirmed by SEM and TEM studies to be on the surface of the ball milled MgH₂ particles is formed by an evaporation condensation method. Samples prepared in this way can be exposed to air for a week without observing major structural changes or the progressive conversion to Mg(OH)₂ and MgO. Moreover, hydrogen sorption of the sulfur coated samples presents the same profiles as freshly ball milled MgH₂.

Thus, the present thesis addresses innovative ways to improve several of the most critical properties of MgH₂ as a hydrogen storage system by generation of Mg based nanomaterials through spark discharge. Detailed

structural studies are coupled with kinetic and thermodynamic investigations to understand the behavior of the Mg based spark discharge nanomaterials. Viable and innovative solutions to tackle these challenges are proposed in the form of bottom-up synthesis of Mg based nanomaterials through spark discharge, *in situ* hydrogenation with ionic hydrogen, protective coating with sulfur and *in situ* addition of transition metal catalysts.

References

- (1) Okamoto, H. H-Mg (Hydrogen-Magnesium). *JPE* 2001, 22, 598-599.
- (2) Jones, L. W. Liquid Hydrogen As a Fuel for the Future. *Science* 1971, 174, 367-370.
- (3) Winsche, W. E.; Hoffman, K. C.; Salzano, F. J. Hydrogen: Its Future Role in the Nation's Energy Economy. *Science* 1973, 180, 1325-1332.
- (4) Zuettel, A. Materials for Hydrogen Storage. *Materials Today* 2003, 6, 24-33.
- (5) Schlapbach, L.; Zuettel, A. Hydrogen-Storage Materials for Mobile Applications. *Nature* 2001, 414, 353-358.
- (6) Zuettel, A. fuels for hydrogen storage| Hydrides. In *Encyclopedia of Electrochemical Power Sources*; Ed.; Elsevier: Amsterdam, 2009.
- (7) *CRC Handbook of Chemistry and Physics, 88th Edition (CRC Handbook of Chemistry & Physics)*; CRC Press: 2007.
- (8) RamB, G.; Pant, K. K. Fundamentals and Use of Hydrogen As a Fuel. In *Hydrogen Fuel*; CRC Press: 2008.
- (9) Carrette, L.; Friedrich, K. A.; Stimming, U. Fuel Cells: Principles, Types, Fuels, and Applications. *ChemPhysChem* 2000, 1, 162-193.
- (10) Barthelemy, H. Hydrogen Storage - Industrial Prospectives. *International Journal of Hydrogen Energy* 2012, 37, 17364-17372.
- (11) Ruban, S.; Heudier, L.; Jamois, D.; Proust, C.; Bustamante-Valencia, L.; Jallais, S.; Kremer-Knobloch, K.; Maugy, C.; Villalonga, S. Fire Risk on High-Pressure Full Composite Cylinders for Automotive Applications. *International Journal of Hydrogen Energy* 2012, 37, 17630-17638.
- (12) Houf, W. G.; Evans, G. H.; Merilo, E.; Groethe, M.; James, S. C. Releases From Hydrogen Fuel-Cell Vehicles in Tunnels. *International Journal of Hydrogen Energy* 2012, 37, 715-719.
- (13) Zuettel, A.; Borgschulte, A.; Schlapbach, L. Hydrogen as a Future Energy Carrier. 2008. Weinheim, Wiley-VCH.
- (14) Sarkar, A.; Banerjee, R. Net Energy Analysis of Hydrogen Storage Options. *International Journal of Hydrogen Energy* 2005, 30, 867-877.
- (15) Trudeau, M. L. Advanced Materials for Energy Storage. *MRS Bulletin* 1999, 24, 23-24.
- (16) Nishihara, H.; Kyotani, T. Templated Nanocarbons for Energy Storage. *Adv. Mater.* 2012, 24, 4473-4498.

- (17) Hirscher, M. Fuels for Hydrogen Storage | Carbon Materials. In *Encyclopedia of Electrochemical Power Sources*; Garche, J., Ed.; Elsevier: Amsterdam, 2009.
- (18) Weitkamp, J. Fuels for hydrogen storage| Zeolites. In *Encyclopedia of Electrochemical Power Sources*; Ed.; Elsevier: Amsterdam, 2009.
- (19) Panella, B.; Hirscher, M. Fuel for Hydrogen Storage | Metal Organic Frameworks. In *Encyclopedia of Electrochemical Power Sources*; Ed.; Elsevier: Amsterdam, 2009.
- (20) Yan, Y.; Lin, X.; Yang, S.; Blake, A. J.; Dailly, A.; Champness, N. R.; Hubberstey, P.; Schroder, M. Exceptionally High H₂ Storage by a Metal-Organic Polyhedral Framework. *Chem. Commun.* 2009, 1025-1027.
- (21) Lim, K. L.; Kazemian, H.; Yaakob, Z.; Daud, W. R. W. Solid-State Materials and Methods for Hydrogen Storage: A Critical Review. *Chem. Eng. Technol.* 2010, 33, 213-226.
- (22) Van Mal, H. H.; Buschow, K. H. J.; Miedema, A. R. Hydrogen Absorption in LaNi₅ and Related Compounds: Experimental Observations and Their Explanation. *Journal of the Less Common Metals* 1974, 35, 65-76.
- (23) Miedema, A. R. The Electronegativity Parameter for Transition Metals: Heat of Formation and Charge Transfer in Alloys. *Journal of the Less Common Metals* 1973, 32, 117-136.
- (24) DOE. U.S. Department of Energy, Targets for onboard hydrogen storage systems for light-duty vehicles, 2014, http://www1.eere.energy.gov/hydrogenandfuelcells/storage/pdfs/targets_onboard_hydro_storage.pdf. 2014.
- (25) Stander, C. M.; Pacey, R. A. The Lattice Energy of Magnesium Hydride. *Journal of Physics and Chemistry of Solids* 1978, 39, 829-832.
- (26) Bogdanovic, B. Catalytic synthesis of organolithium and organomagnesium compounds and of lithium and magnesium hydrides-applications in organic synthesis and hydrogen storage *Angewandte Chemie - International Edition in English* 1985, 24, 262-273.
- (27) Bogdanovic, B.; Bohmhammel, K.; Christ, B.; Reiser, A.; Schlichte, K.; Vehlen, R.; Wolf, U. Thermodynamic Investigation of the Magnesium-Hydrogen System. *Journal of Alloys and Compounds* 1999, 282, 84-92.
- (28) Bogdanovic, B.; Hartwig, T. H.; Spliethoff, B. The Development, Testing and Optimization of Energy Storage Materials Based on the MgH₂---Mg System. *International Journal of Hydrogen Energy* 1993, 18, 575-589.

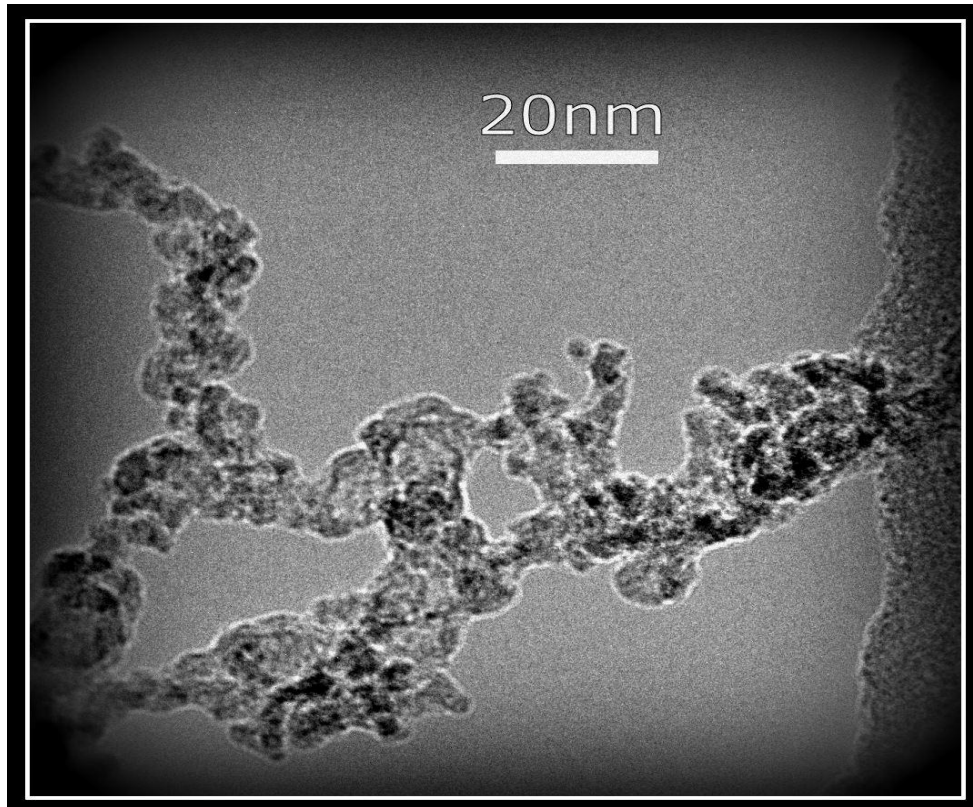
- (29) Bogdanovic, Catalytic synthesis of organolithium and organomagnesium compounds and of lithium and magnesium hydrides-applications in organic synthesis and hydrogen storage *Angewandte Chemie - International Edition in English* 1985, 24, 262-273.
- (30) Bogdanović, B.; Ritter, A.; Spliethoff, B. Active MgH_2 - Mg Systems for Reversible Chemical Energy Storage. *Angew. Chem. Int. Ed. Engl.* 1990, 29, 223-234.
- (31) Varin, R. A.; Jang, M.; Czujko, T.; Wronski, Z. S. The Effect of Ball Milling Under Hydrogen and Argon on the Desorption Properties of MgH_2 Covered With a Layer of Mg(OH)_2 . *Journal of Alloys and Compounds* 2010, 493, L29-L32.
- (32) Fernández, J. F.; Sánchez, C. R. Rate Determining Step in the Absorption and Desorption of Hydrogen by Magnesium. *Journal of Alloys and Compounds* 2002, 340, 189-198.
- (33) Borsa, D. M.; Gremaud, R.; Baldi, A.; Schreuders, H.; Rector, J. H.; Kooi, B.; Vermeulen, P.; Notten, P. H. L.; Dam, B.; Griessen, R. Structural, Optical, and Electrical Properties of $\text{Mg}_y\text{Ti}_{(1-y)}\text{H}_x$ thin Films. *Phys. Rev. B* 2007, 75, 205408.
- (34) Srinivasan, S.; Magusin, P. C. M. M.; van Santen, R. A.; Notten, P. H. L.; Schreuders, H.; Dam, B. Siting and Mobility of Deuterium Absorbed in Cosputtered $\text{Mg}_{0.65}\text{Ti}_{0.35}$. A MAS 2H NMR Study. *J. Phys. Chem. C* 2010, 115, 288-297.
- (35) Gialanella, S.; Ceccato, R.; Casari, F.; Ischia, G.; Molinari, A. Microstructural Refinement Using Ball-Milling and Spark-Plasma Sintering of MgH_2 Based Materials for Hydrogen Storage. *Calphad* 2009, 33, 82-88.
- (36) Mulder, F. M.; Singh, S.; Bolhuis, S.; Eijt, S. W. H. Extended Solubility Limits and Nanograin Refinement in Ti/Zr Fluoride-Catalyzed MgH_2 . *J. Phys. Chem. C* 2011, 116, 2001-2012.
- (37) Huot, J.; Tremblay, M. L.; Schulz, R. Synthesis of Nanocrystalline Hydrogen Storage Materials. *Journal of Alloys and Compounds* 2003, 356-357, 603-607.
- (38) Huot, J.; Liang, G.; Boily, S.; Van Neste, A.; Schulz, R. Structural Study and Hydrogen Sorption Kinetics of Ball-Milled Magnesium Hydride. *Journal of Alloys and Compounds* 1999, 293-295, 495-500.
- (39) Liang, G.; Boily, S.; Huot, J.; Van Neste, A.; Schulz, R. Mechanical Alloying and Hydrogen Absorption Properties of the Mg-Ni System. *Journal of Alloys and Compounds* 1998, 267, 302-306.

- (40) Liang, G.; Huot, J.; Boily, S.; Schulz, R. Hydrogen Desorption Kinetics of a Mechanically Milled MgH₂+5at.%V Nanocomposite. *Journal of Alloys and Compounds* 2000, 305, 239-245.
- (41) Liang, G.; Huot, J.; Boily, S.; Van Neste, A.; Schulz, R. Catalytic Effect of Transition Metals on Hydrogen Sorption in Nanocrystalline Ball Milled MgH₂-Tm (Tm=Ti, V, Mn, Fe and Ni) Systems. *Journal of Alloys and Compounds* 1999, 292, 247-252.
- (42) Tabrizi, N.; Ullmann, M.; Vons, V.; Lafont, U.; Schmidt-Ott, A. Generation of Nanoparticles by Spark Discharge. *Journal of Nanoparticle Research* 2009, 11, 315-332.
- (43) Vons, V. A.; Leegwater, H.; Legerstee, W. J.; Eijt, S. W. H.; Schmidt-Ott, A. Hydrogen Storage Properties of Spark Generated Palladium Nanoparticles. *International Journal of Hydrogen Energy* 2010, 35, 5479-5489.
- (44) Vons, V. Spark discharge generated nanoparticles for hydrogen storage applications. 2009. Ridderkerk, Ridderprint B.V.
- (45) Jongh, P. E. d.; Wagemans, R. W. P.; Eggenhuisen, T. M.; Dauvillier, B. S.; Radstake, P. B.; Meeldijk, J.; Geus, J. W.; Jong, K. P. The Preparation of Carbon-Supported Magnesium Nanoparticles Using Melt Infiltration. *Chem. Mater.* 2007, 19, 6052-6057.
- (46) de Jongh, P. E. Hydrogen Storage: Keeping Out the Oxygen. *Nat Mater* 2011, 10, 265-266.
- (47) Gasan, H.; Celik, O. N.; Aydinbeyli, N.; Yaman, Y. M. Effect of V, Nb, Ti and Graphite Additions on the Hydrogen Desorption Temperature of Magnesium Hydride. *International Journal of Hydrogen Energy* 2012, 37, 1912-1918.
- (48) Schimmel, H. G.; Huot, J.; Chapon, L. C.; Tichelaar, F. D.; Mulder, F. M. Hydrogen Cycling of Niobium and Vanadium Catalyzed Nanostructured Magnesium. *Journal of the American Chemical Society* 2005, 127, 14348-14354.
- (49) Callini, E.; Pasquini, L.; Rude, L. H.; Nielsen, T. K.; Jensen, T. R.; Bonetti, E. Hydrogen Storage and Phase Transformations in Mg--Pd Nanoparticles. *J. Appl. Phys.* 2010, 108, 073513-073517.
- (50) Vons, V. A.; Anastasopol, A.; Legerstee, W. J.; Mulder, F. M.; Eijt, S. W. H.; Schmidt-Ott, A. Low-Temperature Hydrogen Desorption and the Structural Properties of Spark Discharge Generated Mg Nanoparticles. *Acta Materialia* 2011, 59, 3070-3080.
- (51) Anastasopol, A.; Pfeiffer, T. V.; Schmidt-Ott, A.; Mulder, F. M.; Eijt, S. W. H. Fractal Disperse Hydrogen Sorption Kinetics in Spark Discharge Generated Mg/NbO_x and Mg/Pd Nanocomposites. *Applied Physics Letters* 2011, 99, 194103.

- (52) Wagemans, R. W. P.; van Lenthe, J. H.; de Jongh, P. E.; van Dillen, A. J.; de Jong, K. P. Hydrogen Storage in Magnesium Clusters: Quantum Chemical Study. *Journal of the American Chemical Society* 2005, 127, 16675-16680.
- (53) Vigeholm, B.; Kj ller, J.; Larsen, B.; Pedersen, A. S. Formation and Decomposition of Magnesium Hydride. *Journal of the Less Common Metals* 1983, 89, 135-144.
- (54) Stampfer, J. F.; Holley, C. E.; Suttle, J. F. The Magnesium-Hydrogen System¹⁻³. *Journal of the American Chemical Society* 1960, 82, 3504-3508.
- (55) Pedersen, A. S. d.; Jensen, K.; Larsen, B.; Vigeholm, B. The Formation of Hydride in Pure Magnesium Foils. *Journal of the Less Common Metals* 1987, 131, 31-40.
- (56) Duan, H. L.; Karihaloo, B. L.; Wang, J. Thermo-Elastic Size-Dependent Properties of Nano-Composites With Imperfect Interfaces. In *IUTAM Symposium on Modelling Nanomaterials and Nanosystems*; Pyrz, R., Rauhe, J. C., Eds.; Springer Netherlands: 2009.
- (57) Schwyn, S.; Garwin, E.; Schmidt-Ott, A. Aerosol Generation by Spark Discharge. 1988, 19, 639-642.

Chapter 2

Fractal disperse desorption kinetics and structure of spark discharged Mg and Mg/Pd, Mg/Nb nanocomposites



Abstract

Mg nanoparticles synthesized using spark discharge, result in large-scale structures of agglomerated nanoparticles with primary particle sizes of ~10 nm, surrounded by MgO shells 1–2 nm thick. Using thermal desorption spectroscopy, it is observed that hydrogen desorption starts at remarkably low temperatures of ~350 K and extends over a broad temperature range to beyond 700 K. The desorption at low temperatures is due to the presence of nanoparticles while the desorption at higher temperatures is caused by the presence of oxide shells acting as activation barriers.

In this chapter, a kinetic model based on multiple reaction rates is proposed, in contrast to the Johnson-Mehl-Avrami-Kolmogorov (JMAK) model which is commonly applied to explain the kinetics of metal hydride transformations. The broad range of reaction rates arises from the disperse character of the particle size and the dendritic morphology of the samples. The model is expected to be generally applicable for metal hydrides which show a significant variation in particle sizes, in configuration and/or chemical composition of local surroundings of the reacting nanoparticles.

This chapter is based on the published papers:

Low-temperature hydrogen desorption and the structural properties of spark discharge generated Mg nanoparticles, V.A. Vons, A. Anastasopol, W.J. Legerstee, F.M. Mulder, S.W.H. Eijt, A. Schmidt-Ott, Acta Materialia, 2011, 59, (8), 3070-3080, 10.1016/j.actamat.2011.01.047

Fractal disperse hydrogen sorption kinetics in spark discharge generated Mg/NbO_x and Mg/Pd nanocomposites, Anca Anastasopol, Tobias V. Pfeiffer, Andreas Schmidt-Ott, Fokko M. Mulder, Stephan W.H. Eijt, Applied Physics Letters, 2011, 99, 194103, dx.doi.org/10.1063/1.3659315

*“... ori să se revizuiască, primesc! Dar să nu se schimbe nimica; ori să nu se revizuiască,
primesc! dar atunci să se schimbe pe ici pe colo,
și anume în punctele... esențiale...”*

(...review, I accept! But without any changes;
or, don't review and then change some ...essential parts)

Ion Luca Caragiale, “O scrisoare pierdută” (A lost letter),
Act III, Scene 1.

In chemical kinetics, the rate of a reaction is determined by the slowest step, otherwise known as the rate determining step. The reaction of Mg with hydrogen is a succession of several processes: H₂ physisorption, H₂ dissociation, H chemisorption, H migration from the surface to bulk, H diffusion and nucleation and growth of the hydride or metal phase. The rate determining step for both bulk Mg and MgH₂, was found to be the diffusion of hydrogen in the crystalline lattice^{2,3,4}. This changed with nanosized Mg and MgH₂ when the surface of the particle has a bigger contribution and bulk diffusion is no longer an issue, so the rate determining step becomes the surface absorption of hydrogen.³

However, the reaction continues to present a rather high activation barrier. To tackle this issue, transition metals are incorporated in the magnesium nanoparticles to act as catalysts, by splitting the hydrogen molecule into atoms and decreasing in this way the activation barrier for hydrogen sorption. Recent studies^{5,6} have indicated that the sorption reaction is not symmetrical. The mechanism for absorption is decoupled from that of desorption. On a closer look, desorption does not occur with a nucleation and growth mechanism but rather as a continuous transformation. However, for the most part, desorption data is treated in the same way as the absorption though the growth parameters lose their physical meaning.

The addition of catalysts to the sample, further complicates the model of desorption by increasing the topochemistry of the reaction, meaning that the reaction will occur at preferred regions in the sample e.g. where the catalyst is present^{7,8}. Solid state transformations are essentially different from classical kinetics and the main reason for it is that the mobility of the atoms is severely limited by slower diffusion in the solid. For this reason, the morphology of the reactant can influence the course and rate of the reaction. Thus, the preparation, the storage and the uniformity of the composition affect the kinetics of the reaction.

Here we propose to account for this topochemical effect by the pragmatic approach of treating the reactant as a sum of systems, each characterized by its own reaction rate and activation energy.

As spark discharge generation proved to be a versatile method to produce metallic nanoparticles, it was further extended to producing mixtures of nanoparticles. In this way, palladium and niobium nanoparticles can be in situ incorporated into the magnesium fractal like structures. And the hydrogen sorption reaction is visibly speeded.

2.2 Experimental section

2.2.1. Synthesis – Spark discharge generation

The synthesis of the Mg nanoparticles is performed in a dedicated spark discharge generator. Two Mg rods (99.9 + % purity, Mateck GmbH) of 1/4 in. diameter were used as electrodes of the first spark generator, which were sparked at a capacitor charging current of 12 mA, with a capacitance of 20 nF and a gap distance of 2 mm. The synthesis takes place at atmospheric pressure, under a constant flow of Ar gas of 1 l/min. For the synthesis of the Mg/Pd and Mg/NbO_x nanocomposites, a dual spark generator setup was used. In this configuration, the spark generator setup contains a set of two working electrodes connected in parallel: the first set is Mg vs. Mg placed at the top part of the reactor chamber and the second set is Pd vs. Pd (99.95% pure, Goodfellow)

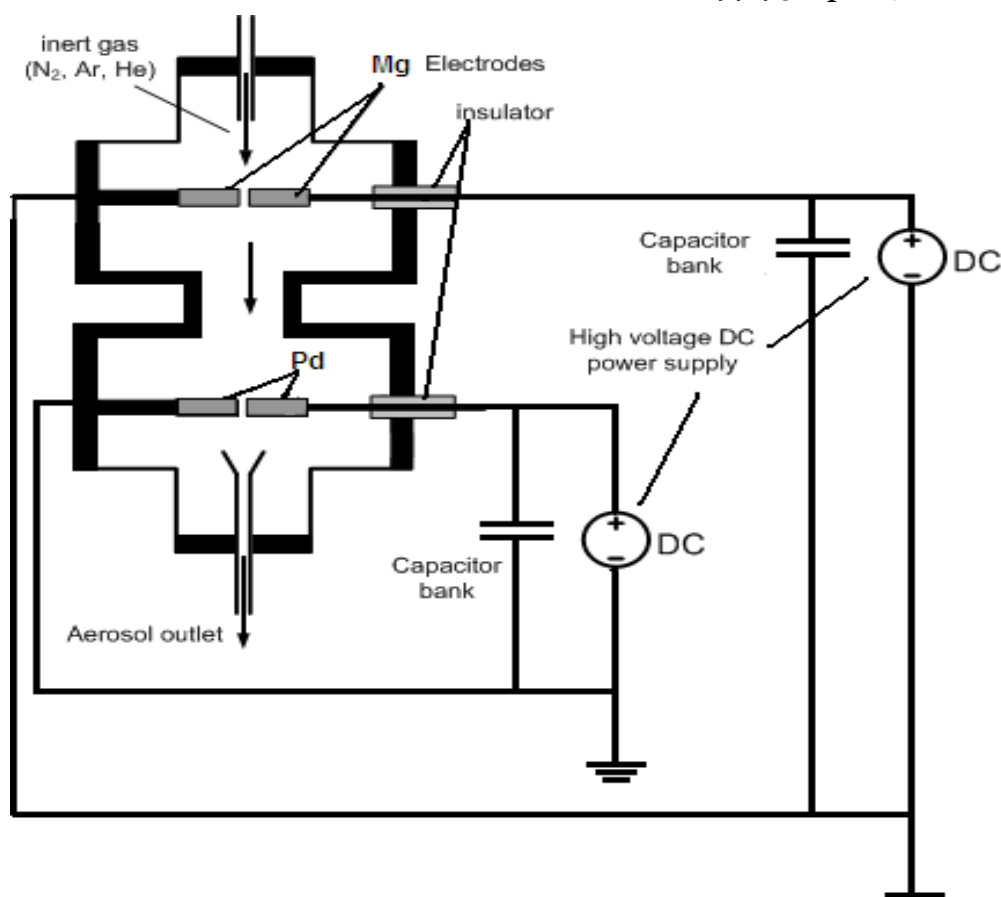


Figure 2.1. Schematic representation of the spark discharge generator setup used in the synthesis of Mg/Pd and Mg/NbO_x nanocomposites. Image adapted from ¹.

or NbO_x vs. NbO_x placed at the bottom part of the reaction chamber. The nano mixtures are formed by carrying the nanoparticles of Mg produced from the upper electrodes in between the transition metal electrodes. In order to be able to adjust the production rate of each of the metals, the frequency of the sparks is tuned. Thus, the frequency of the 40 mJ Mg sparks is 300 Hz. In order to produce a targeted amount of a few at.% of catalyst (Pd or NbO_x), the second spark is operated with 14 mJ pulses at a frequency of 34 Hz. The nanocomposites produced in this way were collected on Millipore Durapore membrane filters (PVDF) held in a special filter holder perpendicular to the gas flow positioned ~20 cm downstream of the second spark generator.

2.2.2. Powder X-ray diffraction

Both synthesized and hydrogen-cycled Mg and Mg/Pd nanoparticle samples were analyzed by XRD in an inert environment using a PANalytical X'Pert PRO diffractometer with a Cu K α source, $\lambda = 1.5415 \text{ \AA}$. The measured background due to the poly methyl methacrylate (PMMA) substrate of the XRD holder was subtracted for all spectra (see appendix A). Rietveld refinement of the data was performed using the EXPGUI-GSAS software^{9,10}. The instrumental parameters were calibrated using a Rietveld fit to the measured powder diffraction pattern of a LaB₆ (660b standard NIST) reference. The crystallite sizes were calculated from the determined profile line shapes, taking the Scherrer shape factor equal to 1¹¹. The phase fractions and crystallite sizes for each of the phases present in the as-produced and hydrogen-cycled samples were extracted from the Rietveld refinement.

2.2.3. Thermal desorption measurement

Thermal desorption spectrometry (TDS) was used to measure the rate of desorption of hydrogen into a vacuum at a controlled temperature ramp, using the homebuilt TDS set-up HYDRA^{1,12}. The hydrogen TDS spectra were measured with a quadrupole mass spectrometer. The hydrogen released from the sample during desorption passes through a heated and calibrated Pd filter before reaching the mass spectrometer. During the measurement, the pressure inside the TDS setup is monitored. The pressure signal is correlated to the mass spectrometer signal, indicating that no other gases than H₂ are being released during the heating treatment. In order to determine the amount of hydrogen released from the sample, a prior calibration measurement is performed. The measurement consists of the detection of a known amount of H₂, leaking at a constant rate. The Mg nanoparticle samples were inserted into the HYDRA sample-holder inside an Ar-filled glovebox. Hydrogen loading was performed inside the HYDRA set-up using a hydrogen pressure of 6.2 bar at a temperature of 573 K for 10 h. Desorption experiments were performed at selected temperature ramp rates in the range of 0.5–10 K/min. The samples were heated under a base pressure of 10⁻⁷ bar to a maximum temperature of 750 K which was subsequently kept fixed, using a hydrogen cycle of typically 24 h. The weight of samples ranged from 1.0 to 4.7 mg. Kissinger analysis was performed on two Mg nanoparticle samples. A reference thermal desorption measurement was performed on ball-milled mixture of MgH₂ (Sigma Aldrich) and 1 wt.% Pd (Sigma Aldrich) powders consisting of submicron-sized particles. The

isothermal measurements were performed on the Mg/Pd and Mg/NbO_x nanocomposites at temperatures ranging from 473K to 573K.

2.2.4. Transmission electron microscopy

Transmission Electron Microscopy (TEM) was performed on a FEI TECNAI TF20 monochromatic electron microscope operated at 200 kV. The samples were transferred on copper grids in an Ar filled glovebox.

2.3. Results and discussion

2.3.1. Structure characterization

X-ray diffraction is used to determine the crystalline phases present in the sample. In order to gain a quantitative insight into the evolution of phases and corresponding particle sizes, XRD patterns were analyzed using Rietveld refinement in GSAS^{9,13} software. The results obtained are summarized in Table 2.1.

The X-ray diffraction pattern of the spark discharge generated Mg nanoparticles is plotted in Figure 2.2a. The as produced sample shows the presence of both hexagonal Mg ($P6_3/mmc$) and cubic MgO ($Fm\bar{3}m$). No indication for the presence of metastable wurtzite MgO¹⁴ was seen in the XRD pattern. Clear peak broadening is observed for the Mg peaks and the average crystallite size is found to be about 21 nm for the Mg nanoparticles. In the Rietveld refinement, the size of the MgO crystallites is found to be about 3 nm, indicated by the broad features at 43° and 62°. MgO is most likely present in the form of thin shells as seen in the TEM images (Figure 2.5).

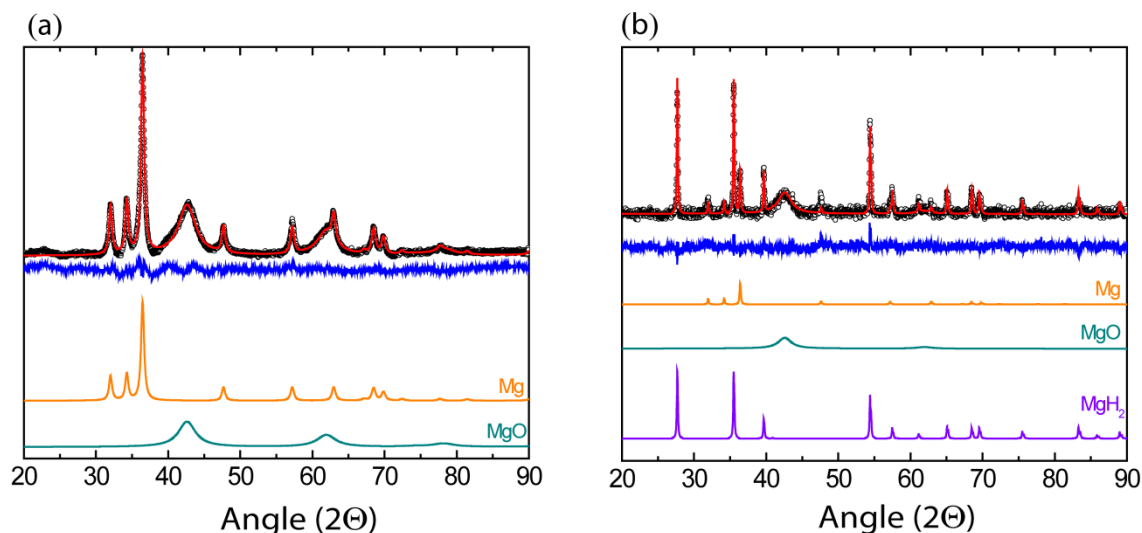


Figure 2.2. X-ray diffraction patterns and the results of the Rietveld refinement (measured spectra-black, calculated spectra – red, residual – blue) of spark discharge generated Mg a. as produced; b. after hydrogen loading. The sample container background is subtracted. The individual phase contributions are given below (scaled down by 1/2)

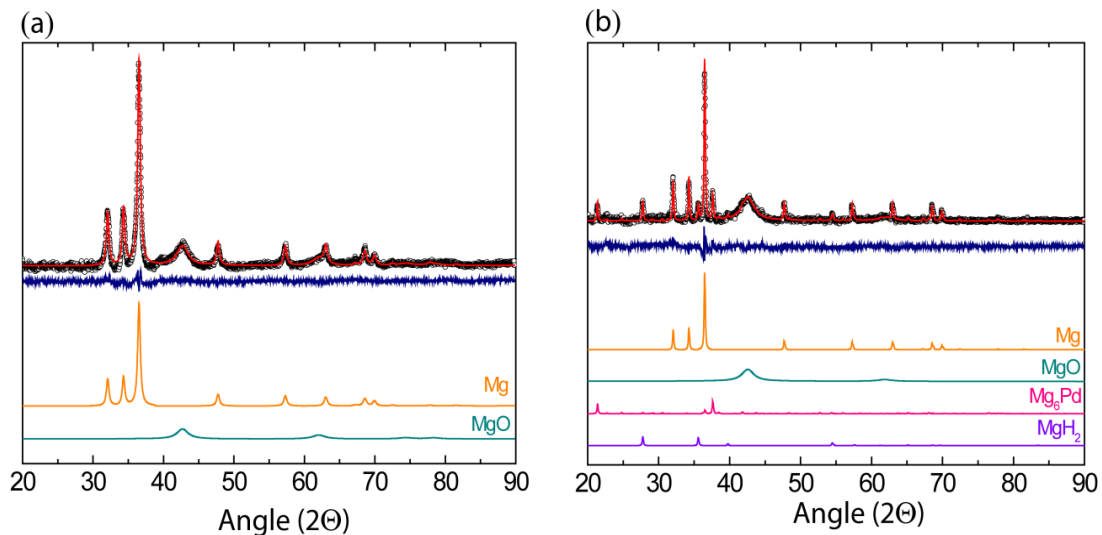


Figure 2.3. X-ray diffraction patterns and the results of the Rietveld refinement (measured spectra – black, calculated spectra – red, residual – blue) of spark discharge generated Mg/Pd nanocomposites a. as produced; b. after hydrogen cycling. The sample container background is subtracted. The individual phase contributions are given below (scaled down by $1/2$)

After a few cycles of absorption and desorption of hydrogen, the diffraction peaks clearly become narrower due to an increase in the crystallite size as it appears in Figure 2.2b. The size of the Mg grains grows to about 100 nm but the apparent MgO grain sizes remain about 3-4 nm, which indicates that the thickness of the MgO shells surrounding Mg and MgH₂ does not increase during cycling. A set of diffraction peaks of the rutile β -MgH₂ phase is clearly resolved in the diffraction pattern obtained after the hydrogen loading. The crystallite sizes for MgH₂ grow to about 100 nm during cycling. The particle growth upon hydrogenation is similar to that observed in studies by Friedrichs¹⁵

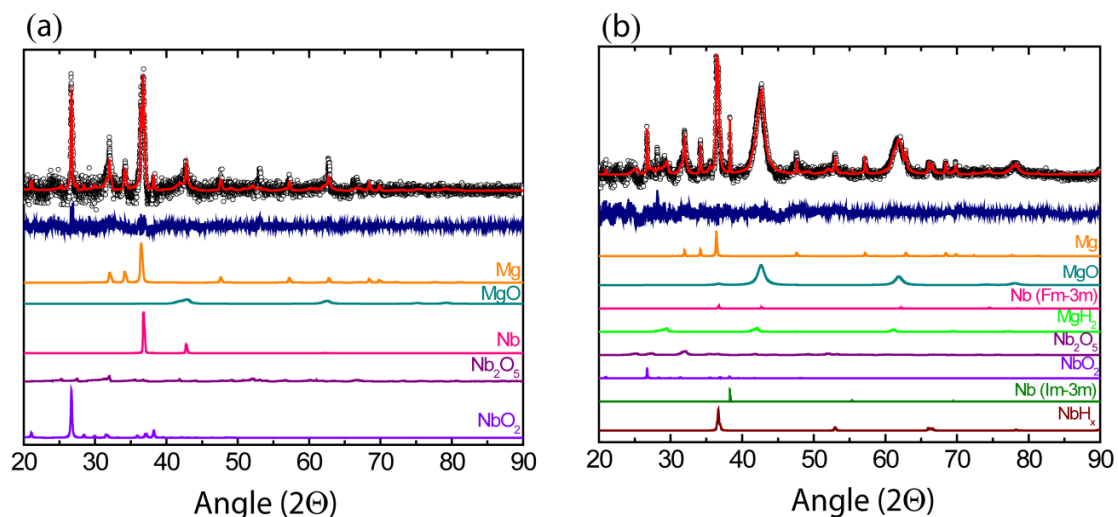


Figure 2.4. X-ray diffraction patterns and the results of the Rietveld refinement (measured spectra – black, calculated spectra – red, residual – blue) of spark discharge generated Mg/NbO_x nanocomposites a. as produced; b. after hydrogen cycling. The sample container background is subtracted. The individual phase contributions are given below (scaled down by $1/2$ for a. and $1/4$ for b.)

Using the double spark discharge generator, a transition metal catalyst can be synthesized and mixed with the Mg nanoparticles in situ. A second set of nanoparticle samples was synthesized with the dual SDG set-up using settings to produce of the order of ~1 wt.% of Pd nanoparticles intermixed with Mg nanoparticles. The XRD pattern of the Pd catalyzed sample is plotted in Figure 2.3. Both Mg and MgO phases are visible in the XRD pattern of the as-produced Mg/Pd nanoparticle sample, which resembles closely that of the non-catalyzed sample. The size of the Mg and MgO grains are similar to the pure Mg sample, ~20 nm and 4 nm, respectively. After cycling, the size increases again to almost 100 nm for Mg and remains unchanged for MgO.

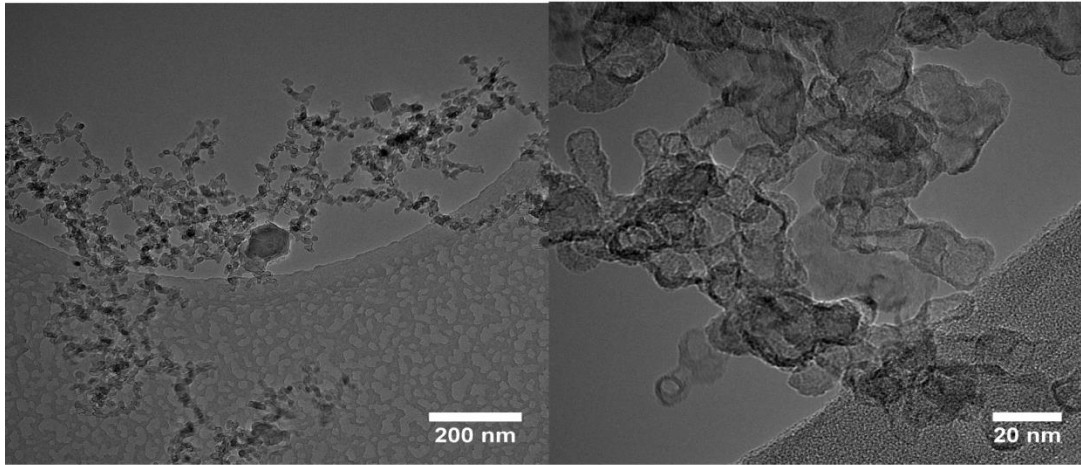
The presence of Pd in the sample could not be observed in the diffraction pattern. However, after a few cycles of absorption and desorption, a new crystalline phase could be distinguished in the diffraction pattern by additional peaks at $2\theta = 21.4^\circ$ and $2\theta = 37.6^\circ$. These additional peaks fit to the most intense peaks of the known XRD pattern of the intermetallic Mg₆Pd. According to the phase diagram published by Makongo et al.¹⁶, the Mg₆Pd phase is the most likely compound at low concentrations of Pd in Mg below 807 K. The presence of this alloy proves the initial presence of Pd in the sample as introduced by the second spark generator. The amount of 0.6 wt.% of Mg₆Pd alloy formed, as deduced from the XRD spectrum, is relatively small, and accounts for ~0.25 wt.% of Pd actually present in the sample (Table 2.1). The formation of Mg/Pd alloys is often observed in hydrogen cycling of Pd-capped Mg and Mg₂Ni thin films^{17,18}, and is related to enhanced diffusion of Pd in Mg at relatively modest temperatures of at least as low as 480 K^{18,19}. The formation of the Mg₆Pd alloy shows that close contact between Pd and Mg nanoparticles is established either upon synthesis or during hydrogen cycling at elevated temperatures. Huot et al.^{20,21} have investigated the hydrogen uptake characteristics of the Mg₆Pd alloy and found a hydrogen capacity of about 2.85 wt.%, involving the formation of MgH₂ and a disproportionation of the Mg-Pd alloy.

Using the same dual spark discharge generator, an Nb catalyzed Mg sample is produced. Nb is used for its good catalytic properties in the hydrogen sorption but also because it does not form any alloys or intermetallic compounds with Mg.^{22,23,24,25} The Nb electrodes consisted of Nb metal core covered in a thin NbO_x shell. During the synthesis, the NbO_x shell is etched away in the form of NbO₂ and Nb₂O₅ together with metallic Nb from the core of the electrode. NbO_x can also improve the hydrogen sorption reaction of Mg. In the XRD pattern in Figure 2.4a, Mg could be identified in the form of 100 nm grains. MgO is found in a very low fraction (4.7 wt. %) in the form of 16 nm grains. Unlike the Pd catalyzed sample, where the presence of Pd in the as produced sample was difficult to determine, here, Nb is present in several species. The dominant Nb phase is the tetragonal NbO₂ (*I4₁/a*) followed by cubic metallic Nb (*Fm $\bar{3}m$*) and monoclinic Nb₂O₅ (*C₂*). All the Nb phases are represented by sharp peaks in the XRD which correspond to large grains > 100 nm. The large size of the NbO_x species points to an etching mechanism rather than an evaporation/condensation mechanism that is assumed for Mg and Pd.^{1,12,26} However, the metastable face centered cubic phase of Nb (*Fm $\bar{3}m$*) indicates a rapid condensation of Nb.

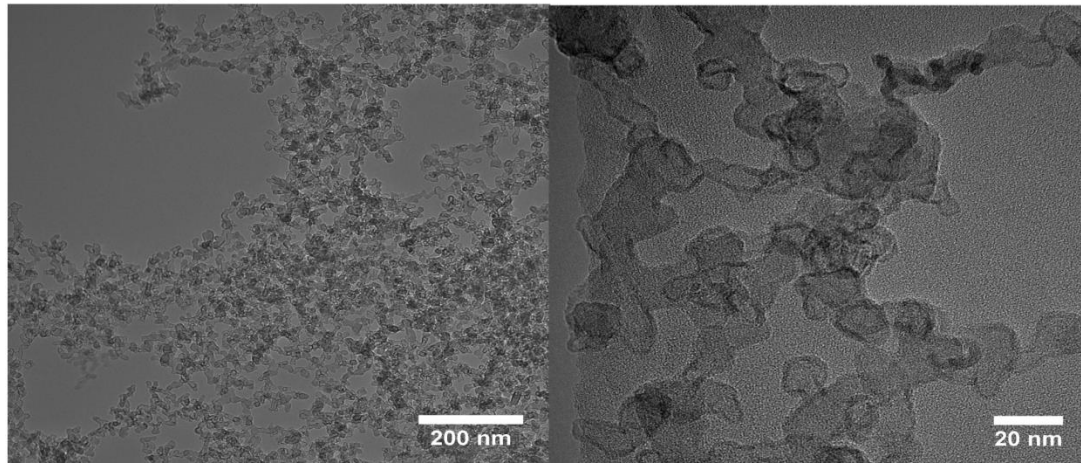
After a few cycles of hydrogen loading and unloading (Figure 2.4b), metallic Nb is found mostly in the more stable body centered cubic form ($Im\bar{3}m$) with a size of the crystallites of about 15 nm. Though the sample is analyzed after hydrogen unloading, small fractions of MgH_2 (6.4 wt. %) and a nonstoichiometric NbH_x (2.3 wt. %) can be found in the XRD spectrum.

The catalyst mixing as well as the morphology of the samples could be investigated by TEM. The representative TEM image of the Mg/Pd and Mg/ NbO_x nanocomposites are presented in Figure 2.5. The Mg nanoparticles are gathered into fractal like structures. These agglomerates contain the transition metal catalysts. Nb containing nano particles are found to be uniformly dispersed among the Mg nanoparticles. TEM images of the Mg/Pd nanocomposites showed a similar dendritic morphology.¹

(a) Mg nanoparticles



(b) Mg/Pd nanocomposites



(c) Mg/Nb nanocomposites

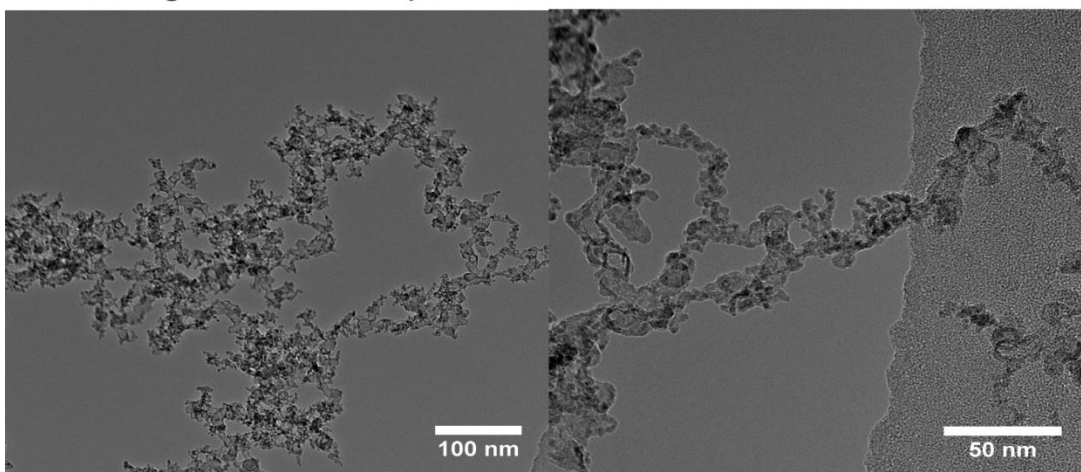


Figure 2.5. TEM images depicting the morphology of spark discharge generated a) Mg nanoparticles, b) Mg/Pd nanocomposites and c) Mg/Nb nanocomposites.

Table 2.1. Particle sizes and phase fractions in wt% extracted from Rietveld refinement of the XRD patterns of freshly synthesized Mg and Mg/Pd, Mg/NbO_x nanocomposites and after hydrogen sorption. N.B. The sample before and after hydrogen sorption are not identical.

Phase	Freshly prepared						After hydrogen sorption					
	Mg (R _{wp} =2%)		Mg/Pd (R _{wp} =2%)		Mg/NbO _x (R _{wp} =2.2%)		Mg (R _{wp} =1%)		Mg/Pd (R _{wp} =1%)		Mg/NbO _x (R _{wp} =2.6%)	
	Size (nm)	Fraction (wt.%)	Size (nm)	Fraction (wt.%)	Size (nm)	Fraction (wt.%)	Size (nm)	Fraction (wt.%)	Size (nm)	Fraction (wt.%)	Size (nm)	Fraction (wt.%)
Mg	21 nm	38 wt %	24 nm	67 wt %	103 nm	10.7 wt %	107 nm	1.6 wt%	91 nm	6.6 wt%	170 nm	8.4 wt %
Pd	-	-	-	-	-	-	-	-	-	-	-	-
Nb (Fm-3m)	-	-	-	-	-	21.6 wt %	-	-	-	-	-	0.2 wt %
Nb (Im-3m)	-	-	-	-	-	-	-	-	-	-	15 nm	1.3 wt%
Nb₂O₅	-	-	-	-	-	2.4 wt%	-	-	-	-	28 nm	7.4 wt %
NbO₂	-	-	-	-	80 nm	60.6 wt%	-	-	-	-	-	20 wt%
MgO	3.4 nm	62 wt%	3.9 nm	33 wt%	16 nm	4.7 wt%	3.6 nm	91 wt%	4.8nm	92 wt%	10 nm	54 wt%
Mg₆Pd	-	-	-	-	-	-	-	-	84 nm	0.6 wt%	-	-
MgH₂	-	-	-	-	-	-	106 nm	7.4 wt%	80 nm	1.1 wt%	51 nm	6.4 wt %
NbH_x	-	-	-	-	-	-	-	-	-	-	113 nm	2.3 wt%

2.3.2. General aspects of hydrogen sorption kinetics on Magnesium

The classic description of the reaction rate of solid state reactions is depicted in *Eq. 2.1*:

$$r = \frac{dx}{dt} = A \cdot e^{-\frac{E_a}{RT}} f(x) \quad (2.1)$$

$$r = \frac{dx}{dt} = A \cdot e^{-\frac{E_a}{RT}} (1-x) \quad (2.2)$$

where A is the preexponential factor, also known as the frequency factor, E_a is the activation energy for the reaction and $f(x)$ is a function of the reactants concentration. *Eq. 2.2* represents the limiting case of a first order reaction.

In classical heterogeneous kinetics, the activation energy is related to the potential barriers associated with a typical configuration of the reacting species. Stable chemical compounds are characterized by occupying the energy minimums on the surface potential energy landscape. The transition from one stable state to another occurs via an “activated complex” state. The energy difference between the activated complex and the potential energy of the reactants represents the activation energy for the transformation. It is the minimum energy that needs to be supplied to the system so the reaction could proceed and it usually represents the kinetic energy of the molecules or atoms. The fraction of hydrogen molecules that posses high enough energy for the chemical reaction to occur is determined by Maxwell – Boltzmann statistics represented in the term $e^{-\frac{E_a}{RT}}$. It is clear from this factor that by increasing the temperature, the fraction of species that can participate to the reaction is increased. ^{27,28}

As *Eq. 2.1* suggests, the rate of a chemical transformation can be accelerated by either decreasing the activation energy of the reaction or increasing the thermal kinetic energy of the hydrogen atoms.

The common route of decreasing the activation energy for a reaction is the use of catalysts which are able to modify the shape and magnitude of the potential energy of the activated complex.

The mechanism of hydrogen sorption in a metal was synthesized by Mintz and Bloch⁴ into a few major steps:

- a) Surface processes (physisorption, chemisorption, dissociation, *etc.*);
- b) Transport processes (bulk diffusion, grain boundary diffusion, *etc.*);
- c) Nucleation process ;
- d) Interface processes (solid state transformations, *etc.*).

For a bulk metal hydride, the rate determining step is found to be the transport in the bulk. ^{2,29,30}. Therefore, the main term in the activation energy of the process will be hydrogen diffusion through the hydride or metal lattice. However, in the case of nanoparticles with a diameter of about 10 nm as those synthesized by spark discharge generation, diffusion distances are relatively low which means that the energy barrier due to diffusion is negligible. A direct consequence of using nanoparticulate materials with a high surface area is that

surface processes become rate determining in the hydrogen sorption reactions. Consequently, the source of the activation energy for the reaction of hydrogen with nanosized metallic materials lies in the surface processes mentioned under point a). Thus, the formation of a surface oxide layer will have a major influence on the hydrogen sorption kinetics.^{1,5,31,32,33,34}

However, in some cases, the adsorption of H₂ molecule occurs spontaneously when the intersection point of the physisorption Lennard-Jones potential profile and the chemisorption Lennard-Jones potential profile is below zero. This is the case for metals such as Pd, Nb, Ni among others^{35,36,37}. Because of their capacity of exothermically dissociating the H₂ molecule, Pd and Nb are chosen as catalysts for the hydrogen sorption in Mg.

In contrast to the case of spontaneous H₂ adsorption in Pd and Nb, the adsorption of H₂ in Mg is an activated process. Nørskov et al.³⁸ found two activation barriers for the adsorption of H₂ on Mg (0001) surface. In their rigorous analysis they identified four steps of H₂ adsorption:

- a) H₂ molecule approaches the surface of the metal and the energy barrier of the interaction is determined by both the orientation of the incoming H₂ molecule as the geometry of the metal surface;
- b) H₂ molecule is physisorbed and free to move on the surface of the metal. The energy of this interaction is very weak and the length is comparable to the free molecule;
- c) Closer to the Mg surface, the metal electrons occupy the anti-bonding states of H₂. At this stage, H-H bond is still present but the potential energy of the system is decreased. The molecule is in the chemisorbed state: H₂⁻;
- d) A second energy barrier is overcome when the anti-bonding orbitals are completely filled and H₂ molecule is completely dissociated into H⁻.

Once dissociated, H⁻ can diffuse in the metal lattice and form chemical bonds. The formation of MgH₂ occurs with a change in the crystal symmetry from the hexagonal Mg structure to the tetragonal, rutile type of structure of MgH₂. The Mg-H bond has a strong covalent character as it was determined from its vibration spectra.³⁹

The desorption process can be seen as the reverse of the absorption process. In the following sections, we will concentrate on the kinetic analysis of hydrogen desorption from MgH₂ nanoparticles with and without transition metal catalysts.

2.3.3 Thermal desorption of hydrogen from spark discharge generated magnesium

Before presenting the kinetic analysis of the hydrogen desorption from spark discharge generated nanomaterials, a description of the method based on Kissinger analysis for extracting the kinetic parameters is necessary. Thus, as stated before, the important factors that determine whether the reaction will proceed or not are the activation energy and the frequency factor. Conventionally, they can be extracted from thermal desorption curves obtained from TDS. *Eq. 2.1* and *Eq.2.2* represent the case of isothermal desorption if $T=T_0$ is fixed.

For non isothermal hydrogen desorption, the rate equation *Eq. 2.1* could be transformed to include a heating rate:

$$\frac{dx}{dT} = \frac{dx}{dt} \frac{dt}{dT} \quad (2.3)$$

where $\beta = dT/dt$ represents a constant heating rate. If Eq.2.2 is substituted in Eq.2.3, the equation for the non isothermal rate law is obtained:

$$\frac{dx}{dT} = A \cdot e^{-\frac{E_a}{RT}} \frac{1}{\beta} (1-x) \quad (2.4)$$

When the temperature rises during a chemical reaction, the reaction rate will reach a maximum and then decrease as the reactants are being transformed into the products and the transformed fraction $x \rightarrow 1$. At the maximum rate, the time derivative of the reaction rate is equal to zero.

$$\frac{d^2x}{dt^2} = 0 \quad (2.5)$$

$$\frac{d^2x}{dt^2} = \frac{dx}{dt} \left(\frac{\beta E_a}{RT^2} - A e^{-\frac{E_a}{RT}} \right) = 0 \quad (2.6)$$

The equation is solved for the maximum temperature T_m :

$$\frac{\beta E_a}{RT_m^2} = A e^{-\frac{E_a}{RT_m}} \quad (2.7)$$

It results directly in the logarithmic form:

$$\ln \left(\frac{\beta E_a}{RT_m^2} \right) = -\frac{E_a}{RT_m} + \ln(A) \quad (2.8)$$

Which can be rearranged to resemble a line equation:

$$\ln \left(\frac{\beta}{T_m^2} \right) = -\frac{E_a}{RT_m} + \ln \left(\frac{RA}{E_a} \right) \quad (2.8')$$

The plot of $\ln \left(\frac{\beta}{T_m^2} \right)$ versus $\frac{1}{T_m}$ represents a straight line from which the kinetic parameters, activation energy E_a and frequency factor A can be extracted as the slope and intersect respectively.

This type of analysis developed by several scientists in the early 1960's is widely used in thermal decomposition reactions of the type *Solid* \rightarrow *Gas* + *Solid* takes into account only the temperature of maximum desorption rate T_m ^{40,41,42}. It is widely known as the Kissinger method by the name of one of the scientists that proposed it. It predicts that by increasing the heating rate, the maximum desorption temperature will also be increased, according to Eq. 2.9.

We applied the Kissinger method to the thermal desorption curves of *ex situ* hydrogenated Mg nanoparticles. The desorption curves in Figure 2.6a were measured at different heating rates ranging from 0.5 K/min to 4 K/min. Indeed, the hydrogen desorption peaks shift towards higher temperatures when faster heating rates are applied. In Figure 2.6b, the corresponding Kissinger plots are represented for two separate samples. The slope of the lines determined the height of the activation barrier for hydrogen desorption. Thus, for the two separate samples, the activation energy is found to be 94 ± 15 kJ/molH₂ for sample *a* and 90 ± 15 kJ/molH₂ for sample *b*.

However, the shape of the desorption curves in Figure 2.6a is entirely ignored in this analysis. Unlike the hydrogen desorption from bulk and ball milled MgH₂, which present narrow desorption peaks at elevated temperatures, the desorption curves of hydrogenated spark discharge Mg nanoparticles are much wider. In order to gain a better insight into the nature of the broad desorption spectra, we calculated the temperature dependence of the rate of hydrogen desorption using two models, the first assuming the existence of a single activation energy, and the second based on the existence of a broad range of activation energies resulting from the disperse nature of the nanoparticulate samples. They spread over a wide temperature range from temperatures as low as 400 K to beyond 750 K. This indicates an inhomogeneity in the reactivity of the MgH₂ nanoparticles. In order to support this affirmation, we applied the inverse analysis for the desorption curve. Given the activation energy and frequency factor determined via the Kissinger method described earlier, we have calculated the desorption profile by numerically solving the differential equation Eq. 2.4. and plotted it in Figure 2.7a. The red line represents the measured desorption curve while using a single activation energy yields a much narrower curve represented by the black dotted line. It follows from here that by using only a single activation energy does not describe the desorption kinetics entirely.

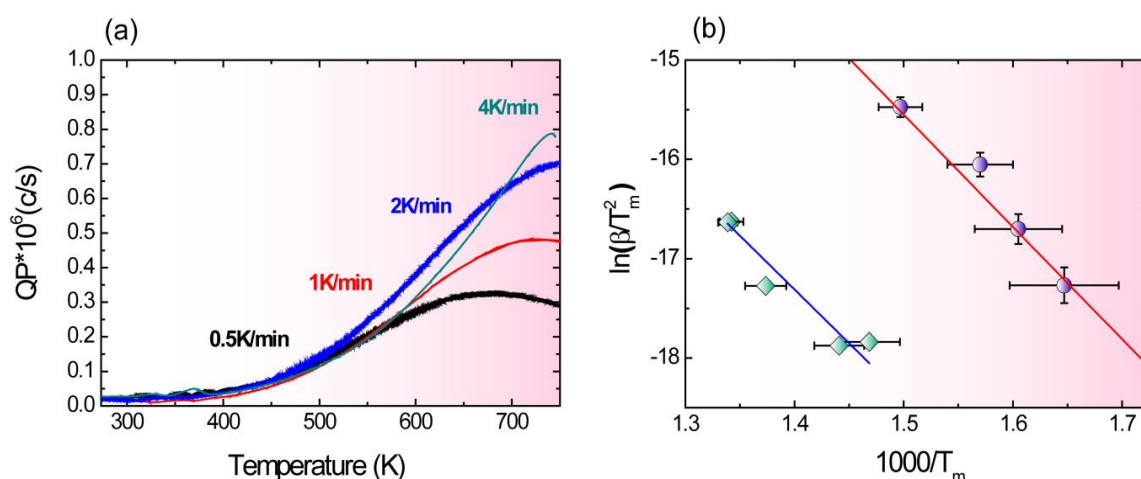


Figure 2.6. Kinetic analysis of hydrogen desorption from Mg nanoparticles produced by spark discharge generation: a) Thermal programmed desorption profiles at different heating rates; b) Kissinger plots used to determine the activation energy of hydrogen desorption.

This means that the reactivity of the sample is not homogeneous and there are faster and slower reacting parts in the sample. We subsequently assumed the presence of a distribution of activation energies ranging from about ~ 60 to ~ 120 kJ mol^{-1} as shown in Figure 2.7b. Using the same values for the heating rate β and the pre-exponential factor A , good agreement with the measured TDS profile can indeed be obtained within this model as the blue curve in Figure 2.7a indicates. This broad range of apparent activation energies can be attributed to the wide variation in the morphology of the nanoparticles: both in size and state of agglomeration, as well as to the presence of the MgO shells.

The observed desorption at rather low temperatures (*i.e.* at low values for the apparent activation energy) can be induced by the small sizes of metal hydride particles because of a number of factors, including (i) the presence of small diffusion distances, which aids to remove hydrogen diffusion as a rate-limiting step; and (ii) the large availability of surface sites per hydrogen atom (since the surface-to-volume ratio increases as l^{-1} with the reduced particle size), which reduces the effect of slow accessibility of surface sites due to long surface residence times of hydrogen atoms which slowly recombine into hydrogen molecules. Interestingly, our data indicate that the intrinsic contribution to the activation energy of the surface barrier to recombination could be as low as 60 kJ mol^{-1} .

We consider here the case when hydrogen diffusion acts as the rate-limiting step to demonstrate the particle size effect in more detail. One may estimate the timescale of hydrogen diffusion from:

$$\tau = \frac{l^2}{6D} \quad (2.8)$$

which decreases quadratically with reduced particle size. Typical values for the hydrogen diffusion constant for MgH_2 at 573 K reported in the literature are

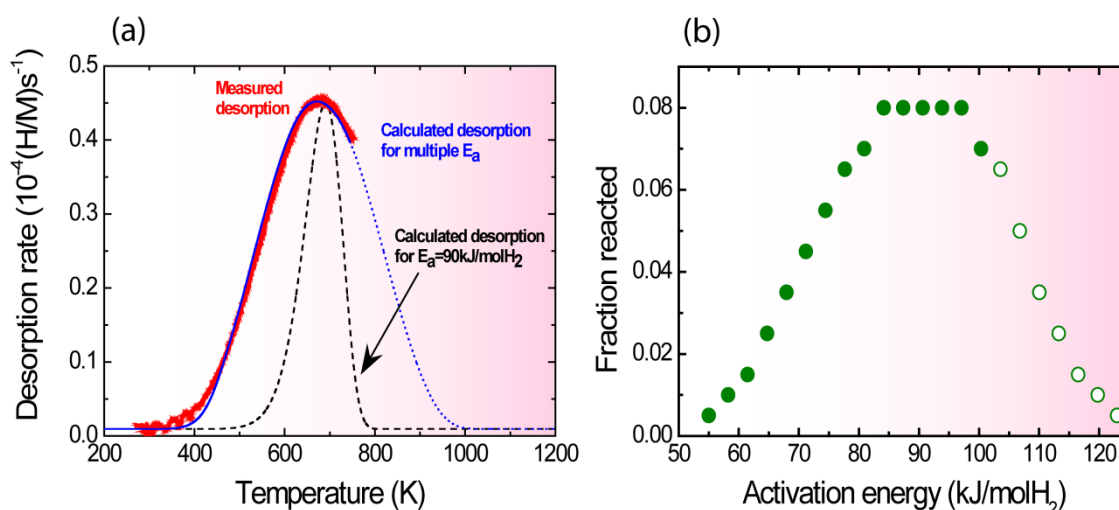


Figure 2.7. (a) Hydrogen desorption profile for spark discharged generated Mg nanoparticles measured by thermal programmed desorption at a heating rate of $0.5\text{K}/\text{min}$: red curve – measured data, black dotted curve – single activation energy model, blue curve – multiple activation energy model; (b) Distribution of apparent activation energies used in the calculation of the multiple activation energy model.

$D = 10^{-13} - 10^{-14} \text{ m}^2/\text{s}$ which are about three orders of magnitude lower than for hydrogen diffusion in the metallic Mg phase.^{43,44,45} Using the temperature dependence of the diffusion constant, the impact of the particle size on the hydrogen diffusion can be estimated:

$$D(T) = D_0 e^{-\frac{E_m}{RT}} \quad (2.9)$$

with $D_0 = 2.8 \cdot 10^{-4} \text{ m}^2/\text{s}$ and migration energy $E_m = 98 \text{ kJ/mol}$ at 573 K, it follows that $D = 3.6 \cdot 10^{-13} \text{ m}^2/\text{s}$. Given these values, a diffusion time of $\sim 2.3 \text{ h}$ can be estimated for $1 \mu\text{m}$ particles at 400 K. In contrast, the estimated diffusion time is only 10 s for 35 nm particles at 400 K, showing that diffusion-limited desorption combined with the presence of small particle sizes can indeed play a key role in explaining the observed low-temperature hydrogen desorption in the range around 400 K. Clearly, the diffusion time depends strongly on both temperature and on the size of particles; particles of different sizes will therefore show hydrogen desorption at widely different temperatures, leading to substantial differences in the extracted apparent activation energies.

Indeed, in another study by Bogerd et al.⁴⁶ relatively low desorption temperatures, starting around 473 K, were also reported for $\sim 20\text{--}25 \text{ nm}$ MgH_2 nanoparticles produced by melt infiltration inside carbon frameworks, with the main desorption peak positioned near 650 K. Other processes, such as the previously indicated scaling of the relative abundance of surface sites with the inverse of the particle size, may also be a factor leading to the low-temperature hydrogen desorption for small particles.

While the particle size distribution may explain why hydrogen desorption occurs at such low temperatures, it cannot explain why the desorption profile extends to higher temperatures than for ball-milled MgH_2 . One plausible reason is the presence of MgO shells surrounding specific Mg domains, as identified in the TEM images. Thin film studies showed that a MgO oxide layer on top of Mg may have two opposite effects on the hydrogen sorption, depending on the thickness and nature of the layer. For very thin layers of up to $\sim 14 \text{ \AA}$ in thickness consisting of fine-grained MgO⁴⁷, the presence of such an oxide layer was in fact found to promote the hydrogen sorption kinetics. For thicker, denser MgO layers, in contrast, the kinetics is severely hampered^{47,48}. Ostenfeld⁴⁸ showed that Mg films capped by a MgO layer are characterized by an increased activation energy for hydrogen desorption. A recent ab initio study by Wu et al.⁴⁹ supports these findings, since high calculated values for the hydrogen migration energy of $E_m \sim 1.0\text{--}1.2 \text{ eV}$ in MgO were obtained. A diffusion constant of $D \sim 3 \cdot 10^{-15} \text{ m}^2/\text{s}$ at 573 K, *i.e.* two orders of magnitude smaller than for MgH_2 , can be derived from the calculations. Further, an even higher diffusion barrier between the surface and subsurface sites was found. The presence of thick and dense oxide shells for some of the particles may thus explain the high-temperature part of the broad hydrogen desorption profile observed in our study, as these shells may effectively block hydrogen desorption, regardless of small particle size, at lower temperatures.

2.3.4 Thermal desorption of hydrogen from Pd and Nb catalyzed magnesium hydride synthesized by spark discharge generation

The hydrogen desorption from the hydrogenated Mg nanoparticles determined previously can further be improved by the use of transition metal catalysts such as Pd and Nb.

The isothermal hydrogen desorption curves were measured at 473 K, 523 K and 573 K for a series of Mg/Pd and Mg/Nb samples which are depicted in Figure 2.8. The total amount of hydrogen desorbed is about 1 wt. % in each case. Clearly, the hydrogen desorption becomes systematically faster at higher temperatures. While the experimental desorption curves initially show a fast decay, they subsequently show a slower decaying tail relative to a simple exponential decay. Clearly, a fit of the desorption curves with a single component representing a single activation energy represents an oversimplification to the real behavior of the sample. This is similar to the case of non-catalyzed MgH₂ described in the previous section where a distribution of activation energies needed to be used. In the present case, the curves could be fitted satisfactorily by two exponential terms but only upon including an unrealistically high background term. Instead, we found that an adequate description involves the use of a stretched exponential decay, according to:

$$I(t)/I_0(t) = a \cdot \exp(-(k_1 \cdot t)^n) + (1-a) \cdot \exp(-k_2 \cdot t) \quad (2.10)$$

with I/I_0 the normalized hydrogen desorption rate, a the relative intensity of the stretched exponential, k_1 and k_2 reaction constants and n is the fractional exponent. The addition of a simple exponential term was necessary to fit the tail of the curve.

In Figure 2.9, the experimental desorption curves for Mg/Pd sample are replotted according to $\ln(-\ln(I/I_0))$ versus $\ln(t)$, demonstrating the validity of this approach. A stretched exponential decay will result in a straight line in these plots with a slope equal to the value of the fractional exponent. Clearly, the kinetic curves in Figure 2.9 closely follow a straight line, with an additional bending at the longest timescales, which could be properly accounted for by adding the simple exponential decay term describing the contributions of the slowest particles. The kinetic parameters obtained from the fits are provided in Table 2.2

Under specific conditions, the Johnson-Mehl-Avrami-Kolmogorov (JMAK) model also predicts a stretched exponential decay for hydrogen sorption kinetics. These conditions are that the new phase nucleates randomly throughout the volume of the sample and grows at a constant growth rate. For the case of three-dimensional growth, a fractional exponent $n \geq 3$ is obtained. This simple mechanism, nevertheless, does not fit most solid state reactions⁵⁰, hence the numerous special cases of the JMAK model for the growth mechanism of the nucleated phase were studied.⁵¹ The fractional exponents found in this study, however, are lower than 1, typically in the range of 0.7 to 0.8, for all fits, which cannot be explained in the currently available versions of the JMAK model.

We found that a kinetic model based on the presence of a wide range of reaction rates within the sample can consistently describe the results from our studies, in contrast to the JMAK model which assumes a homogeneous initial state of the sample. Both spark discharge generated samples have a distribution of particle sizes and a complex dendritic morphology evident from TEM (Figure 2.5), leading to strong local variations in the sample which violate the presumption of the same nucleation and growth conditions throughout the sample. Dispersion in the reactivity of solid state reactions has been successfully applied to describe oxidation of organic or polymeric glasses^{52,53,54} and free radical recombination reactions⁵⁵. The origin of heterogeneity in the reaction rates within one sample can be either different configurations of the reacting particles or the varying chemical composition of the surroundings.^{56,57}

Such a reactive disperse solid state sample can effectively be described as a sum of subsystems, each of which is characterized by a different rate constant. If each subsystem reacts according to the first order kinetic law, then the rate of the transformation for the whole ensemble of subsystems is described by Eq.2.13:

$$I(t)/I_0 = \int_0^{\infty} H(k) \cdot \exp(-k \cdot t) dk \quad (2.11)$$

where k is the rate constant, $H(k)$ is the distribution of rate constants and the inverse Laplace transform of $I(t)$, normalized according to , and t is the desorption time.

A general analytical approximation for the shape of $H(k)$ was derived by Saito et al.⁵⁸, according to:

$$H(k) = \frac{bn}{(1-n)\sqrt{2\pi n}} (kb)^{\frac{-n+2}{2n-2}} \exp\left[-(kb)^{\frac{n}{n-1}}\right]$$

$$\text{with } b = \left(k^{1/n} n(1-n)^{\frac{(1-n)/n}{n}}\right)^{-1} \quad (2.12)$$

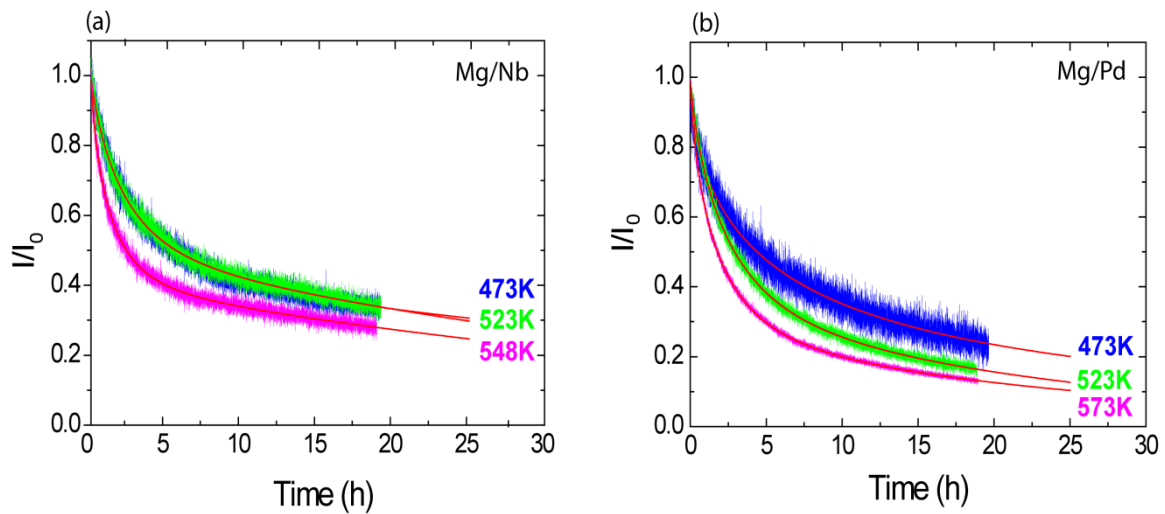


Figure 2.8. Isothermal hydrogen desorption of a) Mg/Nb and b) Mg/Pd nanocomposites at 473K, 523K and 573K.

where n is the fractional exponent, k and k_1 are the reaction constants in Eq. 2.12. The rate constant distributions $H(k)$ calculated for both the Mg/Nb and Mg/Pd samples are plotted in Figure 2.10. In all cases, a broad distribution of rate constants is observed. The distributions of the Mg/Nb sample maintain nearly the same shape with increased temperature in Figure 2.10, while they systematically shift towards higher k values with increased temperatures, reflecting the increase in the sorption kinetics. The Mg/Pd sample presents a slightly different kinetic profile at 473 K, where the sample reacts slowly compared to the Mg/Nb sample, while a similar distribution is observed at 523 K and 573 K.

The temperature dependence of the rate constant distributions is better understood upon realizing that the rate constants typically follow an Arrhenius behavior with temperature, according to:

$$k = A \exp(-E_a / RT) \quad (2.13)$$

assuming that the preexponential factor A is a constant and equal to $1.2 \cdot 10^3 \text{ s}^{-1}$ as obtained from Kissinger analysis of hydrogen desorption from non-catalyzed hydrogenated Mg nanoparticles, values for the involved activation energies E_a can be derived. In the insets of Figure 2.10a and Figure 2.10b, the activation energies corresponding to the lower and higher boundaries of the broad k distribution curves are plotted, defined by the respective k values at 1% of the maximum intensity of the distribution.

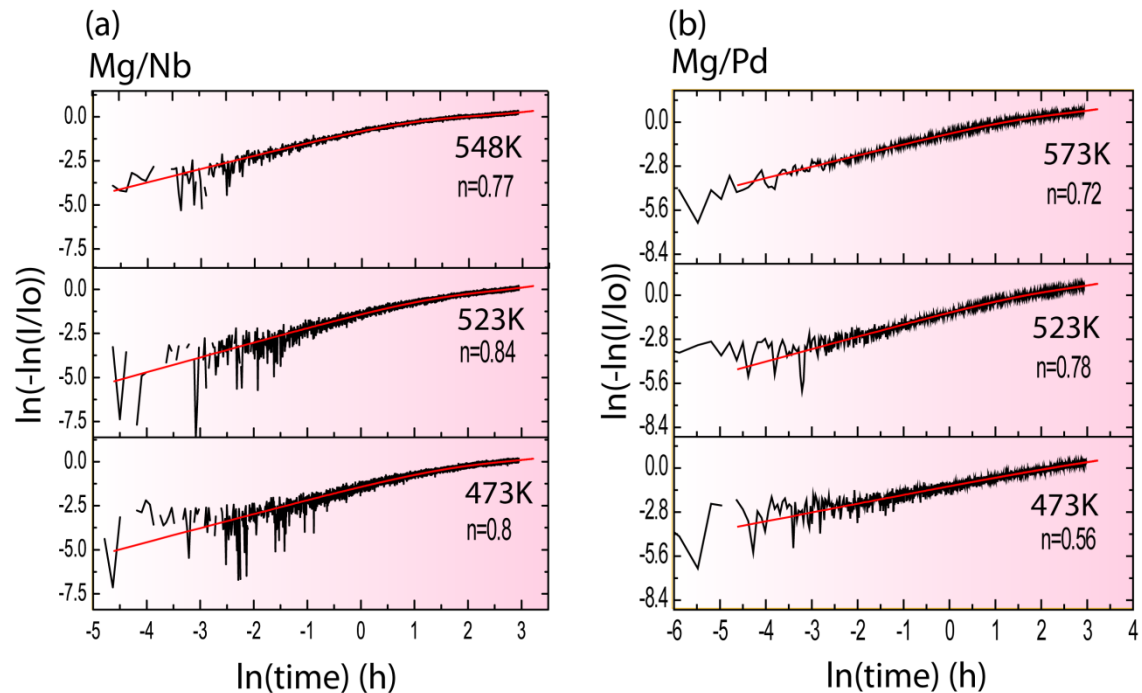


Figure 2.9. Logarithmic plot of the normalized reaction rate versus time for a)Mg/Nb nanoparticles and b)Mg/Pd nanoparticles.

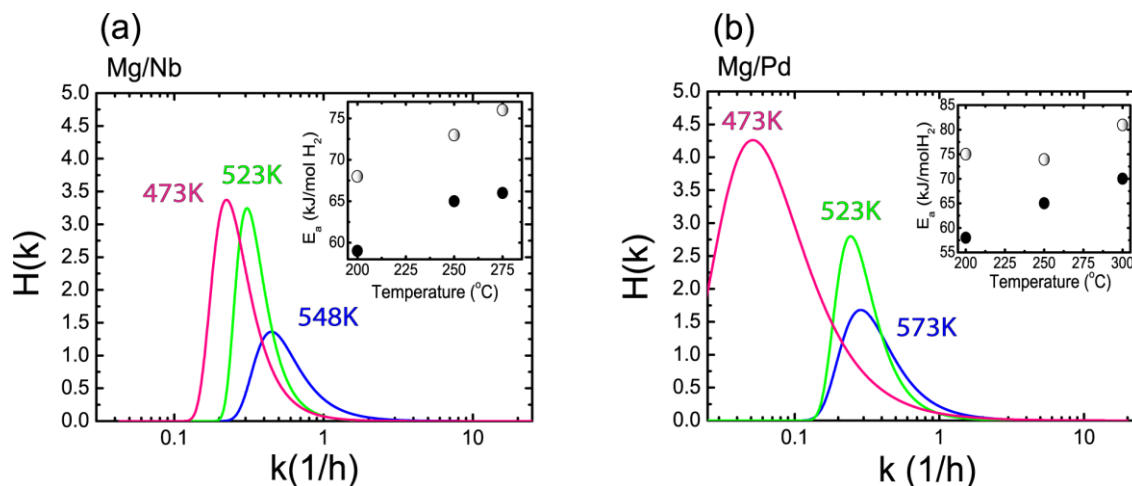


Figure 2.10. Distribution of reaction rates calculated from isothermal desorption curves of a) Mg/Nb and b) Mg/Pd nanocomposites. In the inset, the distribution of the activation energies is plotted.

At 473 K, the extracted lowest activation energy of ~ 58 kJ/mol is representative of the fastest reacting parts of the samples, *i.e.* the smallest sized particles, as judged from a comparison with the broad overall distribution of apparent activation energies deduced in our previous study on non-catalyzed Mg, (see section 2.3) which starts at about 55 kJ/molH₂. The observed spread in contributing activation energies ranges from 8 kJ/mol to 17 kJ/mol. With increased temperature, the slower reacting parts of the samples with higher apparent activation energies up to at least ~ 80 kJ/mol start to contribute to the hydrogen desorption. The contribution of simple exponential term with very low reaction rates of $k_2 \sim 0.015h^{-1} - 0.04h^{-1}$ reflects the slower reacting part of the sample.

As already discussed previously (see section 2.3.3.) this is probably related to coverage of part of the MgH₂ nanoparticles with thin MgO shells of up to ~ 2 nm, leading to high apparent activation energies up to ~ 120 kJ/mol¹. Part of the sample therefore effectively does not desorb in the temperature range of 473 K-573 K studied here. This result is supported by our XRD study which revealed the presence of a small fraction of typically ~ 7 wt. % MgH₂ in

Table 2.2 Kinetic parameters obtained from the stretched exponential fitting in Figure 2.9

Kinetic Parameters	Mg/Nb nanocomposite		
	200°C	250°C	275°C
a	0.554±0.004	0.491±0.002	0.589±0.001
n	0.805±0.004	0.846±0.004	0.769±0.002
k ₁	0.383±0.005	0.475±0.004	0.845±0.003
k ₂	0.015±0.0005	0.021±0.0003	0.020±0.0002
Kinetic Parameters	Mg/Pd nanocomposite		
	200°C	250°C	300°C
a	0.792±0.004	0.658±0.003	0.733±0.001
n	0.565±0.007	0.788±0.002	0.725±0.001
k ₁	0.206±0.002	0.436±0.003	0.613±0.001
k ₂	0.016±0.004	0.039±0.0005	0.038±0.0002

the desorbed samples (see Table 2.1). Further prevention of partial oxidation during the synthesis process therefore may lead to fast hydrogen desorption kinetics for spark discharge MgH_2 particles, for which apparent activation energies as low as 58 kJ/mol can be achieved.

2.4. Conclusion

Spark discharge generation allowed the synthesis of Mg/Pd and Mg/ NbO_x nanocomposites. The nanoscale mixing of the elements allows the formation of a variety of chemical compounds which are not always the most thermodynamically stable.

A distribution of reaction rates is a more appropriate description for the spark discharge generated MgH_2 nanoparticles, rather than the conventional homogeneous nucleation and growth mechanism of the JMAK model. This model for the hydrogen sorption kinetics is expected to be generally applicable for metal hydride nanoparticles with a clear particle size distribution, a complex (dendritic) morphology and/or coverage with oxides forming a barrier for hydrogen sorption. The reaction rate distributions can be straightforwardly calculated from the stretched exponential decay of the hydrogen desorption. We deduced that at each temperature, only a part of the sample contributes to the hydrogen desorption, corresponding to a temperature dependent specific window of apparent activation energies that characterize the active parts of the samples. Selection of the smallest particle sizes and further prevention of oxidation may lead to very low activation energies and fast hydrogen desorption at low temperature.

References

- (1) Vons, V. A.; Anastasopol, A.; Legerstee, W. J.; Mulder, F. M.; Eijt, S. W. H.; Schmidt-Ott, A. Low-Temperature Hydrogen Desorption and the Structural Properties of Spark Discharge Generated Mg Nanoparticles. *Acta Materialia* 2011, *59*, 3070-3080.
- (2) Fernández, J. F.; Sánchez, C. R. Rate Determining Step in the Absorption and Desorption of Hydrogen by Magnesium. *Journal of Alloys and Compounds* 2002, *340*, 189-198.
- (3) Liang, G.; Huot, J.; Boily, S.; Schulz, R. Hydrogen Desorption Kinetics of a Mechanically Milled MgH₂+5at.%V Nanocomposite. *Journal of Alloys and Compounds* 2000, *305*, 239-245.
- (4) Mintz, M. H.; Bloch, J. Evaluation of the Kinetics and Mechanisms of Hybridizing Reactions. *Progress in Solid State Chemistry* 1985, *16*, 163-194.
- (5) Callini, E.; Pasquini, L.; Piscopiello, E.; Montone, A.; Antisari, M. V.; Bonetti, E. Hydrogen Sorption in Pd-Decorated Mg--MgO Core-Shell Nanoparticles. *Applied Physics Letters* 2009, *94*, 221905-3.
- (6) Callini, E.; Pasquini, L.; Rude, L. H.; Nielsen, T. K.; Jensen, T. R.; Bonetti, E. Hydrogen Storage and Phase Transformations in Mg--Pd Nanoparticles. *J. Appl. Phys.* 2010, *108*, 073513-073517.
- (7) Cohen, M. D.; Schmidt, G. M. J. 383. Topochemistry. Part I. A Survey. *J. Chem. Soc.* 1964, 1996-2000.
- (8) Prodan, E. A. Some Kinetic Problems of Inorganic Topochemistry. *Journal of Thermal Analysis* 1987, *32*, 1635-1644.
- (9) Toby, B. H. EXPGUI, a Graphical User Interface for GSAS. *J. Appl. Cryst.* 2001, *34*, 210-213.
- (10) Toby, B. H.; Von Dreele, R. B.; Larson, A. C. CIF Applications. XIV. Reporting of Rietveld Results Using PdCIF: GSAS2CIF. *J. Appl. Cryst.* 2003, *36*, 1290-1294.
- (11) Langford, J. I.; Wilson, A. J. C. Scherrer After Sixty Years: A Survey and Some New Results in the Determination of Crystallite Size. *J. Appl. Cryst.* 1978, *11*, 102-113.
- (12) Vons, V. A.; Leegwater, H.; Legerstee, W. J.; Eijt, S. W. H.; Schmidt-Ott, A. Hydrogen Storage Properties of Spark Generated Palladium Nanoparticles. *International Journal of Hydrogen Energy* 2010, *35*, 5479-5489.
- (13) Toby, B. H.; Von Dreele, R. B.; Larson, A. C. CIF Applications. XIV. Reporting of Rietveld Results Using PdCIF: GSAS2CIF. *J. Appl. Cryst.* 2003, *36*, 1290-1294.

- (14) Yuan, H. T.; Liu, Y. Z.; Zeng, Z. Q.; Mei, Z. X.; Guo, Y.; Zhang, P.; Du, X. L.; Jia, J. F.; Zhang, Z.; Xue, Q. K. Formation of Metastable MgO Structures on Type-III Oxide Surfaces: Effect of Periodic Out-of-Plane Electric Dipole Moment of Substrates. *Journal of Crystal Growth* 2009, *311*, 425-428.
- (15) Friedrichs, O.; Kolodziejczyk, L.; Sánchez-López, J. C.; Fernández, A.; Lyubenova, L.; Zander, D.; Köster, U.; Aguey-Zinsou, K. F.; Klassen, T.; Bormann, R. Influence of Particle Size on Electrochemical and Gas-Phase Hydrogen Storage in Nanocrystalline Mg. *Journal of Alloys and Compounds* 2008, *463*, 539-545.
- (16) Makongo, J. P. A.; Prots, Y.; Burkhardt, U.; Niewa, R.; Kudla, C.; Kreiner, G. A Case Study of Complex Metallic Alloy Phases: Structure and Disorder Phenomena of Mg-Pd Compounds. *Philosophical Magazine* 2006, *86*, 427-433.
- (17) Eijt, S. W. H.; Kind, R.; Singh, S.; Schut, H.; Legerstee, W. J.; Hendrikx, R. W. A.; Svetchnikov, V. L.; Westerwaal, R. J.; Dam, B. Positron Depth Profiling of the Structural and Electronic Structure Transformations of Hydrogenated Mg-Based Thin Films. *J. Appl. Phys.* 2009, *105*, 043514-13.
- (18) Slack, J. L.; Locke, J. C. W.; Song, S. W.; Ona, J.; Richardson, T. J. Metal Hydride Switchable Mirrors: Factors Influencing Dynamic Range and Stability. *Solar Energy Materials and Solar Cells* 2006, *90*, 485-490.
- (19) Eijt, S. W. H.; Kind, R.; Singh, S.; Schut, H.; Legerstee, W. J.; Hendrikx, R. W. A.; Svetchnikov, V. L.; Westerwaal, R. J.; Dam, B. Positron Depth Profiling of the Structural and Electronic Structure Transformations of Hydrogenated Mg-Based Thin Films. *J. Appl. Phys.* 2009, *105*, 043514-13.
- (20) Huot, J.; Yonkeu, A.; Dufour, J. Rietveld Analysis of Neutron Powder Diffraction of Mg₆Pd Alloy at Various Hydriding Stages. *Journal of Alloys and Compounds* 2009, *475*, 168-172.
- (21) Dufour, J.; Huot, J. Study of Mg₆Pd Alloy Synthesized by Cold Rolling. *Journal of Alloys and Compounds* 2007, *446-447*, 147-151.
- (22) Schimmel, H. G.; Huot, J.; Chapon, L. C.; Tichelaar, F. D.; Mulder, F. M. Hydrogen Cycling of Niobium and Vanadium Catalyzed Nanostructured Magnesium. *Journal of the American Chemical Society* 2005, *127*, 14348-14354.
- (23) Okada, M.; Goto, Y.; Kataoka, R.; Yambe, Y.; Kamegawa, A.; Takamura, H. Novel Hydrides in Mg-TM Systems Synthesized by High Pressure (TM=Zr, Nb, Hf and Ta). *Journal of Alloys and Compounds* 2007, *446-447*, 6-10.
- (24) Gasan, H.; Celik, O. N.; Aydinbeyli, N.; Yaman, Y. M. Effect of V, Nb, Ti and Graphite Additions on the Hydrogen Desorption Temperature of

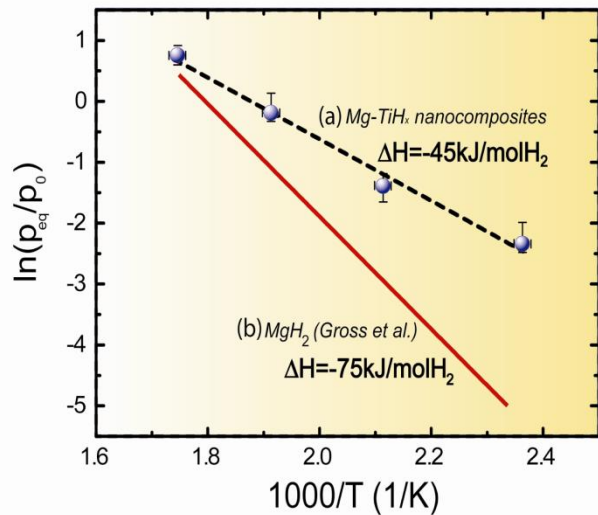
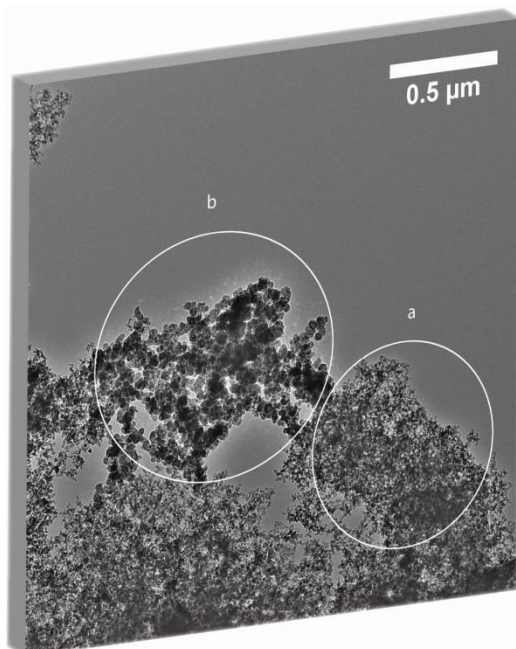
- Magnesium Hydride. *International Journal of Hydrogen Energy* 2012, 37, 1912-1918.
- (25) Luna, C. R.; Macchi, C. E.; Juan, A.; Somoza, A. Electronic and Bonding Properties of MgH₂-Nb Containing Vacancies. *International Journal of Hydrogen Energy* 2010, 35, 12421-12427.
 - (26) Tabrizi, N.; Ullmann, M.; Vons, V.; Lafont, U.; Schmidt-Ott, A. Generation of Nanoparticles by Spark Discharge. *Journal of Nanoparticle Research* 2009, 11, 315-332.
 - (27) Atkins, P. W. *Physical Chemistry*. 1995. Oxford, Oxford University Press.
 - (28) Ioffe, I. I.; Pismen, L. M. *Cataliza eterogena in ingineria chimica*. 1967. Bucharest, Editura Tehnica.
 - (29) Huot, J.; Liang, G.; Boily, S.; Van Neste, A.; Schulz, R. Structural Study and Hydrogen Sorption Kinetics of Ball-Milled Magnesium Hydride. *Journal of Alloys and Compounds* 1999, 293-295, 495-500.
 - (30) Fernandez, J. F.; Sanchez, C. R. Simultaneous TDS/DSC Measurements in Magnesium Hydride. *Journal of Alloys and Compounds* 2003, 356-357, 348-352.
 - (31) Varin, R. A.; Jang, M.; Czujko, T.; Wronski, Z. S. The Effect of Ball Milling Under Hydrogen and Argon on the Desorption Properties of MgH₂ Covered With a Layer of Mg(OH)₂. *Journal of Alloys and Compounds* 2010, 493, L29-L32.
 - (32) Aguey-Zinsou, K. F.; Ares Fernandez, J. R.; Klassen, T.; Bormann, R. Using MgO to Improve the (De)Hydriding Properties of Magnesium. *Materials Research Bulletin* 2006, 41, 1118-1126.
 - (33) Krishnan, G.; Kooi, B. J.; Palasantzas, G.; Pivak, Y.; Dam, B. Thermal Stability of Gas Phase Magnesium Nanoparticles. *J. Appl. Phys.* 2010, 107.
 - (34) Anastasopol, A.; Pfeiffer, T. V.; Schmidt-Ott, A.; Mulder, F. M.; Eijt, S. W. H. Fractal Disperse Hydrogen Sorption Kinetics in Spark Discharge Generated Mg/NbO_x and Mg/Pd Nanocomposites. *Applied Physics Letters* 2011, 99, 194103.
 - (35) Strongin, M.; El-Batanouny, M.; Pick, M. A. Structure of Pd Overlayers on Nb and Ta and the Relationship to Hydrogen Uptake. *Phys. Rev. B* 1980, 22, 3126-3129.
 - (36) Christmann, K. Interaction of Hydrogen With Solid Surfaces. *Surface Science Reports* 1988, 9, 1-163.
 - (37) Bloch, J.; Mintz, M. H. Kinetics and Mechanisms of Metal Hydrides Formation - A Review. *Journal of Alloys and Compounds* 1997, 253-254, 529-541.

- (38) Norskov, J. K.; Stoltze, P. Theoretical Aspects of Surface Reactions. *Surface Science* 1987, 189–190, 91-105.
- (39) Mikheeva, V. I.; Mal'tseva, N. N. Infrared Absorption Spectra of Some Simple Hydrides. *J Struct Chem* 1964, 4, 643-646.
- (40) Redhead, P. A. Thermal Desorption of Gases. *Vacuum* 1962, 12, 203-211.
- (41) Kissinger, H. E. Reaction Kinetics in Differential Thermal Analysis. *Analytical Chemistry* 2002, 29, 1702-1706.
- (42) Kissinger, H. E. Variation of peak Temperature with heating rate in Differential Thermal Analysis. *Journal of Research of the National Bureau of standards* 57[4], 217-221. 2009.
- (43) Gabis, I. E.; Chernov, I. A.; Voyt, A. P. Decomposition Kinetics of Metal Hydrides: Experiments and Modeling. *Journal of Alloys and Compounds* .
- (44) Schimmel, H. G.; Kearley, G. J.; Huot, J.; Mulder, F. M. Hydrogen Diffusion in Magnesium Metal (Phase) Studied by Ab Initio Computer Simulations. *Journal of Alloys and Compounds* 2005, 404/406, 235-237.
- (45) Stioui, M.; Grayevsky, A.; Moran, A.; Kreitzman, S.; Kaplan, N.; Shaltiel, D. Proton Magnetic Resonance Study of Diffusion-Related Properties in Magnesium-Rich Compounds. *Journal of the Less Common Metals* 1984, 104, 119-124.
- (46) Bogerd, R.; Adelhelm, P.; Meeldijk, J. H.; De Jong, K. P.; de Jongh, P. E. The Structural Characterization and H₂ Sorption Properties of Carbon-Supported Mg_{1-x}Ni_x Nanocrystallites. *Nanotechnology* 2009, 20.
- (47) Hjort, P.; Krozer, A.; Kasemo, B. Hydrogen Sorption Kinetics in Partly Oxidized Mg Films. *Journal of Alloys and Compounds* 1996, 237, 74-80.
- (48) Ostefeld, C. W.; Chorkendorff, I. Effect of Oxygen on the Hydrogenation Properties of Magnesium Films. *Surface Science* 2006, 600, 1363-1368.
- (49) Wu, G.; Zhang, J.; Wu, Y.; Li, Q.; Chou, K.; Bao, X. Adsorption and Dissociation of Hydrogen on MgO Surface: A First-Principles Study. *Journal of Alloys and Compounds* 2009, 480, 788-793.
- (50) Malek, J. The Applicability of Johnson-Mehl-Avrami Model in the Thermal Analysis of the Crystallization Kinetics of Glasses. *Thermochimica Acta* 1995, 267, 61-73.
- (51) F.Liu, F. S. C. B. E. J. M. Analysis of Solid State Phase Transformation Kinetics: Models and Recipes. *International Materials Reviews* 2007, 52, 193-212.

- (52) Avramov, I. Kinetics of Structural Relaxation of Glass-Forming Melts. *Thermochimica Acta* 1996, 280-281, 363-382.
- (53) Calka, A.; Radlinski, A. P. The Local Value of the Avrami Exponent: a New Approach to Devitrification of Glassy Metallic Ribbons. *Materials Science and Engineering* 1988, 97, 241-246.
- (54) Weinberg, M. C. A Few Topics Concerning Nucleation and Crystallization in Glasses. *Journal of Non-Crystalline Solids* 1999, 255, 1-14.
- (55) Doba, T.; Ingold, K. U.; Siebrand, W. Evaluation of Reaction Rate Constants in Media Where They Show Dispersion: Hydrogen Abstraction by Methyl Radicals in a Methanol Glass. *Chemical Physics Letters* 1984, 103, 339-342.
- (56) Davydov, E. Y.; Vorotnikov, A. P.; Pariyskii, G. B. Kinetic Peculiarities of Solid Phase Reactions. 5-24. 1998. John Wiley & Sons Ltd.
- (57) Tolkatchev, V. A. The Effect of Local Environment Relaxation on Elementary Homolytic Reaction Kinetics in Glass. Interpretation of the Kohlrausch-Williams-Watts Relaxation Function. *Chemical Physics* 1987, 116, 283-298.
- (58) Saito, R.; Murayama, K. A Universal Distribution Function of Relaxation in Amorphous Materials. *Solid State Communications* 1987, 63, 625-627.

Chapter 3

Reduced Enthalpy of Metal Hydride Formation for Mg–Ti Nanocomposites Produced by Spark Discharge Generation



Abstract

Spark discharge generation was used to synthesize Mg–Ti nanocomposites consisting primarily of a metastable body-centered-cubic (bcc) alloy of Mg and Ti. The bcc Mg–Ti alloy transformed upon hydrogenation into the face-centered-cubic fluorite $Mg_{1-y}Ti_yH_x$ phase with favorable hydrogen storage properties. Both metal and metal hydride nanocomposites showed a fractal-like porous morphology, with a primary particle size of 10–20 nm. The metal content of 70 atom % (at %) Mg and 30 at % Ti, consistently determined by XRD, TEM-EDS, and ICP-OES, was distributed uniformly across the as-prepared sample.

Pressure–composition isotherms for the Mg–Ti–H nanocomposites revealed large differences in the thermodynamics relative to bulk MgH_2 , with a much less negative enthalpy of formation of the hydride as small as -45 ± 3 kJ/mol H_2 as deduced from van't Hoff plots. The plateau pressures of hydrogenation were substantially higher than those for bulk MgH_2 in the low temperature range from 423 to 523 K. The reaction entropy was simultaneously reduced to values down to 84 ± 5 J/K mol H_2 , following a linear relationship between the enthalpy and entropy.

Plausible mechanisms for the modified thermodynamics are discussed, including the effect of lattice strains, the presence of interfaces and hydrogen vacancies, and the formation of excess free volume due to local deformations. These mechanisms all rely on the finely interdispersed nanocomposite character of the samples which is maintained by grain refinement.

This chapter is based on the published paper:

Reduced Enthalpy of Metal Hydride Formation for Mg–Ti Nanocomposites Produced by Spark Discharge Generation, Anca Anastasopol, Tobias V. Pfeiffer, Joost Middelkoop, Ugo Lafont, Roger J. Canales-Perez, Andreas Schmidt-Ott, Fokko M. Mulder, Stephan W.H. Eijt, Journal of the American Chemical Society, 2013, 135, 7891-7900, dx.doi.org/10.1021/ja3123416

“Horatio:
O day and night, but this is wondrous strange!
Hamlet:
And therefore as stranger give it welcome.
There are more things in heaven and earth, Horatio,
Than are dreamt of in our philosophy”

William Shakespeare, Hamlet, Act 1, scene 5

The ability of Mg to react with hydrogen is in a great measure influenced by its enthalpy of formation which is experimentally determined to be about -75 kJ/molH₂. A lower enthalpy of formation for Mg combined with improved kinetics would allow the reaction with hydrogen to proceed in much milder conditions of temperature and pressure than currently employed. Recent studies revealed that the interaction between Mg and Ti offers several opportunities to modify the thermodynamics and kinetics of the hydrogenation reaction. Intense research has shown the use of non-equilibrium synthesis techniques such as magnetron sputter deposition^{1,2,3,4,5} of Mg-Ti thin films, may result in the formation of an hcp Mg-Ti coherent phase despite the positive enthalpy of mixing of Mg and Ti. Upon hydrogenation of the Mg-Ti thin films, a cubic fluorite Mg_{1-y}Ti_yH_x phase was formed for Ti fractions above ~15 at. % with favorable hydrogen sorption kinetics. The hydrogen absorption equilibrium pressure of multilayers thin films consisting of alternating Mg and Ti nanolayers⁶ is significantly higher than the equilibrium pressure of bulk MgH₂ and TiH₂. The use of thin films as hydrogen storage devices, however, has obvious strong limitations. For this reason, intense research is being carried out on the synthesis of Mg-Ti-H alloys^{7,8,9} by means of ball-milling. The first Mg-Ti hydride phase, a cubic Mg₇TiH₁₆ compound was found by Kyojima et al.¹⁰ using a high pressure synthesis method.

Spark discharge generation is a versatile method of producing metal nanoparticles.¹¹ One of the main advantages of the spark discharge generation as opposed to ball milling is the synthesis of nanoparticles instead of just nanocrystalline grains in a continuous rather than batch process. In the previous chapter, transition metal (Pd, Nb) catalyzed Mg nanocomposites have been synthesized by spark discharge generation.^{12,13} Through this bottom up method of producing nanoparticles, small scale mixing of the Mg with the transition metal catalyst is successfully achieved as it was shown in the Chapter 2. Because of the non-equilibrium nature of the particle production, metastable alloys can also be produced by spark discharge generation¹¹. Other bottom up approaches involving inert gas condensation methods^{14,15,16}, focused thus far

on the synthesis of elemental Mg nanoparticles. Further, Mg-based and MgH₂-based nanoparticles for hydrogen storage applications were produced by melt infiltration^{17,18} and by decomposition of organometallic precursors under suitable conditions^{19,20}.

In this chapter, a study on Mg/Ti nanocomposites synthesized by spark discharge generation is presented. Alongside the presence of Mg and Ti nanoparticles, a nanosized, metastable intermetallic body centered cubic Mg-Ti alloy phase has been identified in the as prepared samples. The very low solubility of Mg in Ti makes the presence of this cubic Mg-Ti phase an interesting result in itself. Moreover, a detailed structure analysis of the hydrogenation products revealed the formation of a fluorite type hydride Mg-TiH_x phase which remains in a nanoparticulate state after long heating treatments. Pressure composition isotherm (PCT) measurements, obtained using a Sieverts' apparatus revealed a much less negative enthalpy of formation of -45 ± 3 kJ/molH₂. Such a small value for the enthalpy of formation for the Mg-Ti-H nanocomposites has not been reported before. Essentially, the plateau pressures are significantly higher than for bulk MgH₂ at low temperatures but remain close to bulk values at higher temperatures, changing in this manner the enthalpy of formation. However, this effect is accompanied by a high degree of disorder of the hydride phase, which acts as an extra barrier in the overall free energy change during hydrogenation of the system, partially compensating the enthalpy gain.

3.2. Experimental section

3.2.1. Synthesis - Spark discharge generation

Using a spark discharge setup previously described²¹, Mg-Ti nanocomposites were synthesized from the elements (Ø6.35 mm rods, 99.9+% purity, Mateck GmbH). A spark discharge between a Ti cathode placed opposite a grounded Mg anode was used to ablate material from both electrodes, and the resultant mixed metal vapor cloud was quenched rapidly to form the Mg/Ti nanocomposites. A series of five different batches of samples were produced, in which the electrode spacing was varied between 1 and 2 mm. For the samples described here, the electrode spacing was 2.0 mm, and the working gas was Ar purified as previously reported¹². In this study, we concentrated on the hydrogen storage properties of two selected samples with a mass of 5.1 and 4.5 mg, respectively. Sparks were generated at a rate of 200 Hz using a 20 nF capacitance and a charging current of 8.5 mA, for a total power input of 9.3 W. Particles were collected during 9 hour runs at a rate of 0.14 mg/hr on Ø47 mm PVDF membrane filters with 0.45 µm pore size (Durapore, Millipore) in a special filter holder, and transferred to an Ar filled glovebox (<0.1 ppm H₂O and O₂) for further sample preparation.

3.2.2. Powder X-ray diffraction

The structure of the crystalline samples was investigated by X-ray diffraction using a PANalytical X'Pert PRO diffractometer with a Cu K_α ($\lambda=1.5415$ Å) operated at 40 kV and 40 mA. The samples were loaded in an Ar filled glovebox in air tight sample holders. To reduce the background due to the low amount of sample used, a silicon single crystal disk was used as a support

plate. The background measured from the silicon disk and sample holder is subtracted from the X-ray diffraction patterns. The X-ray diffraction patterns with background can be found in appendix A. Rietveld analysis was performed on the measured patterns, using GSAS^{22,23} software.

3.2.3. Transmission electron microscopy

Transmission electron microscopy (TEM), including energy-dispersive X-ray spectrometry (EDS), selected-area electron diffraction (SAED) and electron loss near edge spectroscopy (ELNES), were performed using a FEI Tecnai TF20 electron microscope operated at 200 kV. Samples were mounted on Quantifoil[®] microgrid carbon polymer supported on a copper grid

3.2.4. Sieverts measurements

Hydrogen absorption isotherms were measured using a commercial Sieverts' apparatus, PCT Pro 2000 by Hy-Energy. For the measurements, hydrogen gas of purity 5.0 was used. The accuracy of the pressure reading is 1%. The drift in the pressure reading is between 14 mbar and 42 mbar within six months. For the setup, a dry scroll pump was used with a base pressure at the inlet of $5 \cdot 10^{-2}$ mbar. Pressure composition isotherms were measured with the use of the MicroDoser attachment and the typical size of the aliquot was 0.663 ml.

3. 3. Results and Discussion

3.3.1. Structural characterization of the Mg/Ti nanocomposites

The overall composition of the samples was studied using X-ray diffraction. The analysis of the diffraction patterns revealed that the spark discharge generated nanocomposites consist of several different crystalline phases: nanoparticles with the hexagonal Mg and Ti phases ($P6_3/mmc$) are present along with rock salt cubic MgO ($Fm\bar{3}m$), as shown by the representative example in Figure 3.1a. A series of samples were synthesized by varying the gap between the spark electrodes from 1 mm to 2 mm.

The X-ray diffraction patterns are gathered in Figure 3.2. Interestingly, all samples showed the presence of a body-centered-cubic (bcc) Mg-Ti alloy phase ($Im\bar{3}m$), as revealed by the presence of a dominant (110) diffraction peak at 35.1° , corresponding to a lattice parameter of 3.61 Å. Such a bcc Mg-Ti alloy with random site occupation was previously observed by Asano *et al.*^{7,8,9} in $Mg_{1-y}Ti_y$ alloys ($0.25 < y < 0.65$) synthesized by means of ball-milling, where smaller lattice parameters near 3.42 Å were found. The presence of the face-centered cubic and hcp Mg-Ti alloy phases observed by Asano *et al.*^{7,8,9} can be ruled out for the spark discharge generated nanocomposites, based on our X-ray diffraction results. The presence of the bcc $Mg_{1-y}Ti_y$ alloy phase is quite remarkable, given the positive enthalpy of mixing of Mg and Ti.

Unlike our previous studies^{12,13}, where a set of two spark generators was used to produce nanocomposites of Mg particles interdispersed with Pd or Nb

catalyst particles (see Chapter 2), the use of an Mg electrode against a Ti electrode in a single spark generator allows the formation of the Mg-Ti alloy phase, as the particles now form in a mixed metal vapor cloud. Samples generated with this electrode configuration using a spacing of 1 to 2 mm between the two electrodes consisted for a large part of the bcc Mg-Ti phase with phase fractions in the range of 30 wt. % to 52 wt. % (see Table 3.1). This demonstrates the capability of spark discharge generation to synthesize metastable Mg-Ti alloys by rapid quenching of the Mg and Ti clouds that are intermixed at an atomic scale. Such a bcc $\text{Mg}_{1-y}\text{Ti}_y$ alloy was previously also obtained after prolonged ball milling of 20-200 hours of Mg and Ti powders^{7,8,9}, for compositions reportedly in the range of $0.25 < y < 0.65$. The bcc Mg-Ti alloy phase stabilizes most easily near a composition of $\text{Mg}_{0.5}\text{Ti}_{0.5}$.^{24,25}

An essential difference is that during ball milling, the size of the grains building up a micron-sized particle is reduced to nanoscale dimensions, whereas in the case of spark discharge, the particles themselves are nanosized as TEM indicates. This key difference has a pronounced impact on the hydrogen sorption properties of these types of samples, as shown further on.

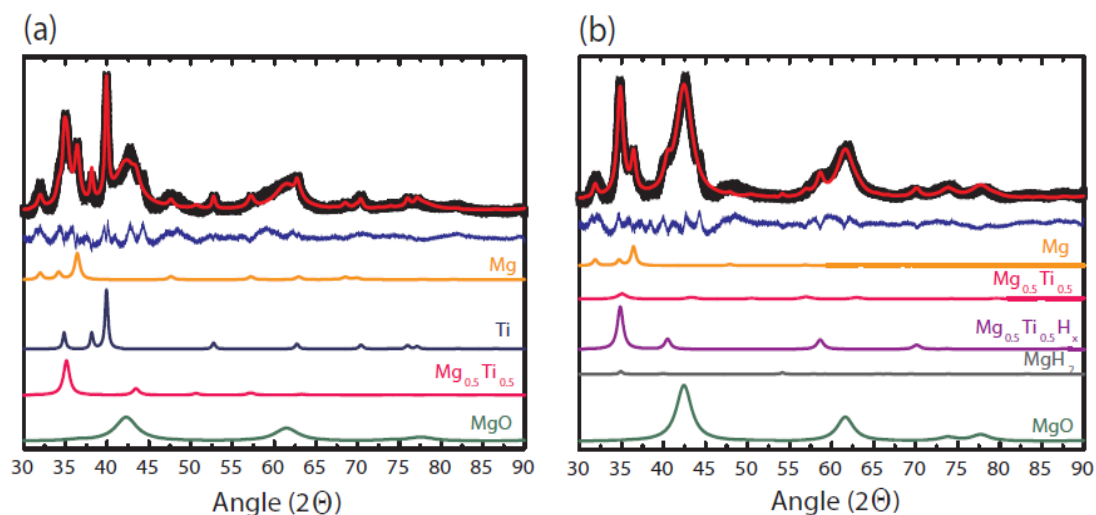


Figure 3.1. X-ray diffraction patterns of Mg/Ti nanocomposites and the results of the Rietveld refinement (measured spectra – black, calculated spectra- red, residual-blue): a. as produced by spark discharge generator; b. after partial loading with hydrogen. The sample container background is subtracted. The individual phase contributions are given below (scaled down by $1/2$).

Table 3.1. Particle sizes and phase fractions in wt% extracted from Rietveld refinement of the XRD patterns of freshly synthesized Mg-Ti nanocomposites and Mg-Ti-H nanocomposites after hydrogen sorption.

Phase	Freshly prepared								After hydrogen sorption			
	2 mm ($R_{wp}=2\%$)		1.8 mm ($R_{wp}=2.4\%$)		1.25 mm ($R_{wp}=2.2\%$)		1 mm ($R_{wp}=4\%$)		Sample 1 ($R_{wp}=2.8\%$)		Sample 2 ($R_{wp}=2.6\%$)	
	Size	Fraction	Size	Fraction	Size	Fraction	Size	Fraction	Size	Fraction	Size	Fraction
Mg	14±2nm	10 wt.%	21±3nm	5 wt.%	31±3nm	4.5 wt.%	12±2nm	86 wt.%	16±2nm	13 wt.%	45±2nm	13.7wt.%
Ti	27±5nm	9 wt.%	32±4nm	9 wt.%	28±5nm	4 wt.%	27±5nm	0.3 wt.%	-	-	-	-
Mg_{0.5}Ti_{0.5}	11±2nm	45 wt.%	9±2nm	31 wt.%	9±2nm	53 wt.%	10±2nm	2.4 wt.%	8±1nm	2.2 wt.%	-	-
MgO	3±2nm	36 wt.%	2±1nm	55 wt.%	2±2nm	38.5wt.%	1±1nm	11 wt.%	5±1nm	58 wt.%	4±2nm	76 wt.%
Mg_{1y}Ti_yH_x	-	-	-	-	-	-	-	-	12±2nm	26 wt.%	10±2nm	10.3wt.%
MgH₂	-	-	-	-	-	-	-	-	21±4nm	0.8wt.%	-	-

Rietveld refinement²⁶ was successfully performed on the XRD patterns, and the results are summarized in Table 3.1. The extracted particle sizes were found to be small for each of the phases. The size of the bcc phase Mg-Ti particles is found to be below ~ 11 nm. The apparent crystallite size of MgO is 3 ± 1 nm for as-prepared samples, which indicates that the MgO is present as a thin shell around the particles of Mg, as seen in our previous studies^{12,13} and for Mg nanoparticles produced by inert gas condensation methods^{14,15,16}. According to the refinement results, hexagonal Mg and Ti are present in the sample synthesized at an electrode distance of 2 nm at relatively small fractions of 10 wt. % and 9 wt. %, respectively. The sample is dominated by a high fraction of about 45 wt. % of the cubic Mg-Ti alloy. The fractions obtained from the XRD measurements point to an overall metal fraction of Mg of 70 at. % and of Ti of 30 at. %. This result is very similar to the fractions obtained from ICP-OES and TEM-EDS, as it is summarized in Table 3.2. Both XRD and ICP-OES characterize a bulk average of the sample, while TEM-EDS give very local information about the sample composition, obtained for several parts of the sample. Since the same composition is obtained from both global average and local measurements, one may conclude that the composition is uniform throughout the as-prepared sample. Thus, spark discharge generation not only allows the mixture of metals on a very small scale but also as a uniform mixture.

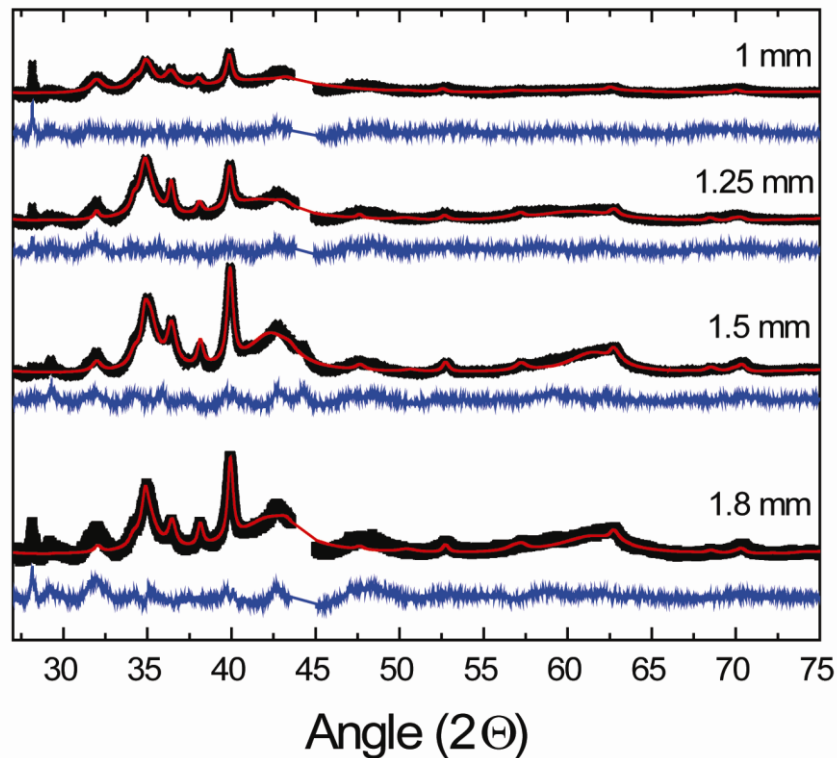


Figure 3.2. X-ray diffraction patterns of Mg/Ti nanocomposites and the results of the Rietveld refinement (measured spectra – black, calculated spectra- red, residual-blue). The samples are synthesized with varying the gap between the spark electrodes from 1.8mm to 1 mm. The sample container background is subtracted and the peak at 44° due to the sample container was removed.

The sample was subjected to several cycles of hydrogen loading and unloading at temperatures up to 573 K in a Sieverts' setup. After the cycling, XRD patterns were again measured. In the partially loaded state, a noteworthy fact is the disappearance of the crystalline Ti phase and the appearance of a face centered cubic (fcc) phase similar to a fluorite TiH_2 with expanded lattice parameter. Rietveld refinement was performed with a R_{wp} of 2.8 % and the results are summarized in Table 3.1. The lattice parameter obtained for the distorted TiH_2 is $a=4.44\text{\AA}$, a visible increase from the typical value of 4.36\AA . From studies on Mg/Ti thin films³ but also on ball milled Mg/Ti systems^{24,25}, it is known that the presence of Mg in the TiH_2 , leads to an increase in unit cell. According to Vegard's law, that predicts a linear increase, the amount of Mg present in the sample should then be 20 %, indicating the composition of the hydride is: $\text{Mg}_{0.2}\text{Ti}_{0.8}\text{H}_x$ (assuming $x=2$). However, because of the uncertainty in the amount of hydrogen present in the sample and the lattice expansion that it can generate, the precise composition of the hydride phase is impossible to be determined using Vegard's law only. This hydride will be further generically referred to as Mg-TiH_x. The crystallites of the Mg-TiH_x are small, $12\pm 2\text{ nm}$ as determined from peak broadening in the XRD pattern. Though the fraction of the MgO oxide is increased after hydrogen cycling, the average size of MgO crystallites remains small, about $5\pm 1\text{ nm}$.

In a study of the structural transformations of Mg -Ti ball milled nanocomposites upon hydrogen cycling, Rousselot et al.^{24,25} have found that in a first cycle, a stabilization of the nanocomposites to a fluorite face centered cubic phase (Mg-TiH_x) occurred and the extraction of hydrogen was only accompanied by a change in the lattice parameter and not a change in the symmetry. On the other hand, in studies^{1,27} on Mg-Ti films, where the fluorite type hydride is also created, the extraction of hydrogen results in the hexagonal Mg-Ti phase. In the present study, it could not be distinguished whether upon hydrogen extraction the cubic symmetry is maintained or a transition to the hexagonal symmetry occurs.

Table 3.2. Mg and Ti fractions as obtained through XRD, ICP-OES and EDS for the as produced Mg-Ti nanocomposites synthesized with a 2 mm electrode gap distance

Element	XRD	ICP-OES	TEM - EDS
	At. %	At. %	At. %
Mg	70	67	69
Ti	30	33	31

To have a better understanding of the changes that occur during the heating treatment and the exposure to hydrogen, the morphology and the composition of the sample was investigated locally by transmission electron microscopy. The general aspect of the freshly synthesized sample is of a nanomaterial of a very porous nature (see Figure 3.3 left). Particles close to a spherical shape of about 10 to 20 nm are organized in fractal like structures. Small area electron diffraction confirms that even locally the samples are of crystalline nature but formed of small size crystallites which give rise to broad and diffuse diffraction rings. This result is also confirmed by the analysis of the XRD patterns.

At the edge of the primary particles, a thin shell of a different density can be identified as MgO. The MgO fraction increases with the repeated hydrogen

loading and unloading and the sintering of the particles is more pronounced in the MgO rich regions as it will be further explained.

After several hydrogen loading and unloading cycles, the initial morphology is mostly kept as it can be seen in Figure 3.3 (right). However, a more detailed analysis reveals the appearance of nonuniformity in the sample morphology and composition after the exposure to hydrogen. In the micrograph from Figure 3.4, the two representative morphologies of the sample after cycling are depicted. Region *a* has very similar morphology to the freshly prepared sample, also, the total fraction for this area is 70 at. % Mg to 30 at. % Ti. Particles maintain the small size and their porous aspect.

Region *b* is formed of agglomerated spherical particles of significantly larger sizes of 50 to 100 nm. The ratio between Mg and Ti is about 96.7 at. % Mg to 3.3 at. % Ti. A high fraction of O is detected using EDS, leading to the conclusion that Mg in region *b* is oxidized to MgO.

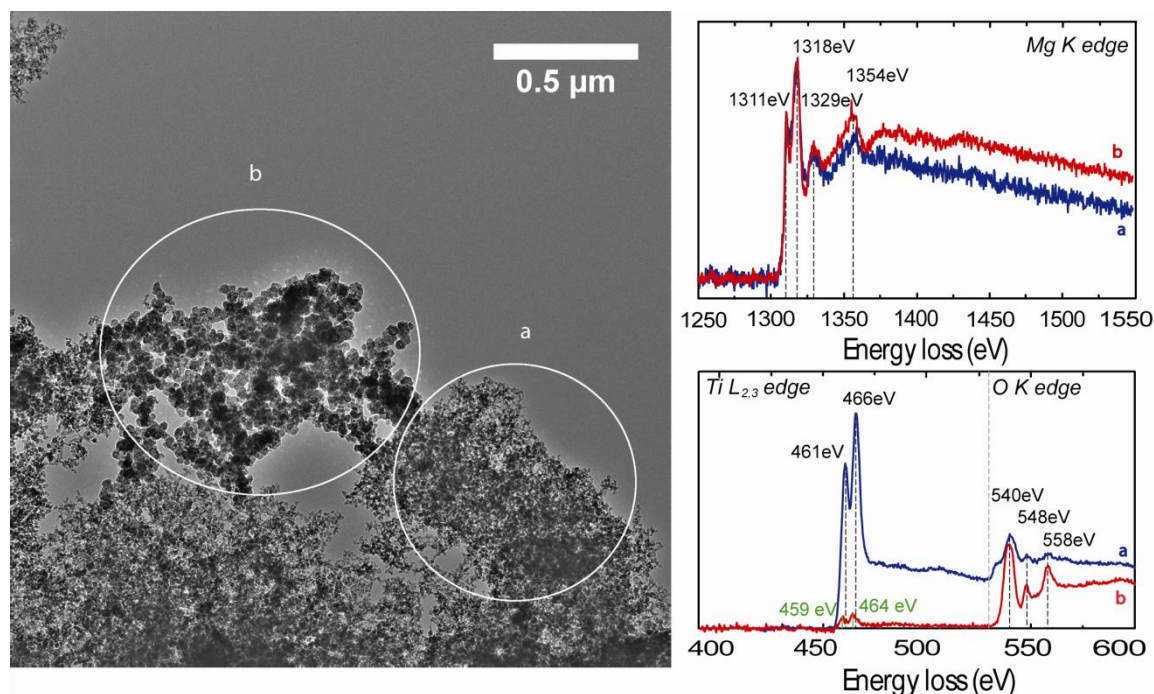


Figure 3.4. Morphology and composition changes after hydrogen sorption. Left: TEM image revealing regions of different morphology; Right: Electron energy loss near edge spectroscopy for the regions *a* and *b* depicted in the micrograph: Mg K edge (top) and Ti L_{2,3} edge together with O K edge (bottom).

Electron loss near edge spectroscopy (ELNES) was performed in both region *a* and region *b*. The position of these element dependent edges in the spectrum depends on the binding energy of the core electrons. The structure of the edges depends on the valence and the chemical environment of the element. The Mg K edge and Ti L_{2,3} edge are the main regions of interest we studied.

The Mg K edge spectrum essentially reflects the conduction band of Mg. In Figure 3.4, the Mg K edge is formed of two main peaks at 1311 eV and 1318 eV and lower intensity broader peaks at 1329 eV and 1354 eV. The edge position measured by X-ray absorption spectroscopy (XAS)^{28,29} and expected from X-ray photoelectron spectroscopy (XPS)³⁰ is at about 1304 eV for Mg metal and about 1310 eV for Mg in MgO. The shift of the Mg K edge reflects the changes in the binding energy of the Mg 1s electrons. The effect of a transition metal on the Mg ionization edge is a shift towards lower energies as reported by Farangis et. al.²⁸ while the effect of the O neighbors is a shift to higher energies. XAS measurements have shown that a positive shift of 2.5 eV can be expected in the hydride state²⁹. The position of 1311 eV of our measured ionization edge is the result of a combination between Mg present in MgO, MgH₂ and metallic Mg. The coordination of Mg is revealed by the peaks in the backscattered electrons regions at 1329 eV and 1354 eV. Qualitatively, the higher the intensity of the peaks in this region, the stronger the interaction of the backscattered electrons to the atoms coordinated around Mg. Thus, the relatively low intensity of the peaks in the spectrum measured in region *a*, reveals mostly H nearest neighbors and the higher intensity in region *b*, suggests O atoms as being nearest neighbors. In a nutshell, MgH₂ could be found in both regions while MgO could be predominantly found in region *b*.

The Ti L_{2,3} excitation edge presents two sharp peaks representative for the electronic transitions 2p_{1/2}-3d (L₂) and 2p_{3/2}-3d (L₃), at 459 eV and 464 eV respectively as it can be seen in Figure 3.4 (right) for region *a* and region *b*. These two edges arise from the spin-orbit coupling of the p orbitals. The L_{2,3} edge of transition metals is typically used to determine their oxidation state. Here, we measured the ionization band positions close to the expected Ti values of 458 eV and 463 eV³¹ for region *b*, suggesting that Ti is in metallic form. The much lower intensity of the Ti L_{2,3} edge in region *b* is directly related to the very

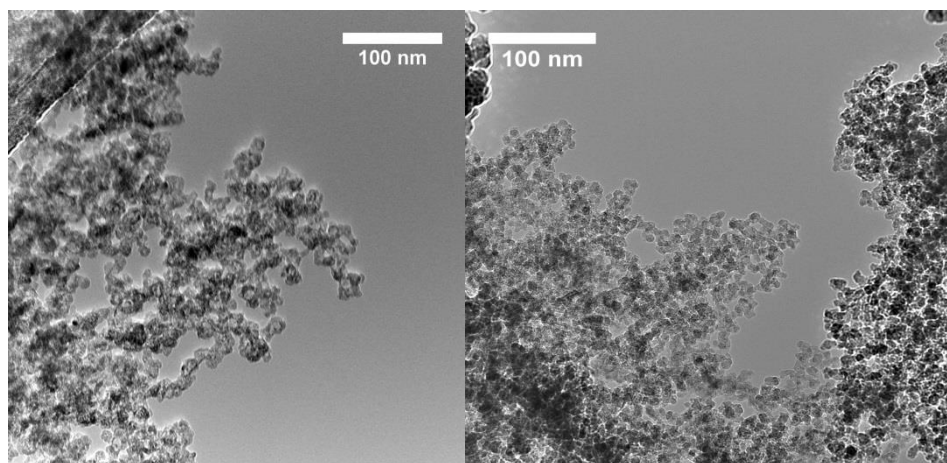


Figure 3.3. Transmission electron micrographs of Mg/Ti nanocomposites: left – as produced ; right – after hydrogen sorption experiments

small fraction of Ti present in this region as was determined also by EDS. Region *a* on the other side, presents a chemical shift of 2eV compared to the region *b* spectrum. In their X-ray absorption spectroscopy studies of Mg-Ti thin films, Farangis et al.^{28,29} report a small positive chemical shift for TiH₂ as compared to Ti metal.

Apart from the analysis of the chemical shift of the ionization edges, the oxidation state could also be determined by calculating the ratio between the integrated area of the L₂ and L₃ edge^{32,33} and comparing it to reference values. However, different authors^{31,34,35} report different values of the binding energy of the 2p electrons of Ti and a direct comparison with literature data is difficult. In this study, the ratio was calculated for the Ti L_{2,3} edge for a freshly prepared sample and the sample exposed to hydrogen. Though a quantitative result regarding the oxidation state of Ti cannot be made, the ratio for the freshly prepared sample is the same as the one calculated for region *b*. This implies that the oxidation state of Ti in the fresh sample is the same as in region *b* and Ti is in its metallic form. The ratio calculated for region *a* is different than for region *b*, suggesting Ti is in a different oxidation state, most likely as TiH₂ or TiO₂. However, in the case of transition metal oxides, backscattering from nearest oxygen neighbors gives rise to a prominent and broad peak at about 40 eV from the ionization edge³⁶. In both spectra of the Ti edge, this feature is not present, indicating the absence of TiO₂ in the sample. This result together with the observation of the chemical shift and the absence of Ti metal from the XRD patterns suggests the presence of Ti as mainly in its hydride form in region *a* and as Ti metal in region *b*.

An interesting fact related to region *a* is that Mg retains its nanostructure in the proximity of TiH₂ which acts in this case as a grain refiner. Similar observations^{24,37} have also been reported for ball milled Mg-Ti systems. Moreover, the results obtained from the ELNES analysis complement the findings from the XRD patterns. The presence in region *a* of the TiH₂ in close proximity of Mg and MgH_x corresponds to the fluorite Mg-TiH_x phase identified in XRD. The high fraction of MgO found in XRD can then be directly related to region *b*. In the hydrogen cycling experiments, region *a* is considered to be the active phase while region *b* that mainly contains MgO is seen as inert.

3.3.2. Hydrogen storage properties of the Mg/Ti nanocomposites

As stated earlier, the capacity of a material to react with hydrogen is greatly influenced by the enthalpy of formation of the hydride. In the case of bulk MgH_2 , the enthalpy of formation is -75 kJ/molH_2 ³⁸. For a practical use of a metal hydride as a viable hydrogen storage system, an enthalpy of formation of about -40 kJ/molH_2 is desired. Pressure composition isotherms (PCI) for the Mg-TiH_x nanocomposites are shown in Figure 3.5. The concentration of hydrogen in the samples is given as weight percent of the total mass of the sample. Because the samples contain also MgO and unreactive Mg particles, the hydrogen content is also calculated as weight percent of the active Mg/Ti fraction as it is obtained from XRD. Two separate samples synthesized under the same conditions are measured consecutively. The PCI presented in Figure 3.5 are measured at 423 K, 473 K, 523 K and 573 K. The isothermal curves measured in this way present a region where the pressure remains constant and the hydrogen content of the sample increases. This region is commonly defined as a plateau and the pressure at which it appears is the equilibrium pressure. The values of the equilibrium pressures are increased compared to the bulk or ball milled MgH_2 . The strongest effect appears at 423 K when $p_{\text{eq}}=96 \text{ mbar}$ compared to the $p_{\text{eq}}=5.2 \text{ mbar}$ for MgH_2 (or $p_{\text{eq}}=0.72 \text{ mbar}$ for TiH_2). These plateaus cannot be attributed to either Mg or Ti hydrogenation.

Assuming that the Mg-TiH_x nanocomposite is stable during the experiments and that the hydrogenation and dehydrogenation reaction is of first

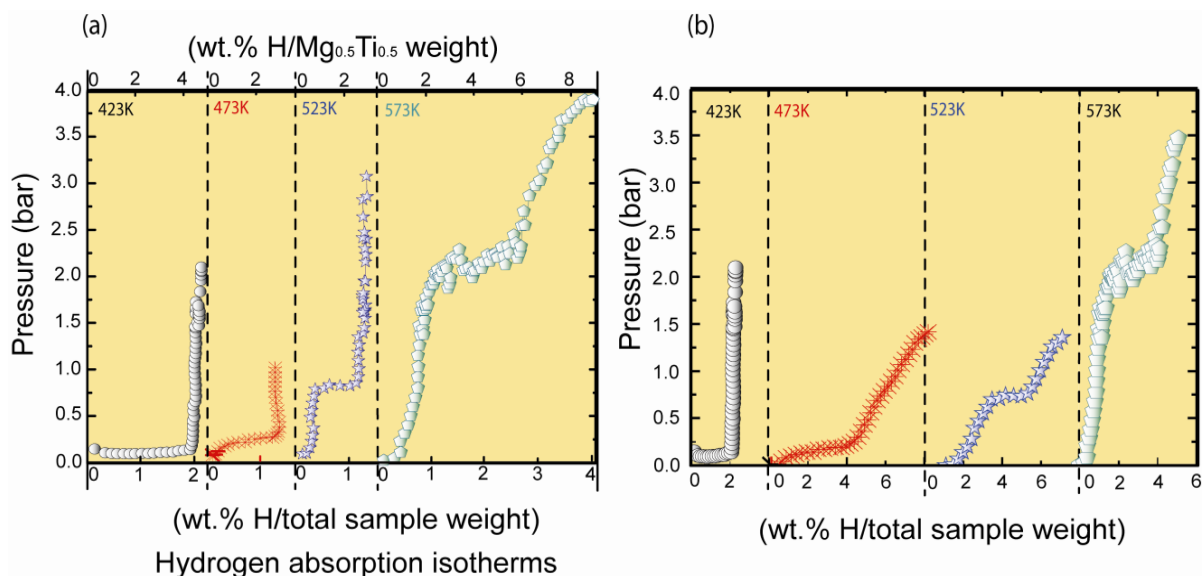


Figure 3.5. Hydrogen absorption isotherms for Mg/Ti nanocomposites measured at 423K, 473K, 523K, 573K. The amount of hydrogen absorbed is expressed as weight % as a function of the total sample weight on the bottom and as a function of the $\text{Mg}_{0.5}\text{Ti}_{0.5}$ weight on the top. a) and b) represent the results obtained for two separate samples synthesized under the same conditions. Both samples present increased equilibrium pressures. In this way, the reproducibility of the results is confirmed.

order in both directions, a van't Hoff analysis can be made for the determination of the enthalpy and entropy of reaction. As the pressure and temperature remain constant at the plateaus, it implies that the chemical potential of both the gas and the coexisting solid phases during the transformation is constant for the width of the plateau. The natural logarithm of the equilibrium pressure plotted against the reciprocal temperature gives a line, $\ln\left(\frac{p_{eq}}{p_0}\right) = \frac{\Delta H}{RT} - \frac{\Delta S}{R}$ as it can be seen in Figure 3.6. The enthalpy change is

calculated from the slope of curve *a* in Figure 3.6 and is -45 ± 3 kJ/molH₂ for sample 1 and -55 ± 3 kJ/molH₂ for sample 2. In the analysis of sample 2, the equilibrium pressure measured at 423 K is discarded because of uncertainties in the plateau pressure caused by a measurement error. The change in entropy is obtained from the intercept of curve *a* and is 84 ± 5 J/K molH₂ for sample 1 and 98 ± 7 J/KmolH₂ for sample 2.

This values are well below any heat of formation reported so far for Mg-TiH_x nanocomposites. Lu et al.^{39,40} have also reported a reduced enthalpy of formation, but the effect is much milder, only -68 kJ/molH₂ for ball milled Mg-TiH₂ nanocomposites of 5-10 nm grain size (see Figure 3.7).

Along with the energetic conditions for achieving chemical equilibrium, the sample needs to achieve a mechanical equilibrium during the transformation from the metallic to the hydride state which essentially means that the chemical transformation is accompanied by a rearrangement of the

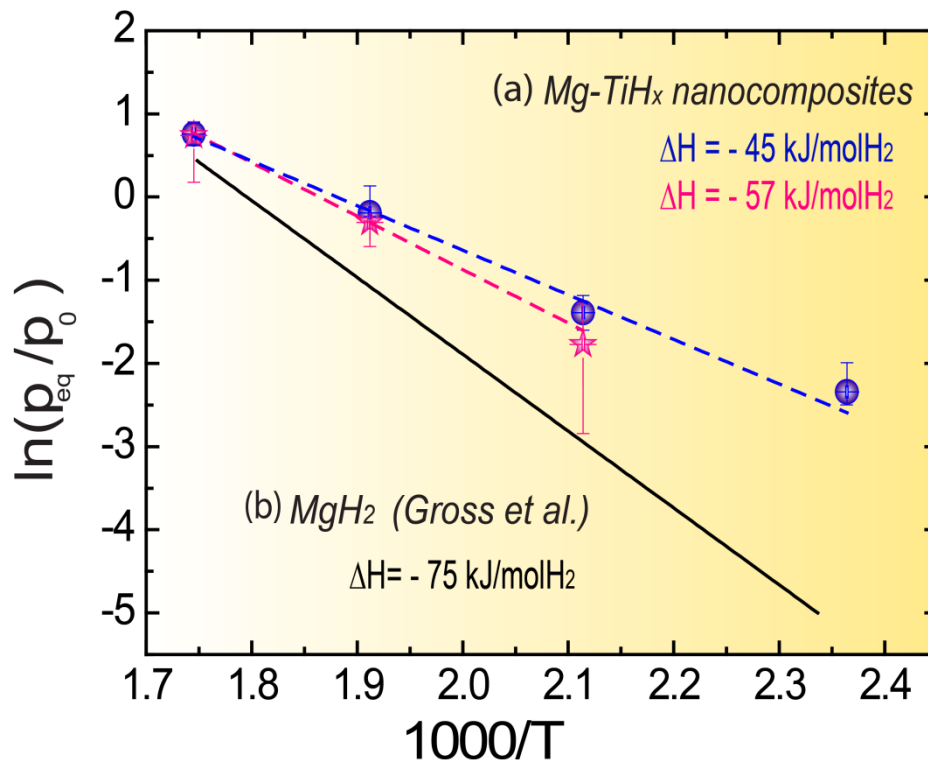


Figure 3.6. (a) van't Hoff plot obtained from equilibrium measurements of Mg/Ti nanocomposites for two separate samples. The dotted lines represent the linear fit to the data. (b) van't Hoff plot for bulk MgH₂ as measured by Gross et al.

structure. Thermodynamic equilibrium is reached only when both chemical and mechanical equilibrium is achieved. In this case, the micro and nanostructure of the sample will play an important role.

A theoretical study of Sholl et al.^{41,41} predicts a significant reduction of the enthalpy of formation of up to 12 kJ/molH₂ for a composite of the type Mg-TiH₂ based on a model of the strain on the Mg lattice in the close proximity of TiH₂ crystal. In our EELS structure analysis of the composites, the presence of small TiH₂ domains in close proximity of Mg domains could clearly be proven. Other theoretical studies^{40,41,42,43,44} have also predicted thermodynamic changes for a coherent fluorite Mg_yTi_{1-y}H_x hydride. It is expected that a destabilization of the fluorite Mg_yTi_{1-y}H_x hydride occurs above a critical composition of y=0.8~0.87⁴². The enthalpy difference between the rutile and the fluorite hydride is then about 10 kJ/molH₂⁴². The predominant nanocomposite character of our Mg-TiH_x sample in contrast to a coherent rutile Mg_yTi_{1-y}H_x hydride, makes the latter theoretical model improbable in this case. To this we can also add the observation that in the XRD we could find y~0.2 in which case the enthalpy of formation for a coherent fluorite hydride was calculated to be about -115 kJ/molH₂⁴².

Furthermore, Mooij et al.⁴⁵ have experimentally determined the magnitude of the interface energy of Mg-TiH₂ interface and explained in this way the increase in the equilibrium pressures and presence of hysteresis. However, using the model of Mooij et al., the effect of the interface energy on the equilibrium pressure is estimated to be about 4.5 kJ/molH₂ for particles with radii of about 10 nm, much lower than the total change in enthalpy observed in our materials. This indicates that the mechanism for the higher absorption equilibrium pressures in the materials presented here is more complex. In this case, the interface energy and the lattice strain at the Mg and

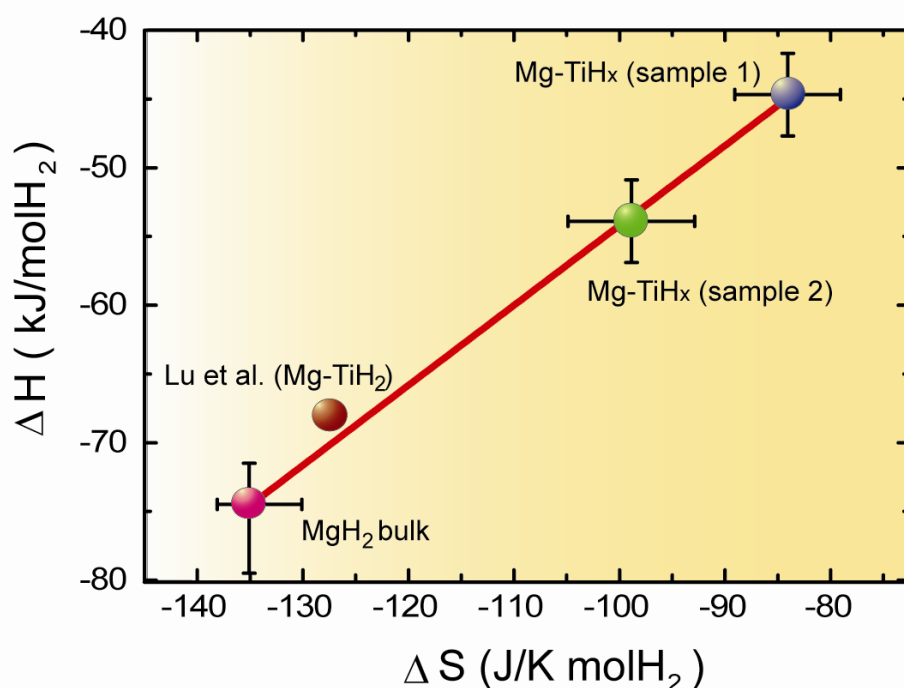


Figure 3.7. Linear relation between enthalpy and entropy as obtained for several Mg/Ti nanocomposites samples compared to literature values for bulk MgH₂.

TiH₂ boundaries can only partly explain the increased equilibrium pressures and enthalpy of formation.

Berube et al.⁴⁶ show that crystalline lattice distortions will directly lead to a destabilization of the hydride state and hence a lower magnitude of the enthalpy of formation. The defects in the crystalline structure are included in the equation of state as a generic term: the excess volume, which represents the ratio between the actual volume and the equilibrium volume. Though XRD and TEM analysis both confirmed the crystalline structure of the sample, only 10% of excess volume is enough to account for the dramatic enthalpy change of about 30kJ/molH₂.

Though the model proposed by Berube et al.^{46,47,48} predicts the most severe enthalpy change, the complexity of the sample in terms of composition, morphology and crystallinity, points to a combination of the different mechanisms discussed to explain the reduction in enthalpy of formation.

Moreover, the Berube model^{46,47,48} also predicts an increase in the entropy in the distorted regions. As the entropy of the hydride is increased, the entropy difference will be reduced compared to the bulk values. This entropy change to 84 ± 5 J/KmolH₂, affects the free energy of the system by acting as a barrier. It thus appears that a decrease of the heat of formation is accompanied by an increased disorder of the hydride lattice. This effect has already been observed for systems containing a TiF₃ catalyst produced by ball milling by Mulder et al.³⁷ Moreover, the enthalpies and entropies of formation follow a linear behavior as it can be seen in Figure 3.7. It should be noted here that for Mulder et al.³⁷ it could not be determined that ΔH and ΔS were representative for the whole sample and that here we use full pressure-composition isotherms that are representative for the entire active sample.

However, since the van't Hoff plot is obtained solely from absorption data, we should have in consideration the presence of a hysteresis between the absorption and desorption isotherms which could result in a difference between the values for enthalpy and entropy. This effect has already been reported for ball milled MgH₂ nano powders^{49,50}. Indeed, when desorption isotherms are measured at 423 K, 473 K, 523 K and 573 K, the equilibrium pressures are found to be lower than for absorption indicating the presence of a hysteresis. The reason for this behavior can be explained by the fact that apart from the chemical equilibrium, a mechanical equilibrium in the microstructure would also play an important role. The mechanical equilibrium will strongly depend on the changes in lattice parameters and symmetry of the phases involved.

3.4. Conclusions

Though intensive research has been carried out on the synthesis and analysis of the Mg-TiH_x system, the spark discharge generation synthesis of these composites has proven to be very attractive for producing small scale mixtures of Mg-Ti. The mixture of the two metals is uniform across the sample and it corresponds to the targeted 70 at % Mg and 30 at % Ti as determined by three different analysis methods, XRD, TEM –EDS and ICP-OES. A direct product of the spark discharge synthesis is a metastable body centered cubic Mg-Ti phase which was identified in the XRD pattern. The reaction of this phase to hydrogen leads to the formation of a fluorite hydride Mg-TiH_x in striking contrast to the rutile MgH₂ commonly observed.

A severe reduction in magnitude of the enthalpy of formation of the hydride is observed. Its origin stems from the nanoparticle character of the sample and the presence of strong interface effects between Mg and TiH₂. Essentially, largely increased equilibrium pressures are found at low temperatures. In the same time, the entropy of reaction is also lowered to 84±5 J/KmolH₂ corresponding to an increase in the degree of disorder of the hydride phase.

The present study represents an important step in the challenge to alter the thermodynamics of the hydrogen sorption in Mg. The combination of Mg and Ti nanoparticles shows great promise as a hydrogen storage material. Further investigations on the interplay of microstructure and chemical composition can shed more light on the mechanism of the enthalpy reduction of Mg-TiH_x nanocomposites.

References

- (1) Borsa, D. M.; Baldi, A.; Pasturel, M.; Schreuders, H.; Dam, B.; Griessen, R.; Vermeulen, P.; Notten, P. H. L. Mg--Ti--H Thin Films for Smart Solar Collectors. *Applied Physics Letters* 2006, 88, 241910-241913.
- (2) Vermeulen, P.; Niessen, R. A. H.; Borsa, D. M.; Dam, B.; Griessen, R.; Notten, P. H. L. Effect of the Deposition Technique on the Metallurgy and Hydrogen Storage Characteristics of Metastable Mg_yTi_(1 - Y) Thin Films. *Electrochemical and Solid-State Letters* 2006, 9, A520-A523.
- (3) Baldi, A.; Gremaud, R.; Borsa, D. M.; Balde, C. P.; van der Eerden, A. M. J.; Kruijtzter, G. L.; de Jongh, P. E.; Dam, B.; Griessen, R. Nanoscale Composition Modulations in Mg_yTi_{1-y}H_x Thin Film Alloys for Hydrogen Storage. *International Journal of Hydrogen Energy* 2009, 34, 1450-1457.
- (4) Baldi, A.; Borsa, D. M.; Schreuders, H.; Rector, J. H.; Atmakidis, T.; Bakker, M.; Zondag, H. A.; van Helden, W. G. J.; Dam, B.; Griessen, R. Mg-Ti-H Thin Films As Switchable Solar Absorbers. *International Journal of Hydrogen Energy* 2008, 33, 3188-3192.
- (5) Niessen, R. A. H.; Notten, P. H. L. Electrochemical Hydrogen Storage Characteristics of Thin Film MgX (X = Sc, Ti, V, Cr) Compounds. *Electrochemical and Solid-State Letters* 2005, 8, A534-A538.
- (6) Baldi, A.; Gonzalez-Silveira, M.; Palmisano, V.; Dam, B.; Griessen, R. Destabilization of the Mg-H System Through Elastic Constraints. *Phys. Rev. Lett.* 2009, 102, 226102.
- (7) Asano, K.; Enoki, H.; Akiba, E. Synthesis of HCP, FCC and BCC Structure Alloys in the Mg-Ti Binary System by Means of Ball Milling. *Journal of Alloys and Compounds* 2009, 480, 558-563.
- (8) Asano, K.; Enoki, H.; Akiba, E. Synthesis of Mg-Ti FCC Hydrides From Mg-Ti BCC Alloys. *Journal of Alloys and Compounds* 2009, 478, 117-120.
- (9) Asano, K.; Enoki, H.; Akiba, E. Synthesis Process of Mg-Ti BCC Alloys by Means of Ball Milling. *Journal of Alloys and Compounds* 2009, 486, 115-123.
- (10) Kyoi, D.; Sato, T.; Rönnebro, E.; Kitamura, N.; Ueda, A.; Ito, M.; Katsuyama, S.; Hara, S.; Noréus, D.; Sakai, T. A New Ternary Magnesium-Titanium Hydride Mg₇TiH_x With Hydrogen Desorption Properties Better Than Both Binary Magnesium and Titanium Hydrides. *Journal of Alloys and Compounds* 2004, 372, 213-217.
- (11) Tabrizi, N.; Ullmann, M.; Vons, V.; Lafont, U.; Schmidt-Ott, A. Generation of Nanoparticles by Spark Discharge. *Journal of Nanoparticle Research* 2009, 11, 315-332.

- (12) Vons, V. A.; Anastasopol, A.; Legerstee, W. J.; Mulder, F. M.; Eijt, S. W. H.; Schmidt-Ott, A. Low-Temperature Hydrogen Desorption and the Structural Properties of Spark Discharge Generated Mg Nanoparticles. *Acta Materialia* 2011, 59, 3070-3080.
- (13) Anastasopol, A.; Pfeiffer, T. V.; Schmidt-Ott, A.; Mulder, F. M.; Eijt, S. W. H. Fractal Disperse Hydrogen Sorption Kinetics in Spark Discharge Generated Mg/NbOx and Mg/Pd Nanocomposites. *Applied Physics Letters* 2011, 99, 194103.
- (14) Krishnan, G.; Kooi, B. J.; Palasantzas, G.; Pivak, Y.; Dam, B. Thermal Stability of Gas Phase Magnesium Nanoparticles. *J. Appl. Phys.* 2010, 107.
- (15) Callini, E.; Pasquini, L.; Piscopiello, E.; Montone, A.; Antisari, M. V.; Bonetti, E. Hydrogen Sorption in Pd-Decorated Mg--MgO Core-Shell Nanoparticles. *Applied Physics Letters* 2009, 94, 221905-3.
- (16) Pasquini, L.; Montone, A.; Callini, E.; Antisari, M. V.; Bonetti, E. Formation of Hollow Structures Through Diffusive Phase Transition Across a Membrane. *Applied Physics Letters* 2011, 99, 021911-021913.
- (17) Jongh, P. E. d.; Wagemans, R. W. P.; Eggenhuisen, T. M.; Dauvillier, B. S.; Radstake, P. B.; Meeldijk, J.; Geus, J. W.; Jong, K. P. The Preparation of Carbon-Supported Magnesium Nanoparticles Using Melt Infiltration. *Chem. Mater.* 2007, 19, 6052-6057.
- (18) Bogerd, R.; Adelhelm, P.; Meeldijk, J. H.; De Jong, K. P.; de Jongh, P. E. The Structural Characterization and H₂ Sorption Properties of Carbon-Supported Mg_{1-x}Ni_x Nanocrystallites. *Nanotechnology* 2009, 20.
- (19) Bogdanovic, B. Catalytic synthesis of organolithium and organomagnesium compounds and of lithium and magnesium hydrides-applications in organic synthesis and hydrogen storage, *Angewandte Chemie - International Edition in English* 1985, 24, 262-273.
- (20) Zlotea, C.; Andersson, Y. Microstructural Modifications Induced by Hydrogen Absorption in Mg₅Ga₂ and Mg₆Pd. *Acta Materialia* 2006, 54, 5559-5564.
- (21) Vons, V.; de Smet, L.; Munao, D.; Evirgen, A.; Kelder, E.; Schmidt-Ott, A. Silicon Nanoparticles Produced by Spark Discharge. *Journal of Nanoparticle Research* 2011, 13, 4867-4879.
- (22) Toby, B. H. EXPGUI, a Graphical User Interface for GSAS. *J. Appl. Cryst.* 2001, 34, 210-213.
- (23) Toby, B. H.; Von Dreele, R. B.; Larson, A. C. CIF Applications. XIV. Reporting of Rietveld Results Using PdCIF: GSAS2CIF. *J. Appl. Cryst.* 2003, 36, 1290-1294.

- (24) Rousselot, S.; Guay, D.; Roué, L. Synthesis of Fcc Mg-Ti-H Alloys by High Energy Ball Milling: Structure and Electrochemical Hydrogen Storage Properties. *Journal of Power Sources* 2010, *195*, 4370-4374.
- (25) Rousselot, S.; Bichat, M. P.; Guay, D.; Roué, L. Structure and Electrochemical Behaviour of Metastable Mg₅₀Ti₅₀ Alloy Prepared by Ball Milling. *Journal of Power Sources* 2008, *175*, 621-624.
- (26) Mccusker, L. B.; Von Dreele, R. B.; Cox, D. E.; Louer, D.; Scardi, P. Rietveld Refinement Guidelines. *J. Appl. Cryst.* 1999, *32*, 36-50.
- (27) Borsa, D. M.; Gremaud, R.; Baldi, A.; Schreuders, H.; Rector, J. H.; Kooi, B.; Vermeulen, P.; Notten, P. H. L.; Dam, B.; Griessen, R. Structural, Optical, and Electrical Properties of Mg_yTi_{1-y}H_xThin Films. *Phys. Rev. B* 2007, *75*, 205408.
- (28) Farangis, B.; Nachimuthu, P.; Richardson, T. J.; Slack, J. L.; Meyer, B. K.; Perera, R. C. C.; Rubin, M. D. Structural and Electronic Properties of Magnesium - Transition Metal Switchable Mirrors. *Solid State Ionics* 2003, *165*, 309-314.
- (29) Farangis, B.; Nachimuthu, P.; Richardson, T. J.; Slack, J. L.; Perera, R. C. C.; Gullikson, E. M.; Lindle, D. W.; Rubin, M. In Situ X-Ray-Absorption Spectroscopy Study of Hydrogen Absorption by Nickel-Magnesium Thin Films. *Phys. Rev. B* 2003, *67*, 085106.
- (30) Yates, K.; West, R. H. Monochromatized Ag La X-Rays As a Source for Higher Energy XPS. *Surf. Interface Anal.* 1983, *5*, 133-138.
- (31) Lisowski, W.; van den Berg, A. H. J.; Leonard, D.; Mathieu, H. J. Characterization of Titanium Hydride Films Covered by Nanoscale Evaporated Au Layers: ToF-SIMS, XPS and AES Depth Profile Analysis. *Surf. Interface Anal.* 2000, *29*, 292-297.
- (32) Tan, H.; Verbeeck, J.; Abakumov, A.; Van Tendeloo, G. Oxidation State and Chemical Shift Investigation in Transition Metal Oxides by EELS. *Ultramicroscopy* 2012, *116*, 24-33.
- (33) Graetz, J.; Ahn, C. C.; Ouyang, H.; Rez, P.; Fultz, B. White Lines and D-Band Occupancy for the 3d Transition-Metal Oxides and Lithiumtransition-Metal Oxides. *Phys. Rev. B* 2004, *69*, 235103.
- (34) Paulin, I.; Donik, I.; Mandrino, D.; Vonina, M.; Jenko, M. Surface Characterization of Titanium Hydride Powder. *Vacuum* 2012, *86*, 608-613.
- (35) Liu, G. W.; Li, W.; Qiao, G. J.; Wang, H. J.; Yang, J. F.; Lu, T. J. Microstructures and Interfacial Behavior of Zirconia/Stainless Steel Joint Prepared by Pressureless Active Brazing. *Journal of Alloys and Compounds* 2009, *470*, 163-167.

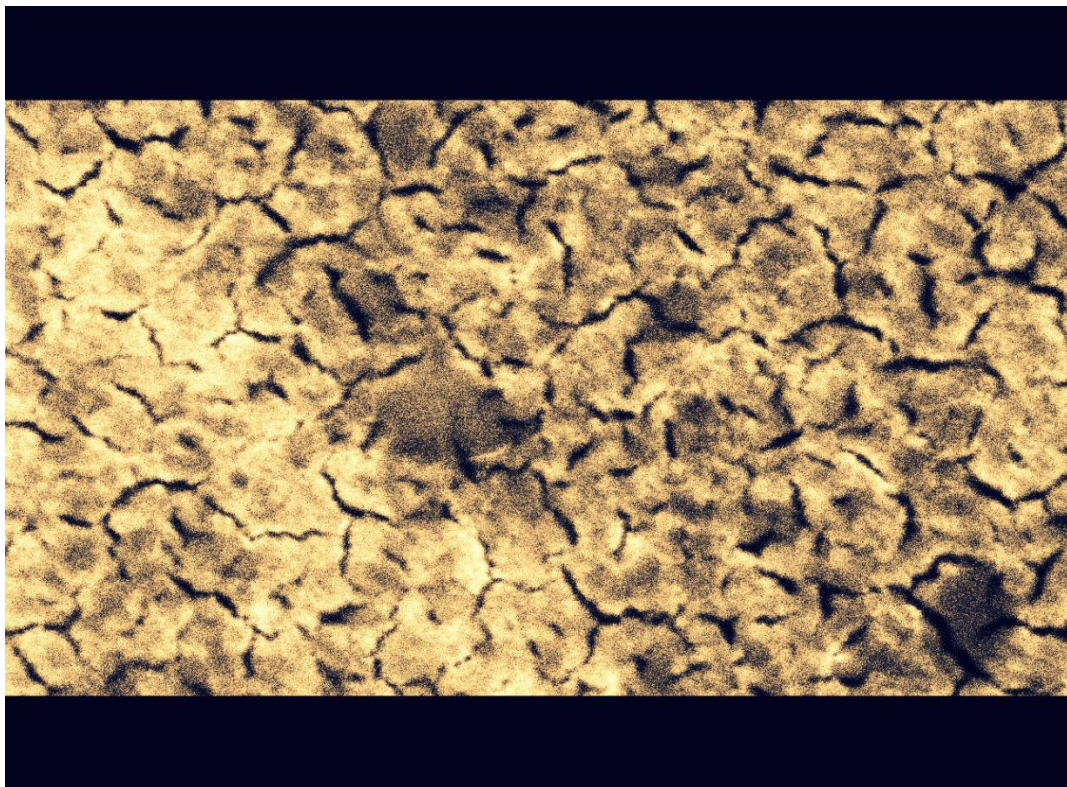
- (36) Egerton, R. F. Physics of Electron Scattering. In *Electron Energy-Loss Spectroscopy in the Electron Microscope*; Springer US: 2011.
- (37) Mulder, F. M.; Singh, S.; Bolhuis, S.; Eijt, S. W. H. Extended Solubility Limits and Nanograin Refinement in Ti/Zr Fluoride-Catalyzed MgH₂. *J. Phys. Chem. C* 2011, *116*, 2001-2012.
- (38) Gross, K. J.; Spatz, P.; Zuttel, A.; Schlapbach, L. Mechanically Milled Mg Composites for Hydrogen Storage the Transition to a Steady State Composition. *Journal of Alloys and Compounds* 1996, *240*, 206-213.
- (39) Lu, J.; Choi, Y. J.; Fang, Z. Z.; Sohn, H. Y.; Rönnebro, E. Hydrogen Storage Properties of Nanosized MgH₂G_{0.1}TiH₂ Prepared by Ultrahigh-Energy - High-Pressure Milling. *J. Am. Chem. Soc.* 2009, *131*, 15843-15852.
- (40) Lu, J.; Choi, Y. J.; Fang, Z. Z.; Sohn, H. Y.; Rönnebro, E. Hydrogenation of Nanocrystalline Mg at Room Temperature in the Presence of TiH₂. *J. Am. Chem. Soc.* 2010, *132*, 6616-6617.
- (41) Hao, S.; Sholl, D. S. Effect of TiH₂ Induced Strain on Thermodynamics of Hydrogen Release From MgH₂. *J. Phys. Chem. C* 2011, *116*, 2045-2050.
- (42) Er, S.; Tiwari, D.; de Wijs, G. A.; Brocks, G. Tunable Hydrogen Storage in Magnesium-transition Metal Compounds: First-Principles Calculations. *Phys. Rev. B* 2009, *79*, 024105.
- (43) Er, S.; de Wijs, G. A.; Brocks, G. Tuning the Hydrogen Storage in Magnesium Alloys. *J. Phys. Chem. Lett.* 2010, *1*, 1982-1986.
- (44) Song, Y.; Guo, Z. X.; Yang, R. Influence of Selected Alloying Elements on the Stability of Magnesium Dihydride for Hydrogen Storage Applications: A First-Principles Investigation. *Phys. Rev. B* 2004, *69*, 094205.
- (45) Mooij, L. P. A.; Baldi, A.; Boelsma, C.; Shen, K.; Wagemaker, M.; Pivak, Y.; Schreuders, H.; Griessen, R.; Dam, B. Interface Energy Controlled Thermodynamics of Nanoscale Metal Hydrides. *Adv. Energy Mater.* 2011, *1*, 754-758.
- (46) Berube, V.; Chen, G.; Dresselhaus, M. S. Impact of Nanostructuring on the Enthalpy of Formation of Metal Hydrides. *International Journal of Hydrogen Energy* 2008, *33*, 4122-4131.
- (47) Berube, V.; Dresselhaus, M. S.; Chen, G. Entropy Stabilization of Deformed Regions Characterized by an Excess Volume for Hydrogen Storage Applications. *International Journal of Hydrogen Energy* 2009, *34*, 1862-1872.
- (48) Berube, V.; Dresselhaus, M. S.; Chen, G. Temperature Dependence of the Enthalpy of Formation of Metal Hydrides Characterized by an Excess

Volume. *International Journal of Hydrogen Energy* 2008, 33, 5617-5628.

- (49) Varin, R. A.; Czujko, T.; Chiu, C.; Wronski, Z. Particle Size Effects on the Desorption Properties of Nanostructured Magnesium Dihydride (MgH_2) Synthesized by Controlled Reactive Mechanical Milling (CRMM). *Journal of Alloys and Compounds* 2006, 424, 356-364.
- (50) Varin, R. A.; Jang, M.; Czujko, T.; Wronski, Z. S. The Effect of Ball Milling Under Hydrogen and Argon on the Desorption Properties of MgH_2 Covered With a Layer of Mg(OH)_2 . *Journal of Alloys and Compounds* 2010, 493, L29-L32.

Chapter 4

Thermal stability of $\text{Mg}_y\text{Ti}_{1-y}$ and $\text{Mg}_y\text{Ti}_{1-y}\text{H}_x$ thin films



Abstract

Mg_yTi_{1-y} thin films synthesized by sputter deposition have a high reactivity with hydrogen at low temperatures and pressures which makes them interesting materials for hydrogen storage. The coherent crystalline Mg_yTi_{1-y} phase shows a remarkable kinetic stability when exposed to high temperatures of up to 523K. However, the prolonged heating treatment (30 h) induces irreversible changes in the structure that further block the rehydrogenation of the films and the capping layer.

In situ X-ray diffraction and electron microscopy are used to investigate the structural changes that occur upon heating. Clear segregation of Mg and Ti occurs in the films heated at 573 K on a time scale of ~10 h. Using positron annihilation spectroscopy, an increased concentration of open volume defects is observed as a result of the heating treatment. The defects might act as positron traps, blocking the rehydrogenation of the films.

This chapter is based on the published papers:

Layer-resolved study of the Mg to MgH₂ transformation in Mg–Ti films with short-range chemical order, S. W. H. Eijt, H. Leegwater, H. Schut, A. Anastasopol, W. Egger, L. Ravelli, C. Hugenschmidt, B. Dam, *Journal of alloys and compounds*, (2011), 509, 2, S567–S571, DOI: 10.1016/j.jallcom.2010.09.157

Thermal stability of Mg_yTi_{1-y} thin films investigated by positron annihilation spectroscopy, A. Anastasopol, S. W. H. Eijt, H. Schut, F.M. Mulder, F. Plazaola, B. Dam, *Physics Procedia*, (2012), 35, 16-21, DOI: 10.1016/j.phpro.2012.06.004

Phase segregation of Mg_yTi_{1-y} and Mg_yTi_{1-y}H_x thin films at high temperatures, A. Anastasopol, J. Middelkoop, U. Lafont, H. Schreuders, B. Dam, F.M. Mulder, S.W.H. Eijt manuscript in preparation.

“Would you tell me, please, which way I ought to go from here?”
“That depends a good deal on where you want to get to.”
“I don't much care where –“
“Then it doesn't matter which way you go.”

Lewis Carroll, Alice in Wonderland

$Mg_yTi_{1-y}H_x$ thin films synthesized by sputter deposition have a high reactivity with hydrogen at low temperatures and pressures. This makes them interesting for a wide range of applications like hydrogen sensors^{1,2}, switchable mirrors^{3,4} solar collectors^{5,6} or electronic devices⁷. Their high hydrogen storage capacity makes them attractive study cases for hydrogen storage materials.

They are crystalline and grow with a preferred orientation, along the c-axis of the hexagonal structure of the metal. The lattice parameter of the structure is a linear function of the fraction of Mg and Ti present and it closely follows Vegard's law^{8,9}. When loaded with hydrogen, the films maintain their preferred crystallographic orientation. However, the symmetry of the crystal changes from hexagonal to cubic or tetragonal depending on the Ti fraction present. At a Ti content lower than 15%, the structure of the hydride is tetragonal, isomorphic to the rutile type β - MgH_2 ⁸. As the Ti fraction is increased, the cubic symmetry is preferred and the hydride resembles fluorite type TiH_2 . Both types of hydrides have been intensely studied^{5,6,8,10} especially because of their remarkable reversibility and fast dehydrogenation reaction but also because of their optical properties^{6,8}.

Moreover, given the immiscibility of Mg and Ti, the mere existence of coherent Mg_yTi_{1-y} structures has attracted a lot of interest^{11,12,13,14,15,16}. Though an X-ray absorption study has revealed chemical segregation of the metals at the nanometer scale in the films¹⁷, the coherent Mg - Ti films are kinetically stable at room temperature as it was also observed for the Mg-Ti nanocomposites discussed in Chapter 3. Remarkable, upon dehydrogenation, the coherent Mg_yTi_{1-y} mixture is maintained and the films can be further rehydrogenated. Though there is no clear explanation as to why that happens, several studies have pointed to the formation of Ti and TiH_2 clusters which further stabilize the mixtures^{8,10}. In theoretical studies it has been shown that nanoclusters of Ti can be stabilized by even low amounts of hydrogen and that these are prerequisites to the reversibility of the system¹⁸. Thus, the structure of these samples is the key to understand their behavior during hydrogen sorption.

Mg_yTi_{1-y} films exhibit a complex structure: being immiscible, they do not form real alloys but spinodal variations in the chemical composition at the nanometer scale^{17,19}. This special structure is believed to be the source of their high stability and reversibility. Studies on Mg-Ti multilayers were used to investigate the structural coherence of the films²⁰ because they provide a highly controllable system to study the already phase separated Mg-Ti system. However, though this approach is very useful in understanding the hydrogen loading process in the films, it does not provide information on the high stability of the metallic alloy. In this study we investigate the threshold conditions and processes occurring in the decomposition of the coherent Mg-Ti and Mg-Ti-H films by prolonged heating treatments. In this manner, a better understanding of their remarkable kinetic stability is achieved.

For this purpose, both metallic and hydride samples were annealed at temperatures up to 573 K for about 40 h. Because of their thermodynamic instability, on exposure to high temperatures, it is expected that the metals in the mixtures will segregate, forming big clusters of the constituents. However, in this study, a high stability of the coherent Mg-Ti structure has been observed below 523 K. Nevertheless, irreversible microstructural changes occur in the sample during the heating treatment and the rehydrogenation reaction is blocked despite the existence of TiH₂ clusters and the maintenance of the coherent structure. Also, a loss of the catalytic activity of the capping layer may play a role in the rehydrogenation reaction. The analysis of Doppler broadening positron annihilation (DBAR) profiles has revealed that during the heating treatment, the concentration of open volume defects is increased. This suggests, that on top of the existence of the Mg_yTi_{1-y} phase and TiH₂ clusters in the films, also, the defect structure is important for the behavior in the presence of hydrogen.

In this chapter, two compositions, Mg_{0.9}Ti_{0.1} and Mg_{0.7}Ti_{0.3} are investigated. In order to protect from oxidation, a thin Pd or Ni capping layer is deposited on the surface of the films. The evolution of the crystalline structure is followed using *in situ* X-ray diffraction. The microstructural changes that occurred on the films were measured *ex situ* by electron microscopy, positron annihilation spectroscopy and X-ray photoelectron spectroscopy.

4.2 Experimental section

4.2.1. Synthesis – DC magnetron sputtering

Films of about 300 nm thickness of Mg_{0.7}Ti_{0.3} and Mg_{0.9}Ti_{0.1} were deposited on Suprasil substrates using a DC magnetron sputter coater with Mg and Ti targets. The deposition is performed under ultra high vacuum conditions at room temperature. To protect them from oxidation, 1-2 nm thick Pd or Ni capping layers are deposited on top of the films.

4.2.2. *In situ* X-ray diffraction

The structure of the films was investigated by X-ray diffraction using a PANalytical X'Pert PRO diffractometer with a Cu K_α beam of 1.5415 Å operated at 40 kV and 40 mA. For the *in situ* measurements, samples were loaded in an Anton Paar TTK-450 environmental X-ray diffraction cell. The films were fixed with ZnO based thermal conductive paste. The films were heated to 573 K in

vacuum inside the sample holder while X-ray diffractograms were measured at intervals of 30 minutes. The temperature was increased by 20 K/min in steps of 20 K and let to stabilize for 5 min before every scan. The error in the temperature reading was measured to be of maximum ± 5 K at 573 K.

For every temperature step, an X-ray diffractogram is recorded with a step size of $0.02^\circ 2\theta$. The measurements were conducted under vacuum of about 10^{-3} mbar.

4.2.3. Transmission electron microscopy

The structure and the composition of the films were investigated by electron microscopy. Transmission electron microscopy (TEM), including energy-dispersive X-ray spectrometry (EDS) and selected-area electron diffraction (SAED) were performed using a FEI Tecnai TF20 electron microscope operated at 200 kV. For the TEM measurements, 20 nm $Mg_{0.7}Ti_{0.3}$ and $Mg_{0.9}Ti_{0.1}$ films with a 1 nm Pd capping layer to prevent oxidation were deposited on 30 nm thick SiN membranes (3x3 mm) from AGAR Scientific. The films were heated at 573 K for 40 h in air prior to the TEM measurements.

4.2.4. Scanning electron microscopy

The morphology of the films was investigated with a JEOL JSM 6500F scanning electron microscope operated at 15 kV.

4.2.5. X-ray photoelectron spectroscopy

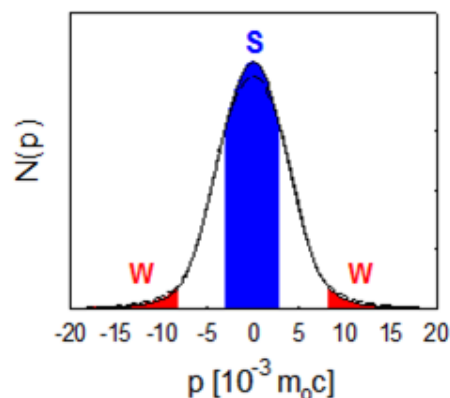
The chemical changes at the surface of the films were investigated by X-ray photoelectron spectroscopy (XPS) using an Axis Ultra XPS setup with a monochromated Al $K\alpha$ source of 1486.6 eV operated at 10 mA and 10 kV. The regional scans are a result of 10 sweep scans with an energy resolution of 1 eV. The measurements are performed under an ultra high vacuum of 10^{-9} - 10^{-10} mbar.

4.2.6. 2D - angular correlation of the annihilation radiation

Two dimensional angular correlation of the annihilation radiation (2D-ACAR) measurements are performed on the thin films using the reactor based intense variable energy positron beam POSH. The beam is magnetically guided and has an intensity of $2 \cdot 10^8$ positrons/s. In order to implant the positrons in the Mg_yTi_{1-y} active film, they are accelerated to an energy of 2 keV. The gamma rays emitted are analyzed using two position sensitive gamma ray detectors, placed at a detector-detector distance of 23 m. The detectors are based on NaI(Tl) single crystals and have an angular resolution of about $(1.1 \cdot 10^{-3}) \times (1.4 \cdot 10^{-3})(m_0c)^2$.

4.2.7. Doppler Broadening of positron Annihilation Radiation

Doppler Broadening of positron Annihilation Radiation (DBAR) is performed using the variable energy positron (VEP) beam with a beam diameter of about 8 mm. The source of positrons used is a ^{22}Na isotope. The positrons emitted are stopped by a W foil and then accelerated from an initial energy of ~ 3 eV to kinetic energies in the range of 0.1 keV to 25 keV in order to probe into the thickness of the films under investigation. The 511 keV gamma rays resulting from the positron-electron annihilation are detected using two germanium detectors with an energy resolution of 1.2 keV ($\sim 4.7 \cdot 10^{-3} m_0 c$). Using the relation $p = 2\Delta E/c$ where p is the momentum and c is the speed of light, the plot in Figure 4.1 can be obtained from the Doppler broadened 511 keV photopeak. The Doppler



broadening of the annihilation is generally analyzed using two parameters, S and W (see Figure 4.1). S is the shape parameter that is defined as the ratio between the central part of the annihilation peak and the total area of the peak. This parameter characterizes the annihilation with low binding energy valence electrons. The other important parameter is W or the wing parameter and it is defined as the ratio between the tail of the annihilation peak and the total area of the peak. The W parameter characterizes the annihilation with more tightly bound semi-core electrons²¹. The S and W parameters thus depend on the materials local electronic structure that is probed by the positrons. The depth profiles are fitted using the VEPFIT program²². By scanning the positron implantation energy S and W parameter, depth profiles of the films are obtained.

Figure 4.1. Illustration of the S and W parameter determination

4.2.8. Hydrogenography

When hydrogen is inserted in the initially metallic films, a metal insulator transition progresses which causes dramatic changes of their optical transmission. The metallic film reflects light, causing a low transmission while the insulator has large transmission in the visible range.

Hydrogenography²³ was used to measure the hydrogen uptake of the films by measuring the change in the optical transmission T/T_0 of the samples as a function of time. Due to the Lambert-Beer law there is a linear relationship between the logarithm of the transmitted light $\ln(T/T_0)$ and hydrogen concentration in the Mg-Ti-H films. The loading of the samples was performed at a constant temperature of 373 K and 1 bar H_2 . All the films were exposed to this treatment simultaneously by being placed in a stainless steel cell with transparent windows. The source of the light is a 150W quartz-tungsten-halogen lamp. The transmitted light is recorded using a 3-CCD camera. The amount of hydrogen loaded is estimated by assuming a change in transmission of 0.069/nm for $\text{Mg}_{0.9}\text{Ti}_{0.1}$ films and 0.033/nm for $\text{Mg}_{0.7}\text{Ti}_{0.3}$ films²⁴.

4.3 Results and discussion

4.3.1 Thermal stability of the $Mg_yTi_{1-y}H_x$ hydride films capped with Pd

In order to understand the source of the films' stability, the hydride $Mg_{0.9}Ti_{0.1}H_x$ and $Mg_{0.7}Ti_{0.3}H_x$ films were subjected to high temperature treatments ranging from 473 K to 573 K. As the enthalpy of mixing of Mg and Ti is positive, it is expected that upon heating, the metals will segregate when fully dehydrogenated.

Thus, in Figure 4.2a, the evolution of the X-ray diffraction pattern of the $Mg_{0.9}Ti_{0.1}H_x$ film with temperature can be seen. The (110) reflection of the rutile hydride is seen at $2\theta=28.3^\circ$. As the sample is heated, hydrogen is released and the hydride peak is replaced by a high intensity (0002) reflection of the metallic phase at $2\theta=34.6^\circ$ and a lower intensity peak at $2\theta=32.4^\circ$ is also observed. Thus, hydrogen desorption appears as a sharp transition from the hydride to the metal.

The assignment of the relatively weak peak at $2\theta=32.4^\circ$ becomes difficult because the spectrum is recorded at high temperatures which implies expansion of crystalline lattices and therefore shifts in the peak positions. However, it is very likely that the peak represents the (10-10) reflection of Ti or $Mg_{0.9}Ti_{0.1}$ as Song et al.²⁵ have reported. A more detailed XRD spectrum is seen in Figure 4.3a where the first and the last diffractogram measured at 300 K are plotted together with the diffractogram when the metallic peak had the highest intensity, measured at 573 K. Because of the high temperature, the metallic lattice expands, having as a result a shift of the (0002) metallic peak towards lower 2θ angles. During the heating treatment, the intensity of the metallic peak decreases. This behavior can be explained by a tilting of the diffracting crystals so they are not in the measuring range. Another explanation for the loss of coherence in the X-ray diffractograms is that it is an effect of the segregation of Mg and Ti leading to incoherently ordered small domains. We have further found more evidence to support this hypothesis.

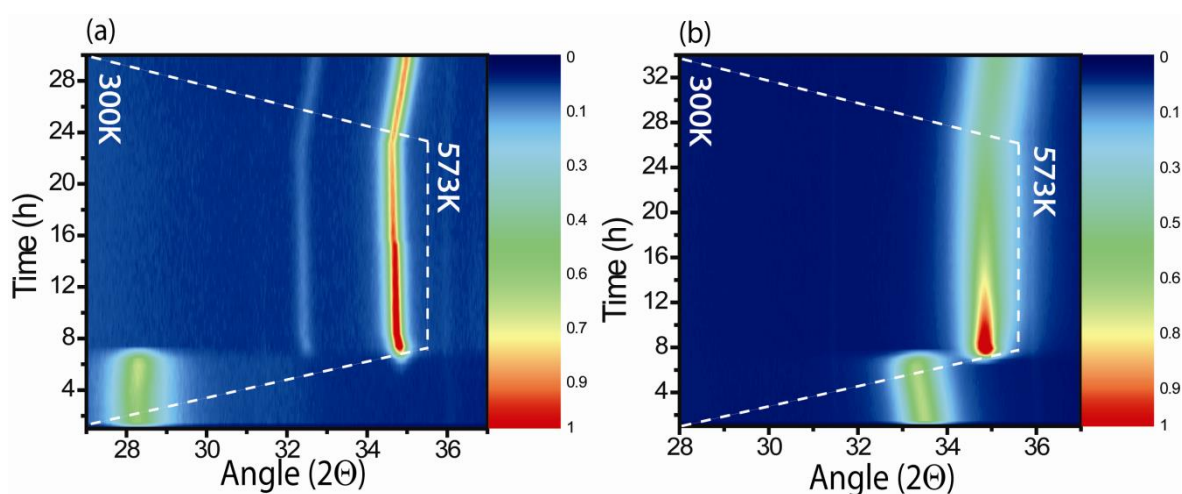


Figure 4.2. *In situ x-ray diffraction spectra measured for $Mg_yTi_{1-y}H_x$ films capped with Pd: a) $Mg_{0.9}Ti_{0.1}H_x$; b) $Mg_{0.7}Ti_{0.3}H_x$ as a function of temperature from 300K to 573K and back at 300K. the temperature treatment can be tracked with the white interrupted line.*

An interesting aspect is observed when a similar experiment is performed on a different composition, $\text{Mg}_{0.7}\text{Ti}_{0.3}\text{H}_x$. In situ XRD diffractograms are plotted in Figure 4.2b, where the (111) reflection of the fluorite type hydride is seen at $2\theta=33.3^\circ$ instead of the rutile MgH_2 (110) reflection. As the heating proceeds, the lattice of the hydride expands and the diffraction peak is shifted to lower 2θ angles. At temperatures close to 573 K, hydrogen desorption is observed as a sharp transition from the hydride to the metallic phase. An intense peak appears at $2\theta=34.9^\circ$ which represents the (0002) reflection of the $\text{Mg}_{0.7}\text{Ti}_{0.3}$ metallic hexagonal structure. As the heating proceeds, the intensity of the metallic peak decreases. So far, the behavior at high temperature of $\text{Mg}_{0.7}\text{Ti}_{0.3}\text{H}_x$ is very similar to the $\text{Mg}_{0.9}\text{Ti}_{0.1}\text{H}_x$.

However, for $\text{Mg}_{0.7}\text{Ti}_{0.3}\text{H}_x$, the decrease in the (0002) intensity is much more severe and the (10-10) reflection is not seen. In Figure 4.3b, a detailed view of the first diffractogram measured at 300 K is plotted together with the most intense metallic peak measured at 573 K and the last diffractogram after the heating run, again measured at 300 K. The intensity of the metallic peak decreases by more than 80% during the heating treatment. Though the decrease in intensity on itself can be due to tilting of the diffracting domains, a θ - 2θ rocking curve measurement revealed that it is not the case. Thus, the decrease in intensity of the (0002) peak has a different source than the tilting of the crystallites. From positron annihilation spectroscopy²⁶ it has been found that the heating treatment has a dramatic influence on the annihilation parameters in the films by an increased contribution from Ti or TiH_2 clusters (see Figure 4.10 and 4.11). This shows that while keeping a preferred orientation, the metallic phase demixes in Mg rich and Ti and TiH_2 rich regions. The reduction of the intensity of the diffraction peaks indicates a loss in the overall coherence of the film.

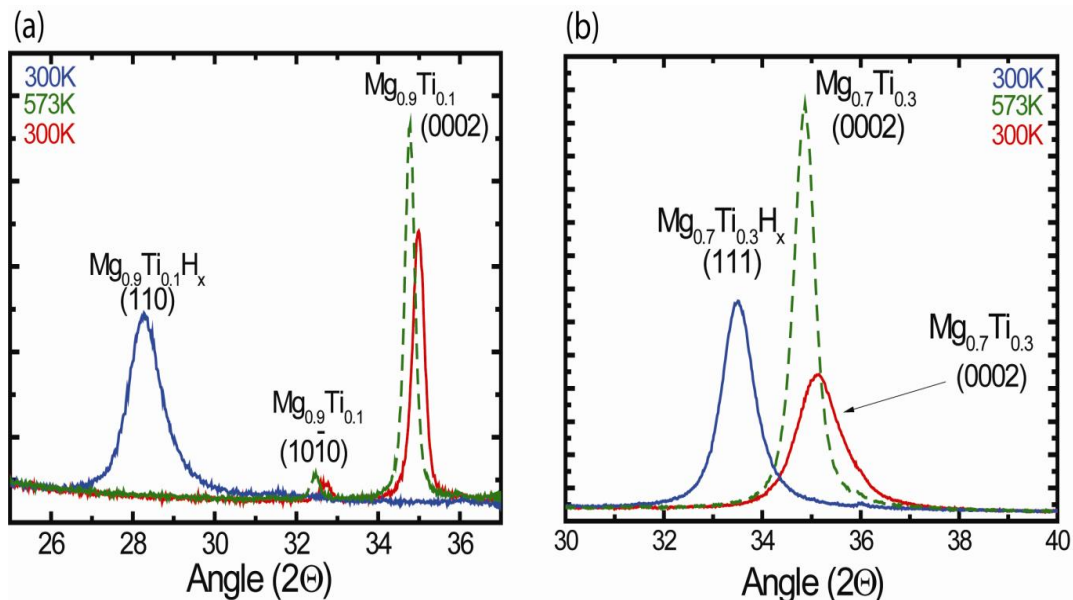


Figure 4.3. X-ray diffractograms of $\text{Mg}_y\text{Ti}_{1-y}\text{H}_x$ films capped with Pd: a) $\text{Mg}_{0.9}\text{Ti}_{0.1}\text{H}_x$; b) $\text{Mg}_{0.7}\text{Ti}_{0.3}\text{H}_x$ measured at 300 K of the initial hydride and the final metallic phase obtained after the heating treatment. The dotted line represents the metallic peak obtained after dehydrogenation, at 573 K.

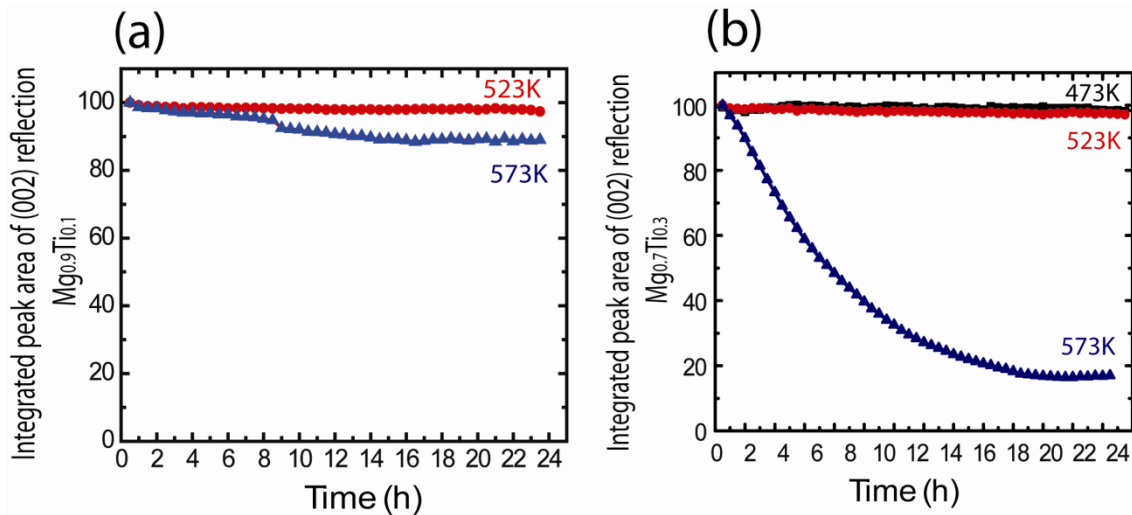


Figure 4.4. Intensity change of the (0002) reflection of (a) $Mg_{0.9}Ti_{0.1}$ and (b) $Mg_{0.7}Ti_{0.3}$ phase as a function of annealing temperature.

The intensity of the metallic peak for the $Mg_{0.7}Ti_{0.3}$ composition was also followed during heating treatments at 473 K and 523 K. The results are presented in Figure 4.4b. At 473 K, the intensity of the peak remains constant, and at 523 K only a small decrease of 0.07 %/h is observed. The most severe loss of peak intensity is at 573 K of about 8 %/h for the initial slope in the first few hours. Thus, the coherent structure with nanoscale chemical segregation appears to be frozen in at low temperatures and at higher temperatures it rapidly unravels. The effect of intensity loss is much less pronounced for $Mg_{0.9}Ti_{0.1}$ of only 0.6 %/h at 573 K. The difference in stability between the two compositions can be explained by the varying amount of TiH_2 that makes $Mg_{0.9}Ti_{0.1}$ appear more stable during heating treatments. However, even at higher fractions of Ti and increased temperatures (573 K), there is loss in coherence of the phase but not a total segregation. This slow rate of demixing is surprising, in the context that the mix is thermodynamically unstable. The explanation for it lies in the special structure of the mix which is characterized as short length scale spinodal composition which hinders full phase separation.

Additional insight into the microstructural changes that occur during heating, is gained from transmission electron images and selected area electron diffraction spectra. The films were deposited on SiN windows and then heated at 573 K for 40 h in air. In Figure 4.5 it can be seen that the porous aspect of the $Mg_{0.7}Ti_{0.3}$ films is maintained during heating. From the TEM images, the size of the crystallites is found to be between 3 and 15 nm, in good agreement to the crystallite size calculated from XRD measurements using the Scherrer formula.

From EDS measurements it is found locally that the ratio of Mg/Ti varies only slightly from the targetted 70/30 to 68/32 and 73/27. The main reflections of the hexagonal phase δ could be identified in the selected area electron diffraction image, confirming that the crystalline state is maintained during heating despite the decrease in intensity in the X-ray diffraction spectra. Also for $Mg_{0.9}Ti_{0.1}$ present in Figure 4.6, the size of the crystallites remains small during the heating, between 5-20 nm. The EDS measurements performed locally reveal that Mg/Ti composition ranges from 89/11 to 96/4. In the selected area electron diffraction, two crystalline structures are identified corresponding to the hexagonal $Mg_{0.9}Ti_{0.1}$ also seen in X-ray diffractograms and the cubic Pd

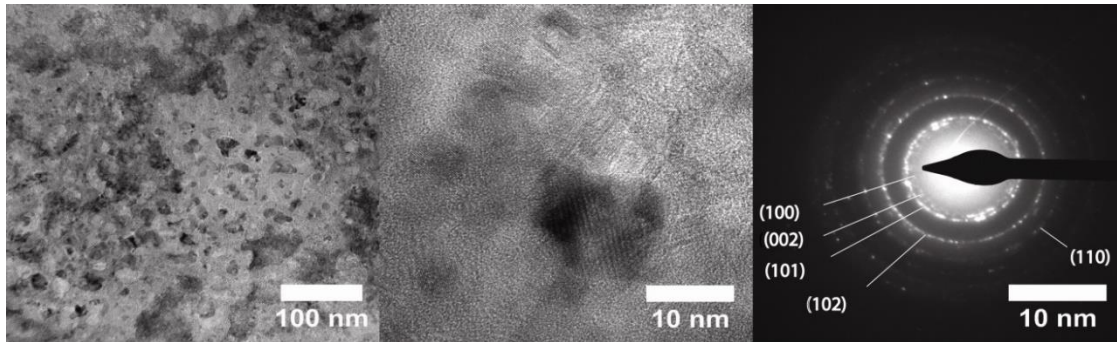


Figure 4.5. Transmission electron images of thin $Mg_{0.7}Ti_{0.3}$ film capped with Pd and deposited on a SiN substrate after annealing at 573 K for 40 h in air. In the and selected area electron diffraction, a hexagonal phase is identified.

structure. The results obtained from transmission electron microscopy confirm at a small scale what the results from the X-ray diffraction have indicated at a large scale, namely that at the small scale, the hexagonal Mg_yTi_{1-y} structure is maintained, though the domains may now have lost part of the overall coherency.

However, the heating treatments do affect the morphology of the films at the large scale. Thus, in spite of the apparent stability and coherence of the films, scanning electron images of the surface of the films heated at different temperatures revealed that the integrity of the film is affected by the appearance of cracks. In Figure 4.7, it can be seen that the evolution of cracks becomes more pronounced by increasing the temperature.

The surface of the films was also investigated by SEM-EDS performed on several spots plotted in Figure 4.7. It revealed that Pd is still present on the surface of the films. A significant contribution in the EDS signal comes from Si. As the surface of the films does not contain Si, we can conclude that the source is the Suprasil (quartz) substrate on which the films are deposited. This would mean that the cracks seen on the surface run all the way through the film.

A detailed investigation of the chemical composition at the surface of the films is performed using X-ray photoelectron spectroscopy. Though the measurements performed are very local, data was collected from four spots on the films surface and the results obtained are compared and analyzed. As a reference for the position of the photoelectron peaks, the C 1s peak (286 eV) is used. In Figure 4.8, XPS spectra of Ti, Mg and Pd in the $Mg_{0.9}Ti_{0.1}$

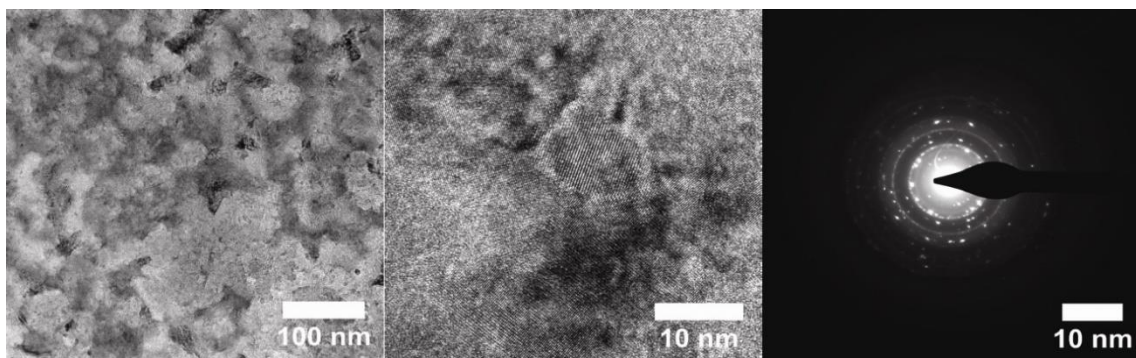


Figure 4.6. Transmission electron images of thin $Mg_{0.9}Ti_{0.1}$ film capped with Pd and deposited on a SiN substrate after annealing at 573 K for 40 h in air.

composition is presented. The $Mg_{0.9}Ti_{0.1}H_x$ heated at 523 K is compared to the $Mg_{0.9}Ti_{0.1}$ metallic and $Mg_{0.9}Ti_{0.1}H_x$ hydride references. A Shirley27 background is subtracted in all the plots presented.

XPS experiments were performed to study the surface Ti, Pd and Mg. Because of the spin-orbit coupling, the Ti 2p transition is split in two components, Ti 2p_{1/2} and Ti 2p_{3/2}, with relative intensity ratio 1:2 separated by 6 eV. The Ti 2p peaks have been fitted in Casa XPS with a Gaussian – Lorentzian curve shape. In the metallic reference, Ti is present in one state, with peaks at 460 eV (Ti 2p_{1/2}) and 454 eV (Ti 2p_{3/2}) as expected for the Ti metal as the close proximity to Mg does not produce a noticeable chemical shift in Ti^{11,28}. Namely, the theoretical predictions of the surface/interface core level shift of Olovsson et al. but also experimental observations on Mg-Ti-H spark discharge generated nanoparticles in Chapter 6 show that this alloying shift is only noticeable at a few monolayers of solute^{29,30}. It is interesting to observe that in

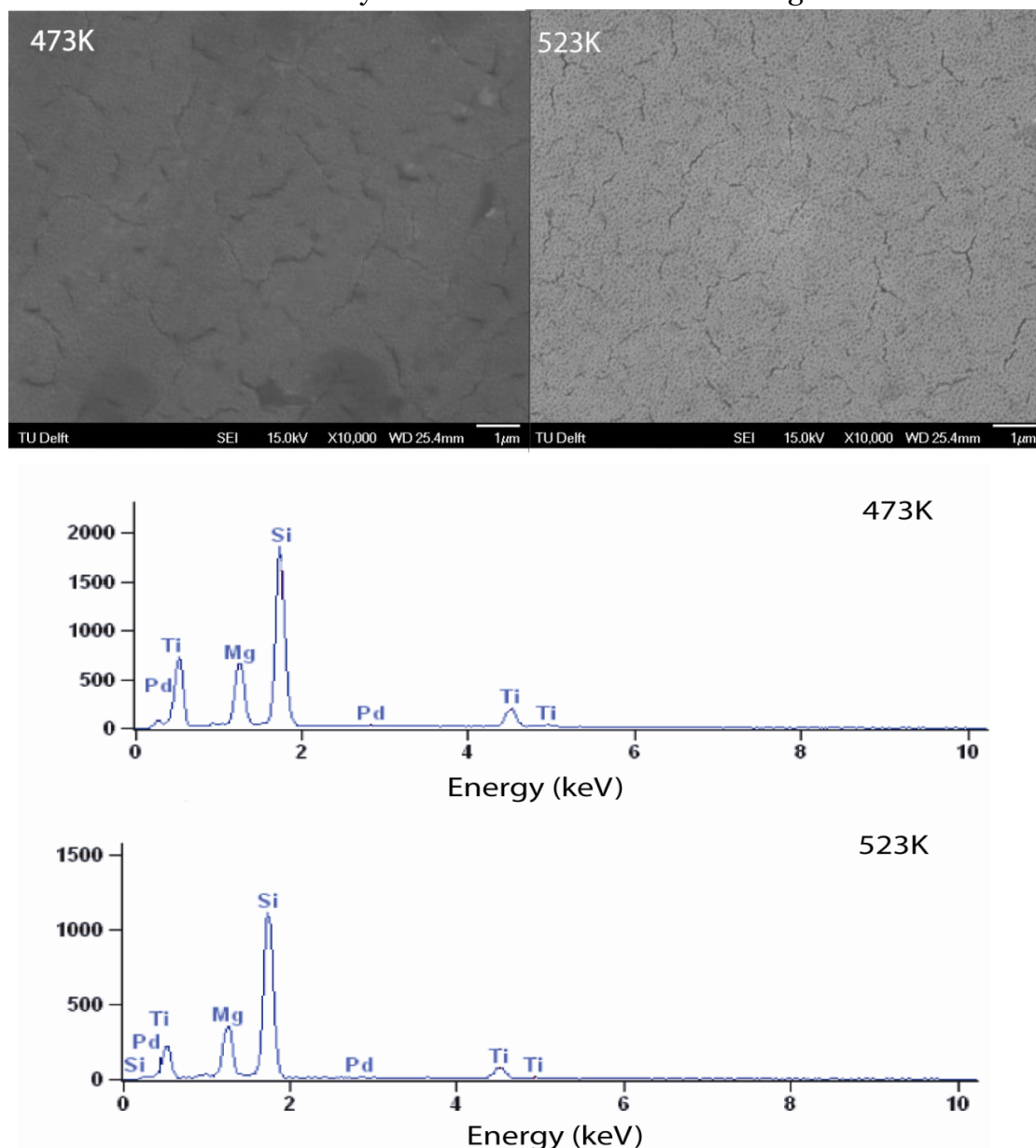


Figure 4.7. SEM images and SEM–EDS measured for the Pd capped $Mg_{0.7}Ti_{0.3}$ films heated at 473K and 523K.

the hydride sample, Ti is present in two states, separated by 4 eV. First and with lower intensity, the Ti metallic state can be identified. With a higher intensity a 2p transition at 464 eV (Ti 2p_{1/2}) and 458 eV (Ti 2p_{3/2}) is observed which is attributed to Ti in TiH₂³¹. A discrimination between the two states of titanium is done in the fitting of Ti 2p_{1/2} and Ti 2p_{3/2} components. For the fitting, a constraint on the peak area ratio of the two components is imposed.

The relative fraction of Ti metal to TiH₂ is found to be 1:3 in the hydride sample and 1:1 after the heating treatment. Since after the heating treatment at 523 K, Ti can still be found as both metallic and hydride, it appears that a partial dehydrogenation occurred during the heating. This result is consistent with the observation of Jensen et al.¹⁸ who argue that the presence of tightly bound H atoms inside TiH₂ domains have a stabilizing effect of the structure (see also Chapter 6). It is also consistent with the observation of TiH₂ in desorbed TiF₃ catalyzed MgH₂ powder samples^{32,33}.

The Pd 3d transition is also split into two components, in the metallic reference, Pd 3d_{3/2} is found at 341.5 eV and Pd 3d_{5/2} at 336.3 eV. These values are shifted by 1.2 eV from the Pd bulk values^{19,20} (340.3 eV for Pd 3d_{3/2} and 335.1 eV for Pd 3d_{5/2}) due to alloying with Mg. An intriguing aspect of the Pd 3d spectra is that the intensity decreases drastically for the sample subjected to a heating treatment at 523 K. Since X-ray photoelectron spectroscopy is only sensitive to the top few nanometers of the films, and the vapour pressure³⁴ of Pd at 523 K is negligible, it can be argued that Pd migrates from the surface to the interior of the film during the heating treatment and alloys with Mg.

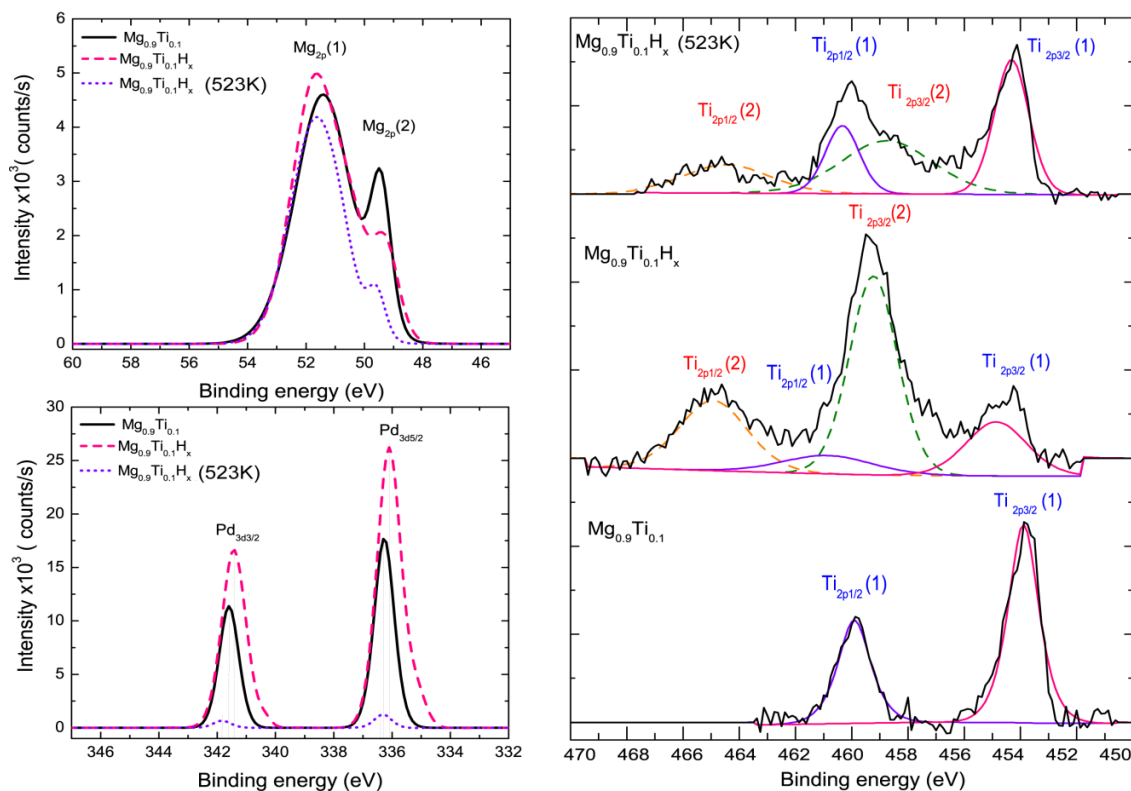


Figure 4.8. X-ray photoelectron spectra of Mg 2p, Pd 3d and Ti 2p regions measured for the Pd capped Mg_{0.9}Ti_{0.1}H_x film annealed at 523 K together with a Mg_{0.9}Ti_{0.1} metallic and Mg_{0.9}Ti_{0.1}H_x hydride reference.

Evidence of the Mg and Pd alloying on the surface is found also when analyzing the Mg 2p peak. It is interesting to note that the Mg 2p peak observed at 49.7 eV due to the alloying of Mg and Pd³⁵ is quite low in intensity compared to the more dominant peak present at 51.4 eV which is commonly attributed³⁶ to MgO or Mg(OH)₂. This indicates that a MgO or Mg(OH)₂ passivation layer is formed on the surface. However, this layer is thin enough to allow the detection of metallic magnesium. In the hydride reference, a third Mg state could be fitted at about 50.3 eV which can be attributed to the Mg in MgH₂ or to free Mg, as the neighbourhood of Ti does not produce a chemical shift on Mg^{11,28}. From the XPS data alone, it is uncertain whether Mg metal can be found on the surface of the hydride sample. But since the X-ray diffraction confirmed the presence of the rutile type Mg_{0.9}Ti_{0.1}H_x in the sample and no metallic Mg could be identified, it is more likely that the metallic magnesium at the surface is mostly found in the form of an alloy with Pd.

Further insight into the electronic structure and coherency of the films but also the evolution of defects can be obtained by positron annihilation spectroscopy.

In Figure 4.9, the anisotropy in the electron momentum distribution is measured for the two compositions, Mg_{0.9}Ti_{0.1} and Mg_{0.7}Ti_{0.3} in both the metal hydride and the metallic states. The metallic films are obtained after hydrogen desorption at high temperature of the hydride films. It is known that positrons have a higher affinity³⁷ for Mg rather than for Ti. Thus, in the analysis of 2D ACAR anisotropy this increased affinity of positrons for Mg leads to a strongly preferred detection of Mg rich areas. Higher degree of anisotropy can be seen in the metallic films as compared to the hydride films indicative of the segregation that occurs during the heating treatment.

A very interesting result is obtained when the 1D projection of the electron momentum distribution is plotted for both the metallic and the hydride samples in Figure 4.9c and 4.9f where the metal-insulator transition can clearly be seen. Magnesium hydride is an electronic insulator while Mg and TiH₂ have metallic character. From the calculation of the density of states for the fluorite and rutile type structures, it has been found that upon increasing the Ti content Mg_yTi_{1-y}H_x hydrides are more similar to the fluorite TiH₂.^{38,39} An increase of the electron momentum distribution peak intensity is comparable to an increase of the S parameter, thus positron annihilation with valence electrons. Both metallic films, Mg_{0.7}Ti_{0.3} and Mg_{0.9}Ti_{0.1}, present increased peak intensity compared to the hydride films, and implicitly higher S parameter. The increase is most pronounced for Mg_{0.7}Ti_{0.3} (see Figure 4.10 and Figure 4.11). This result is consistent with the findings of previous studies where Doppler broadening of the annihilation radiation was performed on metallic and hydride samples^{10,26}. The origin of the increase in the S parameter for the Mg_yTi_{1-y} compared to Mg_yTi_{1-y}H_x is related to a change in the electron momentum density during the insulator – metal transition²¹.

It should be noted that the metallic films studied here were obtained from desorbed metal hydrides. Though from XRD data it could already be seen that the transition from the hydrides to the hexagonal metallic structure occurred during the heating, it is not clear that the hexagonal structure obtained is the same as for the pristine films.

Complementary to XRD, positron DBAR measurements are performed. Positrons with energies ranging from 0 to 25 keV were injected into the films and the S and W profiles are recorded and fitted using VEPFIT. The thickness

of the films is ranging between 250-300 nm and the Pd capping layer is found to have about 1-2 nm. The results of the measurements for $Mg_{0.9}Ti_{0.1}$ and $Mg_{0.7}Ti_{0.3}$ are plotted in Figure 4.10 and Figure 4.11, respectively.

The annihilation parameters of the films heated at 473 K and 523 K are similar to the reference samples (see Figure 4.11). However, at 573 K, the annihilation parameters present a shift towards Ti and TiH_2 for the $Mg_{0.7}Ti_{0.3}$ films, strongly indicating that chemical segregation has occurred (see Figure 4.11)²⁶, leading to the presence of TiH_2 clusters which are large enough to act as effective positron traps. This effect is not seen for $Mg_{0.9}Ti_{0.1}$ at 573 K (Figure 4.10), suggesting that Ti does not form big enough areas to act as positron traps. The result is again consistent with the XRD data where not much change of the spectra could be seen after the heating treatment.

These drastic changes in the local composition of the films could strongly affect the rehydrogenation reaction. For this reason, rehydrogenation of the films was attempted for the films heated at 473 K where at least the metallic peak remains practically unchanged. The experiment was carried out during an *in situ* XRD experiment when the film was exposed to 6 bar of hydrogen at 473 K for about 40 h. X-ray diffractograms were measured at intervals of 30 min. Throughout the experiment, the (0002) reflection of the Mg_yTi_{1-y} phase could be seen and the formation of the Mg_yTi_{1-y} hydride was not observed. Though at 473 K, the coherence of the Mg_yTi_{1-y} is maintained, the reversibility of the films in the reaction with hydrogen is lost. This indicates that even though the composition of the alloy remains constant, the microstructural irreversible changes occurring during the heating treatment hinder the reaction with hydrogen. Among these changes, the formation of a Mg-Pd alloy on the surface of the films is known to have a detrimental effect to the rehydrogenation reaction in two ways. First, the Pd in the alloy does not act as a catalyst by splitting the H_2 molecule into atoms⁴⁰ and secondly, the Mg-Pd alloys formed are often blocking the hydrogen penetration^{41,42}. Therefore, this mechanism may be the major cause to the observed lack of hydrogenation at low temperatures (473 K)

In the search for the source of the irreversibility in the hydrogen loading of the films at low temperature, we have replaced the Pd capping layer with a Ni capping layer. Though Ni is known to form alloys with Mg such as Mg_2Ni ⁴³, these alloys are permeable for hydrogen^{44,45}. We have further simplified the system investigated by not exposing the Mg_yTi_{1-y} films to hydrogen prior to the heating treatment. In this way, hydrogen cannot contribute to the stability against phase separation and reversibility of the films.

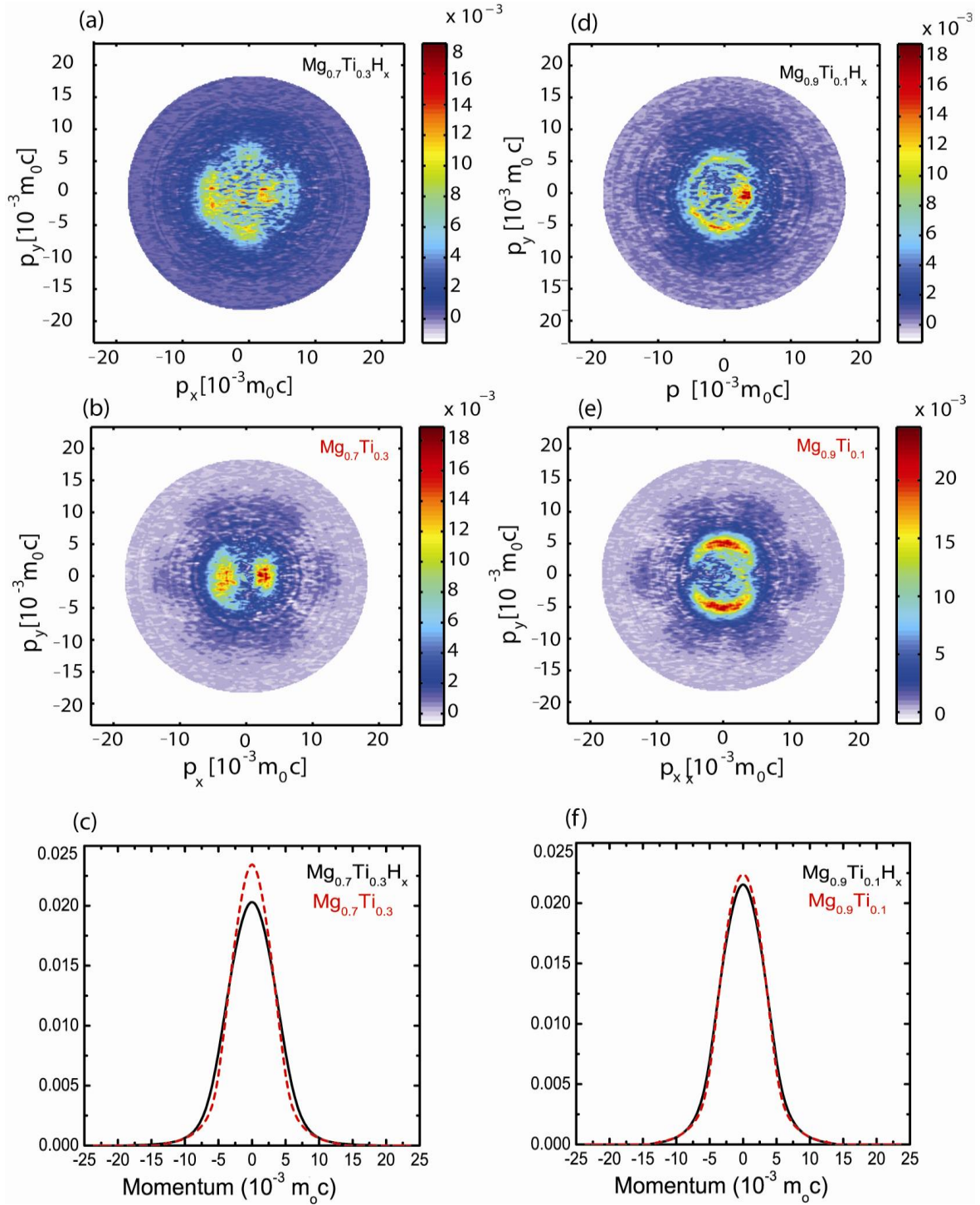


Figure 4.9. 2D ACAR anisotropy in electron momentum distributions for Mg-Ti films capped with Pd a) $Mg_{0.7}Ti_{0.3}H_x$, b) $Mg_{0.7}Ti_{0.3}$, c) 1D projection of the electron momentum distribution for both $Mg_{0.7}Ti_{0.3}$ and $Mg_{0.7}Ti_{0.3}H_x$, d) $Mg_{0.9}Ti_{0.1}H_x$, e) $Mg_{0.9}Ti_{0.1}$, f) 1D projection of the electron momentum distribution for both $Mg_{0.9}Ti_{0.1}$ and $Mg_{0.9}Ti_{0.1}H_x$

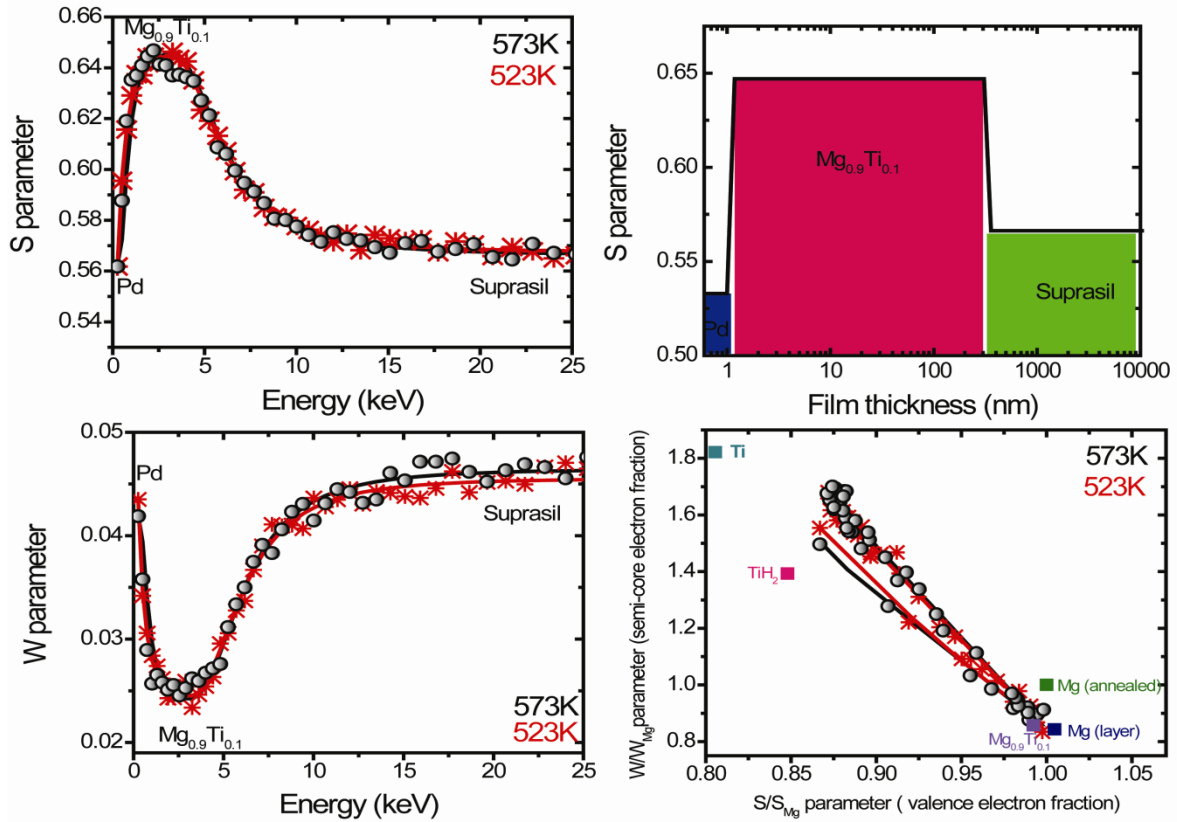


Figure 4.10. Doppler broadening of the annihilation spectroscopy of $Mg_{0.7}Ti_{0.3}$ films capped with Pd, after annealing treatments at 523 K and 573 K. a) Doppler S-parameter depth profile; b) Doppler W-parameter depth profile; c) result of the sample depth profile obtained after VEPFIT fitting; d) S-W map. The measured data is represented by open and closed circles, the solid lines represent the result of the VEPFIT analysis.

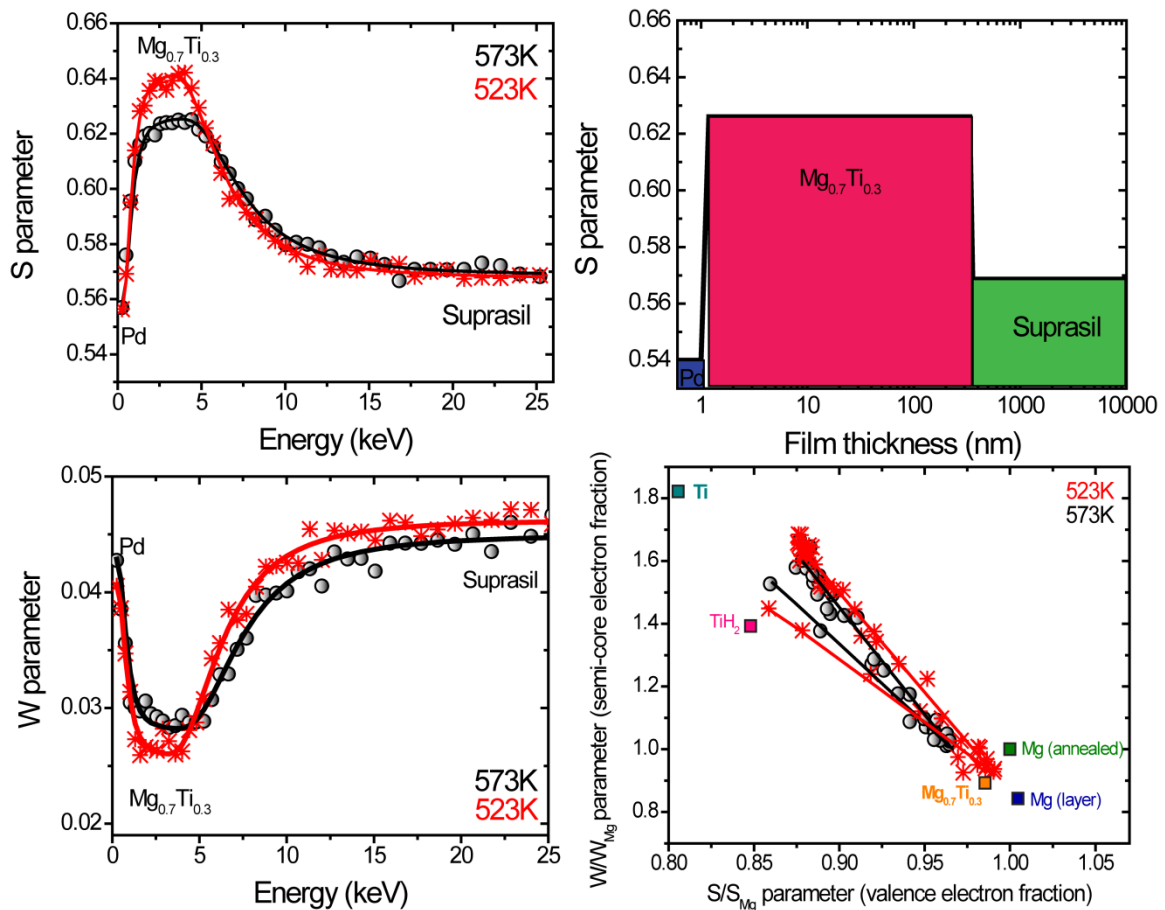


Figure 4.11. Doppler broadening of the annihilation spectroscopy of $Mg_{0.7}Ti_{0.3}$ films capped with Ni, after annealing treatments at 523 K and 573 K. a) Doppler S-parameter depth profile; b) Doppler W-parameter depth profile; c) result of the sample depth profile obtained after VEPFIT fitting; d) S-W map. The measured data is represented by open and closed circles, the solid lines represent the result of the VEPFIT analysis.

4.3.2. Thermal stability of Mg_yTi_{1-y} metallic films capped with Ni

For comparison with the Pd capped films also a series of Ni capped films were investigated. The Mg_yTi_{1-y} films capped with a Ni thin layer have been subjected to heating treatments in an *in situ* XRD setup. The experiment is performed for both compositions, $Mg_{0.7}Ti_{0.3}$ and $Mg_{0.9}Ti_{0.1}$. The results obtained at 573 K are plotted in Figure 4.12. The characteristic (0002) reflection of the hcp phase of $Mg_{0.9}Ti_{0.1}$ can clearly be distinguished at 35.2° and for $Mg_{0.7}Ti_{0.3}$ at 35.9° . In contrast to the films capped with Pd, these films have not been loaded with hydrogen so the hexagonal structure of the compounds is already established at the start of the experiment. As the temperature increases, the position of the peak shifts to lower 2θ angles, corresponding to an expansion of the lattice. As for the films capped with Pd, the intensity of the metallic peak decreases during the heating treatment. In Figure 4.13, the first and the last spectrum (measured at 300 K) during the *in situ* XRD experiment are plotted to show in more detail the changes that occurred. Indeed, for the $Mg_{0.9}Ti_{0.1}$ film,

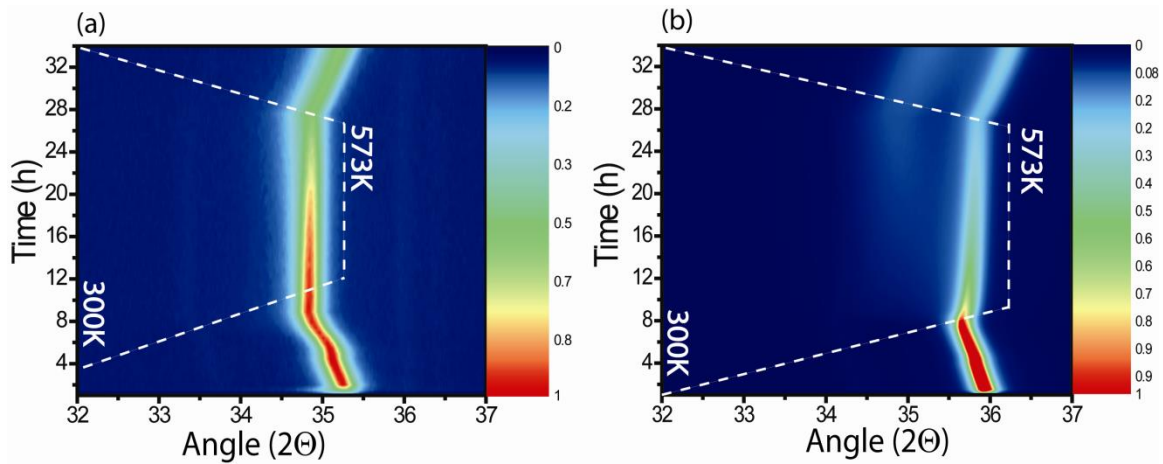


Figure 4.12. *In situ* x-ray diffraction spectra measured for Mg_yTi_{1-y} films capped with Ni: a) $Mg_{0.9}Ti_{0.1}$; b) $Mg_{0.7}Ti_{0.3}$ as a function of temperature from 300K to 573K

a clear decrease in the peak intensity is seen. At the same time a change in the peak shape, which now extends towards smaller angles, suggests the onset of demixing of the metals. However, for the $Mg_{0.7}Ti_{0.3}$, the much more dramatic decrease in intensity of the (0002) reflection is also accompanied by the appearance of other peaks. Assuming that a closed packed hexagonal structure is maintained, the appearance of the new peaks can be directly correlated to the Mg and Ti segregation. The range of the segregation can be approximated using Vegard's law and it spreads between pure hcp Ti and pure hcp Mg. The peak at 35.2° , can be assigned to a Mg rich composition of $Mg_{0.85}Ti_{0.15}$. The main peak still remains close to the initial composition though it is shifted to 36.2° corresponding to a composition of $Mg_{0.65}Ti_{0.35}$. A small intensity but broad peak appears at 38.5° where the pure Ti (0002) reflection is expected.

In Figure 4.14, the intensity of the (0002) peak during heating treatments at 473 K, 523 K and 573 K is presented for both $Mg_{0.9}Ti_{0.1}$ and $Mg_{0.7}Ti_{0.3}$. At 473

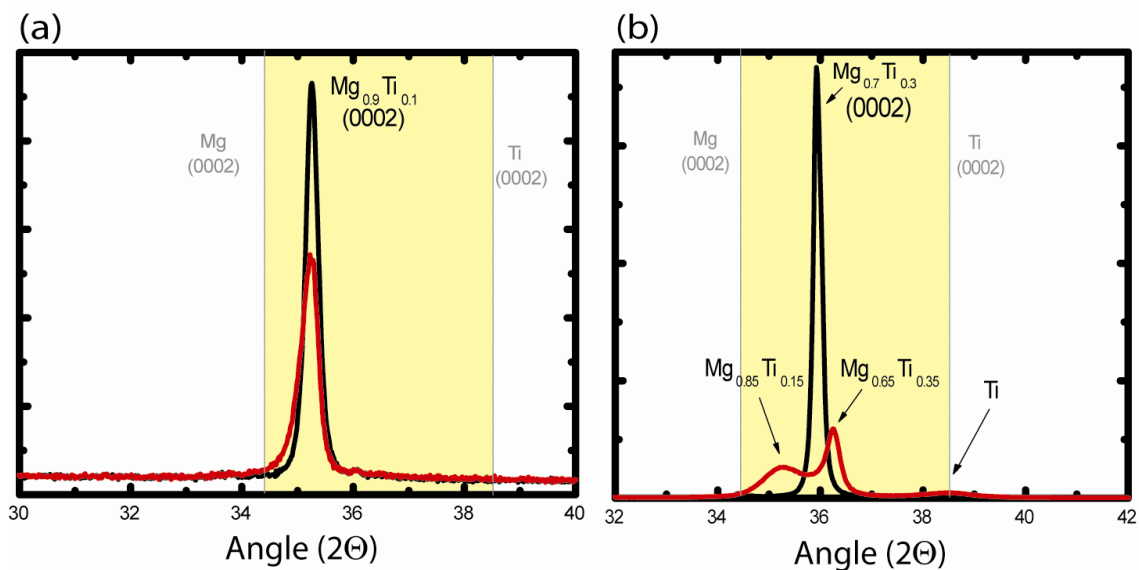


Figure 4.13. X-ray diffractograms of Mg_yTi_{1-y} films capped with Ni: a) $Mg_{0.9}Ti_{0.1}$; b) $Mg_{0.7}Ti_{0.3}$ measured at 300K before (black) and after (red) the annealing treatment at 573K.

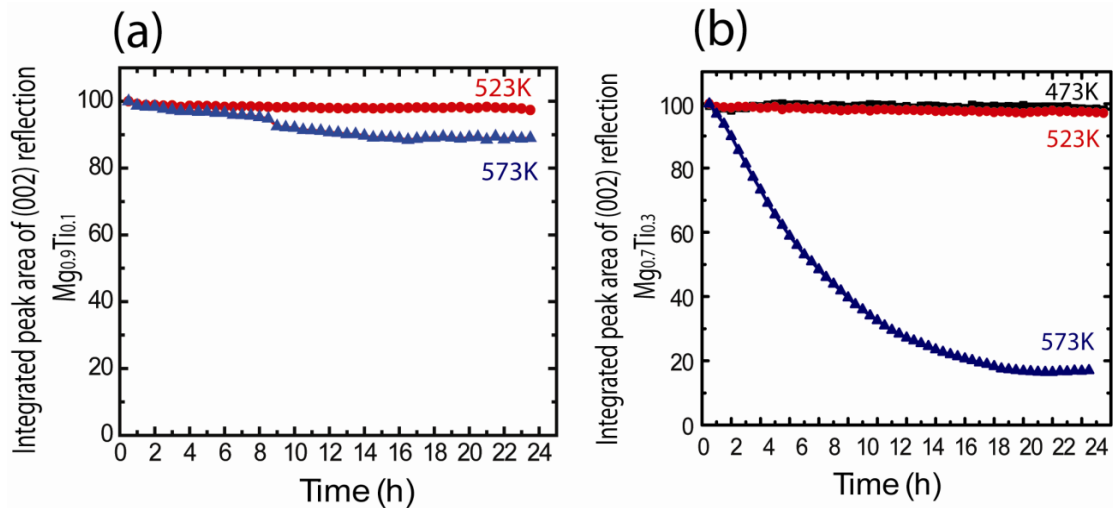


Figure 4.14. Intensity change of the (0002) reflection of (a) $Mg_{0.9}Ti_{0.1}$ and $Mg_{0.7}Ti_{0.3}$ phase as a function of annealing temperature on Ni capped film.

K, the intensity of the peak decreases by 0.02%/h during the first few hours (the peak remaining mainly unchanged) while at 523 K, the decrease is ten times faster, 0.2%/h. Nevertheless, this slow rate of demixing is remarkable, in the context that the mix is thermodynamically unstable. The explanation for it may lie in the special structure of the as prepared Mg-Ti films which is characterized as small scale spinodal composition. At 573 K, the intensity of the peak decreases drastically by more than 5%/h. Comparing these results with the Pd capped films, it is clear to see that the latter were much more stable at temperatures of up to 523 K where hardly any decrease in intensity of the peak could be seen. It can be argued that the presence of hydrogen atoms in the structure has indeed a stabilizing effect on the Mg_yTi_{1-y} mix as was found in theoretical studies¹⁸.

Figure 4.15 shows that nevertheless, in spite of the apparent stability of the Mg_yTi_{1-y} phase after the heating treatment at 473 K, hydrogen reloading of the films was not possible at 373 K and up to 1 bar of H_2 . Since the capping layer is

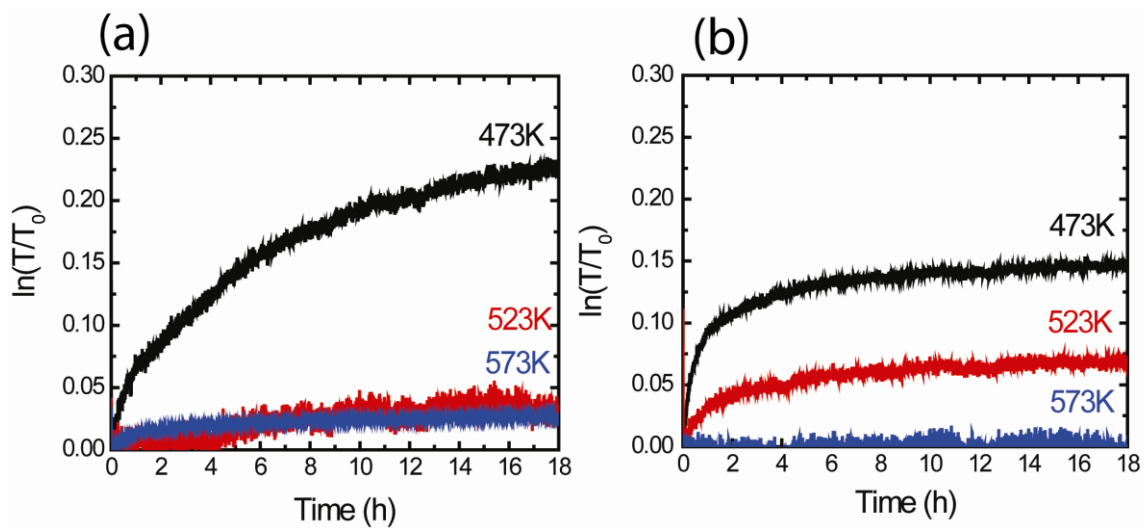


Figure 4.15. Hydrogen loading of (a) $Mg_{0.9}Ti_{0.1}$ and (b) $Mg_{0.7}Ti_{0.3}$ films capped with Ni after heating treatments using Hydrogenography

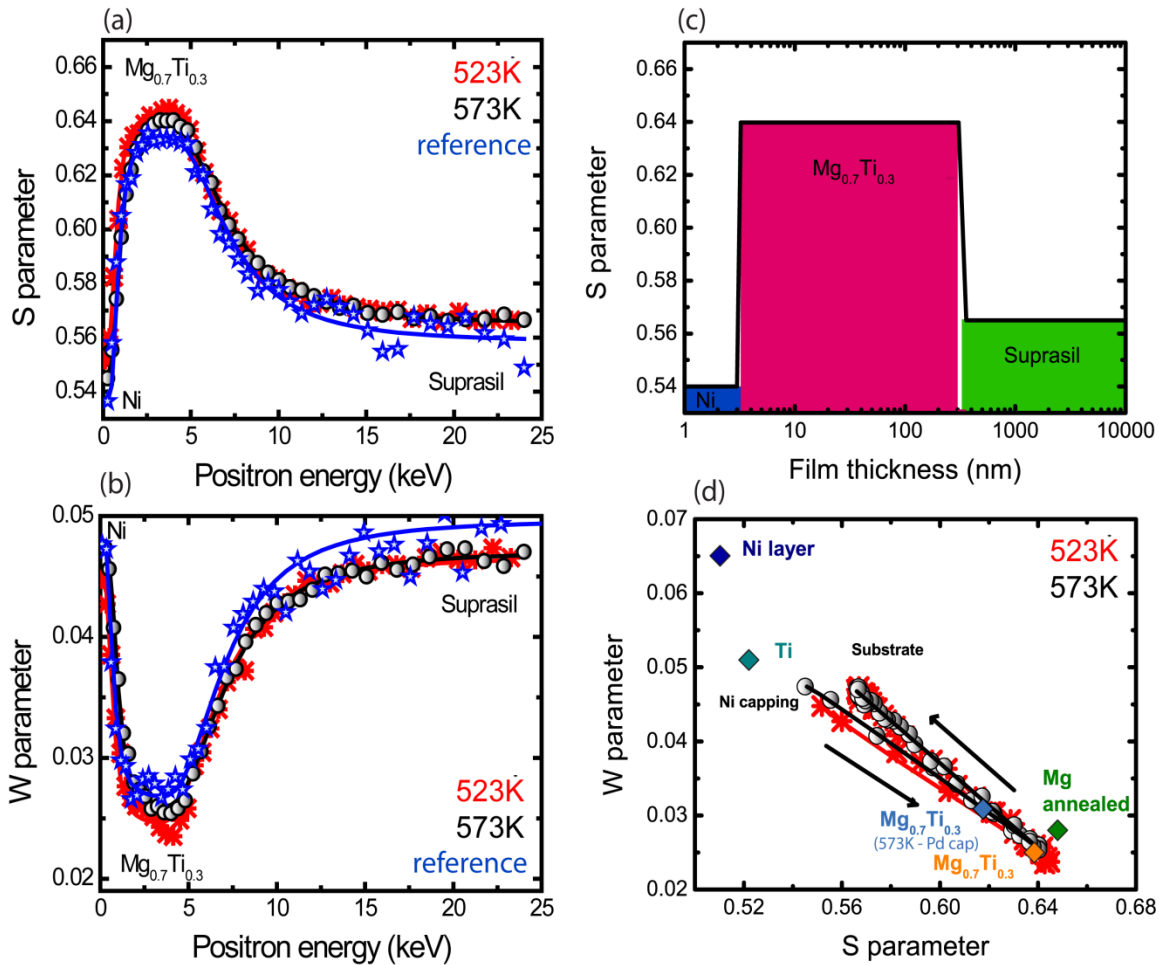


Figure 4.16. Doppler broadening of the annihilation spectroscopy of $Mg_{0.7}Ti_{0.3}$ films capped with Ni, after annealing treatments at 523K and 573K. a) Doppler S-parameter depth profile; b) Doppler W-parameter depth profile; c) result of the sample depth profile obtained after VEPFIT fitting; d) S-W map. The measured data is represented by open and closed circles, the solid lines represent the result of the VEPFIT analysis.

now Ni which forms a hydrogen permeable alloy with Mg, it cannot be argued that the permeability of the capping layer is the cause for the blockage of the hydrogenation reaction since Mg_2Ni alloys possibly formed are known to be highly permeable to hydrogen. And yet, for neither composition, rehydrogenation was possible. This indicates that irreversible microstructural changes do occur during the heating treatments that will prevent the hydrogenation reaction, or reduced catalytic activity of the capping layer.

In order to gain additional insight into the microstructural changes, Doppler Broadening positron annihilation spectroscopy was used to gain more insight in some microstructural aspects of the films exposed to high temperatures. The positron annihilation spectroscopy results for the $Mg_{0.7}Ti_{0.3}$ film capped with Ni are presented in Figure 4.16. S and W parameters plotted as a function of the positron penetration energy are fitted using VEPFIT and assuming a three layer fit, a Ni capping layer, a $Mg_{0.7}Ti_{0.3}$ layer and the substrate. A very good agreement is obtained between the measurement and the fit. The solid lines represent the fitting using VEPFIT while the symbols represent the measured data.

The layered model obtained for the sample heated at 573 K is presented in Figure 4.16c. Thus, the thickness of the Ni capping layer is found to be about 2 nm and the thickness of the $Mg_{0.7}Ti_{0.3}$ film about 300 nm.

An overview of the results obtained by DBAR is presented in a plot of S versus W parameter. Bulk materials are characterised by a specific S-W point on this map. In the plot, also reference points for annealed Mg, an as-deposited Mg layer and $Mg_{0.7}Ti_{0.3}$ reference points are marked. Due to the high affinity of positrons for Mg relative to Ti, very little variation of the annihilation parameters between pure Mg and Ti doped Mg can be seen^{10,37,46}. The measured points are plotted on the S-W maps together with the results of the VEPFIT given by straight lines. The arrows in the figure indicate the increasing positron implantation energies. Thus, low energy positrons annihilate in the Ni surface layer, positrons with energies up to 7 keV annihilate primarily in the $Mg_{0.7}Ti_{0.3}$ layer and higher energy positrons annihilate primarily in the Suprasil substrate. Because of the linear relation⁴⁷ between the S and the W parameter, visible in the S-W plot (see Figure 4.16. d) the existence of the three layers is confirmed as the realistic model by the presence of the straight lines between the capping layer and the film and then the film and the suprasil substrate⁴⁸. The annihilation parameters characteristic for the $Mg_{0.7}Ti_{0.3}$ film can be found at the intersection of the two lines. As Mg and Ti segregate during heating as observed from the XRD experiment, Ti domains could also act as positron traps, provided that these domains are sufficiently large, and the W parameter should increase. Although this effect was clearly observed for the Pd capped films, it is not observed for the Ni capped film. Only a small increase of 2% in the S parameter compared to the reference points was observed for the film heated at 523 K, which reflects an increase of concentration of open volume defects. An increase of 1.4% of the S parameter during annealing treatment of Mg was reported by Eijt et al.²¹ At 573 K, the increase in S is expected to be more pronounced due to an increase in the number of defects but instead it is very close to the reference point of $Mg_{0.7}Ti_{0.3}$. The reason for this behavior can be seen as two competing mechanisms acting in opposites directions. On the one hand, the S parameter increases because of increase in open volume defects in the films but on the other hand, S parameter decreases because the Mg-Ti segregation leads to a more pronounced contribution from phase separated Ti clusters.

Similarly, in Figure 4.17, positron annihilation spectroscopy results for $Mg_{0.9}Ti_{0.1}$ films are presented. The thickness of the $Mg_{0.9}Ti_{0.1}$ film is found to be about 300 nm, with a 1 nm Ni capping layer. In the fit, a three layer model was used as in the previous case. Again, a good agreement between the data and the fit is obtained. A decrease of the S parameter is noted for both samples also here. The effect is more pronounced for the sample heated at 523 K as the segregation of the metals is quite small as the XRD data has also shown. At 573 K, the segregation is more pronounced which leads to the formation of bigger Ti clusters which can act as positron traps leading to the lowering of the S parameter.

The change in microstructure by formation of open volume defects observed for the heated samples could have a detrimental effect on the reaction of the films with hydrogen. Several theoretical but also experimental studies on the interaction of metals like Nb₄₉ and Mg₅₀ with hydrogen have shown that vacancies can act as potential wells, where hydrogen atoms can be trapped. Also,

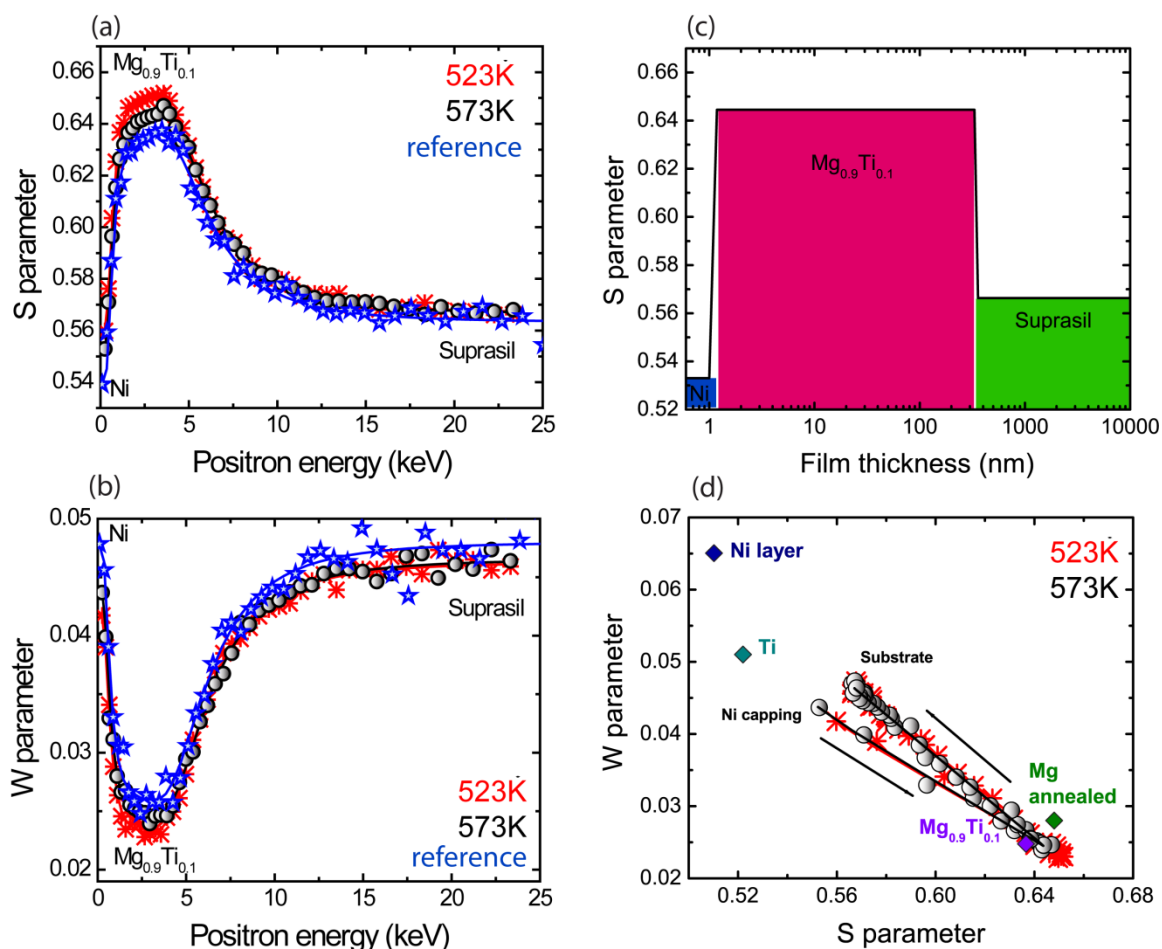


Figure 4.17. Doppler broadening of the annihilation spectroscopy of $Mg_{0.9}Ti_{0.1}$ films capped with Ni, after annealing treatments at 523K and 573K. a) Doppler S-parameter depth profile; b) Doppler W-parameter depth profile; c) result of the sample depth profile obtained after VEPFIT fitting; d) S-W map. The measured data is represented by open and closed circles, the solid lines represent the result of the VEPFIT analysis.

a loss in catalytic activity of the capping layer may lead to the irreversibility of hydrogen loading at low temperatures.

4.4 Conclusions

The remarkable kinetic stability of the Mg_yTi_{1-y} and $Mg_yTi_{1-y}H_x$ films was put to the test in this study by exposing the films to long heating treatments and temperatures up to 573 K. Though nanometer scale spinodal type modulations are already present in the coherent films at low temperature, the heating treatment was expected to lead to severe segregation of Mg and Ti in the films. However, the crystalline structure of the films is maintained up to 523 K. At 573 K, evidence of segregation into Mg rich and Ti rich areas is found from both X-ray diffraction and positron annihilation spectroscopy. The segregation seems to have different mechanisms depending on whether the films were exposed to hydrogen or not. Further, the time scale of phase segregation is largely affected by the initial composition of the films. An analysis of the

chemical species at the surface revealed that during the heating treatment, the Pd from the capping layer migrates to the subsurface of the films and alloys with Mg. In the hydride films, Ti remains in the hydride state even after the thermal desorption of the films up to 573 K.

However, despite the apparent stability of the films upon heating, microstructural changes in the sample have a strong impact on the reaction of the films with hydrogen, and a loss in catalytic activity of the capping layer may have a strong impact. From positron annihilation spectroscopy, it was found that the concentration of vacancies increases which further may have a detrimental effect on the reversibility of the hydrogenation reaction.

References

- (1) Palmisano, V.; Filippi, M.; Baldi, A.; Slaman, M.; Schreuders, H.; Dam, B. An Optical Hydrogen Sensor Based on a Pd-Capped Mg Thin Film Wedge. *International Journal of Hydrogen Energy* 2010, *35*, 12574-12578.
- (2) Pasturel, M.; Slaman, M.; Borsa, D. M.; Schreuders, H.; Dam, B.; Griessen, R.; Lohstroh, W.; Borgschulte, A. Stabilized Switchable "Black State" in Mg₂NiH₄/Ti/Pd Thin Films for Optical Hydrogen Sensing. *Applied Physics Letters* 2006, *89*, 021913.
- (3) Farangis, B.; Nachimuthu, P.; Richardson, T. J.; Slack, J. L.; Meyer, B. K.; Perera, R. C. C.; Rubin, M. D. Structural and Electronic Properties of Magnesium- Transition Metal Switchable Mirrors. *Solid State Ionics* 2003, *165*, 309-314.
- (4) Anders, A.; Slack, J. L.; Richardson, T. J. Electrochromically Switched, Gas-Reservoir Metal Hydride Devices With Application to Energy-Efficient Windows. *Thin Solid Films* 2008, *517*, 1021-1026.
- (5) Baldi, A.; Borsa, D. M.; Schreuders, H.; Rector, J. H.; Atmakidis, T.; Bakker, M.; Zondag, H. A.; van Helden, W. G. J.; Dam, B.; Griessen, R. Mg-Ti-H Thin Films As Switchable Solar Absorbers. *International Journal of Hydrogen Energy* 2008, *33*, 3188-3192.
- (6) Borsa, D. M.; Baldi, A.; Pasturel, M.; Schreuders, H.; Dam, B.; Griessen, R.; Vermeulen, P.; Notten, P. H. L. Mg--Ti--H Thin Films for Smart Solar Collectors. *Applied Physics Letters* 2006, *88*, 241910-241913.
- (7) Karazhanov, S. Zh.; Ulyashin, A. G.; Vajeeston, P.; Ravindran, P. Hydrides As Materials for Semiconductor Electronics. *Philosophical Magazine* 2008, *88*, 2461-2476.
- (8) Borsa, D. M.; Gremaud, R.; Baldi, A.; Schreuders, H.; Rector, J. H.; Kooi, B.; Vermeulen, P.; Notten, P. H. L.; Dam, B.; Griessen, R. Structural, Optical, and Electrical Properties of Mg_yTi_(1-y)H_x thin Films. *Phys. Rev. B* 2007, *75*, 205408.
- (9) Gremaud, R.; Baldi, A.; Gonzalez-Silveira, M.; Dam, B.; Griessen, R. Chemical Short-Range Order and Lattice Deformations in Mg_yTi_(1-y)H_x Thin Films Probed by Hydrogenography. *Phys. Rev. B* 2008, *77*, 144204.
- (10) Eijt, S. W. H.; Leegwater, H.; Schut, H.; Anastasopol, A.; Egger, W.; Ravelli, L.; Hugenschmidt, C.; Dam, B. Layer-Resolved Study of the Mg to MgH₂ Transformation in Mg-Ti Films With Short-Range Chemical Order. *Journal of Alloys and Compounds* .
- (11) Mitchell, T.; Diplas, S.; Tsakirooulos, P.; Watts, J. F.; Matthew, J. A. D. Study of Alloying Behaviour in Metastable Mg-Ti Solid Solutions Using Auger Parameter Measurements and Charge-Transfer Calculations. *TPHA* 2002, *82*, 841-855.

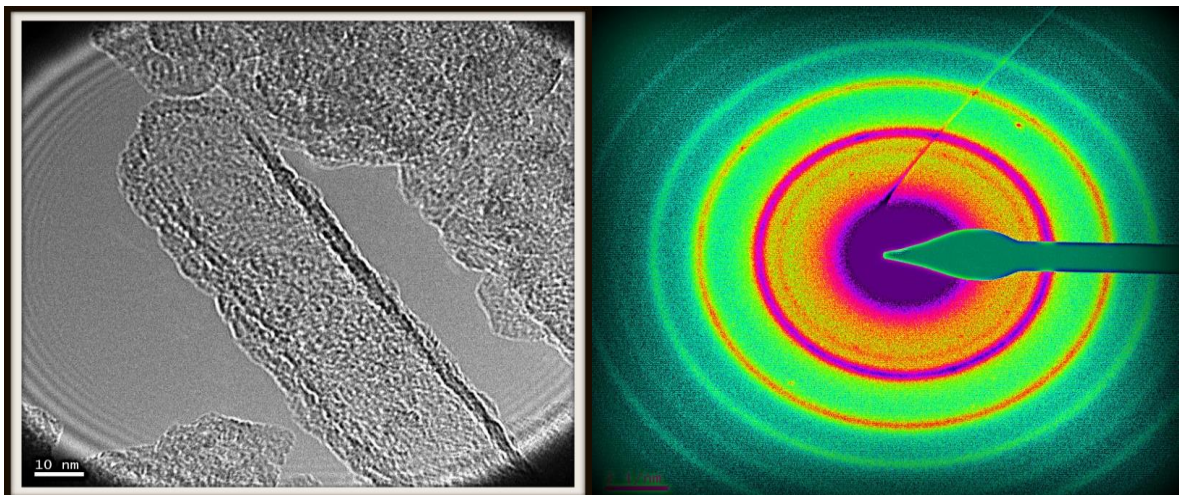
- (12) Asano, K.; Enoki, H.; Akiba, E. Synthesis of Mg-Ti FCC Hydrides From Mg-Ti BCC Alloys. *Journal of Alloys and Compounds* 2009, 478, 117-120.
- (13) Asano, K.; Enoki, H.; Akiba, E. Synthesis of HCP, FCC and BCC Structure Alloys in the Mg-Ti Binary System by Means of Ball Milling. *Journal of Alloys and Compounds* 2009, 480, 558-563.
- (14) Asano, K.; Enoki, H.; Akiba, E. Synthesis Process of Mg-Ti BCC Alloys by Means of Ball Milling. *Journal of Alloys and Compounds* 2009, 486, 115-123.
- (15) Liang, G.; Schulz, R. Synthesis of Mg-Ti Alloy by Mechanical Alloying. *Journal of Materials Science* 2003, 38, 1179-1184.
- (16) Wilkes, D. M. J.; Goodwin, P. S.; Ward-Close, C. M.; Bagnall, K.; Steeds, J. Solid Solution of Mg in Ti by Mechanical Alloying. *Materials Letters* 1996, 27, 47-52.
- (17) Baldi, A.; Gremaud, R.; Borsa, D. M.; Balde, C. P.; van der Eerden, A. M. J.; Kruijtzter, G. L.; de Jongh, P. E.; Dam, B.; Griessen, R. Nanoscale Composition Modulations in Mg_yTi_{1-y}H_x Thin Film Alloys for Hydrogen Storage. *International Journal of Hydrogen Energy* 2009, 34, 1450-1457.
- (18) Jensen, I. J. T.; Diplas, S.; Løwik, O. M. Hydrogen Induced Stabilization of Meta-Stable Mg-Ti. *Applied Physics Letters* 2012, 100.
- (19) Ma, E. Alloys Created Between Immiscible Elements. *Progress in Materials Science* 2005, 50, 413-509.
- (20) Baldi, A.; Pálsson, G. K.; Gonzalez-Silveira, M.; Schreuders, H.; Slaman, M.; Rector, J. H.; Krishnan, G.; Kooi, B. J.; Walker, G. S.; Fay, M. W.; Hjørvarsson, B.; Wijngaarden, R. J.; Dam, B.; Griessen, R. Mg/Ti Multilayers: Structural and Hydrogen Absorption Properties. *Phys. Rev. B* 2010, 81, 224203.
- (21) Eijt, S. W. H.; Kind, R.; Singh, S.; Schut, H.; Legerstee, W. J.; Hendrikx, R. W. A.; Svecnikov, V. L.; Westerwaal, R. J.; Dam, B. Positron Depth Profiling of the Structural and Electronic Structure Transformations of Hydrogenated Mg-Based Thin Films. *J. Appl. Phys.* 2009, 105, 043514-13.
- (22) van Veen, A.; Schut, H.; Clement, M.; de Nijs, J. M. M.; Kruseman, A.; IJpma, M. R. VEPFIT Applied to Depth Profiling Problems. *Applied Surface Science* 1995, 85, 216-224.
- (23) Gremaud, R.; Baldi, A.; Gonzalez-Silveira, M.; Dam, B.; Griessen, R. Chemical Short-Range Order and Lattice Deformations in Mg_yTi_{1-y}H_x Thin Films Probed by Hydrogenography. *Phys. Rev. B* 2008, 77, 144204.
- (24) Christiaan Boelsma, private communication. 2013.

- (25) Song, G. L.; Haddad, D. The Topography of Magnetron Sputter-Deposited Mg-Ti Alloy Thin Films. *Materials Chemistry and Physics* 2011, *125*, 548-552.
- (26) Anastasopol, A.; Eijt, S. W. H.; Schut, H.; Mulder, F. M.; Plazaola, F.; Dam, B. Thermal Stability of Mg_yTi_{1-y} Thin Films Investigated by Positron Annihilation Spectroscopy. *Physics Procedia* 2012, *35*, 16-21.
- (27) Shirley, D. A. High-Resolution X-Ray Photoemission Spectrum of the Valence Bands of Gold. *Phys. Rev. B* 1972, *5*, 4709-4714.
- (28) Jensen, I. J. T.; Løwik, O. M.; Schreuders, H.; Dam, B.; Diplas, S. Combined XPS and First Principle Study of Metastable Mg-Ti Thin Films. *Surf. Interface Anal.* 2012, *44*, 986-988.
- (29) Olovsson, W.; Goransson, C.; Pourovskii, L. V.; Johansson, B.; Abrikosov, I. A. Core-Level Shifts in Fcc Random Alloys: A First-Principles Approach. *Phys. Rev. B* 2005, *72*, 064203.
- (30) Olovsson, W.; Holmstrom, E.; Marten, T.; Abrikosov, I. A.; Niklasson, A. M. N. Interface Core-Level Shifts As a Probe of Embedded Thin-Film Quality. *Phys. Rev. B* 2011, *84*, 085431.
- (31) Hayashi, K.; Nakagawa, S. T.; Mizuno, Y.; Tanaka, A.; Homma, T. Ab Initio Molecular Orbital Calculation for Hydrogen-Induced States of Titanium (III). *Surf. Interface Anal.* 2003, *35*, 104-107.
- (32) Mulder, F. M.; Singh, S.; Bolhuis, S.; Eijt, S. W. H. Extended Solubility Limits and Nanograin Refinement in Ti/Zr Fluoride-Catalyzed MgH₂. *J. Phys. Chem. C* 2011, *116*, 2001-2012.
- (33) Grzech, A.; Lafont, U.; Magusin, P. C. M. M.; Mulder, F. M. Microscopic Study of TiF₃ As Hydrogen Storage Catalyst for MgH₂. *Journal of Physical Chemistry C* 2012, *116*, 26027-26035.
- (34) Nesmeianov, A. N.; Gary, R.; Nesmeianov, A. N. *Vapor Pressure of the Chemical Elements*; Elsevier: Amsterdam, 1963.
- (35) Fischer, A.; Köstler, H.; Schlapbach, L. Hydrogen in Magnesium Alloys and Magnesium Interfaces: Preparation, Electronic Properties and Interdiffusion. *Journal of the Less Common Metals* 1991, *172-174, Part B*, 808-815.
- (36) Friedrichs, O.; Sánchez-López, J. C.; López-Cartes, C.; Dornheim, M.; Klassen, T.; Bormann, R.; Fernández, A. Chemical and Microstructural Study of the Oxygen Passivation Behaviour of Nanocrystalline Mg and MgH₂. *Applied Surface Science* 2006, *252*, 2334-2345.
- (37) Puska et al, M. J. Positron affinities for elemental metals. *Journal of Physics: Condensed Matter* 1[35], 6081. 1989.

- (38) Er, S.; de Wijs, G. A.; Brocks, G. Tuning the Hydrogen Storage in Magnesium Alloys. *J. Phys. Chem. Lett.* 2010, *1*, 1982-1986.
- (39) Er, S.; Tiwari, D.; de Wijs, G. A.; Brocks, G. Tunable Hydrogen Storage in Magnesium transition Metal Compounds: First-Principles Calculations. *Phys. Rev. B* 2009, *79*, 024105.
- (40) Christmann, K. Interaction of Hydrogen With Solid Surfaces. *Surface Science Reports* 1988, *9*, 1-163.
- (41) Zlotea, C.; Andersson, Y. Microstructural Modifications Induced by Hydrogen Absorption in Mg₅Ga₂ and Mg₆Pd. *Acta Materialia* 2006, *54*, 5559-5564.
- (42) Dufour, J.; Huot, J. Study of Mg₆Pd Alloy Synthesized by Cold Rolling. *Journal of Alloys and Compounds* 2007, *446-447*, 147-151.
- (43) Okamoto, H. Mg-Ni (Magnesium-Nickel). *J Phys Equil and Diff* 2007, *28*, 303.
- (44) Liang, G.; Huot, J.; Boily, S.; Van Neste, A.; Schulz, R. Catalytic Effect of Transition Metals on Hydrogen Sorption in Nanocrystalline Ball Milled MgH₂-Tm (Tm=Ti, V, Mn, Fe and Ni) Systems. *Journal of Alloys and Compounds* 1999, *292*, 247-252.
- (45) Baldi, A.; Gonzalez-Silveira, M.; Palmisano, V.; Dam, B.; Griessen, R. Destabilization of the Mg-H System Through Elastic Constraints. *Phys. Rev. Lett.* 2009, *102*, 226102.
- (46) Weiss, A. H.; Yang, S.; Zhou, H. Q.; Jung, E.; Koymen, A. R.; Naidu, S.; Brauer, G.; Puska, M. J. Method for the Measurement of Positron Affinities and Positron Work Functions Suitable for Both Positive and Negative Work Function Materials. *Applied Surface Science* 1995, *85*, 82-86.
- (47) Schultz, P. J.; Lynn, K. G. Interaction of Positron Beams With Surfaces, Thin Films, and Interfaces. *Rev. Mod. Phys.* 1988, *60*, 701-779.
- (48) Clement M. et al. Analysis of positron beam data by the combined use of the shape- and wing-parameters. *Journal of Applied Physics* 79[12], 9029-9036. 2011.
- (49) Cizek, J.; Prochazka, I.; Danis, S.; Brauer, G.; Anwand, W.; Gemma, R.; Nikitin, E.; Kirchheim, R.; Pundt, A., R. K. Hydrogen-Vacancy Complexes in Electron-Irradiated Niobium. *Phys. Rev. B* 2009, *79*, 054108.
- (50) Larsen and, D. S. Calculated Energies and Geometries for Hydrogen Impurities in Al and Mg. *Journal of Physics F: Metal Physics* 1979, *9*, 1975.

Chapter 5

Structure and hydrogen storage properties of *in situ* spark discharge generated MgH_x nanoparticles



Abstract

MgH_x nanoparticles are synthesized in situ in the spark discharge generator in an environment of Ar-H₂. The concentration of the flowing gases has a strong influence on the morphology and crystallinity of the final products.

At 95% Ar/5%H₂, an almost amorphous hydride sample is synthesized. The nanosize character of the sample with a primary particle size < 5 nm, high defect concentration and presence of the MgO shells leads to interesting characteristics of its interaction with H₂.

In this study, infrared spectroscopy, X-ray diffraction and transmission electron microscopy results point to an extended solubility of H₂ in the Mg α phase up to a maximum of MgH₁. Upon several hydrogen loading and unloading experiments at high temperatures, little amount of conventional β -MgH₂ is formed. Instead, a supersaturated α -MgH_x phase with characteristics of an ordered phase, appears to be present. The unusual stability of the α -MgH_x in this case can be explained by the presence of the compact MgO shell around the particles which does not allow the volume expansion that would accompany the phase change hcp Mg - bct MgH₂.

Pressure composition isotherms measured at temperatures from 473 K to 573 K present equilibrium plateaus in the range of the conventional β -MgH₂ but which we here attribute to the supersaturated α -MgH_x. An enthalpy of formation of about -60 ± 15 kJ/molH₂ is determined for the non catalyzed MgH_x nanoparticles.

This chapter is based on the manuscript:

Evidence of the existence of the α -phase in MgH_x nanoparticles synthesized by spark discharge generation, Tobias Pfeiffer, Anca Anastasopol, Joost Middelkoop, Ugo Lafont, Elsa Callini, Andreas Borgschulte, Andreas Schmidt-Ott, Fokko Mulder, Stephan Eijt, in preparation

“Totul e simplu, atat de simplu incat devine de neinteles”
(It is all simple, so simple it is incomprehensible)

Nichita Stanescu, “A unsprezecea elegie”
(The eleventh elegy)

One common approach to obtain nanosized MgH_2 is ball milling and using the obtained product as the starting point for hydrogen sorption reactions. Ball milling provides a kinetic advantage of increased defects and grain boundaries which can act as fast diffusion paths for hydrogen. It also provides a thermodynamic advantage in the formation of less stable $\gamma\text{-MgH}_2$. However, these advantages are short lived as after a first dehydrogenation, $\gamma\text{-MgH}_2$ is decomposed, the concentration of defects is reduced and the grain size increased.¹

Whereas ball milling produces merely a fragmentation of the micron sized particles into nanosized grains, spark discharge generation results into nanoparticles of magnesium arranged in branchy agglomerates. The onset of hydrogen desorption from spark discharge Mg nanoparticles occurs at about 400 K and it extends to beyond 650 K. This interesting behaviour discussed in Chapter 2 is due in part to the unique particle morphology obtained through spark discharge. The synthesis of MgH_2 from the vapour phase has been addressed by several studies² using chemical vapour deposition^{3,4} sputter deposition^{5,6}, pulsed laser deposition⁷ by evaporating Mg in a H_2 atmosphere. Interesting morphologies are obtained through these methods that can be advantageous for hydrogen sorption kinetics.^{8,9}

But the appeal of spark discharge synthesis extends beyond the fractal morphology of the samples because it can also be used to synthesize MgH_x in another way: by both evaporating magnesium and ionizing hydrogen, it provides highly reactive hydrogen species to combine with Mg in vapour phase.

In this chapter, the *in situ* production of MgH_x nanoparticles is demonstrated, reflecting the versatility of the spark discharge synthesis method. Using the simple configuration of the spark discharge reactor of two magnesium electrodes, varying concentrations of hydrogen in argon as the flowing gas can be introduced. This relatively simple addition to the synthesis process leads to radical changes in both the properties of the materials obtained and the spark discharge process itself. The structure and composition of the *in situ* synthesized MgH_x nanoparticles is discussed as a function of the Ar/H_2 gas composition with a focus on the nearly amorphous MgH_x

sample obtained at low H₂ concentration in the Ar/H₂ flowing gas. In the latter case, an increased solubility of H in Mg is observed using X-ray diffraction and infrared spectroscopy.

5.2. Experimental section

5.2.1. Synthesis - Spark discharge generation

MgH_x nanoparticles are synthesized *in situ* in a conventional spark discharge generator using two Mg electrodes opposing each other. The Mg electrodes are rods of ~0.6 cm diameter from Sigma Aldrich. The sparking conditions for the sample synthesized in 100% H₂ are of 5.4 mA and 0.5 kV and a frequency of about 200-300Hz, for the samples synthesized under 5%-75% H₂, a charging current of 15mA and voltage of 1.5-2kV is used with the frequency of about 200-300Hz. The gas mixtures that contain H₂ between 0 - 100% are provided using two mass flow controllers for a total flow rate of 1 l/min. Previous to the mixing, the Ar (purity 5.0) and H₂ (purity 5.0) gases are purified further, separately for the H₂O and O₂ content by using molecular sieves column and BTS catalyst.

5.2.2. Powder X-ray diffraction

The crystallinity of the MgH_x nanoparticles is investigated using a PAN analytical X'pert PRO diffractometer with a Cu K_α source ($\lambda=1.5415\text{\AA}$) operated at 40kV and 40mA. The X-Ray diffractograms were recorded with a step size of 0.004° 2 θ and 385 s/step. The powder samples were mounted in an air tight sample holder on a low background single crystal Si support. The samples were transferred in an Ar filled glovebox.

XRD powder spectra simulations are performed using the Reflex module within Material Studio software package. The spectra are calculated assuming a Cu source with $K_{\alpha 1} = 1.540562 \text{\AA}$ and $K_{\alpha 2} = 1.54439 \text{\AA}$ with an intensity ratio of $K_{\alpha 1}/K_{\alpha 2} = 0.5$. An isotropic temperature factor of 0.025 is considered and a pseudo Voigt line shape.

5.2.3. Infrared spectroscopy

The infrared spectra are recorded using a Platinum Alpha Attenuated Total Reflectance (ATR) infrared spectrometer. The powder sample is mounted on the reflective diamond crystal in direct contact with the mobile pressure applicator without any previous preparation. Spectra are recorded in the range 4000 – 450cm⁻¹ and processed using OPUS 6.5 software.

5.2.4. Transmission electron microscopy

Transmission electron microscopy and the related EDX is performed on a FEI TECNAI TF20 monochromatic electron microscope operated at 200kV. The powder samples were transferred on copper grids in an Ar filled glovebox.

5.2.5. Thermal desorption – Hydra

Thermal hydrogen desorption is measured in a homebuilt TDS setup (Hydra). Hydrogen is detected using a quadrupole mass spectrometer. The samples are mounted under Ar atmosphere and transported in an air tight stainless steel holder. Hydrogen desorption was performed by applying constant heating rate ranging between 0.5K/min to 4K/min and measuring the pressure built up and mass spectrometer signal in parallel. The double recording of the process ensures that no other species than hydrogen are released during the measurement. The hydrogen loading experiments consisted in exposing the unloaded sample to a pressure of 6 bar H₂ (purity 6.0) for 6 hours at 523K.

5.2.6. Sieverts' measurements

Hydrogen absorption isotherms were measured using a commercial Sieverts' apparatus, PCT Pro 2000 by Hy-Energy. For the measurements, hydrogen gas of purity 6.0 was used. The accuracy of the pressure reading is 1% with a drift in pressure reading between 14 mbar and 42 mbar within six months. For the setup, a dry scroll pump was used with a base pressure at the inlet of $5 \cdot 10^{-2}$ mbar. Pressure composition isotherms were measured with the use of the MicroDoser attachment and the typical size of the aliquot was 0.663 ml. The ambient temperature during the measurement varies between 20-35 K while the sample temperature variation is less than 0.5 K over a time span of 10 h.

5.3. Results and discussion

5.3.1. MgH_x samples synthesized as a function of Ar/H₂ gas mixture

There is a clear influence of the concentration of the Ar/H₂ flowing gas on the crystallinity and particle size of the *in situ* synthesized MgH_x (see Figure 5.1). In Figure 5.1. the X-ray diffractograms of samples prepared in different Ar-H₂ gas mixtures are presented. Using X-ray diffraction, it was confirmed that increasing hydrogen content in the gas, the size of the grains is also increased from about 5 nm in 95%Ar/5%H₂ (determined from TEM, see Figure 5.8) to about 400 nm in 100%H₂ (determined from Rietveld refinement of X-ray diffraction pattern).

The reason for this correlation lies in the characteristic breakdown voltage of hydrogen compared to argon. According to Paschen's law, the breakdown voltage of a gas is directly proportional to the pressure of the gas and the distance between the electrodes. Tabrizi et al.¹⁰ has showed in a detailed study that particle size depends in a great measure on the breakdown voltage of the gas. Thus, when the spark discharge occurs in gases with a high breakdown voltage such as nitrogen and air, larger particle sizes are obtained than in gases with lower breakdown voltages such as argon or helium.¹⁰ In the present synthesis, the pressure of the gas mixture was kept constant at atmospheric pressure and the gap distance between the electrodes was 2 mm. The gas mixture used was composed of Ar with a low breakdown voltage and hydrogen which has a higher breakdown voltage.¹¹

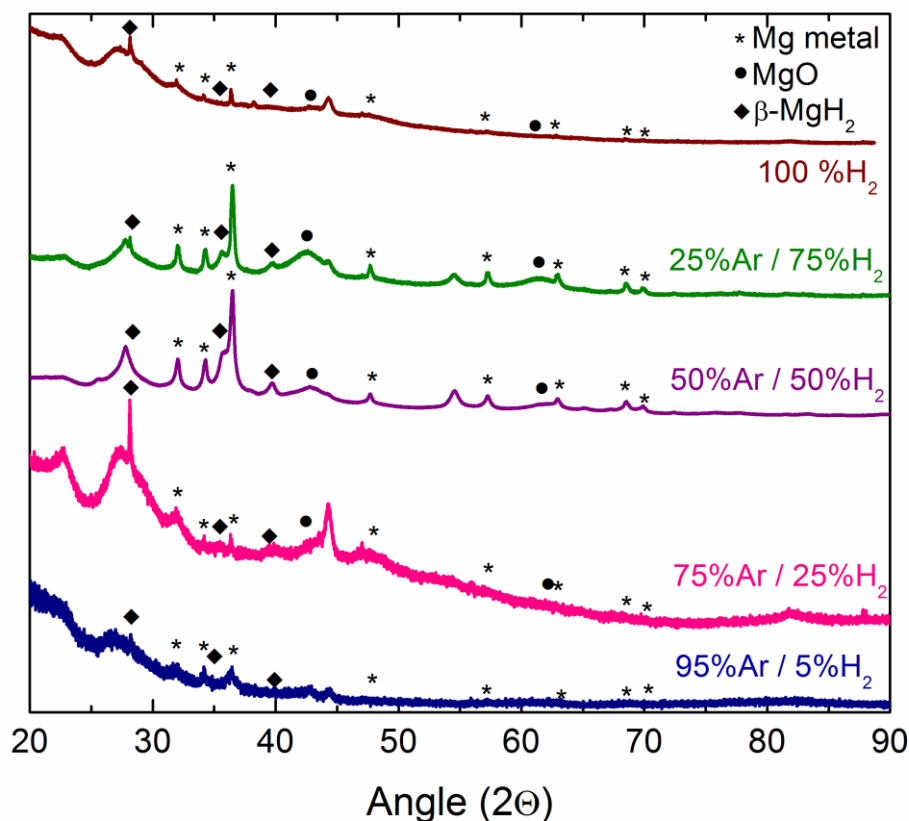


Figure 5.1. X-ray diffractograms of MgH_x synthesized in situ in the spark discharge generator under different concentrations of Ar/ H_2 flowing gas

In 100% hydrogen, the main crystalline phase obtained is the rutile type β - MgH_2 , which is a tetragonal structure belonging to the $P4_2mnm$ space group. Using the Rietveld analysis, the size of the crystallites is found to be about 400 nm. MgO is also present in the form of nanoshells of about 2 nm as it was also shown in Chapter 2.¹²

The sample synthesized using 50%Ar-50% H_2 gas mixture contains nanocrystalline rutile β - MgH_2 , metallic Mg and the typical MgO shells¹². The size of the β - MgH_2 crystallites is very small, about 8 nm, found from Rietveld analysis, suggesting that it forms in the initial stages of the particles coalescence, before the oxidation to MgO shells according to the model proposed by Vons¹³. The Mg metallic grains are larger, about 30 nm, comparable to the particles obtained without using H_2 in the flow gas characterized in detail in Chapter 3.

In 75%Ar-25% H_2 , the particles synthesized appear to be amorphous, with small traces of nanocrystalline β - MgH_2 and metallic Mg. The low intensity of the peaks made it impossible to perform Rietveld refinement. A similar result is obtained for the sample synthesized in 95%Ar – 5% H_2 .

In conclusion, increasing the amount of Ar flow gas leads to smaller particle sizes and even a higher fractions of amorphous phases mainly because of the characteristic breakdown voltages of the mixed gases (Ar and H_2).

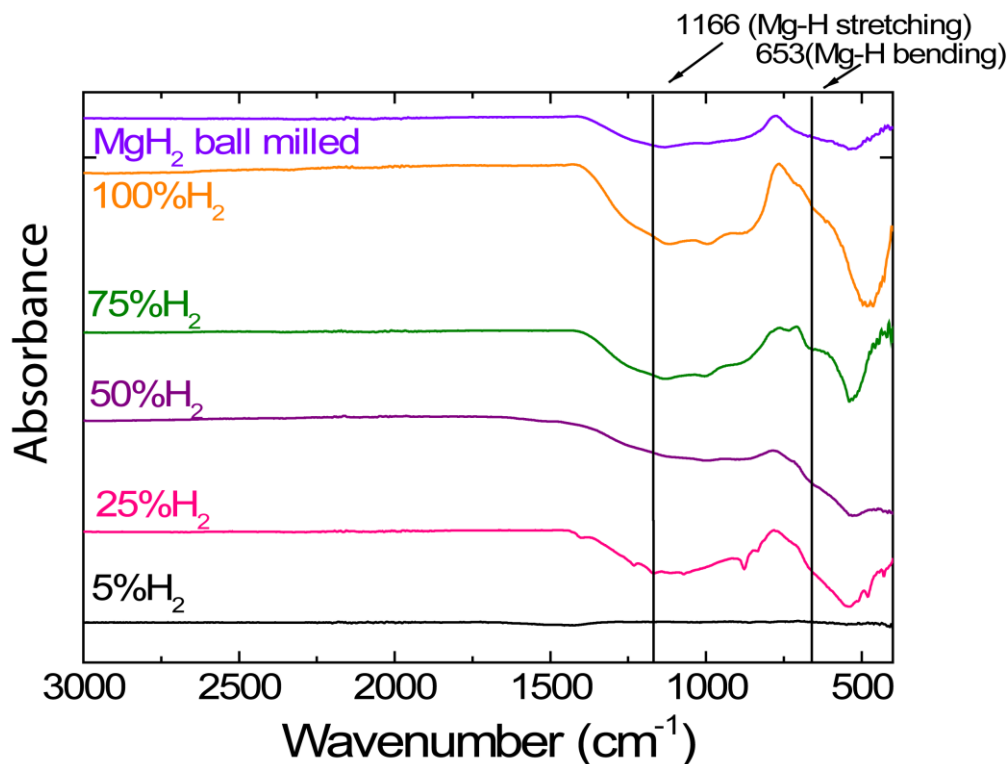


Figure 5.2. FT-infrared spectra of in situ synthesized MgH_x nanoparticles as a function of the H_2 concentrations in the Ar/ H_2 flowing gas

Complementary to X-ray powder diffraction, infrared spectroscopy was used to provide further structural information about the materials. In Figure 5.2, the infrared spectra of the spark discharge materials are compared to reference measurements on ball milled MgH_2 powders. Infrared spectroscopy is sensitive to the type of bonding and the symmetry of the compound. The bonding in MgH_2 is the subject of dispute as it is often treated as an ionic compound^{14,15} in spite of some inconsistencies when the lattice energy is calculated². In infrared spectroscopy, a distinction must be made between the internal modes which depend on intramolecular forces and symmetry and the lattice modes are sensitive to the long range effects and the overall symmetry. The lattice modes appear at low wavenumbers (0-250 cm^{-1}) and are not represented in the spectra in Figure 5.2. Thus, in the present study, the solid MgH_2 is solely characterized by its internal vibration modes mainly consisting of Mg-H bending and Mg-H stretching modes.

The presence of MgH_2 is indicated by the presence of two broad bands which correspond to the Mg-H stretching mode observed around 1166 cm^{-1} and Mg-H bending mode observed around 653 cm^{-1} . The width of the bands is ~ 670 cm^{-1} for the stretching band and ~ 300 cm^{-1} for the bending band. Zheng et al.¹⁶ consider the large broadening of the vibration bands to be related to the degree of local disorder. In the present data set, no direct correlation could be made between the crystallinity of the samples as determined from X-ray diffraction and the broadening of the infrared vibration bands which look very similar to the ones measured for crystalline MgH_2 .

These characteristic vibrations are observed for the materials regardless of their state of crystallinity. Even the apparently amorphous sample obtained in

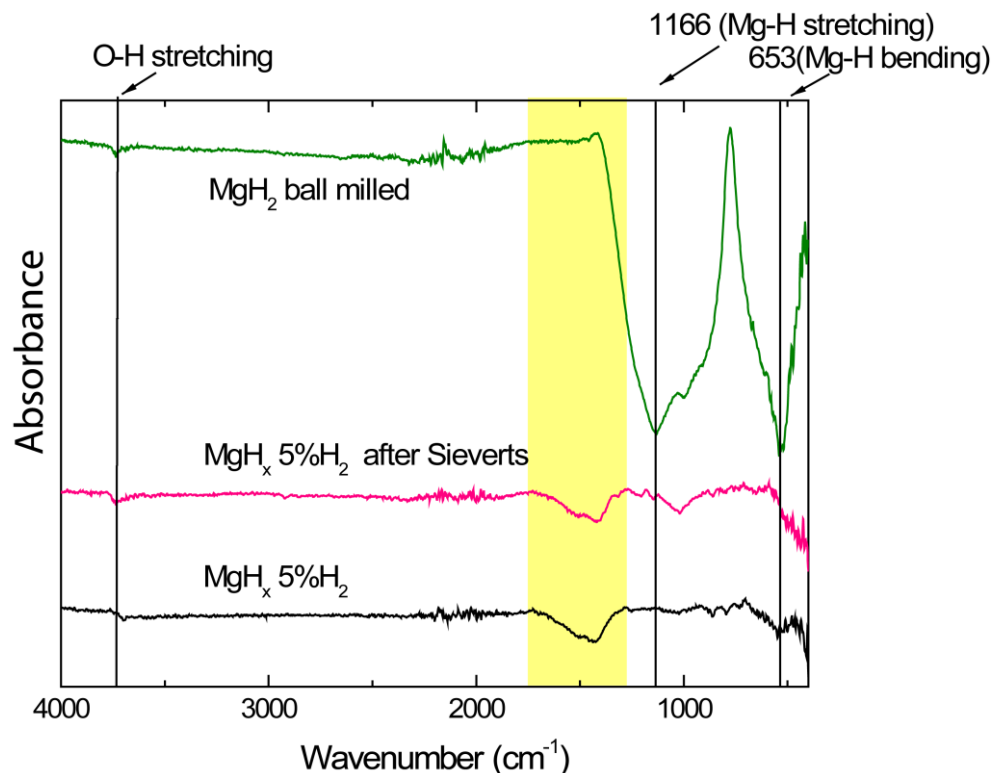


Figure 5.3. FT-infrared spectra of in situ synthesized MgH_x nanoparticles in 95%Ar/5% H_2 as produced and after hydrogen cycling compared to ball milled MgH_2 .

75%Ar25% H_2 presents clear vibration bands characteristic for MgH_2 indicative of local order being present in the sample.

Another interesting fact worth noting in the vibration spectra of Figure 5.2 and Figure 5.3 is the low intensity of the –OH stretching bands which are expected to be present around 3700 cm^{-1} even in the presence of only a few monolayers of $Mg(OH)_2$.¹⁹

5.3.2. MgH_x samples synthesized in 95% Ar/5% H_2 gas mixtures – H in the α -phase

As the samples synthesized in more than 5 % H_2 are very similar in structure to the classical hydride samples, we concentrated on the more exotic and nanosized sample synthesized in a gas mixture of 95 % Ar-5 % H_2 .

Even though traces of crystalline β - MgH_2 are observed in the X-ray diffractogram in Figure 5.4, in the infrared spectrum, the two broad bands of MgH_2 could not be identified (see Figure 5.3). Instead, a lower intensity band centred at 1440 cm^{-1} and a width of ~ 450 cm^{-1} is present. This band is present both in the as produced sample as it is in the sample after final hydrogen loading.

It is interesting to note that after hydrogen loading up to 4 wt. % H_2 (see Figure 5.9), the main crystalline phase present in the sample remains hcp Mg as seen in Figure 5.4 indicating the presence of dissolved H instead of the formation of the β - MgH_2 . Moreover, the infrared spectrum after hydrogen loading presents two weak bands, one at 1440 cm^{-1} and another one at about ~ 1100 cm^{-1} that can be attributed to Mg-H stretching.

In a study of vibration – rotation emission spectrum of the gaseous MgH_2 molecule Shayesteh et al. found a vibration at 1589 cm^{-1} which they assigned to an

antisymmetric stretching mode of the molecule. Moreover, from DFT calculations of phonon dispersion curves of crystalline MgH_2 a vibration mode is found at 1440 cm^{-1} .^{15,20,21} It therefore appears that an Mg-H vibration at lower wavenumbers is permitted, however it does not appear in the IR spectrum of the conventional $\beta\text{-MgH}_2$.

The XRD patterns in Figure 5.4. represent a comparison of the as produced sample to the loaded samples after several cycles at high temperatures. After hydrogen loading, the main crystalline phase is hexagonal Mg, besides MgO. The conventional $\beta\text{-MgH}_2$ is not present in the XRD patterns. This result is in accordance with the IR spectra where the bands for conventional $\beta\text{-MgH}_2$ are not observed. This means that the hydrogen is present in the $\alpha\text{-MgH}_x$.

The solubility of H in Mg is in general difficult to study because of the high vapour pressure and chemical reactivity of Mg. However, both experimental^{22,23,24} and theoretical^{2,25,26} studies have approximated that $x \sim 10^{-3}$ in $\alpha\text{-MgH}_x$ at atmospheric pressure and temperature range 450-925 K. In fact, there is a very wide scattering in the experimentally determined solubility limits of H in Mg, ranging from 0.06 at% to 12.6 at %. This suggests that the solubility of the H in Mg is highly dependent on the on the synthesis method and sample preparation. Popovic et al.²² measured the concentration of H_2 in the $\alpha\text{-Mg}$ to be about 0.06 at. % on 12 cm long Mg rods. The most common results obtained are about 1.1-2 at. % and are obtained on bulk Mg samples. The higher solubility reported by Stampfer et al.²⁵ (12 at %) is obtained on magnesium turnings.

Typically, the concentration of H dissolved in Mg is in the order of the vacancy concentration 27 which means that at a high concentration of defects such as vacancies and grain boundaries where H can be stored in the α -phase. On the other side,

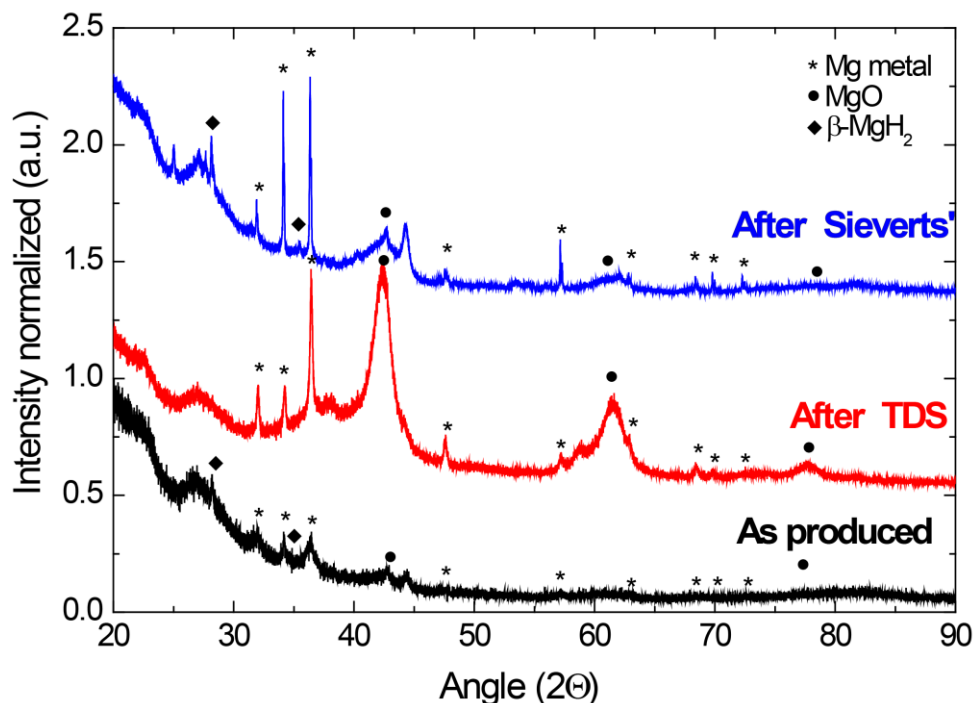


Figure 5.4. X-ray diffractograms of in situ produced MgH_x using 5% H_2 . As produced and after hydrogen loading in Hydra and Sieverts' setup.

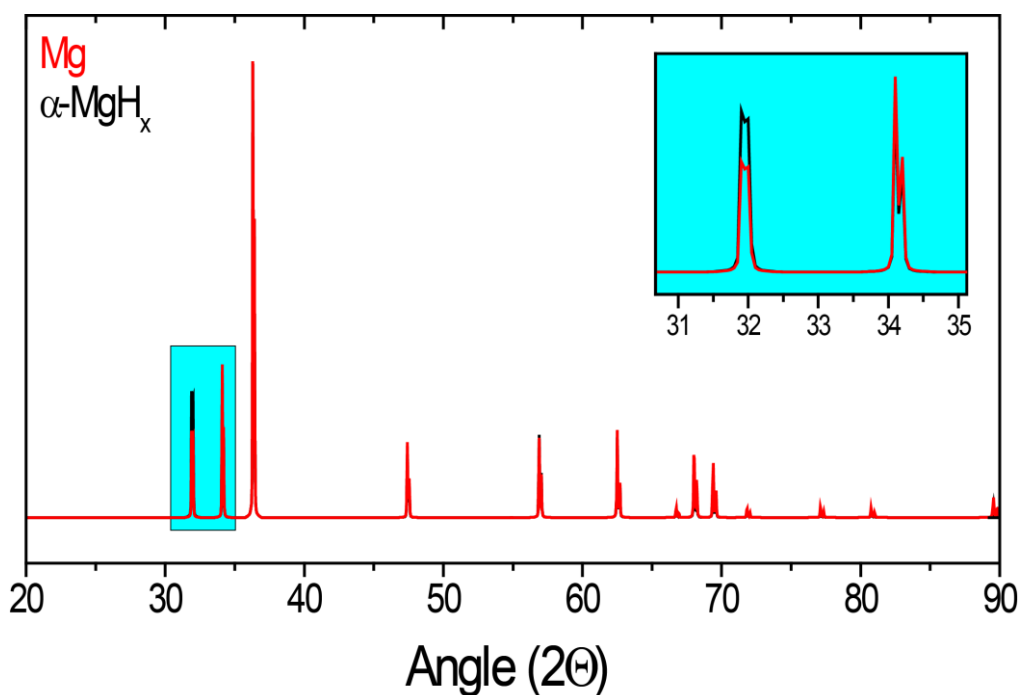


Figure 5.5. Simulated X-ray diffraction spectra of Mg metallic structure (red) and α -MgH_x (black) solute. The dissolution of H in Mg has a small effect on the peak intensity.

the α -phase can also be defined with preferred crystallographic positions for H instead of just grain boundary or surface occupation. Theoretical calculations support these results and predict that H is situated in the tetrahedral 4f (1/3, 2/3, 0.08) and octahedral 2a (0, 0, 0) sites in the α -Mg hexagonal lattice.^{26,28,29} In order to see the changes that these new sites of hydrogen can be measured by XRD, a simulation of an XRD spectrum containing H atoms at the positions previously indicated is performed. The result is plotted in Figure 5.5 in comparison with the conventional Mg spectrum and it reveals that small changes in peak intensities can appear. These discrete changes seem to be also observed in the XRD patterns in Figure 5.4 after thermal desorption measurements and hydrogen reloading in the thermal desorption setup. However, the relatively high background makes a quantitative analysis very delicate.

In a recent neutron diffraction study of TiF₃ catalyzed ball milled MgD₂, Mulder et al.²⁹ report higher dissolution of D in the α -phase up to MgD_{0.3} close to room temperature and 10 bar. The temperature in their reaction chamber rose during hydrogen uptake which means that the process is exothermic. In spite of the high fraction of deuterium dissolved in the sample, the absorption of D produced no phase transition, only slight changes in the hcp Mg lattice. An even higher dissolution of H in Mg up to MgH₁ were obtained by H implantation at 4 K.^{30,30} There, TEM and electrical resistance measurements are used to monitor the structural changes and hydrogen loading.

In the present case, if we consider that all the 4 wt% H₂ loaded at 523K (see Figure 5.8) is present entirely in the α -phase, then the sample has a composition close to MgH₁, assuming no amorphous fraction is present, quite similar to the findings of Kostler et al.³⁰ The ion implantation³⁰ and the present spark discharge generation of MgH_x are similar in the sense that hydrogen loading is done in both cases using

hydrogen ions and not molecular hydrogen gas. In this way, the activation barrier of H₂ molecule splitting is eliminated from the process.³¹

The presence of α -MgH_x is important for the hydrogen storage properties because the diffusion of hydrogen is very fast compared to the tetragonal β -MgH₂. According to Schimmel et al.²⁸ the diffusion coefficient of hydrogen in the α -MgH_x at 673K is $6.6 \times 10^{-9} \text{ m}^2/\text{s}$ while for β -MgH₂ it is $1.55 \times 10^{-16} \text{ m}^2/\text{s}$. Molecular dynamic simulations have revealed that hydrogen hops from tetrahedral (4f) to octahedral (2a) sites.

It is however remarkable that the spark discharge generated sample presents a stable α -MgH_x phase in contrast to the ion implantation synthesis³⁰. In an early study, Champ et al.²⁶ already showed qualitative results indicating that pre-existing hydrogen clusters act as very effective traps for hydrogen. The pre-existence of hydrogen in the as synthesized sample facilitates the hydrogen uptake. The higher stability during cycles of the solid solution state for our samples, can be explained by the presence of MgO shells around the particles besides the initial effect of surfaces and defects. The volume constraint that the rigid MgO layer provides, prevents the transformation to the tetragonal β -MgH₂ which is accompanied by a 30% volume increase.

The morphology and local structure of the sample is investigated using TEM and SAED in comparison with XRD in Figure 5.6. In contrast to XRD, the dominant phase identified in Figure 5.6a was found to be nanosized MgO represented by broad diffuse bands. Tetragonal β -MgH₂ could not be identified locally and it was also not present in the XRD. After hydrogen loading the morphology of the sample is for the most part characterized by nanoparticle agglomerates covered with a thin MgO shell.

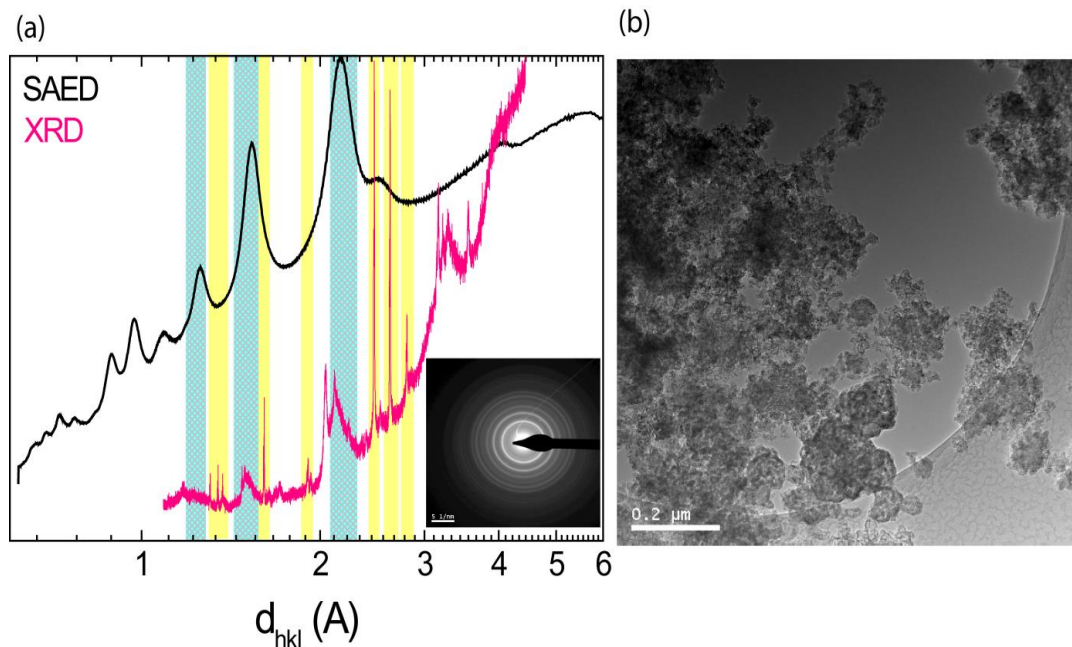


Figure 5.6. a) X-ray diffractogram compared to selected area electron diffraction of *in situ* produced MgH_x using 5%H₂ after hydrogen loading in Sieverts' setup; b) Transmission electron microscope image representative of the area used for electron diffraction also reveals the overall morphology of the powders. The blue bars mark the peak positions of MgO and the yellow bars the peak positions of hcp α -MgH_x.

An interesting observation was that in some regions, Mg rods of about 150-200 nm long and 40-50 nm wide could be identified as seen in Figure 5.7. They are covered by a thin (2 nm) MgO layer. EDS confirmed that they do not contain other impurities. This special morphology could be responsible for the XRD spectrum after Sieverts' Figure 5.4. A preferred orientation in the [0002] direction is observed. This special morphology with Mg rods is observed only for the samples analysed in the Sieverts' apparatus and is a likely result of the sintering of the nanoparticles during the long (150h) equilibrium measurements. The Mg rods could be responsible for the observed (0002) preferred orientation.

A direct comparison of the sample morphology before and after heating treatment and hydrogen sorption experiments can be seen in the TEM images in Figure 5.8. After hydrogen loading, the samples remain nanocrystalline with an increased particle size. A MgO shell can clearly be identified in the samples after hydrogen loading (see Figure 5.8 c and d). The dendritic morphology of the samples is for the most part maintained after the hydrogen cycling.

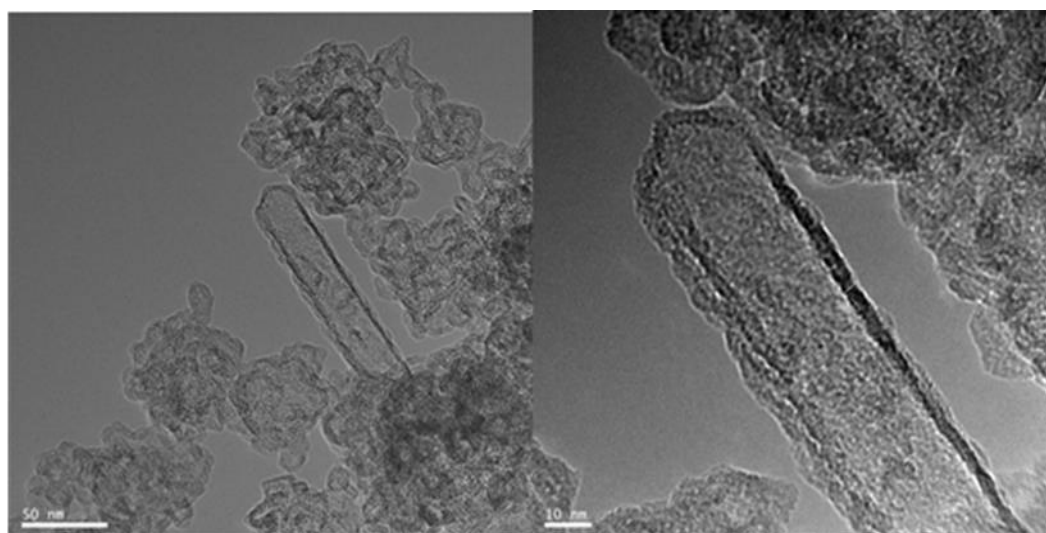


Figure 5.7. Transmission electron microscope images obtained on in situ produced MgH_x using 5% H_2 after hydrogen loading in Sieverts' setup.

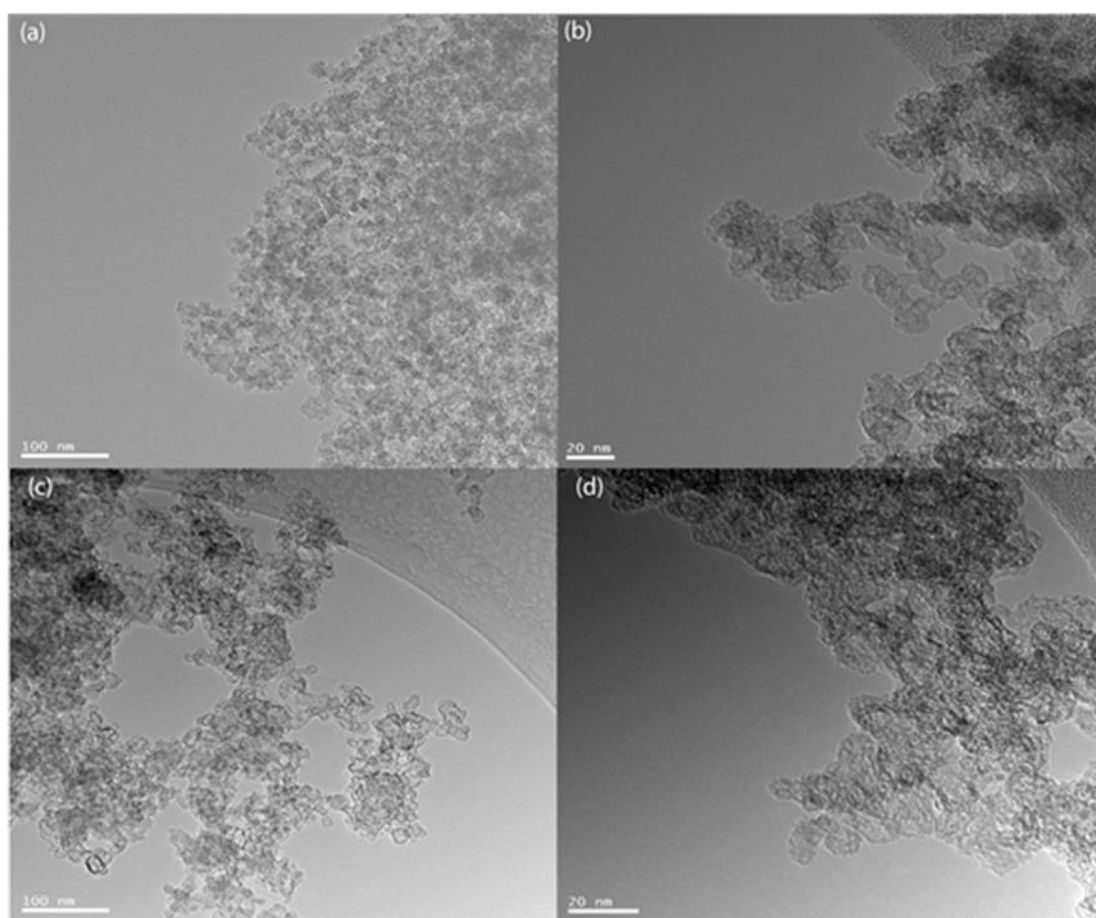


Figure 5.8. Transmission electron images of in situ synthesized MgH_x nanoparticles: a) and b) as produced; c) and d) after hydrogen cycling.

5.3.3. Hydrogen sorption behaviour of the *in situ* synthesized MgH_x (95% Ar/5% H_2)

An important issue that needs to be addressed is how these structural changes affect the hydrogen storage behavior of the *in situ* synthesized MgH_x . For this purpose, pressure-composition isotherms are measured at varying temperatures from 473K to 573K. They are used to determine the equilibrium pressure of the Mg/ MgH_2 / H_2 system. The measured isotherms are plotted in Figure 5.9. At 473K and 523K, clear plateaus can be identified at 0.114 bar and 0.73 bar, respectively. At 573K, the equilibrium plateau shows a slope. The curve between 1-4 wt. % characterized by a high slope with an equilibrium pressure varying from 1.1 bar to 1.65 bar. The slope shows some bumps near 3 wt.%, which are a result from the imperfect equilibration of the pressures in this region. They can be regarded as part of the slope that characterizes the first part of the plateau.^{1,32,33,34}

In spite of the equilibrium plateau pressures being in the range of conventional MgH_2 (see Figure 5.10), the formation of the rutile type β - MgH_2 hydride is not observed in the structural analysis of the sample. The plateaus are here attributed to the presence of MgH_x which orders on a very fine scale at concentrations up to MgH_1 . Beyond a certain hydrogen concentration, the equilibrium pressure increases rapidly. At this point, all Mg is present as containing absorbed H in the alpha phase. The remaining Mg is mostly present as MgO and therefore the still large overall H absorption of 4 wt.% seems to indicate a high capacity for H absorption in the Mg alpha

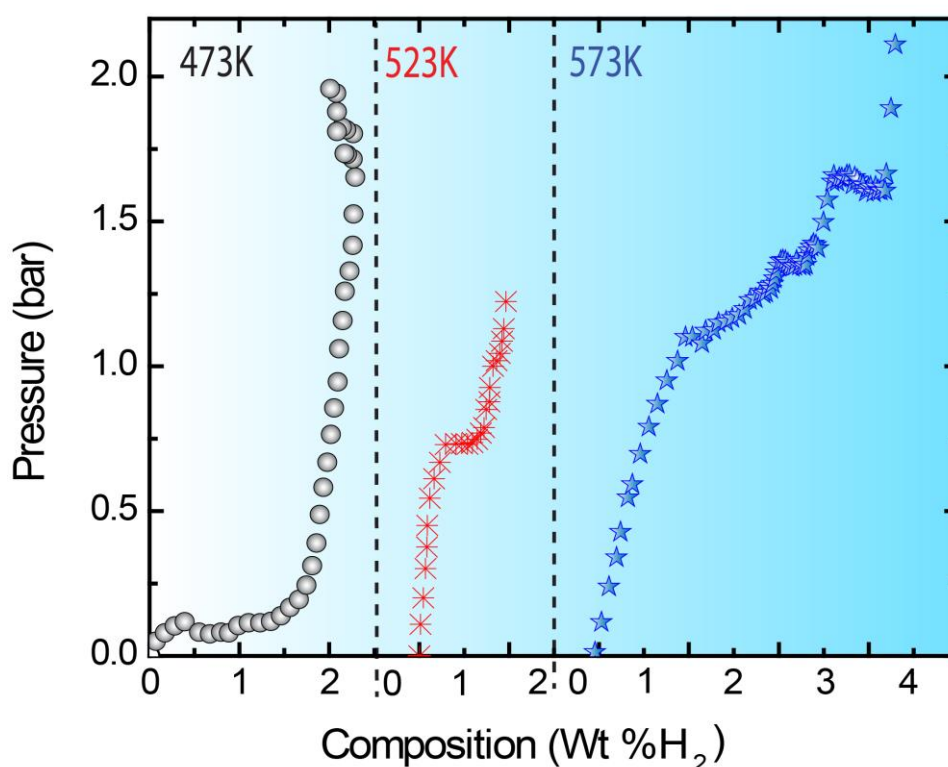


Figure 5.9. Pressure composition absorption isotherms of *in situ* produced MgH_x using 95%Ar/5% H_2 flowing gas .

phase. It cannot be excluded, however, that repulsion between neighboring H atoms in the alpha MgH_x limits the H uptake capacity in the α - MgH_x supersaturated phase.

As the structural characterization in section 5.3.1 lead to the conclusion that H can be in a great measure dissolved in a supersaturated α - MgH_x phase, it is expected that it will also dominate the pressure composition isotherms. Being a single phase, however, it should exhibit solid solution behaviour and sloping PCT equilibrium pressures. The presence of equilibrium plateaus but the absence of a second phase in the form of crystalline β - MgH_2 (see section 5.3.1) is rather unusual and has not been reported before. In the isotherm measured at 573 K, the first 1.5 wt. % H_2 are loaded before the equilibrium plateau is reached and could correspond to the α - MgH_x phase where $x \sim 0.4$, similar to the results found by Mulder et al.²⁹ Although in their study of ball milled MgH_2 -5% TiF_3 they report hydrogen loading up to $MgH_{0.4}$ and the absence of the rutile type hydride, the equilibrium measurements are not entire pressure-composition isotherms but rather a more ingenious approach of measuring temperature dependant equilibrium pressure points at fixed concentrations. Thus, with this type of measurements it is not possible to say whether an equilibrium pressure plateau corresponds to the α -phase they identified.

The difficulty comes when attempting to explain the presence of equilibrium plateaus in the absence of the ordered β - MgH_2 . A simple solid solution of H in Mg is not expected to present an equilibrium pressure plateau.³⁴ Moreover, the equilibrium pressures found are roughly within the boundaries of conventional ball milled β - MgH_2 as it can be seen in Figure 5.10. If MgH_2 which forms is in an amorphous state it also

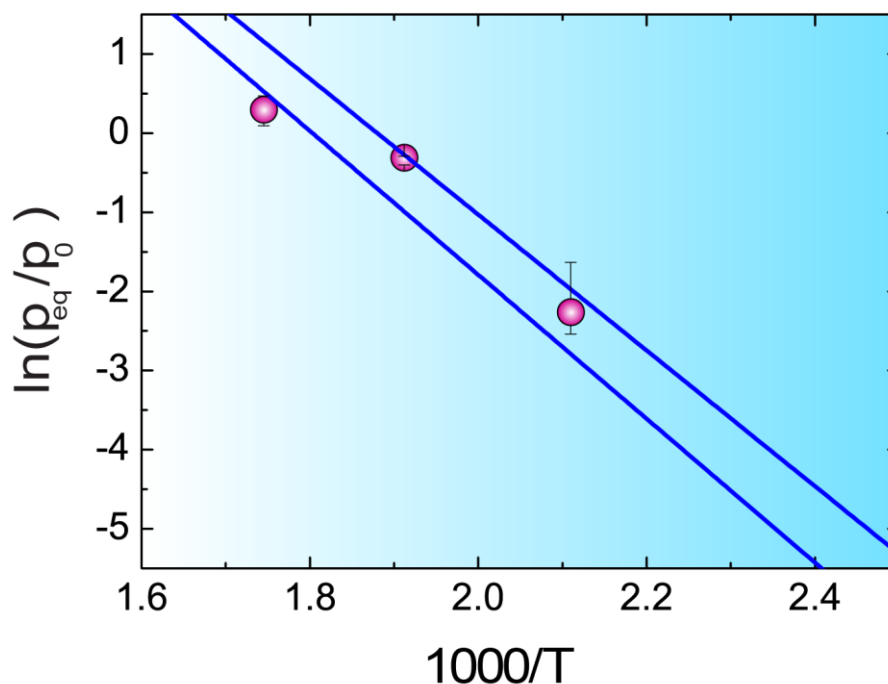


Figure 5.10. Van't Hoff plot obtained from absorption isotherms measured on in situ produced MgH_x using 5% H_2 in the Sieverts' setup. The blue lines delimit the area of results reported in literature for the absorption equilibrium pressures of bulk β - MgH_2 .

cannot give rise to equilibrium plateaus.³⁵ Hydrogen uptake measurements together with the structural findings point to the fact that an ordered MgH_x forms with a structure similar to the hexagonal $\alpha\text{-MgH}_x$. This does not exclude possible diluted superstructures where in fact a larger unit cell is formed with H on specific lattice positions since the XRD will hardly be sensitive to such superstructure. If such superstructure would form next to $\alpha\text{-Mg}$ that could lead to two phase behavior in a PCT diagram; however, no other structural proof is presently available.

A supersaturated $\alpha\text{-MgH}_x$ similar to the one observed by Kostler et al.³⁰ is formed. A van't Hoff analysis applied to the approximated equilibrium pressures that are determined at the middle of the (sloping) sections in Figure 5.9 yields the results that are presented in Figure 5.10.³⁶ The three temperature points are not on a straight line, which makes it difficult to attribute the result to a single reaction enthalpy that is probed. Assuming that a line can be drawn as indicated the slope of the van't Hoff curve is somewhat different from the conventional results obtained for MgH_2 . The enthalpy of formation is found to be $-60 \pm 15 \text{ kJ/molH}_2$ and the entropy difference is about $108 \pm 5 \text{ J/kmolH}_2$.

Both destabilization of the Mg-H_2 system and absence of the transition to the MgH_2 rutile structure can be related to the unique morphology of the spark discharge generated nanoparticles. With the exception of some needle shaped particles observed for the sample subjected to long heating treatments, the overall morphology is of spherical particles with a diameter below 10 nm organized into fractal like agglomerates. In Figure 5.8, it can clearly be seen that this morphology is maintained after the repeated cycles of hydrogen loading and unloading. One feature that should not be neglected in nanoparticles is the overwhelming importance of the surfaces and interfaces in the energetics of chemical transformations. This aspect has been underlined in numerous studies involving nanomaterials.^{29,37,38,39}

The incredible stability of the supersaturated MgH_x phase could be qualitatively explained also by the interface stress. At the nanoscale, the energy cost of creating a new interface is so high that it can tip the overall energetic balance and prevent the transformation to the rutile MgH_2 .^{29,39}

Mooij et al.⁴⁰ demonstrated that nanoconfinement of Mg leads to a destabilization of the MgH_2 because of an energy interface effect. However, in their experiments Mg was studied as a film and the confinement was provided by a top and a bottom layer. The stress induced by the 30% volume increase during the transition from hcp Mg to tetragonal MgH_2 can be accommodated in the lateral directions. TEM images in the present study indicate that the majority of the sample is surrounded by a MgO shell which confines a Mg core. In this way, the phase transition is possibly prevented because the change in volume cannot be accommodated.

5.4. Conclusion

Spark discharge generation of MgH_x nanoparticles produces unique morphologies and sample mixtures which show altered hydrogen storage behaviour.

The crystallinity of the particles is influenced by the concentration of the Ar/H_2 gas. In spite of the simplicity of the three component system Mg, H_2 and the undesired O, the structure of the samples is rather complex. A MgO shell forms around a Mg metallic core which together with the presence of defects and surfaces, stabilizes the $\alpha\text{-MgH}_x$ phase. Structural analysis of the samples using infrared spectroscopy, transmission electron microscopy and X-ray diffraction indicate that the sample

synthesized under 95%Ar/5%H₂ contain a supersaturated α -MgH_x phase instead of the formation of the conventional rutile β -MgH₂ metal hydride phase. Such phase can reversibly desorb and absorb hydrogen, while remaining essentially in the alpha-MgH_x structure. Sloping pressure composition graphs are measured, from which a less negative enthalpy of formation of about -60 ± 15 kJ/molH₂ may be determined for the non-catalyzed MgH_x nanoparticles.

References

- (1) Huot, J.; Liang, G.; Boily, S.; Van Neste, A.; Schulz, R. Structural Study and Hydrogen Sorption Kinetics of Ball-Milled Magnesium Hydride. *Journal of Alloys and Compounds* 1999, 293-295, 495-500.
- (2) Stander, C. M.; Pacey, R. A. The Lattice Energy of Magnesium Hydride. *Journal of Physics and Chemistry of Solids* 1978, 39, 829-832.
- (3) Saita, I.; Toshima, T.; Tanda, S.; Akiyama, T. Hydrogen Storage Property of MgH₂ Synthesized by Hydriding Chemical Vapor Deposition. *Journal of Alloys and Compounds* 2007, 446-447, 80-83.
- (4) Saita, I.; Akiyama, T. Microstructure of the MgH₂ synthesized by hydriding chemical vapor deposition. Materials Research Society Symposium Proceedings 971, 70-75. 2006.
- (5) Vermeulen, P.; Niessen, R. A. H.; Borsa, D. M.; Dam, B.; Griessen, R.; Notten, P. H. L. Effect of the Deposition Technique on the Metallurgy and Hydrogen Storage Characteristics of Metastable Mg_yTi_{1-y} Thin Films. *Electrochemical and Solid-State Letters* 2006, 9, A520-A523.
- (6) Kalisvaart, W. P.; Harrower, C. T.; Haagsma, J.; Zahiri, B.; Lubber, E. J.; Ophus, C.; Poirier, E.; Fritzsche, H.; Mitlin, D. Hydrogen Storage in Binary and Ternary Mg-Based Alloys: A Comprehensive Experimental Study. *International Journal of Hydrogen Energy* 2010, 35, 2091-2103.
- (7) Singh, S.; Eijt, S. W. H.; Zandbergen, M. W.; Legerstee, W. J.; Svetchnikov, V. L. Nanoscale Structure and the Hydrogenation of Pd-Capped Magnesium Thin Films Prepared by Plasma Sputter and Pulsed Laser Deposition. *Journal of Alloys and Compounds* 2007, 441, 344-351.
- (8) Cansizoglu, M.; Karabacak, T. Enhanced Hydrogen Storage Properties of Magnesium Nanotrees With Nanoleaves. *MRS Online Proceedings Library* 2009, 1216, null.
- (9) Jain et al, F. T. The Pd catalyst effect on low temperature hydrogen desorption from hydrided ultrathin Mg nanoblades. *Nanotechnology* 19[46], 465706. 2008.
- (10) Tabrizi, N.; Ullmann, M.; Vons, V.; Lafont, U.; Schmidt-Ott, A. Generation of Nanoparticles by Spark Discharge. *Journal of Nanoparticle Research* 2009, 11, 315-332.
- (11) Gialanella, S.; Ceccato, R.; Casari, F.; Ischia, G.; Molinari, A. Microstructural Refinement Using Ball-Milling and Spark-Plasma Sintering of MgH₂ Based Materials for Hydrogen Storage. *Calphad* 2009, 33, 82-88.

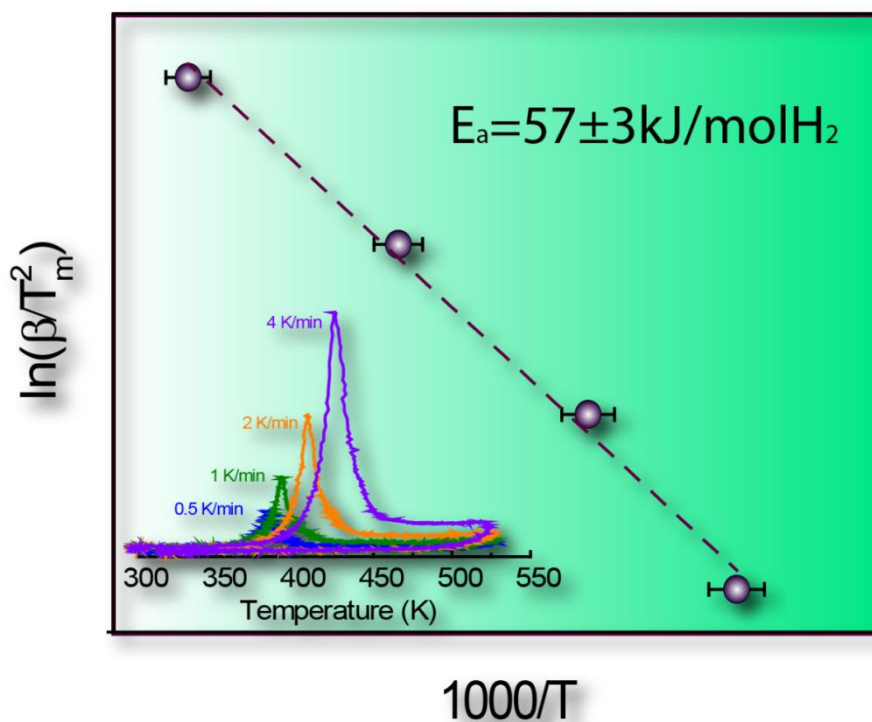
- (12) Vons, V. A.; Anastasopol, A.; Legerstee, W. J.; Mulder, F. M.; Eijt, S. W. H.; Schmidt-Ott, A. Low-Temperature Hydrogen Desorption and the Structural Properties of Spark Discharge Generated Mg Nanoparticles. *Acta Materialia* 2011, 59, 3070-3080.
- (13) Vons, V. Spark discharge generated nanoparticles for hydrogen storage applications. 2009. Ridderkerk, Ridderprint B.V.
- (14) Wang, X.; Andrews, L. Infrared Spectra of Magnesium Hydride Molecules, Complexes, and Solid Magnesium Dihydride. *J. Phys. Chem. A* 2004, 108, 11511-11520.
- (15) Ohba, N.; Miwa, K.; Noritake, T.; Fukumoto, A. First-Principles Study on Thermal Vibration Effects of MgH₂. *Phys. Rev. B* 2004, 70, 035102.
- (16) Zheng, S.; Fang; Zhang, J.; Sun, L.; He, B.; Wei, S.; Chen, G.; Sun, D. Study of the Correlation Between the Stability of Mg-Based Hydride and the Ti-Containing Agent. *J. Phys. Chem. C* 2007, 111, 14021-14025.
- (17) Chen, H. x.; Wang, Z. m.; Zhou, H. y.; Ni, C. y.; Deng, J. q.; Yao, Q. r. Hydrogen Storage Properties and Thermal Stability of Amorphous Mg₇₀(RE₂₅Ni₇₅)₃₀ Alloys. *Journal of Alloys and Compounds* 2013, 563, 1-5.
- (18) Mikheeva, V. I.; Mal'tseva, N. N. Infrared Absorption Spectra of Some Simple Hydrides. *J Struct Chem* 1964, 4, 643-646.
- (19) Varin, R. A.; Jang, M.; Czujko, T.; Wronski, Z. S. The Effect of Ball Milling Under Hydrogen and Argon on the Desorption Properties of MgH₂ Covered With a Layer of Mg(OH)₂. *Journal of Alloys and Compounds* 2010, 493, L29-L32.
- (20) Santisteban, J. R.; Cuello, G. J.; Dawidowski, J.; Fainstein, A.; Peretti, H. A.; Ivanov, A.; Bermejo, F. J. Vibrational Spectrum of Magnesium Hydride. *Phys. Rev. B* 2000, 62, 37-40.
- (21) A.Shayesteh; D.R.T.Appadoo; I.Gordon; P.F.Bernath. The vibration-rotation emission spectrum of MgH₂. *The Journal of Chemical Physics* 119, 7785. 2014.
- (22) Popovic, Z. D.; Piercy, G. R. Measurement of the Solubility of Hydrogen in Solid Magnesium. *MTA* 1975, 6, 1915-1917.
- (23) Koeneman, J.; Metcalfe, A. G. The Solubility of Hydrogen in Magnesium. *Trans. ASM* 1959, 51, 1072-1082.
- (24) Watanabe, T.; Huang, Y. C.; Komatsu, R. Solubility of hydrogen in magnesium. *J Jpn Inst Light Metals* 1976, 26, 76-81.
- (25) Stampfer, J. F.; Holley, C. E.; Suttle, J. F. The Magnesium-Hydrogen System 1-3. *Journal of the American Chemical Society* 1960, 82, 3504-3508.

- (26) Champ, A. C.; Bugeat, J. P.; Ligeon, E. Solid Solutions of the Hydrogen-Magnesium System Produced by Implantation. *Radiation Effects* 1978, 37, 73-81.
- (27) Zeng, K.; Klassen, T.; Oelerich, W.; Bormann, R. Critical Assessment and Thermodynamic Modeling of the Mg-H System. *International Journal of Hydrogen Energy* 1999, 24, 989-1004.
- (28) Schimmel, H. G.; Kearley, G. J.; Huot, J.; Mulder, F. M. Hydrogen Diffusion in Magnesium Metal (Phase) Studied by Ab Initio Computer Simulations. *Journal of Alloys and Compounds* 2005, 404-406, 235-237.
- (29) Mulder, F. M.; Singh, S.; Bolhuis, S.; Eijt, S. W. H. Extended Solubility Limits and Nanograin Refinement in Ti/Zr Fluoride-Catalyzed MgH₂. *J. Phys. Chem. C* 2011, 116, 2001-2012.
- (30) and, H. K. A New Hydride: MgH_x Prepared by Ion Implantation. *Journal of Physics: Condensed Matter* 1991, 3, 8767.
- (31) Norskov, J. K.; Stoltze, P. Theoretical Aspects of Surface Reactions. *Surface Science* 1987, 189-190, 91-105.
- (32) Ellinger, F. H.; Holley, C. E.; McInteer, B. B.; Pavone, D.; Potter, R. M.; Staritzky, E.; Zachariasen, W. H. The Preparation and Some Properties of Magnesium Hydride. *J. Am. Chem. Soc.* 1955, 77, 2647-2648.
- (33) Gross, K. J.; Spatz, P.; Zuttel, A.; Schlapbach, L. Mechanically Milled Mg Composites for Hydrogen Storage the Transition to a Steady State Composition. *Journal of Alloys and Compounds* 1996, 240, 206-213.
- (34) Hjort, P.; Krozer, A.; Kasemo, B. Hydrogen Sorption Kinetics in Partly Oxidized Mg Films. *Journal of Alloys and Compounds* 1996, 237, 74-80.
- (35) Hayashi, S.; Orimo, S. i.; Fujii, H. Local Structures and Hydrogen Dynamics in Amorphous and Nanostructured Mg-Ni-H Systems As Studied by ¹H and ²H Nuclear Magnetic Resonance. *Journal of Alloys and Compounds* 1997, 261, 145-149.
- (36) Martin, M.; Gommel, C.; Borkhart, C.; Fromm, E. Absorption and Desorption Kinetics of Hydrogen Storage Alloys. *Journal of Alloys and Compounds* 1996, 238, 193-201.
- (37) Mooij, L.; Dam, B. Hysteresis and the Role of Nucleation and Growth in the Hydrogenation of Mg Nanolayers. *Phys. Chem. Chem. Phys.* 2013, 15, 2782-2792.
- (38) Grzech, A.; Lafont, U.; Magusin, P. C. M. M.; Mulder, F. M. Microscopic Study of TiF₃ As Hydrogen Storage Catalyst for MgH₂. *Journal of Physical Chemistry C* 2012, 116, 26027-26035.

- (39) Wagemaker, M.; Mulder, F. M.; Van Der Ven, A. The Role of Surface and Interface Energy on Phase Stability of Nanosized Insertion Compounds. *Advanced Materials* 2009, *21*, 2703-2709.
- (40) Mooij, L. P. A.; Baldi, A.; Boelsma, C.; Shen, K.; Wagemaker, M.; Pivak, Y.; Schreuders, H.; Griessen, R.; Dam, B. Interface Energy Controlled Thermodynamics of Nanoscale Metal Hydrides. *Adv. Energy Mater.* 2011, *1*, 754-758.
- (41) Krishnan, G.; Kooi, B. J.; Palasantzas, G.; Pivak, Y.; Dam, B. Thermal Stability of Gas Phase Magnesium Nanoparticles. *J. Appl. Phys.* 2010, *107*.

Chapter 6

Low temperature hydrogen cycling and structural investigation of *in situ* spark discharge generated fluorite $\text{Mg}_y\text{Ti}_{1-y}\text{H}_x$ nanoparticles



Abstract

The metastable fluorite cubic $Mg_yTi_{1-y}H_x$ hydride is synthesized in situ in the spark discharge generator using two opposing Mg and Ti electrodes in an Ar/H₂ carrier gas mixture. From X-ray diffraction, a crystallite size of about 15 nm is found for the fluorite hydride both for the as produced sample as after several hydrogen sorption experiments. In both cases, 2-3 nm thin MgO shells are present. Infrared spectroscopy and X-ray photoelectron spectroscopy are used to characterize the small scale mixing of the Mg and Ti in the cubic hydride. Hydrogen is reversibly inserted and released from the cubic hydride without a change in symmetry. In both the absorbed and the desorbed state, the crystalline active phase is the fluorite hydride which presents only a change in lattice parameter upon hydrogen cycling.

The hydrogen desorption of the $Mg_yTi_{1-y}H_x$ phase is characterized by a single sharp peak at a low hydrogen desorption temperature of about 373 K at a heating rate of 0.5 K/min. Hydrogen thermal desorption profiles measured at different heating rates up to a temperature of 523 K are used to determine the activation energy of 57 ± 4 kJ/molH₂. This finding is in good agreement with the lowest activation energy found in Chapter 2, but now for a single activation energy corresponding to the homogeneous active nanocrystalline fluorite phase.

This chapter is based on the manuscript:

Low temperature hydrogen desorption of in situ spark discharge generated $Mg_yTi_{1-y}H_x$ nanoparticles, A. Anastasopol, M.J. Klein, T.V. Pfeiffer, J. Middelkoop, A.Schmidt-Ott, F.M. Mulder, S.W.H. Eijt, manuscript in preparation.

*The train passes;
how the smoke
swirls round the young leaves!*

Masaoka Shiki, haiku

One of the main disadvantages of using Mg to store hydrogen is the high desorption temperature associated a large negative enthalpy of formation. This is mostly problematic in the scenario that Mg is a store for hydrogen in mobile applications, in combination with *e.g.* a polymer membrane fuel cell which can only operate below 373 K. Also for other applications, whether it is hydrogen detection or stationary hydrogen storage, the slow kinetics of the hydrogenation reaction is a serious limitation.

Throughout this thesis, the slow hydrogen sorption kinetics is addressed in various ways, from nanostructuring to addition of transition metal catalysts and even *in situ* hydrogenation of Mg. All these routes have led to partial alteration of the hydrogen sorption kinetics. The complexity of the samples synthesized by spark discharge generation has led to the elaboration of a multiple reaction rates model described in Chapter 2. The direct implication is that there is a wide range of activation energies from about 55 kJ/molH₂ to well above 180 kJ/molH₂ which in practice means a range of desorption temperatures starting from 400 K up to beyond 700 K. The challenge in this case is to select and stabilize the faster reacting part of the sample that has the lowest reachable activation energy for hydrogen sorption.

In the present chapter, a *single* low activation energy of about 57±4 kJ/molH₂ is observed for Mg-Ti-H_x nanocomposites synthesized by spark discharge generation. The hydrogen desorption temperature for the active part of the material is measured to be about 373 K at a desorption rate of 0.5 K/min and is stable for several hydrogen cycles. On the one hand, the presence of an intimate mixture of Mg and Ti has proven to have a strong effect on the stability of the hydride as presented in Chapter 3, lowering the absolute value of the enthalpy of formation down to 45 kJ/molH₂. On the other hand, the *in situ* hydrogenation of Mg nanoparticles during spark discharge generation has proven to have a strong influence on widening the solubility range of hydrogen in the magnesium lattice and to advance the formation of a metastable hydride as discussed in Chapter 5. When these two synthesis methods: *in situ*

hydrogenation and mixed Mg-Ti spark discharge nanoparticle synthesis - are combined, the result is the *in situ* formation of the metastable fluorite $Mg_yTi_{1-y}H_x$ hydride. This hydride is characterized by fast dehydrogenation kinetics with a correspondingly low activation energy for a large fraction of the stored hydrogen.

In the present chapter, a structural investigation of the Mg-Ti-H spark discharge generated nanocomposites is combined with the analysis of the hydrogen sorption kinetics.

6.2. Experimental section

6.2.1. Synthesis – Spark discharge generation

The precursors for the spark discharge generated nanoparticles are Mg and Ti rods of ~0.6 cm diameter from Sigma Aldrich. The samples are produced using a charging current of 14 mA and 1.5 kV and a frequency of the sparks of 700 Hz. The carrier gas concentration was 50% Ar-50% H_2 and it is provided using two mass flow controllers for a total flow rate of 1 l/min. Before the mixing, the Ar (purity 5.0) and H_2 (purity 5.0) gases are purified further from any remaining H_2O and O_2 content by using two double molecular sieves columns and BTS (Cu(II)O) catalysts. In the following sections, results are presented from three separate similar synthesis batches denoted as batch 1, batch 2 and batch 3. The sample batches are further split into more parts for different analyses and experiments.

6.2.2. Powder X-ray diffraction

The structure of the crystalline samples was investigated by X-ray diffraction using a PANalytical X'Pert PRO diffractometer with a Cu K_α source ($\lambda=1.5415 \text{ \AA}$) operated at 40 kV and 40 mA. The samples were loaded in an Ar filled glovebox in air tight sample holders. The background measured from the single crystal silicon disk and sample holder is subtracted from the X-ray diffraction patterns. (see Appendix A). Rietveld analysis was performed on the measured patterns, using GSAS software ¹.

6.2.3. Infrared spectroscopy

The vibration spectra are recorded using a Platinum Alpha Attenuated Total Reflectance (ATR) infrared spectrometer. The powder sample is mounted on a reflective diamond crystal in direct contact with a mobile pressure applicator without any previous preparation. Spectra are recorded in the range 4000 – 450 cm^{-1} and processed using the OPUS 6.5 software.

6.2.4. Inductive coupled plasma – Atomic emission spectroscopy

Inductive coupled plasma atomic emission spectroscopy (ICP-AES) is measured using a Perkin Elmer Optima 5300 spectrometer. The samples are dissolved in a freshly prepared 'piranha' solution consisting of a 3:1 mixture of sulfuric acid (98%) and hydrogen peroxide (30%). To ensure the complete dissolution of the metallic species, the solutions are heated to 373 K on a heating plate inside a fume hood.

6.2.5. X-ray photoelectron spectroscopy

X-ray photoelectron spectra were measured on a VG EscaLab spectrometer with an X-ray source Mg K α of 1253.6 eV operated at 10 mA and 10 kV. The samples were transferred to the spectrometer via an Ar filled glovebox. Measurements were performed in ultra-high vacuum of 1×10^{-10} mbar. The resulted spectra are analysed using Casa XPS software.

6.2.6. Thermal programmed desorption

Thermal hydrogen desorption is measured in the homebuilt TDS setup HYDRA. Hydrogen is detected using a quadrupole mass spectrometer. The samples are mounted under Ar atmosphere and transported in an air tight stainless steel holder. Hydrogen desorption was performed by applying constant heating rates ranging between 0.5 K/min to 3 K/min and measuring the pressure built up and hydrogen mass spectrometer signal in parallel. The double recording of the process confirms that only hydrogen is released during the measurement. The hydrogen loading experiments comprised of the exposure of the unloaded sample to a pressure of 6 bar H $_2$ (purity 6.0) for 6 hours at 523 K.

6.3. Results and discussion

6.3.1. Structural investigation of the spark discharge generated Mg-Ti-H nanomaterials

In the X-ray diffraction pattern in Figure 6.1, measured on a sample of batch 1, two crystalline phases are identified and fitted: the fluorite type Mg $_y$ Ti $_{1-y}$ H $_x$ hydride and MgO. It is interesting to note the absence of the conventional rutile β -MgH $_2$ or even Mg or Ti metal from the XRD of the as produced sample (see Figure 6.1). This indicates that during the *in situ* synthesis of the hydride, the formation of the fluorite hydride becomes more advantageous.

Indeed, theoretical studies on the stability of the Mg-Ti-H system have indicated that at Ti concentrations above 15 at.%, a cubic Mg $_y$ Ti $_{1-y}$ H $_x$ is thermodynamically more stable than the conventional tetragonal hydride.^{2,3} Cubic Mg $_y$ Ti $_{1-y}$ H $_x$ hydride is isostructural with calcium fluorite, CaF $_2$, and belongs to the $Fm\bar{3}m$ space group. The presence of the fluorite Mg $_y$ Ti $_{1-y}$ H $_x$ for $y > 15$ at. % was reported in thin film research where hydrogen can be cycled at low temperatures^{4,5,6}. A positron lifetime study on Mg-Ti-H thin films suggested that the reason for the low temperature desorption could be related to the increased size of open volume deficiencies in the cubic hydride phase in comparison to the tetragonal one which leads to a higher mobility of hydrogen^{7,8,9}. Alternatively, the availability of empty tetrahedral lattice sites may lead to enhanced interstitial motion of H¹⁰.

In earlier studies, great effort was bestowed upon the synthesis of fluorite Mg $_y$ Ti $_{1-y}$ H $_x$ hydride in powder form with the result that it is possible to obtain it, but without the confinement that the thin films provide, it rapidly phase separates during desorption and absorption cycles and then decays to the conventional titanium hydride next to magnesium^{10,11,12,13,14,15,16}.

In our previous study presented in Chapter 3, the fluorite hydride is formed upon *ex situ* hydrogen exposure of the spark discharge generated cubic Mg-Ti metastable alloy. Here, the hydride is formed *in situ* in the spark discharge generator by using a mixture of 50 %Ar/50 %H₂ carrier gas in the reactor chamber. Using Rietveld refinement, the lattice parameter for the Mg_yTi_{1-y}H_x is found to be 4.46 Å, a slight increase from the 4.44 Å obtained in Chapter 3. The lattice parameter of the cubic structure can vary with both the Mg and H content. The size of the Mg_yTi_{1-y}H_x crystallites is estimated to be about 15 nm using a Scherrer constant of 1¹⁷. Alongside the hydride, MgO is also found in a high fraction (see Table 6.1) with typical crystalline domain sizes of 2 nm. It is known from TEM images of similar spark discharge generated samples (see Chapter 2, 3 and 5) that MgO is present as thin shells around each individual primary particle, which most likely is also the case here.

The low amount of sample of a few mg (~4 mg) and the presence of a high background (see Appendix A) in the X-ray diffractogram make the determination of the alloy composition difficult. However, combining the ICP-AES results of the total Mg/Ti=1.8 ratio to the phase fractions found from Rietveld refinement from Table 6.1 and assuming that no amorphous fraction is present, the composition of Mg_yTi_{1-y}H_x can be estimated to be Mg_{0.64}Ti_{0.36}H_x. As the same result is obtained in the case of two separate batches, we can conclude that the synthesis of the alloy is reproducible.

X-ray diffraction was again measured after seven hydrogen sorption cycles in the homebuilt TPD setup Hydra in both the absorbed and desorbed states. The results are plotted in Figure 6.2. After hydrogen absorption, the XRD is very similar to the as produced sample except for an increase in the MgO fraction (see Figure 6.2a). The lattice parameter of the cubic phase is 4.46 Å,

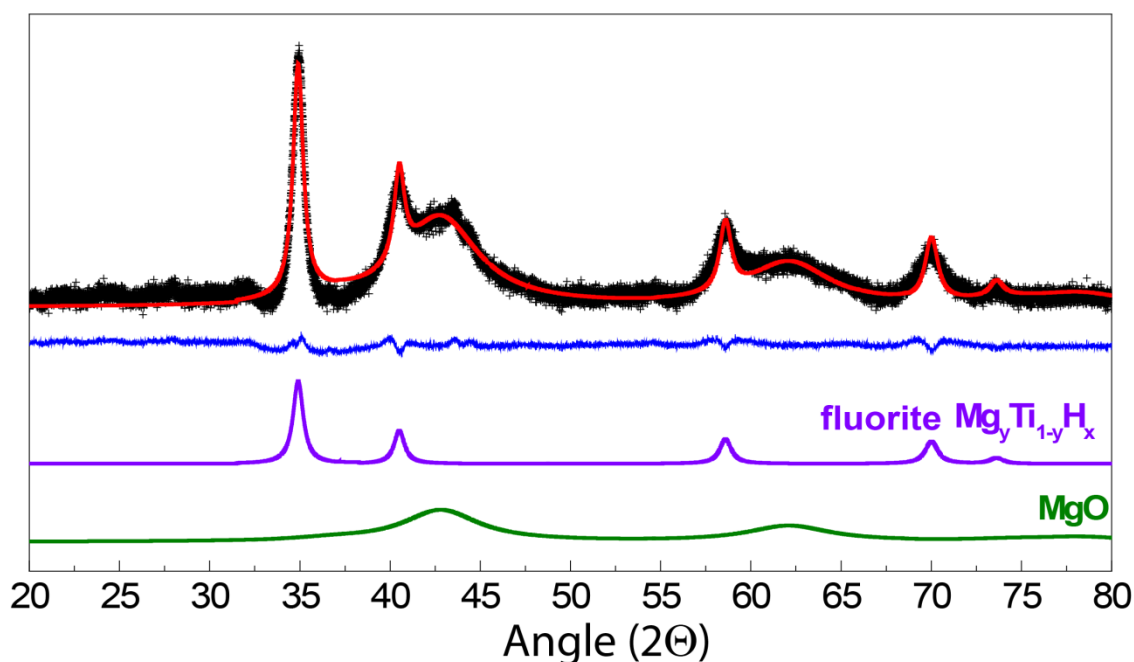


Figure 6.1. X-ray diffraction measurement (open circles) and Rietveld refinement results (fitting – red line, residual–blue line) for as produced spark discharge generated fluorite Mg_yTi_{1-y}H_x, measured on batch 1. The sample container background is subtracted. The individual phase contributions are given below (scaled down by 1/2).

the same as for the as produced sample. This suggests that the same composition as the as produced sample is obtained after hydrogen cycling.

Table 6. 1 Summary of Rietveld refinement results of X-ray diffractograms of Figure 6.1 and 6.2

Phase	Mg-Ti-H nanomaterials					
	As prepared ($R_{wp}=1.7\%$)		After hydrogen absorption ($R_{wp}=1\%$)		After hydrogen desorption ($R_{wp}=1.9\%$)	
	Batch 1		Batch 1		Batch 2	
	Size (nm)	Fraction (wt.%)	Size (nm)	Fraction (wt.%)	Size (nm)	Fraction (wt.%)
$Mg_yTi_{1-y}H_x$ ($Fm\bar{3}m$)	15±1	18	17±1	7	15±1	19
MgO ($Fm\bar{3}m$)	2±0.1	82	3.5±0.1	93	3±0.1	79
β -MgH ₂ ($P4_2/mnm$)	-	-	-	-	-	< 1
TiH ₂ ($Fm\bar{3}m$)	-	-	-	-	-	< 1

The small crystallite size of 15 nm obtained for $Mg_yTi_{1-y}H_x$ after hydrogen sorption experiments is consistent with the observation of small sizes of the Mg-TiH₂ nanocomposites discussed in Chapter 3 where it was argued that TiH₂ present in the sample acts as a grain refiner. Here it is remarkable, however, that the crystalline domains remain that small after cycling. This is unlike the situation in ball milled materials with initially similar crystalline domain sizes. A rationale for these findings may be that the spark discharge generated particles are in principle generated as free particles and form a size confining outer oxide layer around each individual particle when being suspended in the gas stream. In ball milled materials also oxide layers are present, but not around every individual crystalline domain. Then the crystalline domains apparently can grow more easily and demixing of Ti and Mg can occur. Moreover, even among spark discharge samples, in the absence of Ti, particle growth occurs (see Table 2.1). The presence of Ti in the sample is of key importance in keeping the particle size small as it is already observed in Chapter 3.

Combining the elemental analysis results from ICP-AES of a total ratio of Mg/Ti=1.1 and the phase fractions from Table 6.1, the composition can be estimated to $Mg_{0.54}Ti_{0.46}H_x$ after hydrogen desorption. A decrease of the Mg amount in the $Mg_yTi_{1-y}H_x$ from the as produced sample is consistent with an increase in the MgO fraction and the solid solution model for the composition of the fluorite hydride. Upon hydrogen desorption, hardly any rutile β -MgH₂ and TiH₂ are obtained as it can be seen in Figure 6.2b and in Table 6.1. Moreover, the lattice parameter of the fluorite $Mg_yTi_{1-y}H_x$ hydride after

hydrogen desorption is decreased from 4.46Å to 4.43Å. This contraction of the cubic lattice is consistent with hydrogen being released.

Indeed, theoretical studies^{18,19} support that the presence of H in the structure stabilizes the fluorite hydride by preventing the phase separation of the MgH₂ and TiH₂. Hydrogen atoms are trapped on sites at the interface between Mg and Ti with an enthalpy of hydrogenation of -115 kJ/molH₂. Thus, a temperature of minimum 833 K is necessary for this tightly bound hydrogen to spontaneously be released from these sites. As in the present experiments, the maximum temperature that the sample was exposed to was 523 K, it is to be expected that the dehydrogenation is not complete, leaving the TiH₂ associated H in the structure.

From the above, the picture emerges that a large part of the active sample consists of closely arranged MgH₂ and TiH₂ areas in which the TiH₂ does not desorb and forces the MgH₂ in absorbed state or the Mg in desorbed state to remain to crystallize in the cubic structure during the various stages of H sorption.

This can explain why cubic Mg_yTi_{1-y}H_x is still present in the XRD of the sample after desorption. Moreover, in a theoretical study comparing Mg/Ti hydride layered structures with Ti(core)/Mg(shell) hydride structures, Tao et al.¹⁸ distinguished between four different binding energies for hydrogen in the structure with the lowest being H bound in MgH_x (37 kJ/molH₂). Thus, the cubic Mg_yTi_{1-y}H_x hydride acts as a sponge taking up and releasing H₂ at low temperatures from the MgH_x region while part of the H remains in the structure inside TiH₂, stabilizing the cubic structure. In spite of the stepwise dehydrogenation from Mg_yTi_{1-y}H_x, a reversible hydrogen capacity of up to 4.8 wt.% is achievable according to their theoretical model¹⁸.

The small lattice parameter change that results after desorption suggests solid solution like behavior of the cubic Mg_yTi_{1-y}H_x structure upon hydrogen sorption. This is an unusual result when comparing to bulk Mg, but it is more common for Ti and for nanostructured, catalyzed Mg^{20,21}. Since solid solution desorption would not require overcoming significant structural transformation barriers, this would also lead to relatively easy internal hydrogen transport

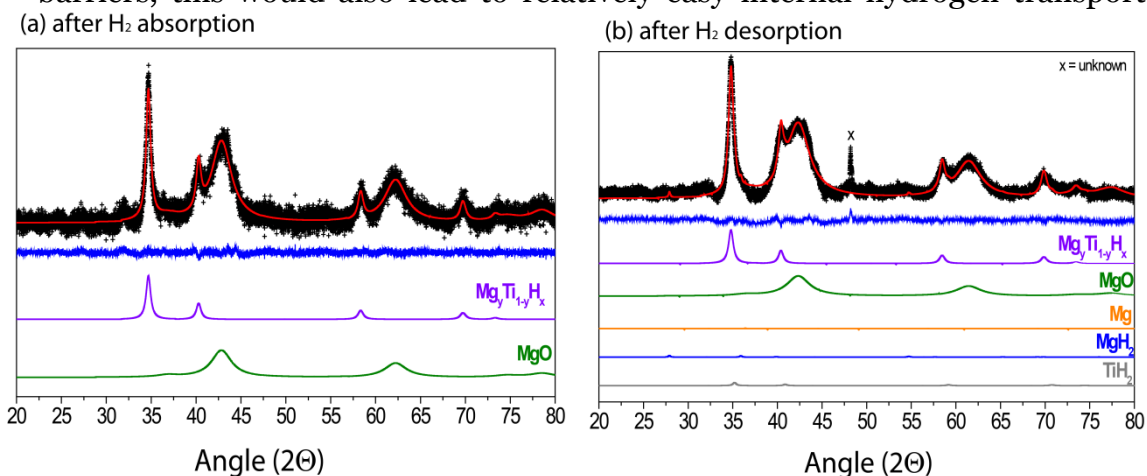


Figure 6.2. X-ray diffraction patterns and results of Rietveld refinement of Mg_yTi_{1-y}H_x (measurement–black, fitting–red, residual–blue) after hydrogen sorption experiments: a. after hydrogen absorption (batch 1); b. after hydrogen desorption (batch 2). Background is subtracted. The individual phase contributions are given below (scaled down by 1/2).

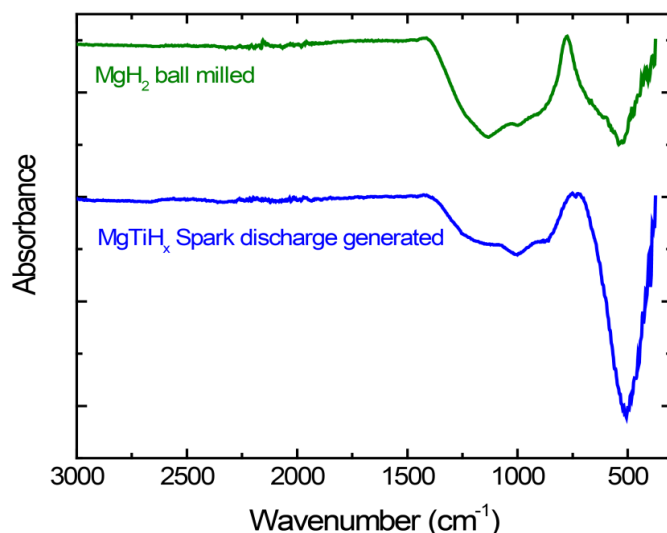


Figure 6.3. Infrared spectra of spark discharge generated $Mg_yTi_{1-y}H_x$ compared to ball milled MgH_2 .

mediated by vacancy diffusion. This can be the reason why hydrogen is released at such low temperatures. If the hydrogen release were to take place with a change in crystal symmetry from cubic hydride to hexagonal metal it would have a higher activation energy difference associated with it, which ultimately would push hydrogen desorption to higher temperatures.

In an experimental study of ball milled fcc $Mg_yTi_{1-y}H_2$, Rousselot et al.^{15,16} also observed that hydrogen can be electrochemically extracted and inserted in the cubic structure without a change in symmetry. However, in electrochemical hydrogen cycling of $Mg_yTi_{1-y}H_x$ thin films, the dehydrogenated state is formed of a metastable hexagonal hcp Mg-Ti intermetallic^{5,22}. In most ball milled $Mg_yTi_{1-y}H_x$ materials, upon a first dehydrogenation, the cubic hydride decomposes to the hexagonal Mg and Ti and it cannot be rehydrogenated to the cubic phase^{11,12,13}. Moreover, theoretical calculations on the stability of the Mg_yTi_{1-y} bulk crystalline intermetallic show that the hcp alloy is more stable than the fcc alloy by about 4 kJ/mol H_2 at $y=0.75$ ³. For the very small limit, the thermodynamic properties nanostructured of the samples studied here will also be altered by surface and interface interactions that are not taken into account in bulk crystalline calculations^{3,18,23}. The unusual behavior of the spark discharge sample can thus be related to nanostructural characteristics of the initial spark discharge material.

The local chemical environment of the Mg and Ti in the sample is probed using infrared spectroscopy and X-ray photoelectron spectroscopy. Indeed, in Figure 6.3, the measured infrared spectrum of the as produced $Mg_yTi_{1-y}H_x$ sample is compared to the spectrum of ball milled MgH_2 . The spectrum of the Mg-Ti-H sample presents two broad bands centered at 1000 cm^{-1} and 504 cm^{-1} .

X-ray photoelectron spectroscopy is used to shed light on the local oxidation states of Mg and Ti present in the sample. The data were analyzed using Casa XPS²⁷ and fitted with a Gaussian-Lorentzian curve shape. A Shirley²⁸ background is subtracted from the graphs plotted in Figure 6.4. The C 1s peak is taken as reference and it is measured at 291 eV. The reference C 1s peak measured here is observed to be shifted by +5 eV compared to the reference C 1s presented in Chapter 4. This implies that in order to compare

the XPS results obtained in this study to the ones presented in Chapter 4, a -5 eV shift has to be taken into account to the measured energies presented in Figure 6.4.

The Mg 2p peak can be fitted using two components, at 57.4 eV and 55.5 eV. If the correction of -5 eV for instrumental shift is taken into consideration, the Mg 2p peaks compare well with the results presented in Chapter 4. The 2 eV shift between the components suggests that Mg is present in two oxidation states. These two contributions to the Mg peak can be attributed to the MgO and metallic Mg or MgH₂. The presence of Mg(OH)₂ can be excluded because it was not observed in the infrared spectrum.

The Mg 2s can also be fitted with two components separated by 3 eV, one at 96.1 eV and the other at 93.1 eV which can be attributed to MgO and Mg metal respectively. The neighborhood of Mg and Ti in sputter deposited films does generally not produce a visible chemical shift in the Mg 2p or Mg 2s peaks as it was already observed in Chapter 4^{19,29}, so in the metallic state these different Mg sites give overlapping signals.

The XPS investigation of the sample in Figure 6.4 revealed that Ti is present in two forms. Due to the spin orbit coupling, the Ti 2p peak is split into two components, Ti 2p_{1/2} and Ti 2p_{3/2} separated by 6 eV. With a correction of 5 eV for the instrumental shift, the peak is present at 465 eV for Ti 2p_{1/2} and 459 eV for Ti 2p_{3/2}. A second Ti component is present with a 4 eV negative shift from the first component. The second component has the Ti 2p_{1/2} peak at 461 eV and the Ti 2p_{3/2} peak at 455 eV. Such a negative shift is expected to appear for metals present in alloys and TiH₂. Assuming that the Ti fraction of the materials remains hydrided throughout all sorption reactions, these two components of Ti can be attributed to TiH₂ on sites near Mg and Ti sites with only Ti nearest neighbors, much like TiH₂. However, there is a considerable overall negative shift of the Ti binding energies that is not observed in XPS on the thin films (see

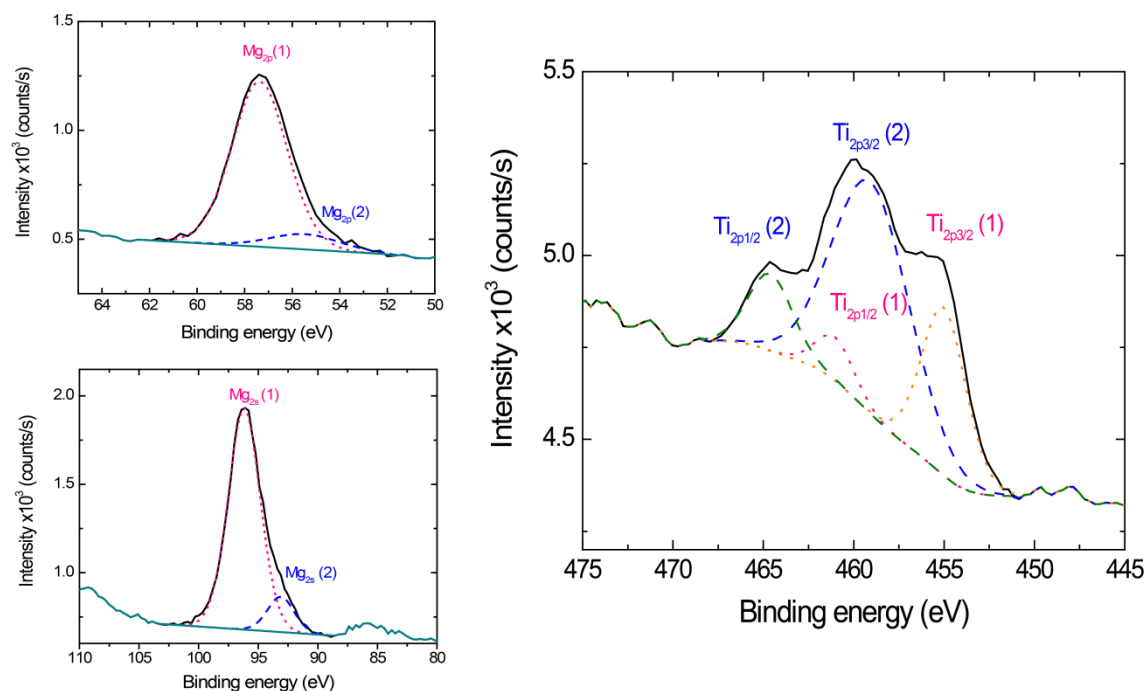


Figure 6.4. X-ray photoelectron spectroscopy measured on batch 3 of as produced Mg_yTi_{1-y}H_x: top left: Mg 2p peak; bottom left: Mg 2s peak; right: Ti 2p

also Chapter 4)³⁰. The reason for this shift can be sought in the nanostructure of the samples and the stronger alloying character of the samples.

Indeed, Olovsson et al.³¹ have calculated the core level chemical shifts for a series of completely random fcc alloys using the complete screening model. This essentially means that the conduction electrons are relaxed when a core hole is created upon the removal of a core electron. The core level shift is then calculated as a difference between the ionization energy of a core electron in an alloy and the ionization energy of the pure element. Depending on the random alloy, the core level chemical shift can be as high as -1.2 eV³¹. For Al₃Ti, the shift is about -0.7 eV³².

One feature of a random alloy is that the local environment of each atom is composed of atoms of the same and the other element. However, EXAFS studies on the cubic Mg_yTi_{1-y}H_x hydride have revealed a certain degree of segregation present in the structure^{33,34}. Therefore, the treatment of the structure as a random combination is not entirely correct as the partial segregation of Mg or MgH₂ from Ti or TiH₂ leads to the creation of interfaces. Moreover, the nanosized character of the spark discharge generated Mg-Ti-H sample leads to high surface to bulk ratio. These effects are expected to produce a negative surface/interface core level shift^{31,35}. Experimentally, this shift was found as high as -1.85 eV for Ti in TiO₂³².

The theoretical predictions of the surface/interface core level shift show that it is only noticeable at a few monolayers of solute according to Olovsson et al.^{31,35} This might explain XPS studies of Mg-Ti alloys in thin films³⁰, including the results discussed in Chapter 4, where the considerable negative shift of 3 eV of the Ti peak was not observed. From these observations, it can be concluded that in the nanoparticulate Mg_yTi_{1-y}H_x phase, there is a higher degree of mixing than present in thin films. In conclusion, the XPS results on Ti 2p photoelectron peak reveal two contributions: Ti in sites with nearby Mg, and Ti with only Ti and H neighbors as in TiH₂.

6.3.2. Kinetic analysis of the hydrogen desorption reaction of spark discharge Mg-Ti-H nanomaterials

Hydrogen desorption profiles are measured at varying heating rates from 0.5 K/min to 4K/min and are plotted in Figure 6.5 for batch 1 and batch 2, respectively. With increase of the heating rate, the desorption peak shifts towards higher temperatures consistent with the model of first order activated reaction kinetics.

It is remarkable that the hydrogen desorption from the Mg_yTi_{1-y}H_x sample occurs in the form of a sharp peak at 373 K. Provided that the sample is not exposed to a temperature higher than 523 K, the desorption peak at 373 K is reproducible over at least seven cycles of hydrogen sorption for both batches (see Figure 6.6). In order to put this result into context, in Table 6.2,

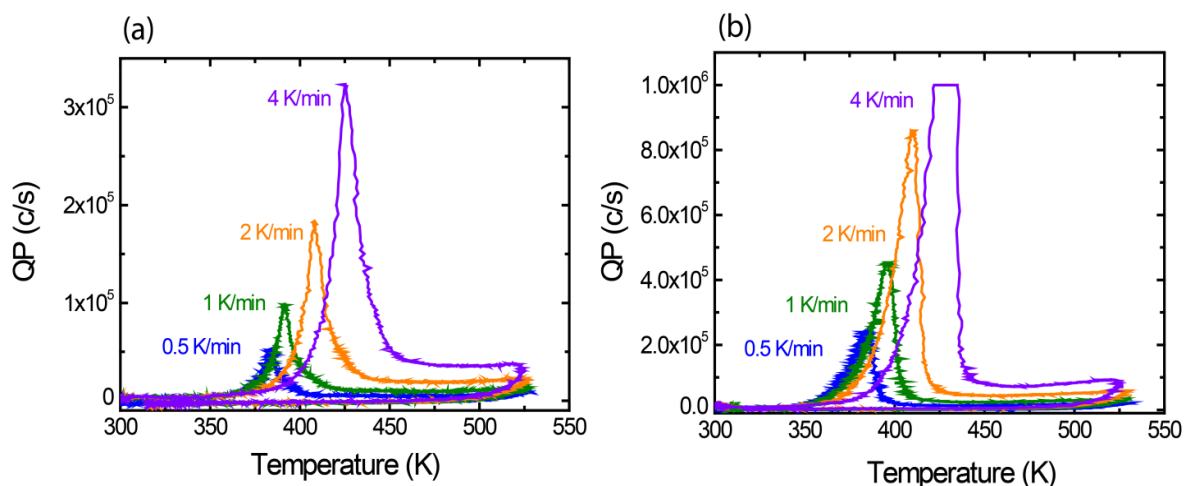


Figure 6.5. Thermal hydrogen desorption profiles of spark discharge generated $Mg_yTi_{1-y}H_x$ measured at varying heating rates: 0.5K/min, 1K/min, 2K/min, 4K/min for a) batch 1 and b) batch 2

the peak desorption temperatures and activation energies obtained from Kissinger analysis (see Figure 6.7) measured for batch 1 and a MgH_2 ball milled sample are compared. A striking difference of about 200 K is immediately evident and also the activation energy is much lower. The remarkable low desorption temperature of the spark discharge sample can be explained by the presence of the fluorite type $Mg_yTi_{1-y}H_x$ hydride that allows faster diffusion of H^{δ} but also by the nanostructure of the sample.^{36,37}

In Figure 6.6, a distinction is made between the amount of hydrogen calculated from the low temperature (373 K) peak attributed to H_2 desorption from $Mg_yTi_{1-y}H_x$ phase and the rest of the spectrum. The high stability of the sample and reproducibility of hydrogen loading and unloading can clearly be seen in the amount of hydrogen desorbed within seven cycles. The lower wt. % calculated for batch 2 in cycle 6 is due to a saturation of the signal that is visible in Figure 6.5b for the 4 K/min desorption curve.

The amount of hydrogen desorbed from the as produced sample is about 0.3 wt % of the total sample weight for the sample from batch 1 and 1.3 wt.% for the sample from batch 2 (see Figure 6.6) as calculated from the low temperature peak. Given the fact that a significant part of the sample weight is inert material, in the form of MgO (see section 6.3.1), the wt. % H_2 desorbed is rather high and corresponds to almost full hydrogenation of the active $Mg_yTi_{1-y}H_x$ phase. The big difference between the wt. % H_2 cycled in batch 1 and batch 2 is directly correlated to the amount of MgO present in the sample. Based on the observed crystalline phases, an estimation was made in which we take into consideration the weight fractions of the active $Mg_yTi_{1-y}H_x$ phase determined from Rietveld refinement (see Table 6.1) and the masses of 4 mg and 5.3 mg for samples from batch 1 and batch 2, respectively. Thus, we find a hydrogen capacity from the low temperature peak per weight of the active part of the sample of 1.5 wt. % and 4.8 wt. % for batch 1 and batch 2 respectively. This result is consistent with the maximum reversible capacity estimated by the theoretical model of Tao et al.¹⁸ and discussed in section 6.3.1.

The activation energy for the system is determined using the Kissinger analysis method which is described in more detail in Chapter 2. The peak temperatures and heating rates extracted from Figure 6.5 and summarized in

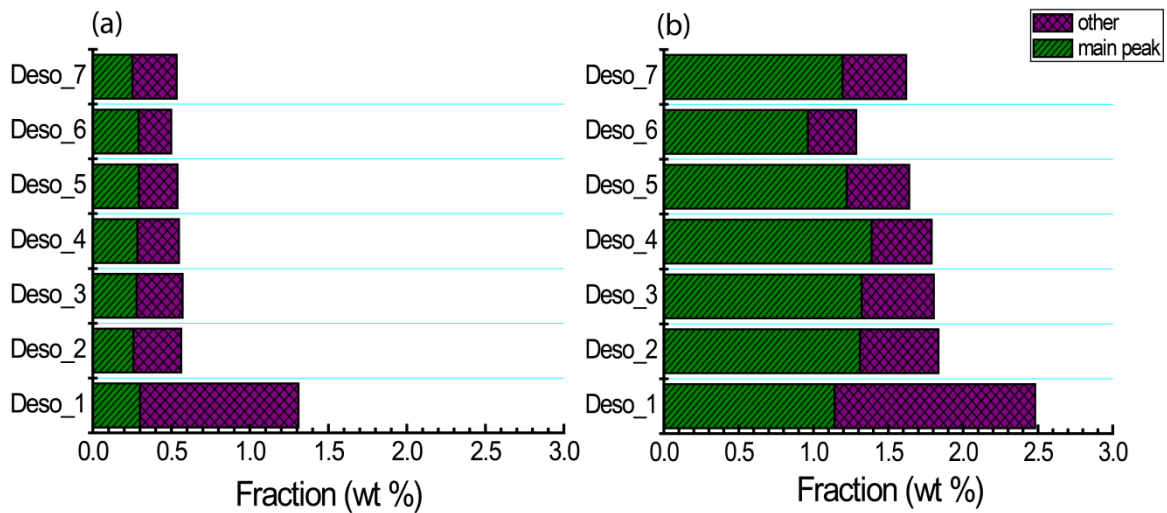


Figure 6.6. Total weight fractions of desorbed hydrogen from $Mg_yTi_{1-y}H_x$ calculated from the main desorption peak at 373 K and other contributions for a) batch 1 and b) batch 2.

Table 6.2 are used to construct the Kissinger plot from Figure 6.7. The activation energy for the desorption reaction is calculated from the slope of the Kissinger plot and it is found to be $57 \pm 3 \text{ kJ/molH}_2$ for sample 1 and $58 \pm 6 \text{ kJ/molH}_2$ for sample 2. The almost identical results obtained for two separate samples synthesized in two batches indicate that the synthesis of the sample is highly reproducible.

The hydrogen desorption reaction can be described using a single reaction constant and, as indicated by the Kissinger analysis, a single activation energy for the main peak; therefore it can be concluded that this active part of the sample is homogeneous. The active phase is the fluorite $Mg_yTi_{1-y}H_x$ because this is the main hydrogen containing phase in the material, and other options like pure $\beta\text{-MgH}_2$ or TiH_2 would have desorption temperatures above the ones observed. The other contributions indicated in Figure 6.6 stem from the higher temperature broad desorption signal that arises in Figure 6.5 as a foot on the right hand side of the main peak. This signal is still attributed to the cubic $Mg_yTi_{1-y}H_x$ phase but then to better bound H sites that are having more Ti in the local environment.

In Table 6.2, a considerable difference between the activation energy of $145 \pm 5 \text{ kJ/molH}_2$ for the ball milled MgH_2 and only $57 \pm 3 \text{ kJ/molH}_2$ for the $Mg_yTi_{1-y}H_x$ nanoparticles is obvious. The typical activation energy values obtained for pure ball milled MgH_2 vary between $140\text{--}210 \text{ kJ/molH}_2$ ^{38,39,40} However, Lu et al.^{41,42} have determined a low activation energy of 58.4 kJ/molH_2 for ball milled $MgH_2\text{-}TiH_2$ nanocomposites. The hydrogen desorption in their case occurred at temperatures starting from 473 K.

Table 6. 2. Comparison of peak desorption temperatures at different heating rates and activation energies between $Mg\text{-}Ti\text{-}H$ spark discharge sample 1 and MgH_2 ball milled sample.

Sample	Desorption Peak Temperature (K)				Activation Energy (kJ/molH ₂)
	0.5 K/min	1 K/min	2 K/min	4 K/min	
$Mg_yTi_{1-y}H_x$ (Spark discharge)	383 ±3	391±4	408±2	425±2	57±3
MgH_2 (Ball mill)	582±5	589±2	600±2	608±1	145±5

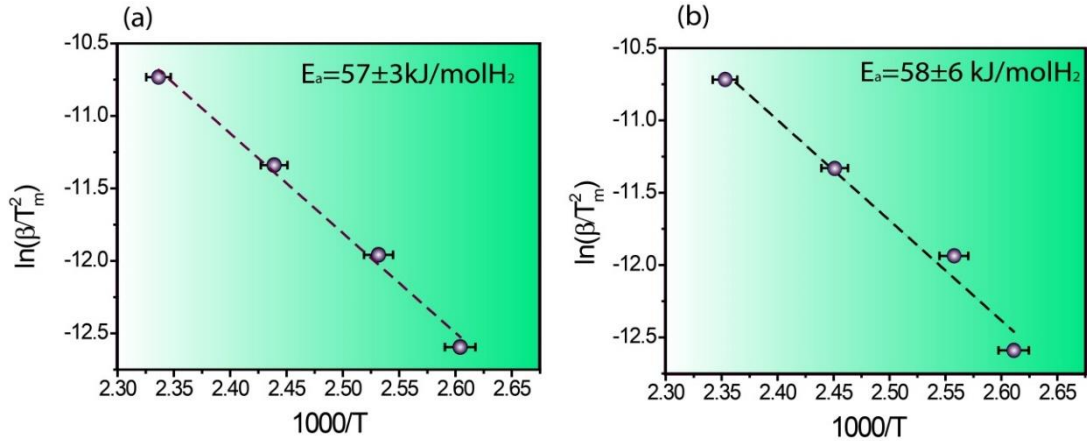


Figure 6.7. Kissinger plots obtained from thermal desorption of hydrogen from spark discharge generated $Mg_yTi_{1-y}H_x$: a) batch 1 and b) batch 2

treatment does not exceed 523 K. But as it is well known and it has been discussed in detail in the course of this thesis (see Chapter 3, Chapter 4), both the intermetallic Mg_yTi_{1-y} and the hydride $Mg_yTi_{1-y}H_x$ are essentially metastable phases. Thus, at sufficiently high temperatures these compounds are expected to decay within the time of the experiment to the lowest energy state which, thermodynamically speaking are hcp Mg and Ti for the metallic state and β -MgH₂ and TiH₂ for the hydride state. In Figure 6.8, three thermal desorption spectra are presented for $Mg_yTi_{1-y}H_x$ collected from the same batch as sample 1 (Figure 6.5a) in an extended temperature range 300 -650 K. In the first desorption run, most of the hydrogen is released at 364 K, similar to the result in Figure 6.5a and a small peak can be distinguished at 581 K. At the third desorption cycle, the low temperature desorption peak shifts to 400 K and loses intensity. At the same time, the high temperature peak at 581 K gains intensity but also more desorption peaks appear between 400 K and 581 K. After seven cycles, the low temperature peak has nearly completely disappeared as it can barely be distinguished at 412 K. This high temperature experiment verifies the hypothesis that the cubic $Mg_yTi_{1-y}H_x$ is in fact a metastable state and the loss of the low temperature desorption peak within seven cycles is the evidence for it.

The high stability of the sample and its homogeneous dehydrogenation kinetics are supported by various experiments provided that the heating

6.4. Conclusions

Using spark discharge generation of Mg and Ti in hydrogen atmosphere, a nanosized fluorite $Mg_yTi_{1-y}H_x$ phase is synthesized *in situ* as observed from XRD.

The nanosized character of the sample and atomic scale mixing of the Mg and Ti elements have a strong effect on the X-ray photoelectron peaks of Ti causing a 3 eV negative shift. XPS also provided evidence for the formation of Mg-Ti-H hydride phase by *in situ* spark discharge generation.

Hydrogen is inserted and released from the sample without a change in symmetry of the cubic $Mg_yTi_{1-y}H_x$. Hydrogen thermal desorption profiles are measured at different heating rates up to a temperature of 523 K. Sharp hydrogen desorption peaks around 373 K are measured, corresponding to

hydrogen released from the MgH_x areas of the sample, leaving TiH_2 areas to stabilize the cubic hydride structure. The activation energy is found to be 57 kJ/mol H_2 from Kissinger analysis and an effective hydrogen capacity of about 4.8 wt % of active sample is estimated.

These results together with the hydrogen cycling stability of the sample, make the *in situ* spark discharge generated $\text{Mg}_y\text{Ti}_{1-y}\text{H}_x$ nanoparticles a very interesting and promising material for hydrogen storage applications.

References

- (1) Toby, B. H. EXPGUI, a Graphical User Interface for GSAS. *J. Appl. Cryst.* 2001, *34*, 210-213.
- (2) Er, S.; de Wijs, G. A.; Brocks, G. Tuning the Hydrogen Storage in Magnesium Alloys. *J. Phys. Chem. Lett.* 2010, *1*, 1982-1986.
- (3) Er, S.; Tiwari, D.; de Wijs, G. A.; Brocks, G. Tunable Hydrogen Storage in Magnesium transition Metal Compounds: First-Principles Calculations. *Phys. Rev. B* 2009, *79*, 024105.
- (4) Vermeulen, P.; Niessen, R. A. H.; Borsa, D. M.; Dam, B.; Griessen, R.; Notten, P. H. L. Effect of the Deposition Technique on the Metallurgy and Hydrogen Storage Characteristics of Metastable Mg_yTi_{1-y} Thin Films. *Electrochemical and Solid-State Letters* 2006, *9*, A520-A523.
- (5) Borsa, D. M.; Baldi, A.; Pasturel, M.; Schreuders, H.; Dam, B.; Griessen, R.; Vermeulen, P.; Notten, P. H. L. Mg--Ti--H Thin Films for Smart Solar Collectors. *Applied Physics Letters* 2006, *88*, 241910-241913.
- (6) Borsa, D. M.; Gremaud, R.; Baldi, A.; Schreuders, H.; Rector, J. H.; Kooi, B.; Vermeulen, P.; Notten, P. H. L.; Dam, B.; Griessen, R. Structural, Optical, and Electrical Properties of Mg_yTi_(1-y)H_xthin Films. *Phys. Rev. B* 2007, *75*, 205408.
- (7) Leegwater, H.; Schut, H.; Egger, W.; Baldi, A.; Dam, B.; Eijt, S. W. H. Divacancies and the Hydrogenation of Mg-Ti Films With Short Range Chemical Order. *Applied Physics Letters* 2010, *96*, 121902-121903.
- (8) Eijt, S. W. H.; Leegwater, H.; Schut, H.; Anastasopol, A.; Egger, W.; Ravelli, L.; Hugenschmidt, C.; Dam, B. Layer-Resolved Study of the Mg to MgH₂ Transformation in Mg-Ti Films With Short-Range Chemical Order. *Journal of Alloys and Compounds* .
- (9) Eijt, S. W. H.; Kind, R.; Singh, S.; Schut, H.; Legerstee, W. J.; Hendrikx, R. W. A.; Svetchnikov, V. L.; Westerwaal, R. J.; Dam, B. Positron Depth Profiling of the Structural and Electronic Structure Transformations of Hydrogenated Mg-Based Thin Films. *J. Appl. Phys.* 2009, *105*, 043514-13.
- (10) Srinivasan, S.; Magusin, P. C. M. M.; van Santen, R. A.; Notten, P. H. L.; Schreuders, H.; Dam, B. Siting and Mobility of Deuterium Absorbed in Cosputtered Mg_{0.65}Ti_{0.35}. A MAS 2H NMR Study. *J. Phys. Chem. C* 2010, *115*, 288-297.
- (11) Asano, K.; Enoki, H.; Akiba, E. Synthesis of HCP, FCC and BCC Structure Alloys in the Mg-Ti Binary System by Means of Ball Milling. *Journal of Alloys and Compounds* 2009, *480*, 558-563.

- (12) Asano, K.; Enoki, H.; Akiba, E. Synthesis of Mg-Ti FCC Hydrides From Mg-Ti BCC Alloys. *Journal of Alloys and Compounds* 2009, 478, 117-120.
- (13) Asano, K.; Enoki, H.; Akiba, E. Synthesis Process of Mg-Ti BCC Alloys by Means of Ball Milling. *Journal of Alloys and Compounds* 2009, 486, 115-123.
- (14) Zheng, S.; Fang; Zhang, J.; Sun, L.; He, B.; Wei, S.; Chen, G.; Sun, D. Study of the Correlation Between the Stability of Mg-Based Hydride and the Ti-Containing Agent. *J. Phys. Chem. C* 2007, 111, 14021-14025.
- (15) Rousselot, S.; Bichat, M. P.; Guay, D.; Roué, L. Structure and Electrochemical Behaviour of Metastable Mg₅₀Ti₅₀ Alloy Prepared by Ball Milling. *Journal of Power Sources* 2008, 175, 621-624.
- (16) Rousselot, S.; Guay, D.; Roué, L. Synthesis of Fcc Mg–Ti–H Alloys by High Energy Ball Milling: Structure and Electrochemical Hydrogen Storage Properties. *Journal of Power Sources* 2010, 195, 4370-4374.
- (17) Langford, J. I.; Wilson, A. J. C. Scherrer After Sixty Years: A Survey and Some New Results in the Determination of Crystallite Size. *J. Appl. Cryst.* 1978, 11, 102-113.
- (18) Tao, S. X.; Notten, P. H. L.; van Santen, R. A.; Jansen, A. P. J. First-Principles Predictions of Potential Hydrogen Storage Materials: Nanosized Ti(Core)/Mg(Shell) Hydrides. *Phys. Rev. B* 2011, 83, 195403.
- (19) Jensen, I. J. T.; Diplas, S.; Løwik, O. M. Hydrogen Induced Stabilization of Meta-Stable Mg-Ti. *Applied Physics Letters* 2012, 100.
- (20) Mulder, F. M.; Singh, S.; Bolhuis, S.; Eijt, S. W. H. Extended Solubility Limits and Nanograin Refinement in Ti/Zr Fluoride-Catalyzed MgH₂. *J. Phys. Chem. C* 2011, 116, 2001-2012.
- (21) Grzech, A.; Lafont, U.; Magusin, P. C. M. M.; Mulder, F. M. Microscopic Study of TiF₃ As Hydrogen Storage Catalyst for MgH₂. *Journal of Physical Chemistry C* 2012, 116, 26027-26035.
- (22) Baldi, A.; Gremaud, R.; Borsa, D. M.; Balde, C. P.; van der Eerden, A. M. J.; Kruijtzter, G. L.; de Jongh, P. E.; Dam, B.; Griessen, R. Nanoscale Composition Modulations in Mg_yTi_{1-y}H_x Thin Film Alloys for Hydrogen Storage. *International Journal of Hydrogen Energy* 2009, 34, 1450-1457.
- (23) Schimmel, H. G.; Kearley, G. J.; Huot, J.; Mulder, F. M. Hydrogen Diffusion in Magnesium Metal (Phase) Studied by Ab Initio Computer Simulations. *Journal of Alloys and Compounds* 2005, 404-406, 235-237.

- (24) Santisteban, J. R.; Cuello, G. J.; Dawidowski, J.; Fainstein, A.; Peretti, H. A.; Ivanov, A.; Bermejo, F. J. Vibrational Spectrum of Magnesium Hydride. *Phys. Rev. B* 2000, *62*, 37-40.
- (25) Moser, D.; Bull, D. J.; Sato, T.; Noreus, D.; Kyoji, D.; Sakai, T.; Kitamura, N.; Yusa, H.; Taniguchi, T.; Kalisvaart, W. P.; Notten, P. Structure and Stability of High Pressure Synthesized Mg-TM Hydrides (TM = Ti, Zr, Hf, V, Nb and Ta) As Possible New Hydrogen Rich Hydrides for Hydrogen Storage. *J. Mater. Chem.* 2009, *19*, 8150-8161.
- (26) Farangis, B.; Nachimuthu, P.; Richardson, T. J.; Slack, J. L.; Meyer, B. K.; Perera, R. C. C.; Rubin, M. D. Structural and Electronic Properties of Magnesium – Transition Metal Switchable Mirrors. *Solid State Ionics* 2003, *165*, 309-314.
- (27) Fairly, N.; Carrick, A. The Casa Cookbook. Part 1: Recipes for XPS Data Processing. 1. 2005. Knutsford, Cheshire, UK, Acolyte Science.
- (28) Shirley, D. A. High-Resolution X-Ray Photoemission Spectrum of the Valence Bands of Gold. *Phys. Rev. B* 1972, *5*, 4709-4714.
- (29) Jensen, I. J. T.; Lowik, O. M.; Schreuders, H.; Dam, B.; Diplas, S. Combined XPS and First Principle Study of Metastable Mg–Ti Thin Films. *Surf. Interface Anal.* 2012, *44*, 986-988.
- (30) Jensen, I. J. T.; Løwik, O. M.; Schreuders, H.; Dam, B.; Diplas, S. Combined XPS and First Principle Study of Metastable Mg–Ti Thin Films. *Surf. Interface Anal.* 2012, *44*, 986-988.
- (31) Olovsson, W.; Goransson, C.; Purovskii, L. V.; Johansson, B.; Abrikosov, I. A. Core-Level Shifts in Fcc Random Alloys: A First-Principles Approach. *Phys. Rev. B* 2005, *72*, 064203.
- (32) NIST XPS Database <http://srdata.nist.gov/xps/> (2013). 2013.
- (33) Baldi, A. "Magnesium and Titanium: The Odd Couple". 2013. Ipskamp Drukkers B.V.
- (34) Baldi, A.; Pálsson, G. K.; Gonzalez-Silveira, M.; Schreuders, H.; Slaman, M.; Rector, J. H.; Krishnan, G.; Kooji, B. J.; Walker, G. S.; Fay, M. W.; Hjørvarsson, B.; Wijngaarden, R. J.; Dam, B.; Griessen, R. Mg/Ti Multilayers: Structural and Hydrogen Absorption Properties. *Phys. Rev. B* 2010, *81*, 224203.
- (35) Olovsson, W.; Holmstrom, E.; Marten, T.; Abrikosov, I. A.; Niklasson, A. M. N. Interface Core-Level Shifts As a Probe of Embedded Thin-Film Quality. *Phys. Rev. B* 2011, *84*, 085431.
- (36) Cansizoglu, M.; Karabacak, T. Enhanced Hydrogen Storage Properties of Magnesium Nanotrees With Nanoleaves. *MRS Online Proceedings Library* 2009, *1216*, null.

- (37) Jeon, K. J.; Theodore, A.; Wu, C. Y. Enhanced Hydrogen Absorption Kinetics for Hydrogen Storage Using Mg Flakes As Compared to Conventional Spherical Powders. *Journal of Power Sources* 2008, *183*, 693-700.
- (38) Fernández, J. F.; Sánchez, C. R. Rate Determining Step in the Absorption and Desorption of Hydrogen by Magnesium. *Journal of Alloys and Compounds* 2002, *340*, 189-198.
- (39) Varin, R. A.; Jang, M.; Czujko, T.; Wronski, Z. S. The Effect of Ball Milling Under Hydrogen and Argon on the Desorption Properties of MgH₂ Covered With a Layer of Mg(OH)₂. *Journal of Alloys and Compounds* 2010, *493*, L29-L32.
- (40) Liang, G.; Huot, J.; Boily, S.; Schulz, R. Hydrogen Desorption Kinetics of a Mechanically Milled MgH₂+5at.%V Nanocomposite. *Journal of Alloys and Compounds* 2000, *305*, 239-245.
- (41) Lu, J.; Choi, Y. J.; Fang, Z. Z.; Sohn, H. Y.; Rönnebro, E. Hydrogenation of Nanocrystalline Mg at Room Temperature in the Presence of TiH₂. *J. Am. Chem. Soc.* 2010, *132*, 6616-6617.
- (42) Lu, J.; Choi, Y. J.; Fang, Z. Z.; Sohn, H. Y.; Ronnebro, E. Hydrogen Storage Properties of Nanosized MgH₂-0.1TiH₂ Prepared by Ultrahigh-Energy High-Pressure Milling. *J. Am. Chem. Soc.* 2009, *131*, 15843-15852.

Chapter 7

Towards air resistant sulfur coated MgH₂ powders



Abstract

Exposed to air, MgH_2 forms a $Mg(OH)_2$ coating which deactivates the Mg involved directly. In addition, during hydrogen sorption it will be reduced to the more stable MgO that increases the activation energy for hydrogen release from MgH_2 and dramatically hinders the hydrogen sorption reaction.

The air sensitivity of MgH_2 particles is addressed by creating a sulfur coating on the surface of MgH_2 particles in ball milled samples. The coating is formed by an evaporation condensation method. Samples are prepared from mixtures containing 20 wt% S and 5 wt% MgH_2 .

Nanostructured samples prepared in this way can be exposed to air for a week without observing major structural and compositional changes as XRD, IR and SEM studies confirm. Moreover, hydrogen sorption of the air exposed sulfur coated samples presents the same desorption profiles as freshly ball milled MgH_2 .

Energy filtered TEM mapping confirmed the sulfur to be on the surface of the MgH_2 ball milled particles. The activation energy of the sulfur coated samples determined using Kissinger analysis is of the same magnitude as ball milled MgH_2 , $\sim 150\text{kJ/molH}_2$. Pressure composition isotherms are similar to those of uncoated ball milled MgH_2 .

This chapter is based on the manuscript:

“Air resistant sulfur coated MgH_2 ” Anca Anastasopol, Joost Middelkoop, Ugo Lafont, S.W.H. Eijt, Fokko M. Mulder, manuscript in preparation.

“...she had never before seen a rabbit with either a waistcoat-pocket, or a watch to take out of it, and burning with curiosity, she ran across the field after it, and fortunately was just in time to see it pop down a large rabbit-hole under the hedge. In another moment down went Alice after it, never once considering how in the world she was to get out again.”

Lewis Carroll, “Alice's Adventures in Wonderland”

The high air sensitivity of the Mg / MgH₂ system makes its manipulation delicate and is one of the main disadvantages in its applicability as a hydrogen storage medium. In contact with air, thin MgO and Mg(OH)₂ layers form at the surface of the Mg/ MgH₂ particles. The MgO shells are generally characterized by a high structural strength and inflexibility and they do not enable the flexible and seamless coverage during expansion and shrinkage of magnesium upon cycling between MgH₂ and Mg.

In Chapter 2 and Chapter 5, the very high air sensitivity of Mg and MgH₂ that results into thin oxide shells are limiting factors in the kinetics of hydrogen sorption and also in reaching the full hydrogen binding capacity of the materials.

Numerous studies addressed and attempted to reduce the oxidation of Mg.^{1,7,8,9,10} Surface oxidation of Mg can be circumvented by embedding them into a polymer matrix^{7,8} or creating a surface coating^{11,12}. This method has a two fold advantage, firstly it provides confinement for the Mg or MgH₂ and secondly it protects against formation of MgO and Mg(OH)₂. In certain cases, nanoconfinement leads to the enhancement of hydrogen sorption reaction rate.⁷ It comes, however, at the cost of the decrease in the energy density of the system because the added polymer fraction constitutes a considerable inert fraction in the system. Thus, the solution of protecting Mg (by nanoconfinement) in high quantities of inert material is in that sense not practically or economically viable, especially in mobile applications where low amounts of passive additives would be preferred.

In this study we propose an alternative route to create air resistant MgH₂ samples. The method consists of creating a thin sulfur layer on the surface of the MgH₂ nanoparticles. As both sulfur and oxygen are placed in group VIa (16) of the periodic system, they share the same number of valence electrons and in general they present similar chemical reactivity.^{13,14} Exposing the freshly prepared MgH₂ sample to S, it creates a layer potentially containing Mg-S-O-H that is in competition with environmental H₂O and O₂

that otherwise would react with the surface. *A priori* it is also possible that such layer is more flexible or soft, which enables that it follows the shape of the nanoparticles and a good coverage can be achieved. In this way, a passivating sulfur coating could prevent the surface oxidation.

The interaction of sulfur with oxidized metal surfaces has been the subject of intensive research since the 1980's and it is known as the "sulfur effect". In both theoretical and experimental studies of Al_2O_3 forming alloys (e.g. Fe-Cr-Al, Ni-Cr-Al), a segregation of sulfur at the metal oxide interface occurs at high temperatures.^{15,16,17,18} It has as effect the weakening and even breaking of the metal-oxygen bonds. The reason for this behavior stems from the fundamental electronic and ionic size differences between oxygen and sulfur as explained below.

As Schaumann¹⁴ puts it, "sulfur is more than the fat brother of oxygen" and this implies that replacing O with S creates differences in the chemistry of the surface. This is immediately apparent from the difference in Pauling electronegativities that is 2.58 for S and 3.44 for O which translates into different electron affinities and ionization potentials for the two elements. Moreover, the bigger atomic radius of S (105 pm) compared to O (70.2 pm) and the difference in electronic affinities make sulfur compounds less polarizable and with a stronger covalent character than the oxygen compounds.

In the present context of limiting the oxide formation at the surface of MgH_2 , the "sulfur effect" is desirable because - as will be shown here for the first time - it makes Mg a more robust and practical storage material for hydrogen. Moreover, sulfur is the 13th most abundant element found in the earth's crust, more abundant than even carbon.¹³ It can be found freely available at the surface in volcanic areas and it is one of the main by-products of the oil industry. Therefore, the embedding of low amounts of passivated, non volatile, sulfur into an energy storage system has great potential of being economically viable.

A study on sulfur coating of the surface of MgH_2 is presented in the present chapter. As a study case for the influence of sulfur on the air resistance and hydrogen storage properties of MgH_2 , ball milled synthesis of nanostructured powders is used. In the following sections, the structure of the MgH_2/S systems is analyzed before and after exposure to air. A main finding is that sulfur acts as an effective inhibitor of the surface oxidation of Mg.

7.2. Experimental section

7.2.1. Synthesis – Ball milling MgH_2

A Fritsch Pulverisette 6 planetary monomill was used to prepare MgH_2 nanocrystalline powders. As starting material, commercial MgH_2 from Sigma Aldrich, 99.9%, spectroscopy grade was loaded in a stainless steel container together with 32 stainless steel balls of 10 mm diameter in an Ar filled glovebox. The powder was ball milled at 400 rpm for 1 h in cycles of 15 min milling and 15 min pause.

The ball milled MgH_2 powder was unloaded from the ball mill inside a Ar filled glovebox. The powder was weighed and mixed with 20 wt% and 5 wt% of Sulfur from Sigma Aldrich in a stainless steel container. The container was sealed and mounted on a heating plate inside the glovebox. The powder

mixture was heated to 423 K for a period of 16h under magnetic stirring. After the heating treatment, the sample is left to cool at ambient temperature and then removed from the container.

7.2.2. Powder X-ray diffraction

The structure of the crystalline samples was investigated by X-ray diffraction using a PANalytical X'Pert PRO diffractometer with a Cu K α ($\lambda=1.5415$ Å) operated at 40 kV and 40 mA. The as prepared samples were loaded in an Ar filled glovebox in air tight sample holders while the air exposed samples were loaded in air. However, for comparison reasons, after one week exposure to air, the samples were stored in a glovebox. The background measured from the silicon disk and sample holder is subtracted from the X-ray diffraction patterns. Rietveld analysis was performed on the measured patterns, using the GSAS software¹⁹.

7.2.3. Transmission electron microscopy

Transmission electron microscopy (TEM), and energy filtered transmission electron mapping (EFTEM) at the sulfur K edge were performed using a FEI Tecnai TF20 electron microscope operated at 200 kV. Energy filtered TEM is a technique that allows quantitative elemental mapping using inelastically scattered electrons emitted from the atomic core shells.²⁰ Samples were mounted on Quantifoil® microgrid carbon polymer supported on a copper grid.

7.2.4. Scanning electron microscopy

Scanning electron microscopy is performed using a Jeol JSM-840A microscope with an acceleration voltage of 5kV. Element analysis topography is performed with an EDX Tracor attachment. Elemental mapping is measured using the K edge energies of O, Mg and S.

7.2.5. Infrared spectroscopy

The vibration spectra are recorded using a Fourier transform Bruker Vertex 70 infrared spectrometer. The powder sample is pressed in between KBr windows in a hand held press and mounted on the spectrometer sample holder. Prior to the measurements, the surface adsorbed water is removed by flushing with nitrogen gas. Spectra are recorded in the range 4000 – 450cm⁻¹ and processed using the OPUS 6.5 software.

7.2.6. Thermal desorption spectroscopy

Thermal hydrogen desorption is measured in a homebuilt TDS setup (Hydra). Hydrogen is detected using a quadrupole mass spectrometer. The samples are mounted under Ar atmosphere and transported in an air tight stainless steel holder. Hydrogen desorption was performed by applying constant heating rate ranging between 0.5K/min to 3K/min and measuring the pressure built up and mass spectrometer signal in parallel. The double recording of the process enables one to verify that no other species than hydrogen are released during the measurement. The hydrogen loading

experiments consisted in exposing the unloaded sample to a pressure of 6 bar H₂ (purity 6.0) for 6 hours at 523K.

7.2.7. Sieverts measurements

Hydrogen absorption isotherms at 523K and 573K were measured using a commercial Sieverts' apparatus, PCT Pro 2000 by Hy-Energy. For the measurements, hydrogen gas of purity 5.0 was used. The accuracy of the pressure reading is 1%. For the setup, a dry scroll pump was used with a base pressure at the inlet of $5 \cdot 10^{-2}$ mbar. Pressure composition isotherms were measured with the use of the Autoclave sample holder and the typical size of the aliquot was 0.663ml.

7.3. Results and discussion

7.3.1. Structural characterization of sulfur coated MgH₂

The structure and composition of the sulfur coated ball milled MgH₂ powders are investigated by X-ray diffraction. In Figure 7.1, the measurements and results of Rietveld refinement are presented for samples coated with 20 wt. % S and 5 wt. % S.

The most prominent crystalline phase present in both samples is the rutile β -MgH₂ and represents 65 wt. % of the MgH₂/20 wt. % S sample and 69 wt. % of the MgH₂/5wt. % S sample (see Table 7.1) The size of the crystallites calculated with the Scherrer formula is about 10 to 16 nm. A small fraction of γ -MgH₂ is present in both samples. γ -MgH₂ is an orthorhombic structure that crystallizes in the *Pbcn* space group. It is essentially a distorted structure from the tetragonal β -MgH₂ typically observed after ball milling.^{21,22,23} The fraction of MgO is very small and it corresponds to large crystallites of about 100 nm. It is different than the spark discharge generated samples where as shown in Chapter 2, 3, 5 and 6, MgO is present as 2 nm thick shell around the particles.^{1,2} In the diffractograms of Figure 7.1, the absence of crystalline Mg(OH)₂ is notable.

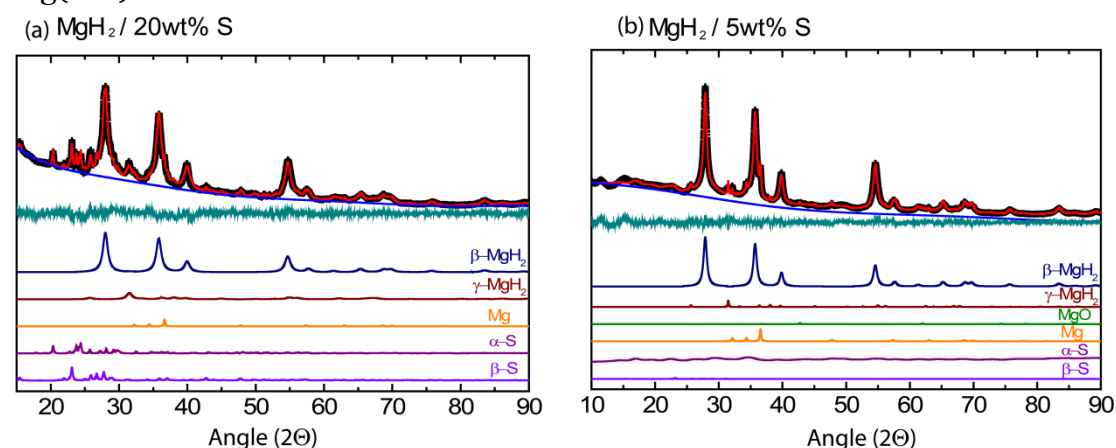


Figure 7.1. X-ray diffraction spectra and Rietveld refinement (measurement spectra – black, calculated spectra – red, residual – blue) for as-prepared ball milled a) MgH₂/20 wt% S and b) MgH₂/5 wt% S. The individual phase contributions are given below

Sulfur has the most complex phase diagram of all the elements due to its many molecular and allotropic forms. In normal conditions of temperature and pressure, S is present as a cyclic molecule formed of eight sulfur atoms. In the solid form it presents many allotropic forms, of which two are more predominant: α -S, an orthorhombic structure belonging to the space group $Fddd$ and β -S, a monoclinic structure belonging to the $P2_1/c$ space group. At about 368 K, orthorhombic sulfur is transformed into monoclinic sulfur which melts at 392 K. In the low pressure regime sulfur can sublime gaseous cycloocta S_8 molecules. An important point in the phase diagram of S occurs at 432 K when the cycloocta molecules begin to break down and form polymeric chains. During the formation of the sulfur coating on the surface of Mg particles, the temperature does not exceed 423 K.²⁴ Upon condensation of the cycloocta sulfur vapors, both orthorhombic and monoclinic sulfur allotropes can be obtained.^{24,25} The monoclinic structure eventually decays to the more stable orthorhombic structure.

For the 20 wt. % S sample, the X-ray diffractogram of Figure 7.1a shows that some of the S is present in two allotropic states: about half of the total sulfur crystallizes as orthorhombic α -S and the other half as monoclinic β -S. The size of the crystallites is found to be between 40 and 60 nm. It can be concluded that for the 20 wt.% samples S is present as a rather thick layer around the particles or clustered on the surface, enabling reaction with the particle surface. In view of the limited amount of S added thick layers of S may however indicate that not all surface area is covered by it. This model is confirmed by electron microscopy characterization of the morphology and

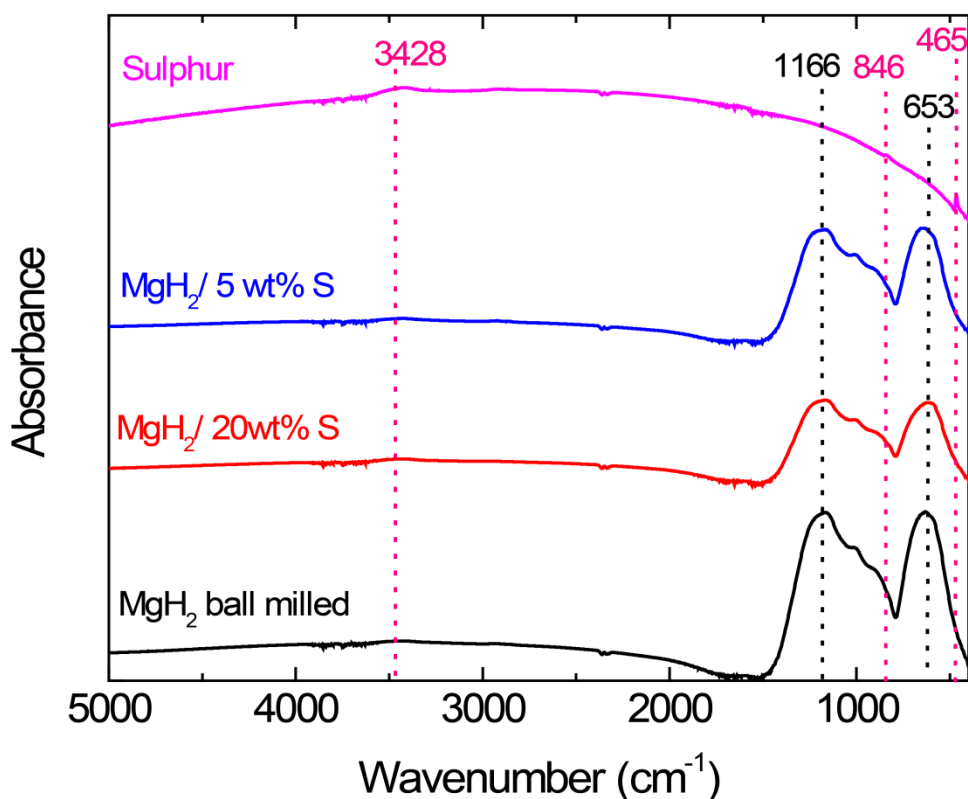


Figure 7.2 Infrared spectra of as-prepared ball milled MgH_2 , $\text{MgH}_2/20\text{wt}\% \text{ S}$, $\text{MgH}_2/5\text{wt}\% \text{ S}$ and S.

elemental composition of the samples (see section 7.3.2)

For the 5 wt. % S sample, in the diffractogram of Figure 7.1b, sulfur is also present in two crystalline states, but the dominant one is the monoclinic β -S. The X-ray diffraction peaks are wider, corresponding to crystallites as small as 5 nm. This observation is consistent to the formation of a sulfur thin coating on the surface of MgH_2 nanoparticles (see section 7.3.2).

Infrared spectra in Figure 7.2 support the structural information obtained from X-ray diffraction. The main contributions are two broad vibration bands which correspond to a stretching mode of MgH_2 centered at 1166 cm^{-1} and a bending mode of MgH_2 at 653 cm^{-1} . As elemental S presents absorption bands in the UV-vis region, no trace of it can be seen in the infrared spectrum. However, MgSO_4 presents distinctive infrared absorption bands ranging from 500 to 1180 cm^{-1} which are not distinguished in the spectra of Figure 7.2.²⁶ This observation is consistent with the results obtained from XRD. The infrared spectrum of MgS is highly dependent on the texture of the compound. The typical absorption spectrum of MgS spherical particles presents four characteristic bands at 248 , 324 , 370 and 400 cm^{-1} and a small broad band at 538 cm^{-1} which will strongly shift to the far infrared region for needle like particles and be outside the measurement range in Figure 7.2. Thus, the presence of nanocrystalline or amorphous MgS at the surface of MgH_2 particles cannot be excluded.

7.3.2. Structural investigation of air exposed sulfur coated MgH_2

The sulfur coated MgH_2 samples are subsequently exposed to air for a period of one week in order to test the hypothesis that the sulfur layer will prevent oxidation. In Figure 7.3, the X-ray diffractograms of the air exposed samples are plotted together with the results of the Rietveld refinement. The results are striking in the sense that only very small traces of MgO can be detected in the sulfur coated samples. The main crystalline phase in both samples is the tetragonal β - MgH_2 amounting to 54 wt. % and 65 wt. % for the $\text{MgH}_2/20\text{ wt. \% S}$ and $\text{MgH}_2/5\text{ wt. \% S}$ samples respectively.

In the sample that contains a larger S fraction and larger crystallites ($\text{MgH}_2/20\text{ wt. \% S}$) the presence of a small amount of about 12 wt. % nanocrystalline $\text{Mg}(\text{OH})_2$ is observed after air exposure in Figure 7.3a. It can

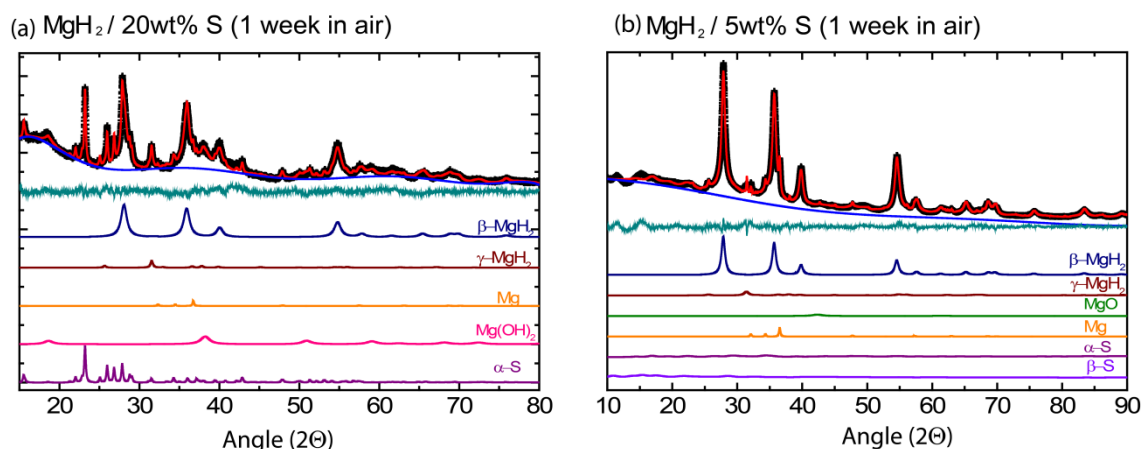


Figure 7.3. X ray diffraction spectra and Rietveld refinement (measurement spectra – black, calculated spectra – red, residual – blue) for a) $\text{MgH}_2/20\text{ wt}\% \text{ S}$ and b) $\text{MgH}_2/5\text{ wt}\% \text{ S}$ after exposure to air for 1 week. The individual phase contributions are given below (scaled down by $1/2$).

also be seen that all monoclinic β -S transformed in the more stable orthorhombic α -S. The enthalpy of transformation is about -0.4 kJ/mol S.²⁵

In contrast, in the sample that contains a lower amount of S in the form of 5 nm crystallites, plotted in Figure 7.3b, no $\text{Mg}(\text{OH})_2$ could be fitted. Moreover, S is still present in two crystalline states but the predominant form is β -S.

For comparison, a pure ball milled MgH_2 sample was also exposed to air for a period of one week. The results obtained in the structure evolution of this sample contrast strongly to the sulfur coated MgH_2 samples. In Figure 7.4, the X-ray diffractograms of the ball milled MgH_2 are plotted together with the results of the Rietveld refinement. The XRD of the freshly ball milled sample is compared to the XRD of the air exposed sample. It can clearly be seen that the air exposed sample is heavily oxidized as $\text{Mg}(\text{OH})_2$ is the dominant phase in the spectrum. Because the crystallite size of $\text{Mg}(\text{OH})_2$ is about 4-5 nm, it can be modeled as a growing layer on the surface of MgH_2 . Thus, the oxidation proceeds through a growing shell mechanism. The reason for the incomplete oxidation of ball milled MgH_2 stems from the sample morphology that is characterized by a wide range of particle sizes from a few hundred nanometers to a few micrometers as it can be seen in the electron microscope images in Figures 7.6-7.9. Thus, the bigger particles will take longer to completely oxidize.

It is known that in the presence of even a few monolayers $\text{Mg}(\text{OH})_2$ on the surface of MgH_2 , the hydrogen desorption activation energy is significantly increased.²¹ Moreover, during the heating treatments, $\text{Mg}(\text{OH})_2$ can be reduced to the more stable MgO which also increases the activation barrier for hydrogen sorption.^{21,27}

Among the sulfur coated samples, the one with 20 wt. % S presents a small fraction of $\text{Mg}(\text{OH})_2$ after exposure to air. The sample coated with 5 wt. % S does not form any crystalline $\text{Mg}(\text{OH})_2$. This will indicate that materials preparation can still be optimized and that only 5 wt. % or less S is required to obtain a passivation of the sample surface.

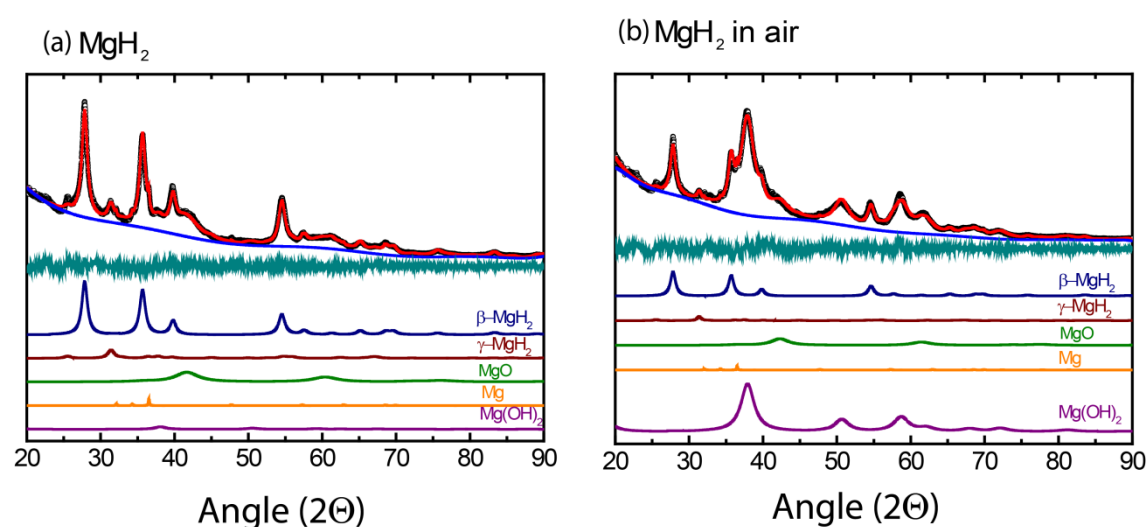


Figure 7.4. X-ray diffraction spectra and Rietveld refinement (measurement spectra – black, calculated spectra – red, residual – blue) results for a) MgH_2 freshly ball milled and b) MgH_2 exposed to air for 1 week. The individual phase contributions are given below (scaled down by $1/2$).

Table 7.1. Crystallite sizes and weight fractions extracted from Rietveld refinement results for the diffractograms plotted in Figure 7.1, Figure 7.3 and Figure 7.4.

Phase	Freshly prepared						After exposure to air					
	MgH ₂ /20wt% S (R _{wp} =3.5%)		MgH ₂ /5wt% S (R _{wp} =4%)		MgH ₂ (R _{wp} =4%)		MgH ₂ /20wt% S (R _{wp} =5.6%)		MgH ₂ /5wt% S (R _{wp} =4%)		MgH ₂ (R _{wp} =7%)	
	Size (nm)	Fraction (wt.%)	Size (nm)	Fraction (wt.%)	Size (nm)	Fraction (wt.%)	Size (nm)	Fraction (wt.%)	Size (nm)	Fraction (wt.%)	Size (nm)	Fraction (wt.%)
β-MgH₂	11	65	16	69.2	11	58.7	11	54	16	65	13	10.9
γ-MgH₂	10	8	83	2	9	8.2	32	4.3	14	6.3	9	8.7
Mg	78	2	63	4.8	130	0.9	94	1.7	54	4.3	139	0.6
α-S	39	13	51	0.5	-	-	58	28	10	0.8	-	-
β-S	61	12	5	23.3	-	-	-	-	6	13.6	-	-
Mg(OH)₂	-	-	-	-	6	4.5	7	12	-	-	5	71
MgO	-	-	92	0.2	3	27.7	-	-	4	10	3	8.7

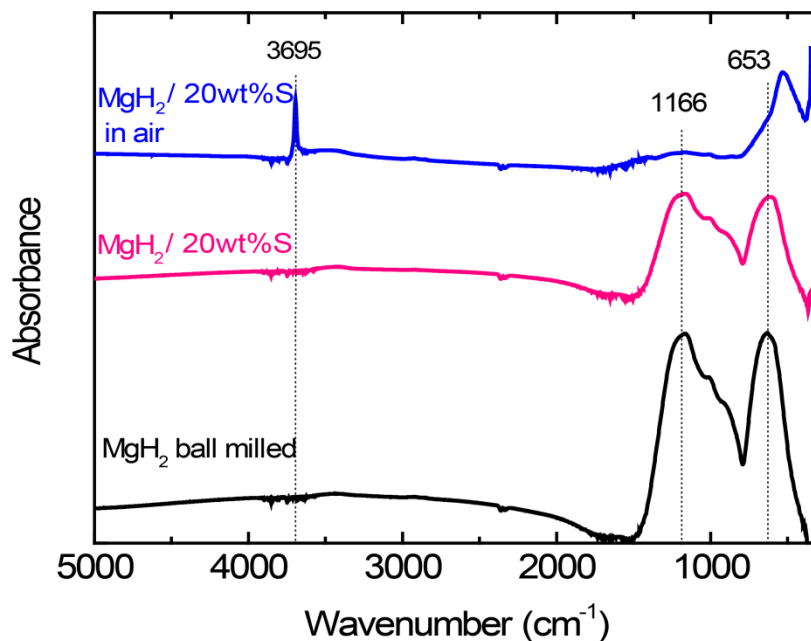


Figure 7.5 Infrared spectra of ball milled MgH_2 , $MgH_2/20wt\%S$ and $MgH_2/20wt\%$ exposed to air for one week (bottom to top)

Infrared spectroscopy is highly sensitive to the vibrations of $-OH$ groups. Thus, the presence of $Mg(OH)_2$ can be detected even when it is present in the form of an amorphous thin layer on the surface of MgH_2 . Four active IR modes are known for $Mg(OH)_2$: one internal mode, one rotational lattice mode and two translational lattice modes. The internal mode is represented by a sharp band corresponding to a stretching vibration at 3671 cm^{-1} . The lattice mode region is below 1000 cm^{-1} and contains the rotational lattice vibration at 310 cm^{-1} , and two translational lattice modes are merged into a broad band centered at 462 cm^{-1} .^{28,29} In the measurement of Figure 7.5 we focus on the internal modes region. A narrow and intense vibration band is measured at 3695 cm^{-1} for the sample containing 20 wt. % S that was exposed to air for one week.

This band corresponds to the internal stretching mode of $-OH$ in $Mg(OH)_2$. Another broad band centered at 500 cm^{-1} can be attributed to the translation lattice vibrations. Also, a very small intensity broad band centered at 1166 cm^{-1} can be linked to the presence of MgH_2 .

The absence of the $-OH$ vibration bands from the samples that were not exposed to air confirm the lack of oxidation of the initial samples, as is supported also by the XRD results. This suggests that the initial sulfur coating is formed on a pure MgH_2 surface.

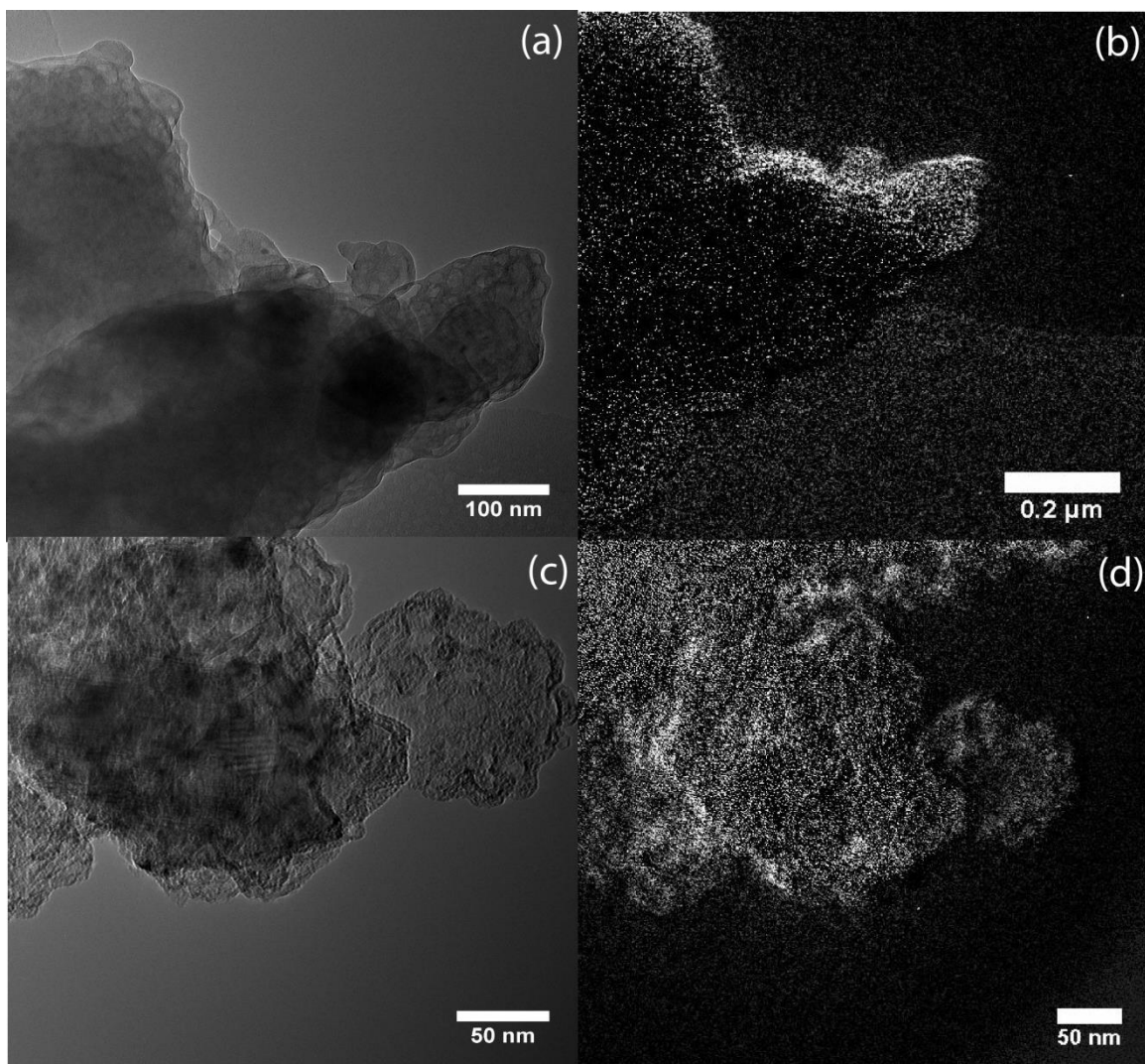


Figure 7.6. Morphology and sulfur coverage of $MgH_2/20wt\%S$: a) TEM image of air exposed $MgH_2/20wt\%S$, b) EFTEM image at the S edge of air exposed $MgH_2/20 wt\% S$, c) TEM image of $MgH_2/20wt\% S$ after hydrogen desorption, d) EFTEM image at the S edge of $MgH_2/20wt\%S$ after hydrogen desorption

From the analysis of the X-ray diffraction spectra of the $MgH_2/20 wt. \% S$ the crystallite size for sulfur is in the order of 50 nm. In order to find out the morphology of the sample and whether sulfur forms a coating around the particles, transmission electron microscopy is used. Energy filtered TEM at the sulfur edge is used to locate sulfur in the sample.

In Figure 7.6a, the TEM image of the air exposed $MgH_2/20 wt. \% S$ sample is presented. Particles of the order of a few hundred nanometers can be distinguished in the image. On the surface of the particles, a thin layer can be observed which using energy filtered TEM can be identified as containing mostly S (see Figure 7.6b). The layer thickness can be estimated to be between 20-50 nm.

This result compares well with the size of the sulfur crystallites that was found from the Rietveld refinement of X-ray diffractograms (see Table 7.1)

In Figure 7.6c, a TEM image of the $\text{MgH}_2/20\text{wt. \% S}$ after hydrogen desorption can be seen. As during hydrogen desorption, the sample is exposed to temperatures as high as 650 K, an increase of the crystallinity is expected. In the TEM image, sharper crystal edges and crystal fringes are now observed. A higher sulfur coverage can be observed at the surface of the particles in Figure 7.6d compared to the Figure 7.6b. Thus, after hydrogen desorption and exposure to air, the sulfur coating is still present. However, the high temperature treatments that the sample was exposed to may have changed the form in which sulfur is present on the surface. Already at 432 K, the cycloocta S_8 molecules start to polymerize into S_n chains. The polymerization reaction is photosensitive and the length of the S_n chains depends on the temperature that the system is subjected to. The polymeric S chains are arranged into double helical structures which present very different physical and chemical properties to the cyclooctan molecules.

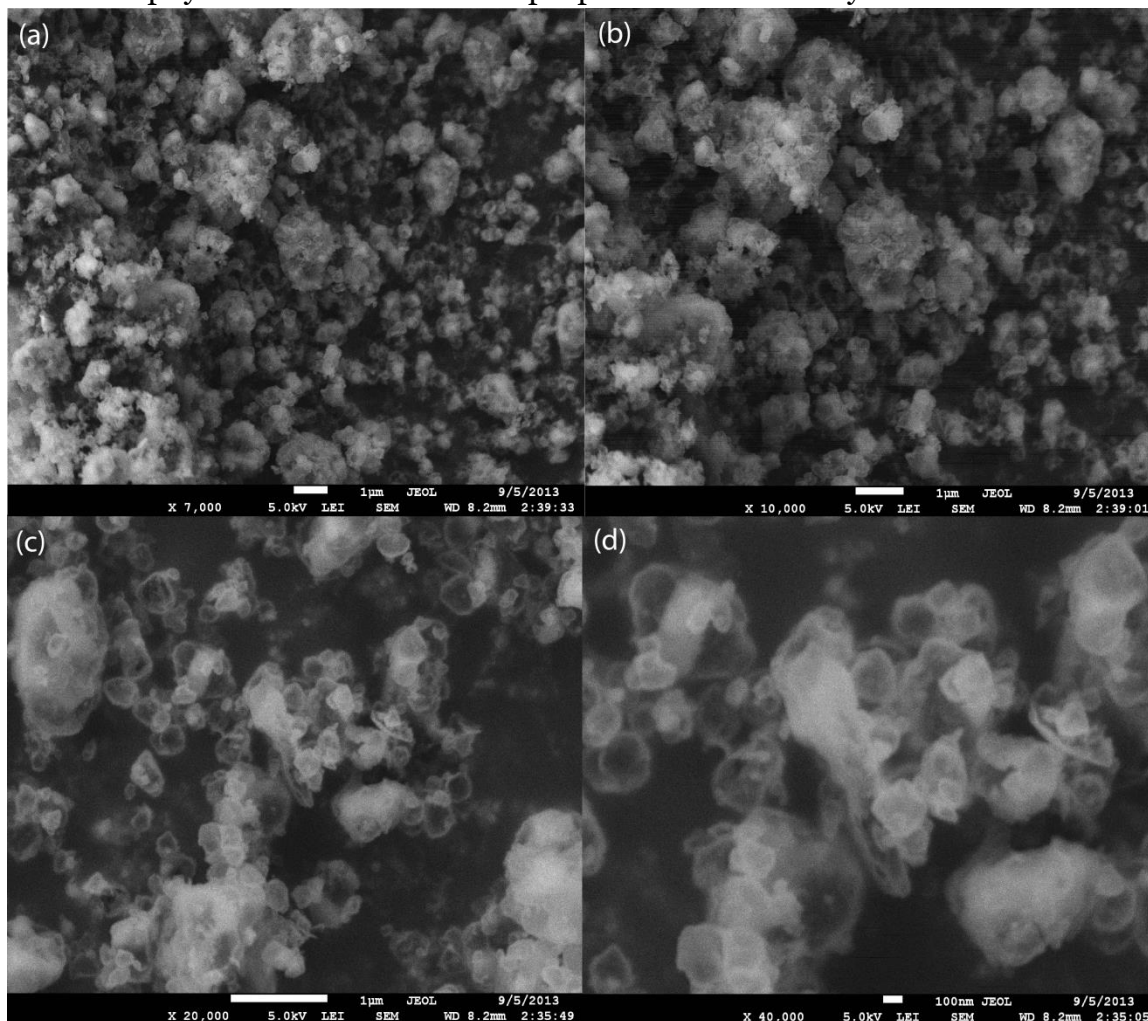


Figure 7.7. Scanning electron images of air exposed $\text{MgH}_2/20\text{ wt}\% \text{ S}$ at increasing magnification: a) $\times 7\,000$, b) $\times 10\,000$, c) $\times 20\,000$ and d) $\times 40\,000$.

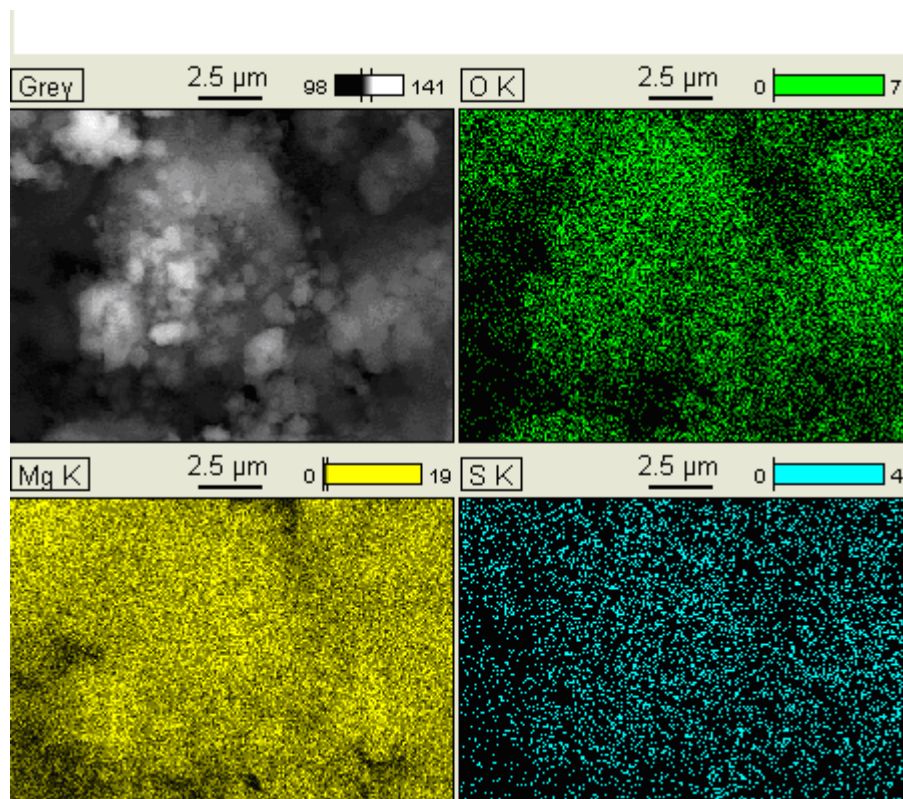


Figure 7.8. Scanning electron micrograph and corresponding energy dispersive spectroscopy elemental mapping for O, Mg and S K shells of air exposed $MgH_2/20wt\%S$ after desorption

However, in time, these structures decay to the conventional orthorhombic α -S, as is also observed in XRD (see Table 7.1).^{13,24,25,30}

In order to characterize the morphology of the samples on a larger scale than TEM permits, scanning electron images (SEM) of the desorbed sample are recorded and presented in Figure 7.7. The shape of the particles appears to be almost spherical. A thin surface layer can be distinguished in Figures 7.7 c and d which can be attributed to the presence of sulfur on the surface.

In order to determine whether the coating is indeed sulfur, energy dispersive spectroscopy (EDX) is used to identify the elements present on the surface of the sample. In Figure 7.8, a surface of from the desorbed sample is imaged at the K shell of oxygen, magnesium and sulfur. The signal from Mg is the most intense. The signal from O is also intense enough that the contours of the image can be followed. It was calculated that the K shell ionization cross section for oxygen upon electron impact is , about 5 times smaller than that of magnesium and sulfur.^{31,32} Thus, the intense signal from oxygen must be measured from the outmost surface of the sample. This observation is in good agreement with the results obtained from both XRD and IR that a thin $Mg(OH)_2$ coating is formed on the surface of $MgH_2/20 wt\% S$ exposed to air for one week.

The signal from sulfur is much weaker than that for magnesium or oxygen. However, as the electron impact K shell ionization cross sections for magnesium and sulfur are almost the same, , we can conclude that the signal from sulfur

originates from the subsurface. 32,33 Indeed, from both XRD and EFTEM we know that a sulfur coating is present on the samples before being exposed to air. The fact that $\text{Mg}(\text{OH})_2$ still forms during air exposure is indicative of the fact that the sulfur coating is not very compact. Also when subjected to high temperatures during desorption it allows Mg to migrate through the sulfur layer to the surface and form a thin layer of $\text{Mg}(\text{OH})_2$. Thus, although scanning electron images indicate that the sulfur coating surrounds uniformly the ball milled MgH_2 particles of varying sizes the coverage is not completely preventing reactions with moisture or air.

The same EDX elemental mapping is measured on an undesorbed $\text{MgH}_2/20\text{wt.}\%$ after exposure to air and presented in Figure 7.9. In this case, the magnesium signal seems to be less intense. This result is not surprising since the sample was previously coated with S without being exposed to high temperatures during synthesis, the mobility of the Mg atoms is reduced, so the $\text{Mg}(\text{OH})_2$ surface coating can be less.

In Figure 7.10, TEM images of the air exposed $\text{MgH}_2/5 \text{ wt.}\% \text{ S}$ are presented. A thin sulfur coating surrounds the particles uniformly. The thickness of the sulfur shell in Figure 7.10. is estimated to be about $\sim 5 \text{ nm}$. This result is in good agreement with the $\alpha\text{-S}$ crystallite size determined from XRD (see Table 7.1). The much better coverage in this case is reflected in the substantially larger

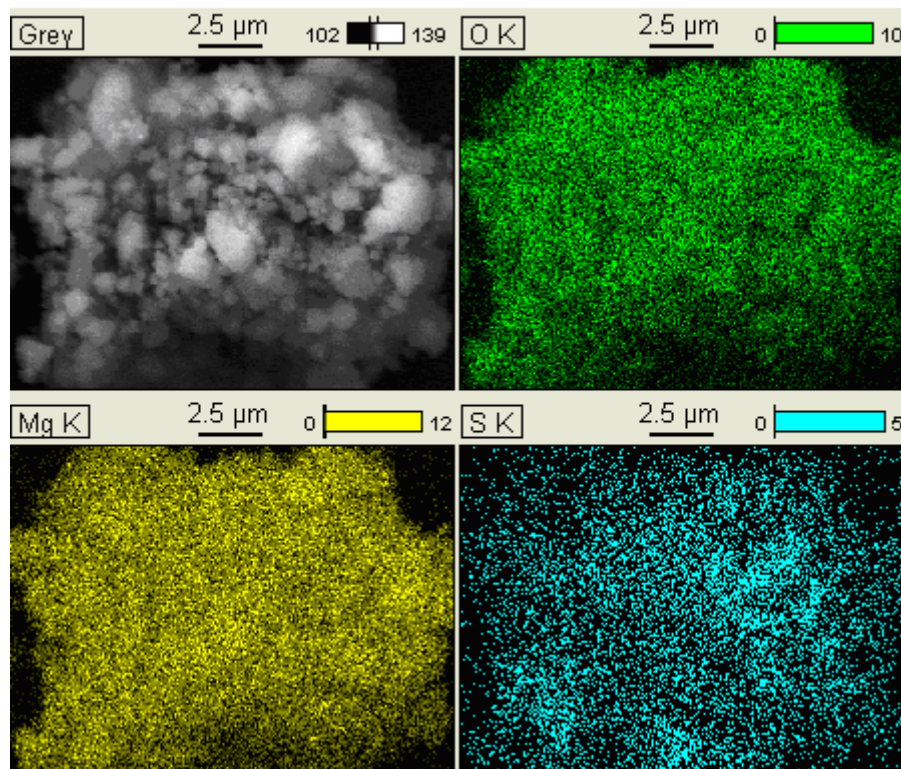


Figure 7.9. Scanning electron micrograph and corresponding energy dispersive spectroscopy elemental mapping for O, Mg and S of air exposed $\text{MgH}_2/20\text{wt.}\% \text{ S}$

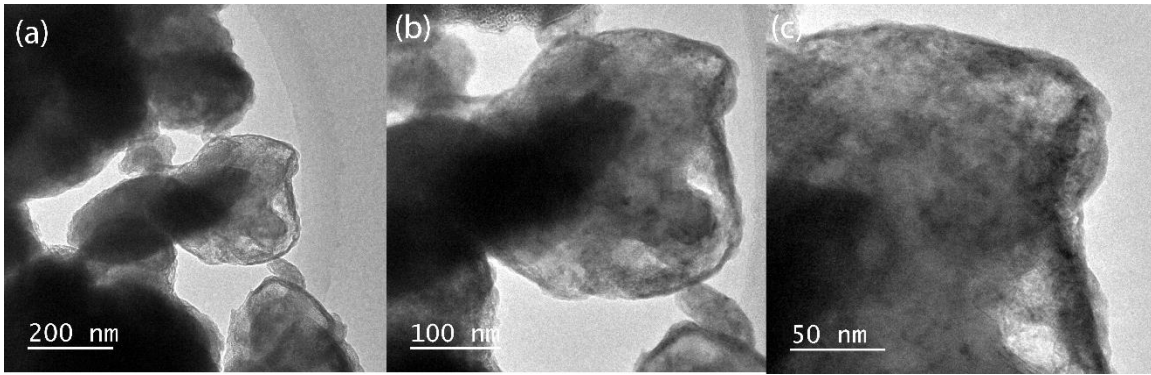


Figure 7.10. Transmission electron micrographs of air exposed $MgH_2/5wt.\%S$

air resistance and improved hydrogen sorption properties.

7.3.3. Hydrogen sorption properties of sulfur coated MgH_2

Hydrogen sorption characteristics of the sulfur coated samples are investigated using thermal programmed desorption. A heating treatment is applied to the samples at constant heating rates and the released hydrogen is detected using a quadrupole mass spectrometer. In Figure 7.11, the thermal desorption profiles of $MgH_2/20 wt.\%S$ and $MgH_2/5wt.\% S$ are plotted as a function of increasing heating rate.

At a heating rate of 0.5 K/min, hydrogen is released from the sample in a sharp peak that has the maximum at about 575 K. This desorption temperature is typical for ball milled MgH_2 samples^{23,34,35} (see Chapter 6), suggesting that S does not have a visible effect on the hydrogen desorption kinetics.

It is observed that the desorption temperature during first cycle is higher, about 590 K. However, after the first cycle the sample stabilizes and the variation in the peak desorption temperature is not more than 3 K. The first higher value of desorption temperature can be attributed to an activation of the sample.^{34,36,36}

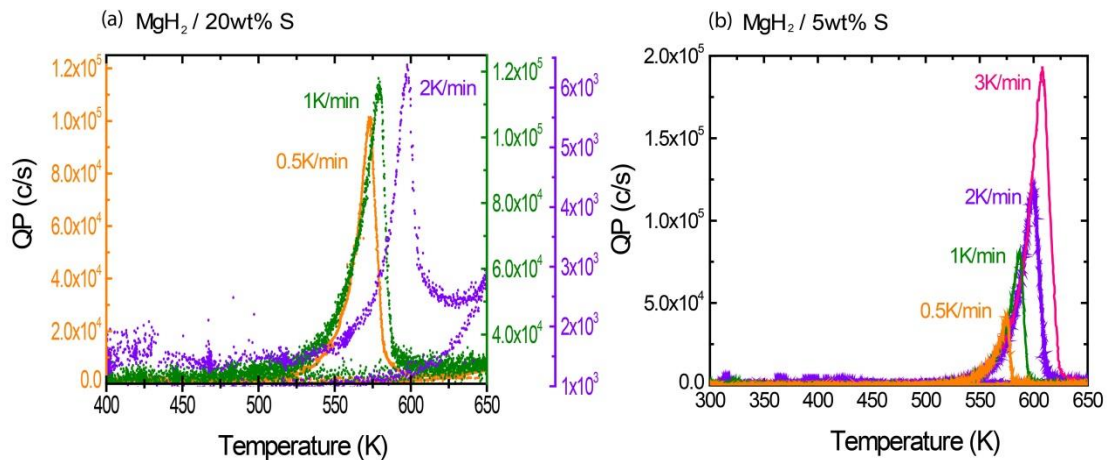


Figure 7.11. Thermal programmed desorption profiles at different heating rates for a) $MgH_2/20wt\% S$, b) $MgH_2/5wt\% S$.

In the case of first order reaction kinetics of a reaction that has an activation barrier as it is generally the case for the hydrogen desorption from MgH_2 , increasing the heating rate for the desorption causes the maximum desorption peak temperature to shift towards higher values. This can be used to determine the height of the activation energy barrier by the Kissinger analysis which is discussed in more detail in Chapter 2.^{1,21,37,38,39,40,41,42,43}

In Figure 7.12, the Kissinger plots of the $\text{MgH}_2/20 \text{ wt.\%S}$ and $\text{MgH}_2/5 \text{ wt.\% S}$ samples are presented. An activation energy of $193 \pm 38 \text{ kJ/molH}_2$ and a prefactor $A = 1 \cdot 10^8 \text{ s}^{-1}$ is found for the $\text{MgH}_2/20 \text{ wt.\% S}$ and $152 \pm 14 \text{ kJ/mol H}_2$ and a prefactor $A = 7.7 \cdot 10^7 \text{ s}^{-1}$ for $\text{MgH}_2/5 \text{ wt.\% S}$.

These values compare well to the pure ball milled MgH_2 activation energy that we measured to be $145 \pm 5 \text{ kJ/molH}_2$. However, in literature, the activation energy values for uncatalyzed ball milled MgH_2 vary within broad ranges, from 150 kJ/molH_2 to 200 kJ/molH_2 .^{21,23,44}

From these observations of the hydrogen desorption temperatures and activation energies we can conclude that the sulfur coating does not have a direct significant effect on the reactivity of the sample. Its role is mostly as a passivating layer against surface oxidation.

Further, the enthalpy of the hydride formation was determined using pressure composition isotherms measured at 523 K and 573 K for the $\text{MgH}_2/5 \text{ wt.\% S}$. The equilibrium pressures extracted from the pressure composition isotherms are used in a van't Hoff plot to determine the enthalpy and entropy of reaction as described in Chapter 3. The enthalpy of hydrogenation is estimated from the slope of the line while the intersect determines the entropy of reaction. The van't Hoff plot of the $\text{MgH}_2/5 \text{ wt.\% S}$ is plotted in Figure 7.13 which indicates that the enthalpy is $\sim 71 \text{ kJ/molH}_2$ and the entropy of reaction $\sim 129 \text{ J/KmolH}_2$. These are the typical values for bulk MgH_2 .^{22,23}

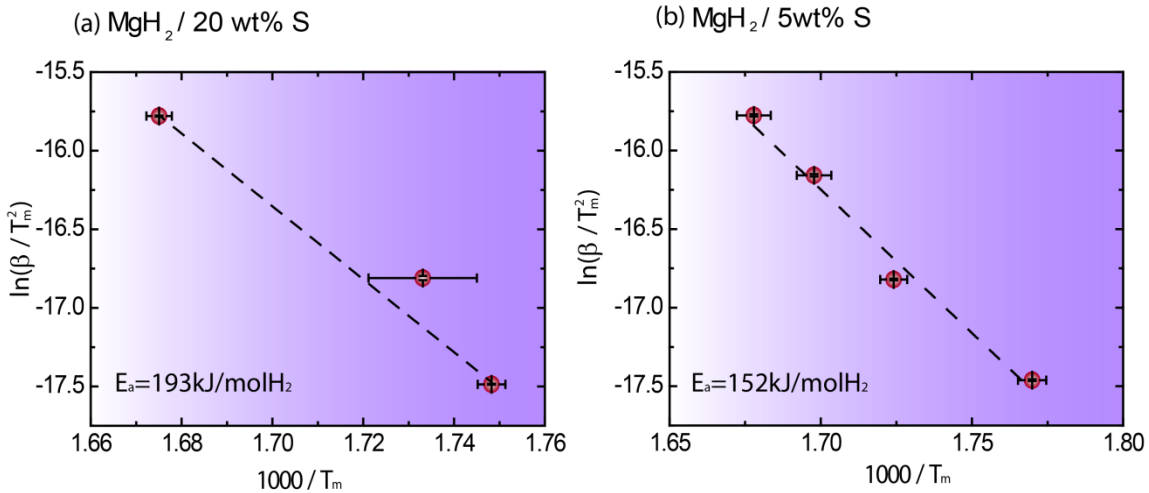


Figure 7.12. Kissinger plots for a) $\text{MgH}_2/20 \text{ wt.\% S}$, b) $\text{MgH}_2/5 \text{ wt.\% S}$

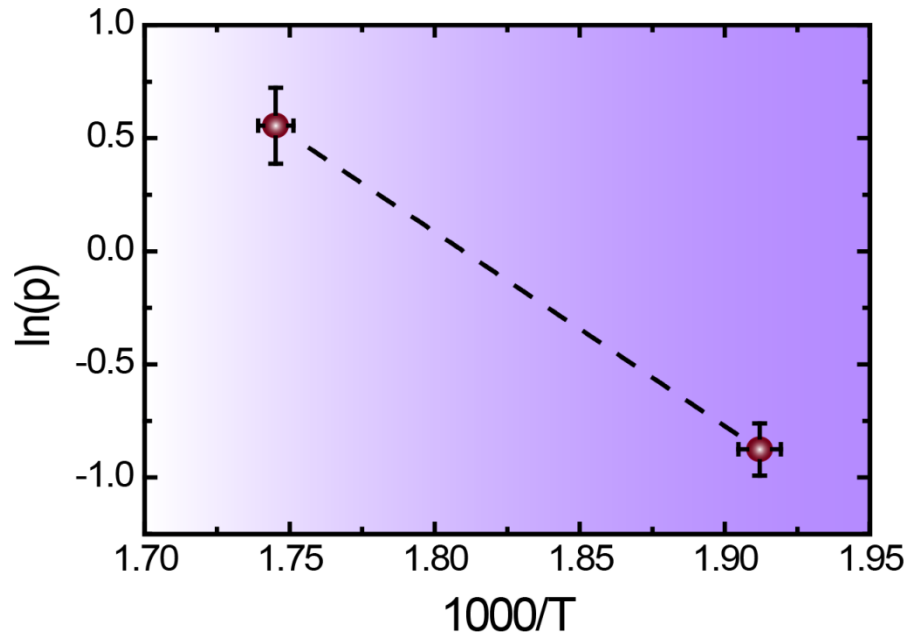


Figure 7.13. *van't Hoff plot determined for MgH₂/5wt%S*

7.3.4. Hydrogen sorption properties of air exposed sulfur coated MgH₂

It was clearly shown in the XRD and IR structural analysis of section 7.3.2 that the sulfur coated samples protect against the oxidation of ball milled MgH₂, when they are exposed in air for one week.

At a higher fraction of sulfur (20 wt. % S) and bigger crystallites, however, a nanosized Mg(OH)₂ still forms at the outermost surface. An important question that needs to be answered is how the hydrogen storage behavior of this type of sample is altered after exposure to air.

In Figure 7.14, two desorption curves measured for MgH₂/20 wt. % S as produced (Figure 7.14a) and after one week in air (Figure 7.14b) are plotted. Both curves are measured at a heating rate of 1 K/min and represent the second desorption of the samples. The S coated sample that was not exposed to air has a desorption peak at 573 K and the one exposed to air, at a slightly increased temperature of 588 K.

It is surprising to observe that in spite of the formation of a $\text{Mg}(\text{OH})_2$ layer at the surface of the S coating, hydrogen can still be inserted and released from the material. In the absence of the sulfur coating, even an amorphous $\text{Mg}(\text{OH})_2$ coating can have a dramatic effect on the kinetics of the kinetics of hydrogen sorption.²¹ Several hydrogen cycles were measured, showing a high reversibility of the hydrogenation/dehydrogenation reaction.

A effect of the reaction with air is observed for the air exposed 20 wt. % S coated samples and it is illustrated in the desorption profiles of Figure 7.15. At a first desorption, the peak temperature is at 589 K but at a second desorption at the same heating rate, the desorption peak is measured at 11 K lower temperature, at 578 K. It is not unusual that after a first cycle the desorption temperature is decreased. It can be regarded as an activation of the samples when lattice defects induced by ball milling are annealed and the sample has a more stable structure throughout the measurements. However, even when a third desorption profile is measured at the same heating rate, the desorption peak shifts 12 K to lower

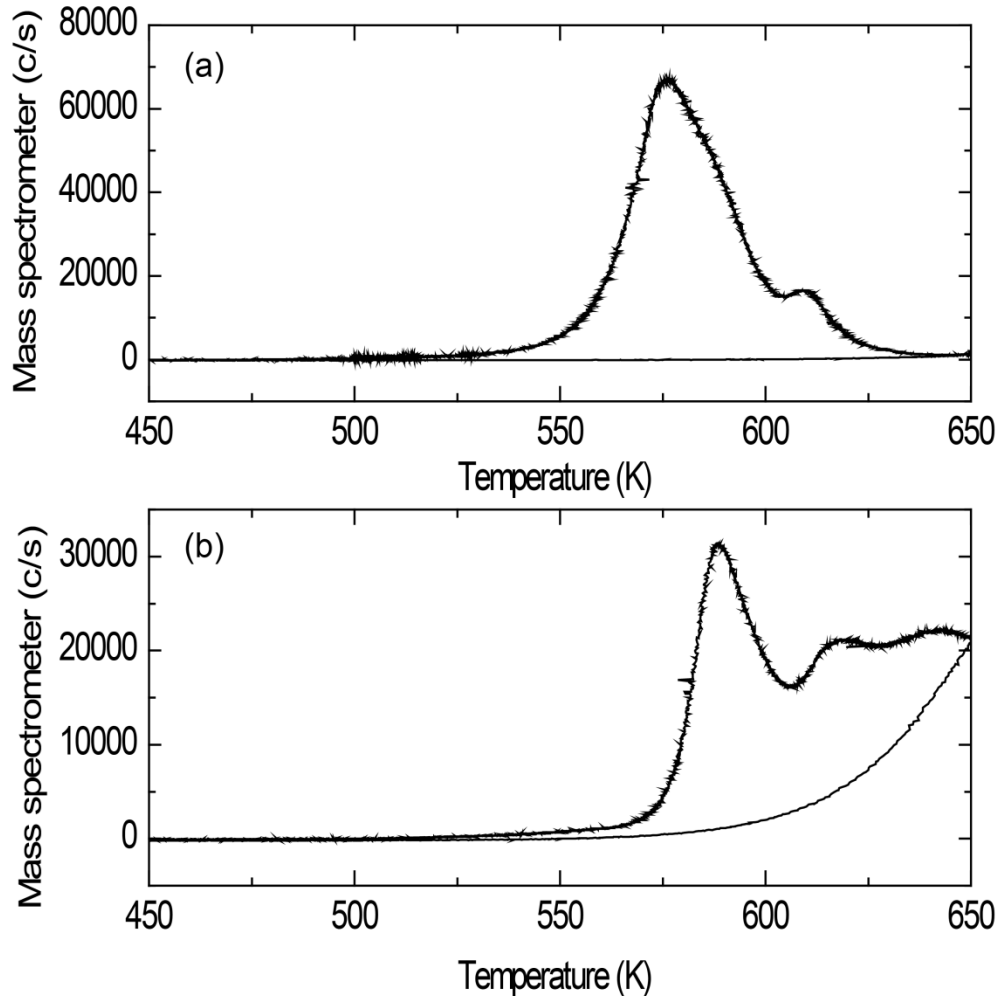


Figure 7.14. Thermal desorption profile measured at 1 K/min for a) as produced $\text{MgH}_2/20\text{wt}\%S$, b) $\text{MgH}_2/20\text{wt}\%S$ after air exposure for 1 week.

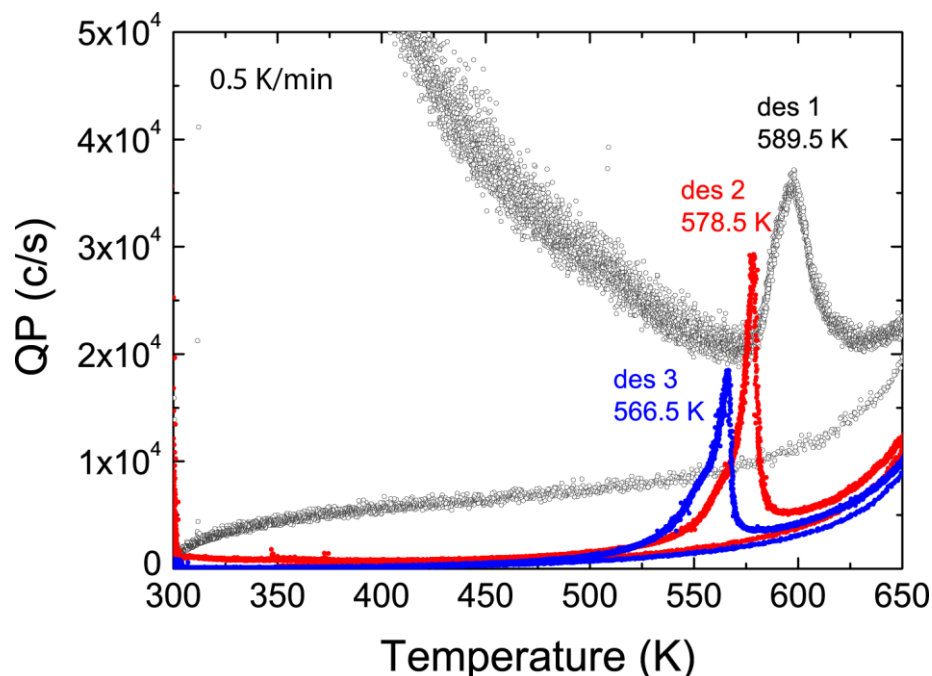


Figure 7.15. Thermal desorption profiles measured at 0.5 K/min for $MgH_2/20wt\%S$ after air exposure for 1 week.

temperatures from the second measurement, to 566 K. This effect was not observed for the S coated 20 wt. % sample that were not exposed to air. For this 20 wt.% S sample an effect of the reaction with air is thus still present. Because of the desorption peak shifts to lower temperatures, the height of the activation energy barrier cannot obviously be determined through a Kissinger analysis of the data.

In contrast to the sample that contains 20 wt. %S, the exposure to air for one week of the 5 wt. % S sample causes little change in the hydrogen cycling behavior. It has already been discussed from the XRD results (see section 7.3.2.) that the passivating coating is especially effective for the $MgH_2/5\text{ wt. \% S}$ because no MgO or $Mg(OH)_2$ could be detected after air exposure. This result is reflected in the hydrogen cycling experiments. The sample is remarkably stable upon cycling which became clear after four desorption measurements at 0.5 K/min that present almost identical desorption profiles. In Figure 7.16. thermal desorption profiles measured at different heating rates are plotted. Due to the high stability of the sample, a Kissinger analysis can be performed in order to determine the activation energy of the sample. Thus, in Figure 7.16b, the activation energy for hydrogen desorption is found to be $124 \pm 15 \text{ kJ/molH}_2$ for the $MgH_2/5\text{ wt. \% S}$ sample exposed to air for one week (the error given here is a collective error determined from two separate measurements and not solely from the linear fit in Figure 7.16b).

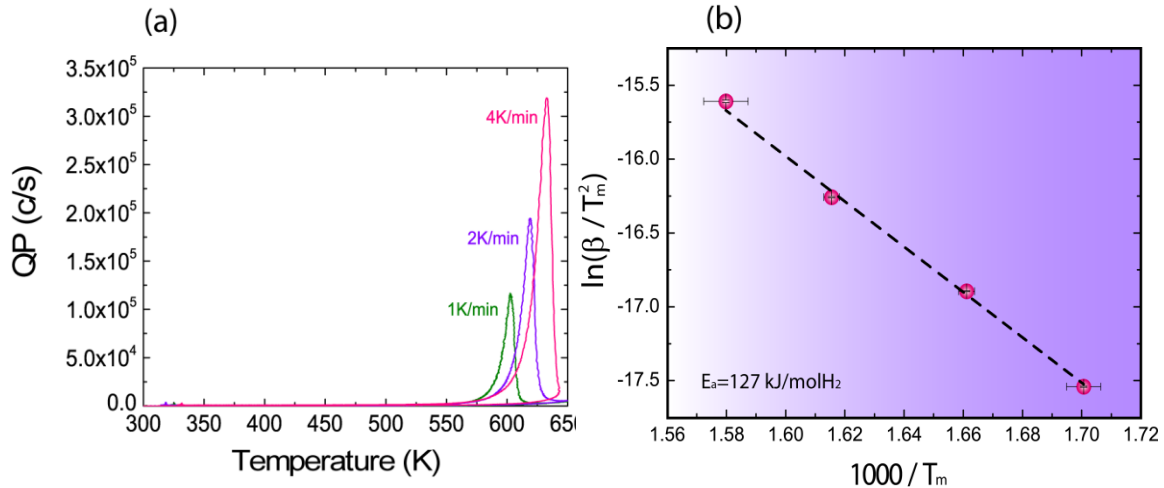


Figure 7.16. a) Thermal programmed desorption profiles measured at different heating rates and b) the resulting Kissinger plot for MgH₂/5wt.% S after exposure to air for one week.

An important characteristic that will make the sulfur containing samples widely accepted and used in devices is if sulfur or derivatives such as H₂S will not be released during heating treatments and hydrogen sorption experiments. In order to verify that S remains bound to the sample, a mass spectrometer scan in the mass range 1-50 is measured while the sulfur containing sample is heated up to 650 K. The result is presented in Figure 7.17 where the main peak is observed in the range 1.5-2.5 which is the typical signal from hydrogen which is desorbed from the sample. A very small signal is also observed in the range 17-18 and it is the typical signal for residual water in the setup. Sulfur has an atomic weight of 32 and H₂S of 34. Thus, if H₂S were released, a signal in the region around 32 and at 34 should be present. The very small signal detected in the region 32-34 can also be due to oxygen ions and it can be correlated with the nitrogen ion signal around 27-28. As our measurement range extends up to mass 50, we can conclude that H₂S is not detected by the mass spectrometer.

This result is an important step forward as it further confirms the stability of the S coating and leads towards the applicability of sulfur coatings in MgH₂ materials.

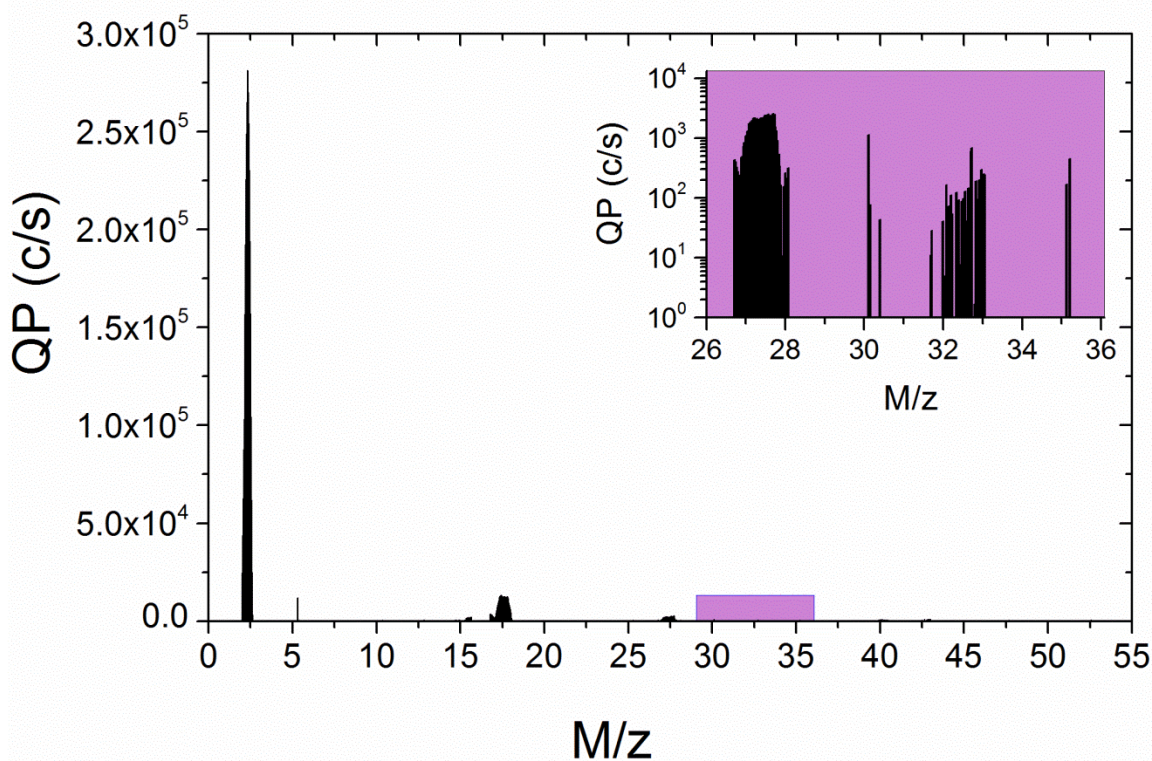


Figure 7.17. Mass spectrometer scan measured at 650 K on the air exposed $MgH_2/5$ wt.% S

7.4. Conclusions

In an attempt to create air resistant MgH_2 samples that will make it more economically viable solution of energy storage, a sulfur coating is created on the surface of ball milled MgH_2 powders. Structural studies showed that the sulfur coating it formed uniformly on the surface of the sample and has the desired effect of protecting from further oxidation for the 5 wt. % S sample. The presence of the sulfur coating acts effectively against surface oxidation of the MgH_2 samples without significantly altering the kinetics or the thermodynamics of the hydrogen sorption. However, from another 20 wt. % S sample it appears that depending on the materials preparation also less perfect protection against air can result, and varying hydrogen desorption characteristics.

References

- (1) Vons, V. A.; Anastasopol, A.; Legerstee, W. J.; Mulder, F. M.; Eijt, S. W. H.; Schmidt-Ott, A. Low-Temperature Hydrogen Desorption and the Structural Properties of Spark Discharge Generated Mg Nanoparticles. *Acta Materialia* 2011, *59*, 3070-3080.
- (2) Anastasopol, A.; Pfeiffer, T. V.; Schmidt-Ott, A.; Mulder, F. M.; Eijt, S. W. H. Fractal Disperse Hydrogen Sorption Kinetics in Spark Discharge Generated Mg/NbOx and Mg/Pd Nanocomposites. *Applied Physics Letters* 2011, *99*, 194103.
- (3) Callini, E.; Pasquini, L.; Piscopiello, E.; Montone, A.; Antisari, M. V.; Bonetti, E. Hydrogen Sorption in Pd-Decorated Mg--MgO Core-Shell Nanoparticles. *Applied Physics Letters* 2009, *94*, 221905-3.
- (4) Ingason, A. S.; Olafsson, S. Influence of MgO Nano-Crystals on the Thermodynamics, Hydrogen Uptake and Kinetics in Mg Films. *Thin Solid Films* 2006, *515*, 708-711.
- (5) Aguey-Zinsou, K. F.; Ares Fernandez, J. R.; Klassen, T.; Bormann, R. Using MgO to Improve the (De)Hydriding Properties of Magnesium. *Materials Research Bulletin* 2006, *41*, 1118-1126.
- (6) Krishnan, G.; Kooi, B. J.; Palasantzas, G.; Pivak, Y.; Dam, B. Thermal Stability of Gas Phase Magnesium Nanoparticles. *J. Appl. Phys.* 2010, *107*.
- (7) Jeon, K. J.; Moon, H. R.; Ruminski, A. M.; Jiang, B.; Kisielowski, C.; Bardhan, R.; Urban, J. J. Air-Stable Magnesium Nanocomposites Provide Rapid and High-Capacity Hydrogen Storage Without Using Heavy-Metal Catalysts. *Nat Mater* 2011, *10*, 286-290.
- (8) Makridis, S. S.; Gkanas, E. I.; Panagakos, G.; Kikkinides, E. S.; Stubos, A. K.; Wagener, P.; Barcikowski, S. Polymer-Stable Magnesium Nanocomposites Prepared by Laser Ablation for Efficient Hydrogen Storage. *International Journal of Hydrogen Energy* 2013, *38*, 11530-11535.
- (9) Cansizoglu, M. F.; Karabacak, T. Enhanced hydrogen storage properties of magnesium nanotrees with nanoleaves. *Materials Research Society Symposium Proceedings* 1216, 194-199. 2010.
- (10) Niessen, R. A. H.; Notten, P. H. L. The Influence of O₂ on the Electrochemistry of Thin Film, Hydrogen Storage, Electrodes. *Electrochimica Acta* 2005, *50*, 2959-2965.

- (11) Vermeulen, P.; Niessen, R. A. H.; Notten, P. H. L. Hydrogen Storage in Metastable $\text{Mg}_y\text{Ti}_{(1-y)}$ Thin Films. *Electrochemistry Communications* 2006, 8, 27-32.
- (12) Niessen, R. A. H.; Notten, P. H. L. The Influence of O_2 on the Electrochemistry of Thin Film, Hydrogen Storage, Electrodes. *Electrochimica Acta* 2005, 50, 2959-2965.
- (13) Earnshaw, A.; Greenwood, N. *Chemistry of the Elements, Second Edition*; Butterworth-Heinemann: 1997.
- (14) Schaumann, E. Sulfur Is More Than the Fat Brother of Oxygen. An Overview of Organosulfur Chemistry. In *Sulfur-Mediated Rearrangements I*; Schaumann, E., Ed.; Springer Berlin Heidelberg: 2007.
- (15) Yang, S.; Wang, F. Effect of Nanocrystallization on Sulfur Segregation in Fe-Cr-Al Alloy During Oxidation at 1000°C . *Oxidation of Metals* 2006, 65, 195-205.
- (16) Smialek, J. L.; Jayne, D. T.; Schaeffer, J. C.; Murphy, W. H. Effects of Hydrogen Annealing, Sulfur Segregation and Diffusion on the Cyclic Oxidation Resistance of Superalloys: a Review. *Thin Solid Films* 1994, 253, 285-292.
- (17) Painter, G. S.; Averill, F. W. Effects of Segregation on Grain-Boundary Cohesion: A Density-Functional Cluster Model of Boron and Sulfur in Nickel. *Phys. Rev. Lett.* 1987, 58, 234-237.
- (18) Kamakoti, P.; Morreale, B. D.; Ciocco, M. V.; Howard, B. H.; Killmeyer, R. P.; Cugini, A. V.; Sholl, D. S. Prediction of Hydrogen Flux Through Sulfur-Tolerant Binary Alloy Membranes. *Science* 2005, 307, 569-573.
- (19) Toby, B. H. EXPGUI, a Graphical User Interface for GSAS. *J. Appl. Cryst.* 2001, 34, 210-213.
- (20) Thomas, P. J.; Midgley, P. A. An Introduction to Energy-Filtered Transmission Electron Microscopy. *Topics in Catalysis* 2002, 21, 109-138.
- (21) Varin, R. A.; Jang, M.; Czujko, T.; Wronski, Z. S. The Effect of Ball Milling Under Hydrogen and Argon on the Desorption Properties of MgH_2 Covered With a Layer of $\text{Mg}(\text{OH})_2$. *Journal of Alloys and Compounds* 2010, 493, L29-L32.
- (22) Liang, G.; Huot, J.; Boily, S.; Van Neste, A.; Schulz, R. Catalytic Effect of Transition Metals on Hydrogen Sorption in Nanocrystalline Ball Milled MgH_2 -Tm (Tm=Ti, V, Mn, Fe and Ni) Systems. *Journal of Alloys and Compounds* 1999, 292, 247-252.

- (23) Huot, J.; Liang, G.; Boily, S.; Van Neste, A.; Schulz, R. Structural Study and Hydrogen Sorption Kinetics of Ball-Milled Magnesium Hydride. *Journal of Alloys and Compounds* 1999, 293-295, 495-500.
- (24) Ferreira, A. G. M.; Lobo, L. Q. The Low-Pressure Phase Diagram of Sulfur. *The Journal of Chemical Thermodynamics* 2011, 43, 95-104.
- (25) Mayer, R. Elemental Sulfur and Its Reactions. In *Organic Chemistry of Sulfur*; Oae, S., Ed.; Springer US: 1977.
- (26) Smith, D. H.; Seshadri, K. S. Infrared Spectra of $Mg_2Ca(SO_4)_3$, $MgSO_4$, Hexagonal $CaSO_4$, and Orthorhombic $CaSO_4$. *Spectrochimica Acta Part A: Molecular and Biomolecular Spectroscopy* 1999, 55, 795-805.
- (27) Friedrichs, O.; Sánchez-López, J. C.; López-Cartes, C.; Dornheim, M.; Klassen, T.; Bormann, R.; Fernández, A. Chemical and Microstructural Study of the Oxygen Passivation Behaviour of Nanocrystalline Mg and MgH_2 . *Applied Surface Science* 2006, 252, 2334-2345.
- (28) de Oliveira, E. F.; Hase, Y. Infrared Study and Isotopic Effect of Magnesium Hydroxide. *Vibrational Spectroscopy* 2001, 25, 53-56.
- (29) Raman, C. V. The Vibrations of the MgO Crystal Structure and Its Infra-Red Absorption Spectrum. *Proc. Indian Acad. Sci.* 1961, 54, 233-243.
- (30) Tobolsky, A. V. Polymeric Sulfur and Related Polymers. *J. polym. sci. , C Polym. symp.* 1966, 12, 71-78.
- (31) Thompson and, W. R. Single and Double Ionization of Atomic Oxygen by Electron Impact. *Journal of Physics B: Atomic, Molecular and Optical Physics* 1995, 28, 1321.
- (32) Paterson, J. H.; Chapman, J. N.; Nicholson, W. A. P.; Titchmarsh, J. M. Characteristic X-Ray Production Cross-Sections for Standardless Elemental Analysis in EDX. *Journal of Microscopy* 1989, 154, 1-17.
- (33) Jha, L. K.; Roy, B. N. Electron Impact Single and Double Ionization of Magnesium. *Eur. Phys. J. D* 2002, 20, 5-10.
- (34) Zaluska, A.; Zaluski, L.; Strom-Olsen, J. O. Synergy of Hydrogen Sorption in Ball-Milled Hydrides of Mg and Mg_2Ni . *Journal of Alloys and Compounds* 1999, 289, 197-206.
- (35) Liang, G.; Huot, J.; Boily, S.; Van Neste, A.; Schulz, R. Catalytic Effect of Transition Metals on Hydrogen Sorption in Nanocrystalline Ball Milled

- MgH₂-Tm (Tm=Ti, V, Mn, Fe and Ni) Systems. *Journal of Alloys and Compounds* 1999, 292, 247-252.
- (36) Zaluska, A.; Zaluski, L.; Strom-Olsen, J. O. Nanocrystalline Magnesium for Hydrogen Storage. *Journal of Alloys and Compounds* 1999, 288, 217-225.
- (37) Liang, G.; Huot, J.; Boily, S.; Schulz, R. Hydrogen Desorption Kinetics of a Mechanically Milled MgH₂+5at.%V Nanocomposite. *Journal of Alloys and Compounds* 2000, 305, 239-245.
- (38) Fernández, J. F.; Sánchez, C. R. Rate Determining Step in the Absorption and Desorption of Hydrogen by Magnesium. *Journal of Alloys and Compounds* 2002, 340, 189-198.
- (39) Redhead, P. A. Thermal Desorption of Gases. *Vacuum* 1962, 12, 203-211.
- (40) Saita, I.; Toshima, T.; Tanda, S.; Akiyama, T. Hydrogen Storage Property of MgH₂ Synthesized by Hydriding Chemical Vapor Deposition. *Journal of Alloys and Compounds* 2007, 446-447, 80-83.
- (41) Liang, G.; Boily, S.; Huot, J.; Van Neste, A.; Schulz, R. Mechanical Alloying and Hydrogen Absorption Properties of the Mg-Ni System. *Journal of Alloys and Compounds* 1998, 267, 302-306.
- (42) Kissinger, H. E. Reaction Kinetics in Differential Thermal Analysis. *Analytical Chemistry* 2002, 29, 1702-1706.
- (43) Kissinger, H. E. Variation of peak Temperature with heating rate in Differential Thermal Analysis. *Journal of Research of the National Bureau of standards* 57[4], 217-221. 2009.
- (44) Zhao-Karger, Z.; Hu, J.; Roth, A.; Wang, D.; Kubel, C.; Lohstroh, W.; Fichtner, M. Altered Thermodynamic and Kinetic Properties of MgH₂ Infiltrated in Microporous Scaffold. *Chem. Commun.* 2010, 46, 8353-8355.

Summary

Reliable and affordable energy storage represents a bottleneck in a scenario where renewable energy sources become prominent on the energy market. With its high potential energy density and the natural abundance of the element, hydrogen gas is an attractive energy storage medium. But its gaseous nature, its high explosive potential and permeability of gaseous hydrogen through materials pose important limitations on its usability. Therefore, in the course of this thesis we set out to investigate hydrogen storage in stable solids, namely magnesium based materials.

The obvious advantages of magnesium as an energy storage material are its light weight, wide availability, high volumetric and gravimetric capacity and reversible reaction with hydrogen. The main challenges, however, are the relatively high stability of the MgH_2 ($\Delta H=75$ kJ/mol H_2), the slow kinetics of the hydrogen desorption and its high reactivity with air.

As hydrogen storage in Mg was intensely studied during the past forty years, it is a well described system. The novelty of our study, however, originates from the use of spark discharge generation as the synthesis method for Mg based nanomaterials. It is a bottom up method for synthesizing nanoparticles of conductive materials. Because it is a non-equilibrium technique it permits the synthesis of metastable phases that are generally not obtained in more conventional approaches. Besides, it is a versatile method that can be used in different gaseous environments and through various electrode configurations. In this manner nanocomposites and nanoscale mixtures of multiple components can be obtained. In this study, Mg nanoparticle agglomerates are obtained with a typical primary particle size below 15 nm (*Chapter 2*). Nanosized Pd and NbO_x catalysts are mixed *in situ* with Mg (*Chapter 2*) but also Mg-Ti nanocomposites are produced (*Chapter 3*). The introduction of an Ar/ H_2 gas mixture allows the *in situ* formation of MgH_x (*Chapter 5*) and $\text{Mg}_y\text{Ti}_{1-y}\text{H}_x$ (*Chapter 6*) hydrides.

The main drive for using nanomaterials and hence spark discharge generation is improving the kinetics of the hydrogen sorption reactions in Mg. As nanomaterials have a high surface to volume ratio, it shifts the rate limiting step from the hydrogen transport through bulk to the surface absorption. In *Chapter 2*, the hydrogen desorption kinetics from Mg, Mg/Pd and Mg/ NbO_x are analyzed. The broad desorption profiles in combination with detailed structural observations of inhomogeneity of the samples lead to the conclusion that the JMAK (Johnson-Mehl-Avrami-Kolmogorov) kinetic model is not applicable here. Instead, a more suitable kinetic model based on multiple activation energies for the system is proposed. In this way, the solid sample is effectively treated as a sum of sub systems with individual hydrogen

desorption characteristics. The distribution of activation energies in the measurement range is found to vary from 55 kJ/molH₂ to 120 kJ/molH₂. In spite of the nanosized character of the sample and the addition of transition metal catalysts (Pd and NbO_x), the average activation energy lies still around ~ 90 kJ/molH₂. A possible explanation for this is the presence of an MgO shell that can act as a barrier for hydrogen sorption. But also inhomogeneities in catalyst distribution combined with the reduced ability of Mg to spontaneously split the H₂ molecule may contribute to a higher activation energy.

Despite the minimum value of the activation energy for hydrogen desorption (55 kJ/molH₂) found for Mg/Pd and Mg/NbO_x mixtures, from the study in *Chapter 2* it is apparent that a purely kinetic approach for improving the cyclability of hydrogen in magnesium is not yet sufficiently homogeneous in these materials. Therefore, a more drastic thermodynamic change in the system will be desirable that can change the thermodynamic characteristics in most of the material.

For this reason, Mg/Ti nanocomposites synthesized by spark discharge generation are studied in *Chapter 3*. Mg and Ti are typically immiscible but when a non-equilibrium synthesis method is used, they can form a metastable alloy. At Ti compositions >15 at. %, a Mg_yTi_{1-y}H_x cubic hydride forms. In the thermodynamic study of Mg/Ti nanocomposites in *Chapter 3*, a reduced decrease in enthalpy of formation equaling -45 kJ/molH₂ is determined experimentally. This remarkably reduced enthalpy of formation change of the hydride is difficult to explain in a simple model. An interplay of several mechanisms such as Mg/MgH₂-TiH₂ interfaces, lattice mismatch between Mg and TiH₂, and open volume defects can be used to explain the thermodynamic properties of the system. Besides the lower enthalpy, the reduction in entropy upon hydride formation is also decreased. A linear relation between enthalpy and entropy is found to hold for several nanoparticulate samples. Moreover, both the Mg/Ti alloy and the Mg_yTi_{1-y}H_x produced by spark discharge show a relatively high stability when exposed at temperatures of about 573 K for hundreds of hours in spite of being thermodynamically immiscible.

This remarkable stabilization of the Mg/Ti systems is studied in more detail in *Chapter 4*. Mg/Ti thin films produced by DC magnetron sputtering are heated up to temperatures up to 573 K and their structure evolution and reactivity with hydrogen is tested. At higher Ti fractions (30 at.%), a clear demixing of the metals is observed. At a low fraction of Ti (10 at.%) the alloy remains coherent in X-ray diffraction. However, the heating treatments induce irreversible microstructural changes that block the reaction with hydrogen. The results obtained in this chapter underline the importance of the micro and nanostructure of the samples and its overwhelming influence on the reactivity with hydrogen.

The reactivity of Mg with hydrogen can be stimulated by introducing hydrogen gas during the spark ablation of Mg. In this way, MgH_x can be formed in situ from the hydrogen plasma. These type of materials are investigated in *Chapter 5*. The concentration of the Ar/H₂ gas mixture has a strong impact on both the crystallinity and amount of product obtained. Moreover, at low hydrogen concentrations, we observed that a large amount of H is dissolved in the Mg lattice. These extended solubility limits of H in the hcp Mg lattice have very rarely been observed in pure Mg samples but they show the altered reactivity of nano scale Mg with H.

Combining the results obtained in *Chapter 2* to obtain low activation energies and *Chapter 3* to achieve low enthalpy of formation and the in situ hydride formation in *Chapter 5* seems promising to achieve a high performance hydrogen storage material.

Indeed, in *Chapter 6*, $Mg_yTi_{1-y}H_x$ is obtained using spark discharge generation. The structural analysis revealed that there is a single active phase and it is a fluorite type hydride also obtained after the hydrogenation of Mg/Ti nanocomposites in *Chapter 3*. Its enthalpy of formation was experimentally determined to be 45 kJ/molH₂. In *Chapter 6*, a detailed kinetic analysis of hydrogen release from $Mg_yTi_{1-y}H_x$ is performed and the single activation energy is found to be 55 kJ/molH₂. This value is the lower limit determined in the multiple activation energy analysis of *Chapter 2*. Thus, by introducing Ti and H₂ gas during the synthesis, we have effectively succeeded in selecting the fast reacting part of the sample. Besides the low activation energy, the actual hydrogen release temperature is about 373 K which makes this material very interesting for mobile applications. On top of this, the cubic $Mg_yTi_{1-y}H_x$ remains stable provided that temperature treatments do not exceed ~ 523 K. The amount of hydrogen that can be cycled is somewhat less than the full capacity, however.

Another major practical hindrance of using MgH₂ is its air sensitivity. We tackle this problem in a novel approach by creating a sulfur coating on the MgH₂ surface. In *Chapter 7*, a structural analysis of air exposed sulfur coated samples shows that the ultra-thin coating (5nm) acts effectively in preventing the oxidation of MgH₂ while hydrogen sorption remains unaffected.

In this thesis, Mg based nanomaterials with improved potential for applications as hydrogen stores are developed and analyzed. We have addressed the key issues of slow sorption kinetics, high stability and air sensitivity of MgH₂ and provided viable solution directions to these challenges.

Samenvatting

Betrouwbare en betaalbare energie-opslag is een knelpunt in een scenario waarin hernieuwbare energiebronnen prominenter worden op de energiemarkt. Dankzij de hoge potentiële energie dichtheid, is waterstof gas een aantrekkelijk energie-opslagmedium. Maar het gasvormige karakter, het hoge explosieve potentieel van gasvormige waterstof en de permeatie door materialen vormen een belangrijk beperking voor de praktische bruikbaarheid. Om deze reden wordt in de loop van dit proefschrift waterstofopslag in vaste stoffen uiteengezet, namelijk in magnesium gebaseerde materialen. De voor de hand liggende voordelen van magnesium als een energie-opslag materiaal zijn het lage gewicht, ruime beschikbaarheid, hoge volumetrische en gravimetrische capaciteit en omkeerbare reactie met waterstof. De belangrijkste uitdagingen zijn echter de relatief hoge stabiliteit van de gevormde MgH_2 ($\Delta H = 75 \text{ kJ/molH}_2$), de langzame kinetiek van de waterstofdesorptie en de hoge reactiviteit met lucht.

Doordat waterstofopslag in Mg intensief bestudeerd is tijdens de afgelopen veertig jaar, is er al veel bekend van het systeem. De nieuwigheid van onze studie is echter afkomstig van het gebruik van *spark discharge generation* als de synthesemethode van de Mg gebaseerde nanomaterialen. Het is een *bottom up* werkwijze voor het synthetiseren van nanodeeltjes van geleidende materialen. Omdat het een niet-evenwichts techniek is, het maakt het de synthese van metastabiele fasen mogelijk die doorgaans niet met meer conventionele benaderingen kunnen worden verkregen. Daarnaast is het een veelzijdige werkwijze die kan worden gebruikt in verschillende gasvormige omgevingen en via verschillende elektrode configuraties. Op deze wijze kunnen nanocomposieten en nanoschaal mengsels van meerdere componenten worden gemaakt. In deze studie worden Mg nanodeeltjes in agglomeraten geproduceerd met typische primaire deeltjesgrootte van minder dan 15 nm (Hoofdstuk 2). Nanoschaal Pd en NbO_x katalysatoren worden *in situ* gemengd met Mg (Hoofdstuk 2), maar ook Mg-Ti nanocomposieten worden geproduceerd en bestudeerd (Hoofdstuk 3). De introductie van een Ar / H_2 gasmengsel maakt de *in situ* vorming van MgH_x (Hoofdstuk 5) en $Mg_yTi_{1-y}H_x$ (Hoofdstuk 6) hydrides mogelijk.

De voornaamste drijfveer voor het gebruik van nanomaterialen en dus *spark discharge generation* is de kinetische verbetering van de waterstof opname/ontlading in Mg. Als nanomaterialen een hoge oppervlak en volume verhouding hebben, verschuift de snelheidsbepalende stap van het transport van waterstof van bulk transport naar meer oppervlakte absorptie. In hoofdstuk 2 worden de desorptiekinetiek van waterstof uit gehydreerd Mg,

Mg/Pd en Mg/NbO_x geanalyseerd. De brede desorptie profielen in combinatie met gedetailleerde structurele observaties van inhomogeniteit van de monsters leidt tot de conclusie dat een JMAK (Johnson-Mehl-Avrami-Kolmogorov) kinetisch model hier niet van toepassing is. In plaats daarvan wordt een geschikt kinetisch model op basis van meerdere activeringsenergieën voor het voorgestelde systeem toegepast. Op deze wijze wordt het vaste nanogestructureerde monster effectief behandeld als een som van subsystemen met individuele waterstofdesorptie kenmerken. De verdeling van activeringsenergieën varieert van 55 kJ/molH₂ tot 120 kJ/molH₂. Ondanks de nanostructurering monster en het toevoegen van overgangsmetaal katalysatoren (Pd en NbO_x), ligt de gemiddelde activeringsenergie steeds rond ~90 kJ/molH₂. Een mogelijke verklaring hiervoor is de aanwezigheid van een dunne MgO laag die als een barrière voor waterstof sorptie kan werken. Maar ook inhomogeniteiten in katalysatorverdeling gecombineerd met het minder goed spontaan splitsen of vormen van het H₂ molecuul kan aan een hogere activeringsenergie bijdragen.

Ondanks de lage gemeten waarde van de minimale activeringsenergie voor waterstofdesorptie (55 kJ/molH₂) die gevonden is voor Mg/Pd en Mg/NbO_x mengsels in de studie in hoofdstuk 2, blijkt dat een zuiver kinetische benadering voor het verbeteren van waterstof opname/ontlading in magnesium niet overal in het sample optreedt, niet homogeen is. Daarom is ook een thermodynamische wijziging van het systeem gewenst die liefst het hele materiaal beïnvloedt.

Om de thermodynamica te beïnvloeden zijn Mg/Ti *spark discharge generated* nanocomposieten in Hoofdstuk 3 geanalyseerd. Mg en Ti zijn als bulk materiaal typisch niet mengbaar maar wanneer een non-equilibrium synthesewerkwijze wordt gebruikt, kunnen ze een metastabiele verbinding vormen. Bij Ti > 15 at.%, vormt het een Mg_yTi_{1-y}H_x kubische hydride. In de thermodynamische studie van Mg/Ti nanocomposieten in hoofdstuk 3, is een lage enthalpie van -45 kJ/molH₂ experimenteel bepaald voor een deel van de opgeslagen waterstof. Deze opmerkelijk lage enthalpie kan moeilijk in een eenvoudige model verklaard worden.. Een samenspel van diverse mechanismen zoals Mg/MgH₂-TiH₂ interfaces, kristalrooster mismatch tussen Mg en TiH₂, en open volume gebreken kunnen worden gebruikt om de thermodynamische eigenschappen van het systeem uit te leggen. Naast de lagere enthalpie afname bij hydride vorming, is ook de afname in entropie ook afgenomen. Een lineaire relatie tussen enthalpie en entropie veranderingen blijkt te gelden voor verschillende nanodeeltjes monsters. Bovendien hebben zowel de Mg/Ti en de Mg_yTi_{1-y}H_x een relatief hoge stabiliteit bij blootstelling aan temperaturen van ongeveer 573 K gedurende honderden uren, ondanks de thermodynamische niet-mengbaarheid van Mg en Ti.

Deze opmerkelijke stabilisatie van de Mg/Ti-systemen wordt in meer detail bestudeerd in hoofdstuk 4. Mg/Ti dunne films geproduceerd door DC magnetron sputtering worden verhit tot 573 K. Hun structuur evolutie en reactiviteit met waterstof wordt getest. Bij hogere fracties Ti (30 at.%), wordt een duidelijk ontmenging van de metalen waargenomen. Bij een kleine fractie van Ti (10 at.%) blijft het Mg-Ti mengsel blijft coherent voor röntgendiffractie. De warmte behandelingen induceren een onomkeerbare microstructurele veranderingen die de latere reactie met waterstof blokkeren. Deze resultaten onderstrepen het belang van de micro- en nanostructuren van de monsters en de overweldigende invloed op de reactiviteit met waterstof.

De reactiviteit van Mg met waterstof kan worden gestimuleerd door het introduceren van waterstofgas tijdens de *spark discharge generation* van Mg. Zo kan MgH_x in situ worden gevormd uit het waterstof plasma. Dit soort materialen worden bestudeerd in hoofdstuk 5. De concentratie van de Ar/ H_2 gasmengsel heeft een sterke invloed op zowel de kristalliniteit als de hoeveelheid van het product. Bovendien, bij lage concentraties waterstof, kan een grote hoeveelheid H in de Mg roosters van de nanodeeltjes zijn opgelost. Deze uitgebreidere oplosbaarheidsgrens van H in het hcp Mg rooster is slechts zeer zelden eerder waargenomen in zuivere Mg monsters, maar het geeft de veranderde reactiviteit van nano grootte Mg met H_2 aan.

Het combineren van de resultaten van laag activeringsenergieën, lage enthalpie en de *in situ* vorming van hydride lijkt veelbelovend voor een Mg gebaseerd waterstofopslag materiaal met verhoogde prestaties.

Inderdaad, in hoofdstuk 6, wordt $Mg_yTi_{1-y}H_x$ verkregen met behulp van *spark discharge generation*. Uit de structurele analyse bleek dat er een actieve fluoriet structuur hydride is verkregen na de H opname van Mg/Ti nanocomposieten, vergelijkbaar met wat in hoofdstuk 3 gestudeerd is. In hoofdstuk 6 wordt een gedetailleerde kinetische analyse van waterstof ontlading uit $Mg_yTi_{1-y}H_x$ uitgevoerd, en de activatie-energie bij niet te hoge temperatuur blijkt nu voor het hele materiaal 55 kJ/molH_2 te zijn. Deze waarde is de ondergrens bepaald bij de meervoudige activeringsenergie analyse van hoofdstuk 2. Dus door invoering van H_2 gas tijdens de synthese, hebben wij daadwerkelijk het snel reagerende deel van het monster selectief kunnen produceren. Naast deze lage activeringsenergie, maakt de werkelijke desorptie temperatuur van ongeveer 373 K dit materiaal zeer interessant voor mobiele toepassingen. Daarenboven blijft de kubische $Mg_yTi_{1-y}H_x$ structuur stabiel tot een temperatuurbehandeling van $\sim 523 \text{ K}$.

Een andere belangrijke praktische belemmering van nano MgH_2 materialen is de luchtgevoeligheid. We hebben hiervoor een oplossings richting gevonden door een zwavel coating op het oppervlak MgH_2 te maken. In hoofdstuk 7 blijkt uit een structurele analyse van de monsters met een zwavel coating dat de ultra dunne coating (5 nm) doeltreffend werkt voor het voorkomen van de oxidatie van MgH_2 terwijl de waterstofsorptie onaangetast blijft.

In dit proefschrift worden Mg gebaseerde nanomaterialen met een versterkt potentieel voor toepassingen als waterstofopslag-materialen ontwikkeld en geanalyseerd. We hebben daarbij belangrijke kwesties van de trage absorptie kinetiek, de hoge stabiliteit en de lucht gevoeligheid van MgH_2 aangepakt.

Appendix

Background in X-ray diffraction

Due to the low amount of sample produced by spark discharge generation, intense scattering from the XRD sample holder is recorded in the X-ray diffractograms. Measuring an empty XRD sample holder allows us to account for this significant background contribution as it can be seen in Figure A1.

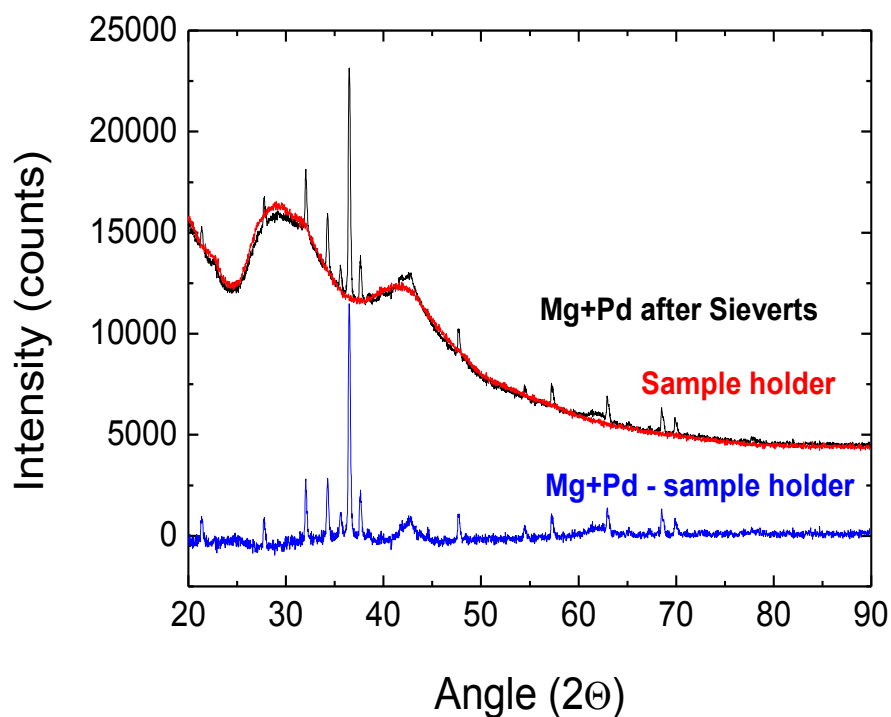


Figure A1. X-ray diffractograms of the spark discharge generated Mg/Pd sample (black) and the empty XRD sample holder (red) and the difference between the two diffractograms (blue) (see Figure 2.3b)

List of Publications

1. *Towards air resistant sulfur coated MgH_2* , Anca Anastasopol, Joost Middelkoop, Ugo Lafont, S.W.H. Eijt, Fokko M. Mulder, manuscript in preparation.
2. *Low temperature hydrogen desorption of in situ spark discharge generated $Mg_yTi_{1-y}H_x$ nanoparticles*, A. Anastasopol, M.J. Klein, T.V. Pfeiffer, J. Middelkoop, A.Schmidt-Ott, F.M.Mulder, S.W.H. Eijt, manuscript in preparation.
3. *Phase segregation of Mg_yTi_{1-y} and $Mg_yTi_{1-y}H_x$ thin films at high temperatures*, A. Anastasopol, J. Middelkoop, U. Lafont, H. Schreuders, B. Dam, F.M. Mulder, S.W.H. Eijt, manuscript in preparation.
4. *Evidence of the existence of the α -phase in MgH_x nanoparticles synthesized by spark discharge generation*, Tobias Pfeiffer, Anca Anastasopol, Joost Middelkoop, Ugo Lafont, Elsa Callini, Andreas Borgschulte, Andreas Schmidt-Ott, Fokko Mulder, Stephan Eijt, manuscript in preparation
5. *Probing hydrogen spillover in $Pd@MIL-101(Cr)$ with a focus on hydrogen chemisorption*, P.A. Szilágyi , E. Callini , A. Anastasopol , C. Kwakernaak , S. Sachdeva , R. van de Krol , H. Geerlings , A. Borgschulte , A. Züttel , B. Dam , Phys Chem Chem Phys. 2014 Mar 28;16(12):5803-9 DOI: 10.1039/c3cp54898h.
6. *Reduced Enthalpy of Metal Hydride Formation for Mg–Ti Nanocomposites Produced by Spark Discharge Generation*, Anca Anastasopol, Tobias V. Pfeiffer, Joost Middelkoop, Ugo Lafont, Roger J. Canales-Perez, Andreas Schmidt-Ott, Fokko M. Mulder, Stephan W.H. Eijt , Journal of the American Chemical Society, 2013, 135, 7891-7900, DOI: dx.doi.org/10.1021/ja312341.
7. *Electrostatic spray pyrolysis of $LiNi_{0.5}Mn_{1.5}O_4$ films for 3D Li-ion microbatteries*, Ugo Lafont, Anca Anastasopol, Esteban Garcia-Tamayo, Erik Kelder, Thin Solid Films, Volume 520, Issue 9, 29 February 2012, Pages 3464-3471, DOI: 10.1016/j.tsf.2011.12.041.
8. *A new feature of the reduction–diffusion process applied for the synthesis of magnetocaloric $LaFe_{13-x}Si_x$ compounds*, C.S. Teixeira, L. Caron, A. Anastasopol, S.W.H. Eijt, J.A. Lozano, E. Brück, P.A.P. Wendhausen, Journal of Alloys and Compounds, Volume 541, 15 November 2012, Pages 84-87, DOI: 10.1016/j.jallcom.2012.05.112.
9. *In-situ Hydrogen Sorption 2D-ACAR Facility for the Study of Metal Hydrides for Hydrogen Storage*, W.J. Legerstee, J. de Roode, A. Anastasopol, C.V. Falub, S.W.H. Eijt, Physics Procedia, Volume 35, 2012, Pages 22-27, DOI: 10.1016/j.phpro.2012.06.005

10. *Thermal stability of Mg_yTi_{1-y} thin films investigated by positron annihilation spectroscopy*, A. Anastasopol, S. W. H. Eijt, H. Schut, F.M. Mulder, F. Plazaola, B. Dam, *Physics Procedia*, (2012), 35, 16-21, DOI: 10.1016/j.phpro.2012.06.004
11. *Fractal disperse hydrogen sorption kinetics in spark discharge generated Mg/NbO_x and Mg/Pd nanocomposites*, Anca Anastasopol, Tobias V. Pfeiffer, Andreas Schmidt-Ott, Fokko M. Mulder, Stephan W.H. Eijt, *Applied Physics Letters*, 2011, 99, 194103, dx.doi.org/10.1063/1.3659315
12. *Low-temperature hydrogen desorption and the structural properties of spark discharge generated Mg nanoparticles*, V.A. Vons, A. Anastasopol, W.J. Legerstee, F.M. Mulder, S.W.H. Eijt, A. Schmidt-Ott, *Acta Materialia*, 2011, 59, (8), 3070-3080, 10.1016/j.actamat.2011.01.047
13. *Layer-resolved study of the Mg to MgH_2 transformation in Mg–Ti films with short-range chemical order*, S. W. H. Eijt, H. Leegwater, H. Schut, A. Anastasopol, W. Egger, L. Ravelli, C. Hugenschmidt, B. Dam, *Journal of alloys and compounds*, (2011), 509, 2, S567–S571, DOI:10.1016/j.jallcom.2010.09.157

Acknowledgements

This PhD project was for me a journey. Now when I stop and look back at the past four years I can say it was a challenging and beautiful period in my life and career. It was a journey towards maturity in both a personal but also professional sense. For the rich experiences of the past four years I want to thank the special people that I had the privilege to meet, to work with and to learn from.

Therefore I acknowledge here the efforts of my supervisors, Dr. Stephan Eijt and Prof. Dr. Fokko Mulder. In the course of the past four and a half years I have learned a lot about project management, research, supervision of students and scientific integrity under their guidance. I would like to personally thank you for your patience, friendliness and dedication.

Next, I would like to thank the technical support staff of FAME who was always ready to answer questions and help in setting up experiments. Here I would like to mention Ing. Walter Legerstee, Ing. Michel Steenvoorde, Drs. Kees Goubitz, Ing. Jan de Roode, Ing. Fred Nastepad, Ing. Piet van der Ende, Ing. Martijn de Boer, and Ing. Anton Lefering and all the technical staff of FAME and NPM2. Thank you Dr. Jouke Heringa for all your support with computer problems. Also, I am very grateful to Dr. Wim Bouwman for his patience in speaking Dutch to me and the beautiful experience of supervising students during the “Duurzame energie” course. I would also like to thank Prof. Ekkes Brueck, Dr. Niels van Dijk for our stimulating conversations, Dr. Marnix Wagemaker, Dr. Iulian Dugulan, Drs. Chris Duif and my office colleagues Swapna, Anna, Luana, Kun, Deepak, Fengjiao, Miao, Romain, Markus, Shasha, Jose, Lucas, Yibole, Wingkee, Leon, Chris, Maurits, Francois, Serge, Andre, Jeroen, Lambert, Prasad, Thang and of course, my dear friend Ines for the friendly and warm atmosphere in the office and outside. Thank you Drs. Jimmy Melskens for the nice discussions. Also, I would like to warmly thank the secretaries, Ilse van de Kraaij and Nicole Banga for their help in administration issues and organization of trips. Thank you to my master students. I have learned a lot from you and with you: Bevan Nyakuma, Gaurav Gupta, Roland Valk and Markus Klein.

The work presented in the current thesis is the result of the effort and collaboration between different groups within TUDelft: FAME, MECS and NSM. Here I would like to firstly mention my colleague Drs. Tobias Pfeifer who during the past four year has provided high quality spark discharge generated samples but also valuable feedback on writing and presentations. I would also like to thank Prof. Bernard Dam who has encouraged and fueled the collaboration with his group. Within the group of MECS, I would like to acknowledge especially Ing. Joost

Middelkoop for his professionalism and technical support in the lengthy thermodynamic measurements but also transmission electron measurements. Also, Ing. Hermann Schreuders for providing high quality thin film samples and Dr. Lennard Mooij for the hydrogenography measurements and Dr. Petra Szilagyi.

Thank you Dr. Luana Caron for introducing me to the research on magnetocaloric materials.

I would also like to thank Prof. Andreas Zuettel, Dr. Andreas Borgschulte and Dr. Elsa Callini for their hospitality during my visit at EMPA.

I am very grateful to Dr. Ugo Lafont who was not only my supervisor during my master project but also my friend. Thank you for being always open and helpful with the projects that I brought to you during my PhD. Thank you for the advice and guidance regarding the very valuable transmission electron measurements and scanning electron measurements.

The positron spectroscopy measurements were only possible with the help of Dr. Henk Schut whom I thank for his promptness and support.

A warm thank you to my paranymphs, Daniela Anastasopol and Ines Carvalho.

Ik wil ook mijn Nederlandse familie bedanken, Clemens and Elsbeth Middelkoop, oma Anna Bernard, Anouk and Patrick Munnik. Jullie hebben mij altijd gestimuleerd om Nederlands te leren. Jullie zijn er altijd voor mij geweest in de moeilijke maar ook gelukkige tijden van de afgelopen vijf jaar.

As vrea sa multumesc in mod deosebit familiei mele din Romania care au fost si continua sa fie punctul meu de sprijin in momente dificile dar si fericite. Va multumesc ca ati fost tot timpul aproape de mine si ca ati facut in asa fel sa nu se simta distanta dintre noi. Ii multumesc in principal mamei mele, Niculina Anastasopol, cea mai remarcabila femeie pe care o cunosc, care a resusit sa tina familia unita in cele mai dificile momente, tatalui meu Gica Anastasopol care nu mai este printre noi dar pe care il port in suflet tot timpul, fratelui meu Alexandru Anastasopol si sotiei lui Simona Anastasopol, surorii mele Daniela Anastasopol pentru ca sunteti cei mai buni prieteni ai mei. Ii multumesc in special bunicului meu tataia Mitica (Dumitru Veliu) pentru lectia de optimism pe care mi-a dat-o intotdeauna, bunicii, mamaia Anica (Anica Veliu) care nu mai este printre noi dar care va ramane pentru mine o sursa de inspiratie continua. Le multumesc nasilor nostri, Lucica si Aurel Nicolae pentru ospitalitatea si generozitatea lor deosebita.

The most important and rewarding project of the past four years was without doubt being pregnant, giving birth and being the mother of Nina. It was a big part of my PhD program. We have participated to the positron conference in Bristol and written articles together. In this role I learned to prioritize my projects and to organize my work more efficiently. Thank you, Nina.

Last but not least, thank you, my dear husband Joost (Iosif) Middelkoop for being sweet, encouraging and for always stimulating me to do better. Your professional and personal support have been invaluable. Moreover, you and Nina are my home.

Curriculum vitae



Anca Anastasopol was born on the 1st of November 1983 in the town of Medgidia, south-east Romania. Between 1990 and 2002 she followed the primary school, gymnasium and secondary school with a physics –mathematics profile in the small village of Baneasa, Constanta, situated in the south of Romania. In spite of her love for languages and literature, she decided at the recommendation of her family to continue her studies in a technical discipline.

Therefore she followed her university studies between 2002-2007 at the Faculty of Physics, Chemistry and Petroleum Technology within the “Ovidius” University in Constanta, Romania. She graduated with the thesis: “Autoignition synthesis of novel high voltage spinels for Li-ion batteries cathode materials” written during an Erasmus exchange programme at the Delft University of Technology (Jan 2006-July 2006). This has been her first introduction to nanoscience in general and energy storage research in particular. A summer internship at the Technical University in Vienna has consolidated her knowledge and laboratory practice in analytical chemistry. At the completion of her studies she obtained the title of Bachelor of Chemistry from the “Ovidius” University in Constanta.

Obtaining a Huygens talent scholarship (Nuffic) allowed her to return to the Netherlands and continue her studies in the period of 2007-2009 by following the Nanoscience master at the Delft University of Technology and Leiden University. She had the opportunity to continue the research in Li-ion battery materials during the entire period of her master studies as a part time research assistant in the Nanostructured materials (NSM) at Delft University of Technology. The master graduation thesis was: “Electrostatic spray pyrolysis of active cathode materials for 3D thin film Li-ion batteries”. She graduated from the master program by obtaining the title of Master of Science and Engineer (Ir.).

Her increasing interest in energy storage materials lead to the PhD in the period 2009-2014 in Hydrogen Storage in Magnesium Nanoparticles at the Reactor Institute in Delft, Department of Radiation, Radionuclides and Reactors, in the group of Fundamental Aspects of Materials and Energy (FAME). The numerous collaborations and participation to national and international conferences lead to an increasing degree of maturity of her research which lead to several scientific publications and culminates with the present doctoral thesis.

